Synthetic models for the analysis and control of composite and sandwich aerospace structures in critical conditions

(Article begins on next page)

04 August 2020

RMIT
UNIVERSITY

Synthetic models for the analysis and control of composite and sandwich aerospace structures in critical conditions

A thesis submitted in fulfilment of the requirements for the degree of Doctor of Philosophy

Alessia Ascione

B.Eng (Aerospace), University of Naples Federico II
M.Eng (Aerospace), Politecnico di Torino

School of Engineering
College of Science Engineering and Health
RMIT University

April, 2019

Synthetic models for the analysis and control of composite and sandwich aerospace structures in critical conditions

Alessia Ascione

* * * * * *

I certify that except where due acknowledgement has been made, the work is that of the author alone; the work has not been submitted previously, in whole or in part, to qualify for any other academic award; the content of the thesis is the result of work which has been carried out since the official commencement date of the approved research program; any editorial work, paid or unpaid, carried out by a third party is acknowledged; and, ethics procedures and guidelines have been followed.

I hereby declare that, the contents and organisation of this dissertation constitute my own original work and does not compromise in any way the rights of third parties, including those relating to the security of personal data.

....

Alessia Ascione
Turin, April, 2019

Summary

The evolution of the aviation industry has always been driven by the achievement of better performances and the reduction of weight. One successful approach for saving weight is the design of aircraft structures able to work in *postbuckling* conditions. In addition, the ongoing trend of replacing metals with high-performance fibre composites has led to both lighter and more efficient airplanes.

However, the approaches employed for the design of isotropic material structures are not suitable for composites because of the different mechanical behaviour of these materials due to their physical and chemical properties. For this reason, new methodologies have been created to properly model the behaviour of composite structures and the phenomena caused by their heterogeneous nature. Moreover, additional failure mechanisms have to be considered for composites, such as the intra-laminar damages (the fibres or the matrix failure) and the delaminations.

The new analytical techniques developed for the analyses of composite beams can be grouped in three main categories: the Higher-Order theories, the Layer-Wise approaches and the Zigzag theories. The Higher-Order theories have been proven to be not enough accurate for highly heterogeneous composite beams that are moderately thick, whereas the Layer-Wise approaches are generally accurate but inefficient for laminates made of many layers. The Zigzag theories are a subclass of the general Layer-Wise theories but they have been developed in the way that the number of variables, thus the computational cost, is independent of the number of layers.

The Finite Element (FE) commercial codes are usually the preferred choice for the structural analysis because of their high accuracy and versatility to analyse even complex geometries and material laminations. However, highly-detailed FE models of composite beams are usually computationally inefficient in the commercial codes. Moreover, the computational effort further increases when nonlinear analyses are performed, as for the postbuckling analysis of composite beams, becoming unacceptable when elements like piezoelectric actuators are involved in nonlinear analyses.

Nevertheless, the finite element formulations based on the Refined Zigzag Theory (RZT), which is one of the Zigzag theories, have proven to be as accurate as the commercial codes and also more efficient. The RZT has already been assessed for

the static and free-vibration analyses of beams with highly heterogeneous material laminations, demonstrating its superior performances.

In this context, the present work has the primary objective of creating a successful methodology for the buckling and postbuckling analyses of composite and sandwich beams with piezoelectric actuators, able to reach the same accuracy as highly-detailed FE commercial code models with lower computational cost.

A literature review was conducted about the methodologies employed for the structural analyses of composite and sandwich beams. The research showed that the analytical and numerical methods used for the buckling and postbuckling analyses of composites were either based on theories not suitable for both composite laminated and sandwich beams or not enough efficient. In addition, the RZT was never employed for nonlinear postbuckling analyses, despite its superior capabilities. Hence, a new method based on the Refined Zigzag Theory was created for more efficient buckling and postbuckling analyses of both composite laminated and sandwich beams with piezoelectric actuators bonded to the structure. A finite element formulation based on the new RZT model was developed to extend the method to the analysis of beams of any laminations, boundary and loading conditions, with either continuous piezoelectric layers or a discrete number of piezoelectric patches, and able to predict the local buckling behaviour in sandwich beams.

As a first step, the RZT was extended introducing both the geometric nonlinearities and the geometric imperfections of the beam and also the inverse piezoelectric behaviour in the theory formulation. The Principle of Virtual Work for electro-mechanical fields was employed to obtain the nonlinear equilibrium equations based on the RZT for composite beams with piezoelectric actuator layers. The equilibrium equations were solved under specific assumptions on the beam properties and loading conditions. A model based on the RZT-beam finite elements was then created to find approximate solutions of the equilibrium equations in general situations. The Newton-Raphson method was employed for solving the nonlinear FE equilibrium equation.

The possibility of having a variation of thickness and lamination along the beam length was also taken into account using a strategy based on the Lagrange Multipliers method. This modification allowed the modelling of discrete piezoelectric patches bonded to the external surfaces of the beam and it was also the basis for modelling the local buckling of pre-delaminated beams.

The new RZT finite element model was numerically assessed for the buckling and postbuckling analyses of sandwich beams and composite laminated beams with piezoelectric actuators through a comparison with highly-detailed FE commercial code models. Firstly, the buckling and postbuckling analyses were performed for various sandwich beams with different geometrical and material properties and the RZT results were compared to those obtained by Abaqus, Nastran and a model based on Timoshenko beam finite elements. Then, the RZT model was assessed for

the analyses of composite beams with piezoelectric patches bonded to the external surfaces. The buckling and postbuckling analyses and the static response to the piezoelectric actuation were calculated using both the RZT and a highly-detailed Abaqus model.

The new model was validated experimentally. Foam core sandwich beams with carbon-fibre reinforced-polymer (CFRP) facesheets and monolithic beams with piezoelectric actuators bonded to their external surfaces were manufactured and tested at the RMIT University material testing laboratory. Specific support for each kind of beam were prepared to realise simply-supported boundary conditions. The sandwich beams were tested using the Instron compression-testing machine and the Southwell method was employed for calculating the critical buckling loads.

Two kind of tests were performed for the monolithic beams. Firstly, the static response increasing the voltage in the actuators was calculated measuring the transversal displacement of the beam. Subsequently, the beams were tested in compression for different values of voltage applied to the actuators to improve the beam postbuckling response. The Southwell method was used also in this case to calculate the effect of the piezoelectric actuation on the critical buckling load.

The tests demonstrated the excellent capabilities of the new RZT model for predicting the buckling and postbuckling behaviour of composite and sandwich beams, even including the effect of the piezoelectric actuation.

The new RZT-FE model was then employed for the numerical buckling analysis of a sandwich beam with a debonding between the core and the top facesheet. It was able to successfully predict the local buckling depending on the length of the debonding. Subsequently, the possibility of controlling the local instability was investigated considering piezoelectric actuators on the external surfaces of the beam and the postbuckling response was optimised through the application of a suitable voltage to the piezoelectric layers. The RZT model could identify the best voltage values and distribution along the beam length to avoid the local buckling of the sandwich beam.

The present work provides a new FE model which can be employed for the buckling and postbuckling analyses of composite laminated and sandwich beams (even highly heterogeneous laminations) with geometric imperfections and piezoelectric actuators. The major outcome of this effort is the possibility to perform complex nonlinear static analyses reaching the same accuracy of highly-detailed FE commercial code models but with a significantly lower computational cost. In addition, using the proposed method, the piezoelectric effect can be efficiently introduced in nonlinear postbuckling analyses, also for beams with delaminations.

Acknowledgements

Firstly, I would like to express my sincerest thanks and gratitude to my supervisors, Prof. Marco Gherlone and Prof. Adrian Orifici, for their guidance, encouragements and motivation during these years. They helped me to improve different aspects of my work and I'm glad I had the opportunity to have them as supervisors. Their support was fundamental to reach all my goals.

I would like to thank Prof. Pier Marzocca for his help during my time at the RMIT and I also thank him for making possible the joint-PhD program between the RMIT and the Politecnico di Torino.

I would like to express my gratitude to Paul, for his extraordinary help and precious advices. I owe him a lot and I will never forget all he has done for me, with patience and kindness.

I wish to thank the other people of the RMIT technical staff who gave their contribution to my experiments: Peter, Michael, David and Huw.

I would like to thank my friends around the world, those with whom I have shared very special moments in these years:
Andrea and Gerardo, without them I would have felt lost when I first arrived in Australia.
Iris, for our everyday talks, the psychological support and the long and relaxing walks; Caitlin, the younger sister I have never had and the sweetest girl ever, and Karen, who made me find a family on the other side of the world.
Elie, Antonio, Rohan, Enrico, Wenxin and Dian, my adventures and craziness mates.
Mary, my Australian friend and mum.
Alberto, Marco, Giovanni and Francesco, I thank them for sharing with me the PhD life in Turin.
Francesco, for having been by my side supporting every decision I made.
My friend Margherita, my soul sister.

I thank my parents and my sister, for being with me always and everywhere I go.

Contents

List of Tables

XI

List of Figures

XIII

Chapter 1

Introduction

A fundamental requirement for the design of aerospace structures is the light weight. One of the approaches adopted to reduce the aircraft weight is the *postbuckling* design, which allows the structures to work even after they buckle. Moreover, the demand of higher performances in the aerospace industry has led to a progressive replacement of conventional metals with high-performance fibre composites, also for primary structural components. Composite materials have superior physical properties and excellent specific strength and stiffness, thus they are widely employed for modern aircraft applications to further reduce the weight.

Among the high-performance composites, sandwiches represent a very smart solution for many applications of lightweight constructions. A typical sandwich structure is made of two facesheets, either thin metallic or composite, which are bonded to a honeycomb or foam core. The low density core increases the stiffness without significantly affecting the overall weight. As a result, the sandwich is stiff, light and has a high energy absorption capability, e.g. under impact loading. Moreover, the foam core sandwich structures have proven to be considerably better than honeycombs in terms of manufacturing costs, time (simpler production process) and structural weight. Helicopter rotor blades, plane flight control surfaces and landing gear doors are just some examples where foam core sandwiches have been successfully employed.

In the framework of improving the structural response without increasing the weight, an approach which has got great attention is the use piezoelectric sensors and actuators to modify the postbuckling response.

The design methodologies used for isotropic structures are not suitable for composites, especially if these are made of highly heterogeneous materials like sandwiches. In addition, the design of active systems made of structures with piezoelectric actuators and sensors, requires models which take into account the electromechanical coupling between the structure and the piezoelectric elements.

In the last 50 years, many theories and numerical methods have been developed to better predict the behaviour of composites. Most of these approaches are usually

efficient but have limitations on their applicability, e.g. they work well only for composite laminates and not for highly heterogeneous material structures. On the other hand, the finite element (FE) commercial codes are very versatile and they can be successfully employed for the analyses of even complex geometries and material laminations. This is why they are usually the preferred choice for structural analyses. However, a major drawback associated to the usage of FE commercial codes is the computational effort, which can be considerably high when the modelled structure is made of composite material.

The computational cost of the FE commercial codes for composites and sandwiches significantly increases when buckling and postbuckling analyses are performed, even in case of simple geometries like beams, especially if they have piezoelectric elements. The demand of accurate predictions of the phenomena that can lead to in-service failures, such as the buckling of primary structural components, and also the possibility to investigate the effect of piezoelectric actuators on the postbuckling response of composite structures leads to the need of new tools and methodologies as accurate as FE commercial codes but more efficient.

1.1   Thesis outline

A literature review about the analytical and numerical approaches employed for the structural analyses of composite beams is presented in Chapter 2. The evolution of the methodologies which led to the latest theories and techniques for the prediction of the composite beams behaviours in static applications is shown, focusing on the compromise between accuracy and computational cost that can be achieved by each method. The review identifies the approaches suitable for both composite laminated and sandwich beams, showing that the Refined Zigzag Theory (RZT) is significantly attractive for its demonstrated accuracy and low computational cost. A research is conducted on the buckling and postbuckling phenomena and on the use of piezoelectric actuators for controlling both the global and local buckling, which are computationally demanding analyses when FE commercial codes are used. Then, the extension of the RZT to these applications appears very attractive because of the proven efficiency and accuracy of the theory, also for highly heterogeneous sandwich structures.

In Chapter 3, the RZT is extended introducing both the geometric nonlinearities, the geometric imperfections and the inverse piezoelectric behaviour in the beam theory formulation. The Principle of Virtual Work for electro-mechanical fields is employed to obtain the nonlinear equilibrium equations based on the RZT for composite beams with piezoelectric actuator layers. The solution of the equilibrium equations is found for a symmetrically laminated beam with two piezoelectric layers on the top and bottom surfaces, in simply-supported boundary conditions and subjected to both an axial-compressive load and a transversal sinusoidal load,

distributed along the beam length. The actuation of constant electric voltage is also considered in the piezoelectric layers. A finite model based on the RZT-beam finite elements is created to generate a tool able to solve the equilibrium problem of imperfect piezo-composite beams for any lamination, boundary and loading conditions. The Newton-Raphson solution of the nonlinear FE equilibrium equation is also calculated. Subsequently, the method is further generalised to the case of beams with geometric discontinuities to model both the presence of discrete piezo-electric patches on the external surfaces of the beam and also the separation of consecutive layers along the beam thickness (a pre-delaminated beam). A strategy based on the Lagrange multipliers method is used for these applications.

In Chapter 4, the new RZT-FE method is numerically assessed comparing its results for the buckling and postbuckling analyses of sandwich beams and composite laminated beams with piezoelectric actuators to those obtained by highly-detailed two-dimensional FE models realised in Nastran and Abaqus. In addition, a finite element model based on Timoshenko beam finite element is also employed for the analyses of the sandwich beams. The results show that RZT is generally very accurate for predicting the buckling and postbuckling behaviour of sandwich beams, even relatively thick or highly heterogeneous, whereas TBT is sufficiently accurate only for higher slenderness ratio. Very accurate results are obtained also for the buckling and postbuckling analyses of composite laminated beams with piezoelectric actuators and also for the evaluation of the static response to a piezoelectric actuation, where RZT is compared to highly-detailed three-dimensional Abaqus FE models. In all cases, the RZT model reaches the same level of accuracy of the commercial codes but with lower computational cost.

In Chapter 5, the tests performed for the experimental validation of the new RZT model are presented. It is shown in detail the manufacturing process of the sandwich beams and the monolithic beams, and the bonding process of piezoelectric actuators to the monolithic beams. It is reported the compression test procedure for both the sandwich and the piezo-composite beams, describing the supports realised for the simply-supported boundary conditions.

The response of the monolithic beams to an increasing voltage is calculated measuring the beam transversal displacement. Subsequently, they are tested in compression to evaluate the postbuckling behaviour for different values of voltage applied to the actuators.

The Southwell method is employed for calculating the critical buckling loads of all the beams.

In Chapter 6, the RZT method is employed for modelling the local buckling of sandwich beams with a debonding between the core and the facesheet. The method is assessed through a comparison to highly-detailed Nastran models in predicting the variation of the buckling loads and mode shapes, depending on the length of

the debonding, and the onset local buckling for extended debondings. Moreover, the method is further extended considering piezoelectric actuators on the beam for studying the best combination of voltage value and distribution along the beam length to control the local buckling.

The conclusion of this work is presented in Chapter 7, where the main outcomes of this project were reported with ideas for future works.

1.2   Outcomes

The primary goal of the present project has been the creation of a general formulation based on the RZT to reduce the computational cost and to increase the accuracy for the buckling and postbuckling analyses of composite laminated and sandwich beams with piezoelectric actuators.

The RZT for beams was extended introducing the geometric nonlinearites and imperfections. The inverse piezoelectric effect was also included in the formulation to take into account the possible presence of piezoelectric actuator layers.

The general form of the nonlinear equilibrium equations based on the RZT for piezo-composite beams was obtained employing the Priciple of Virtual Work for electro-mechanical fields, and a FE formulation was developed to solve the problem in general conditions. It was also indicated how to employ the Newton-Raphson method to iteratively solve the nonlinear FE equilibrium equation.

The finite element formulations allowed to solve the nonlinear equilibrium problem of composite beams with geometric imperfections and piezoelectric actuators, for any kind of boundary and loading condition and lamination, employing a theory suitable also for highly heterogeneous sandwich structures.

The use of a strategy based on the Lagrange multipliers method for the analysis of beams with piezoelectric actuators further generalised the model to the analysis of beams with generic geometric discontinuities, such as variations of the thickness and material lamination, or beams with offsets between consecutive finite elements, or also with a debonding/delamination between consecutive layers.

The comparison between the numerical results of the new RZT method and those of TBT or the FE commercial codes, for the buckling and postbuckling analyses of both sandwich and monolithic beams with piezoelectric actuator patches, demonstrated the superior capabilities of the RZT for its high accuracy and low computational cost.

The results of the experiments proved that the numerical methodologies considered effectively reproduced the buckling and postbuckling of composite laminated

and sandwich beams, thus they completely validated the new RZT model for the buckling and postbuckling analyses and for the static response to a piezoelectric actuation.

The comparison with a Nastran model, demonstrated the accuracy of the new RZT-FE model for the calculation of the buckling load of a sandwich beam with a debonding between the core and the facesheet, obtaining the same result as a highly-detailed two-dimensional model but with lower computational cost and a simpler model (one-dimensional finite elements).

In the new RZT-FE model, the piezoelectric actuators could be used while performing nonlinear postbuckling analyses (piezoelectric finite elements could not be used in Nastran and the Riks analysis could not be performed for the Abaqus models with piezoelectric elements). For this reason, the method was successfully employed for studying the control of the beam response in postbuckling conditions, for both the global buckling and the local buckling of a pre-debonded beam.

Some of the research and results presented in this thesis were published in:

A. Ascione, and M. Gherlone. ≪Nonlinear static response analysis of sandwich beams using the Refined Zigzag Theory≫. In: *Journal of Sandwich Structures and Materials* (2018), DOI: https://doi.org/10.1177/1099636218795381.

Chapter 2

Literature review

The literature review presented in this chapter was conducted to identify some of the gaps in the field of aerospace structures. It mainly focuses on the methods currently employed for modelling the behaviour of composite structures, in particular the trade-off between accuracy and computational cost and the buckling phenomenon.

2.1 Beam and plate theories for composite and sandwich structures

The use of classical theories for predicting the response of composite structures can lead to significantly erroneous results in terms of displacements, strains and stresses, buckling loads and natural frequencies. The kinematic assumptions of the classical Bernoulli-Euler beam Theory (BET) derive from the hypothesis that the beam cross-section remains planar and orthogonal to the beam deformed axis during the deformation, as shown in Fig.[2.1a]. The consequence of this hypothesis is that BET does not take into account the transverse-shear strain. The transverse-shear stresses are null for the Hooke's law and, consequently, the corresponding transversal shear forces vanish. In most cases, the assumption of zero-valued transverse-shear stresses is inconsistent, as for a beam subjected to a bending load. In general, the equilibrium between the internal and external forces cannot be satisfied if the transverse-shear strains are not considered, thus to solve this inconsistency the Cauchy's equilibrium equations are used to evaluate the shear stresses as the integral of the in-plane stresses (*a posteriori* calculation). Despite these limitations, the BET was demonstrated to be sufficiently accurate for predicting the bending response, the natural frequencies and the buckling behaviour of beams, even composite, with a high slenderness ratio, thus it was extensively used for its simplicity.

(a) BET. (b) TBT.
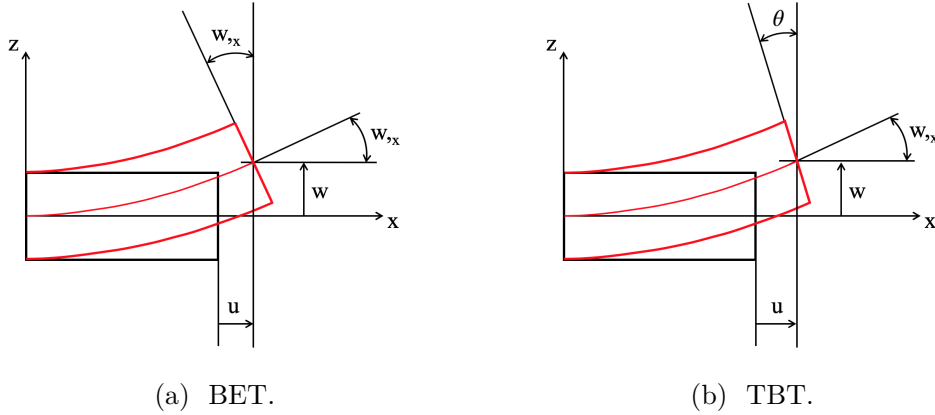
Figure 2.1: Kinematic assumptions of BET and TBT: the axial (u) and the transversal (w) displacements, the bending rotation of the beam transversal section ($w_{,x}$ for BET and θ for TBT).

The Timoshenko Beam Theory (TBT) [1], or more generally the First Order Shear Deformation Theory (FSDT), takes into account the transversal shear strain assuming that the bending rotation of the beam transversal section, θ, is a primary variable and does not correspond to the first derivative of the transversal displacement with respect to the beam longitudinal axis direction, $w_{,x}$ (see Fig.[2.1b]). A constant value of the transversal shear stress can be calculated with the Hooke's law but a shear correction factor is needed to give the exact average value of a C^1-continuous distribution of the stress along the beam thickness [1, 2]. This theory had a big success for its simplicity and because of the higher accuracy than BET in case of non-slender beams.

The classical theory and the TBT are the preferred choice for finding exact solutions to structural problems of homogeneous beams, but sometimes approximate methods are required, as in case of more complex geometries.

The Finite Element Method (FEM) [3] is the most used technique for the structural analysis in general conditions. It allows to find an approximate solution of the equilibrium equations for any kind of boundary and loading conditions. To employ the FEM, the kinematic variables of a theory have to be approximated using certain functions, called *shape functions*. The choice of the particular shape functions depends on the problem considered but the order of their differentiability class has to be sufficiently high to guarantee the correct definition of the strain energy function.

For this reason, one important advantage of TBT is that all the kinematic variables in the displacement field can be approximated using C^0-continuous shape functions. In BET, instead, the presence of the derivative $w_{,x}$, accounting for the bending rotation of the beam cross-section, results in C^1-continuous functions

required for the approximation of the kinematic variables.

The use of C^0 shape functions increases a lot the efficiency of the numerical calculations, thus TBT-based finite elements are widely used for many applications. However, the classical C^0-continuous shape functions used for formulating TBT finite elements can produce an overly-stiff solution in the analysis of slender beams, underestimating the beam response. This phenomenon is commonly known as *shear locking* [4].

Among the methods proposed in the literature to avoid the shear locking, the *anisoparametric* interpolation was proven to be one of the most effective [5–17]. This technique consists of approximating the deflection variable, w, with a complete polynomial one degree higher than the polynomial used for the approximation of the bending rotation variable, θ. Moreover, enforcing a constraint condition, the topology of the finite element (number of nodes and degrees of freedom per node) can be kept the same as the conventional 2-node beam finite elements.

The TBT finite elements are the one-dimensional finite elements in the commercial codes (like Simulia™ Abaqus [18] and MSC Nastran [19]) which allow the transverse-shear strain. In Abaqus, the TBT-based finite elements are optimised to be accurate for both thick and slender beams, thus they are classified as the most effective beam finite elements in Abaqus [20]. In addition, also the two-dimensional shell finite elements of the commercial codes are based on the FSDT and they are widely used for modelling thin-walled structures, even made of multilayer composite materials.

Nevertheless, neither the classical theories (BET for beams and the Classical Laminated Plate Theory for plates) or the FSDTs have enough kinematic variables to accurately describe the complex distribution of axial displacements along the thickness of beams or plates made of composite materials. As a consequence, the predictions of strains and stresses are incorrect. Moreover, the non-homogeneous nature of the composite materials introduces new failure mechanisms that are usually not considered in conventional homogeneous structures. The correct intra- and inter-layer modelling of strains and stresses is fundamental for the design of composite structures, thus new modelling techniques, more suitable than classical theories and FSDTs, had to be developed.

In [21], Pagano pointed out some limitations the classical theories had when used for composite laminates. He found the exact elasticity solutions for orthotropic composite laminates in cylindrical bending demonstrating that the Classical Laminated Plate Theory (CLPT) was accurate only for high span-to-depth ratios. The CLPT not only underestimated the plate transversal deflection, but also it was not able to correctly predict both the axial and the transversal shear stress distribution across the plate thickness for low span-to-depth ratios; his solutions for the axial displacement and axial strain distributions across the thickness of a beam with a span-to-depth ratio equal to 4 are shown in Fig.[2.2].

(a) Through-the-thickness axial displacement.

(b) Through-the-thickness axial stress.
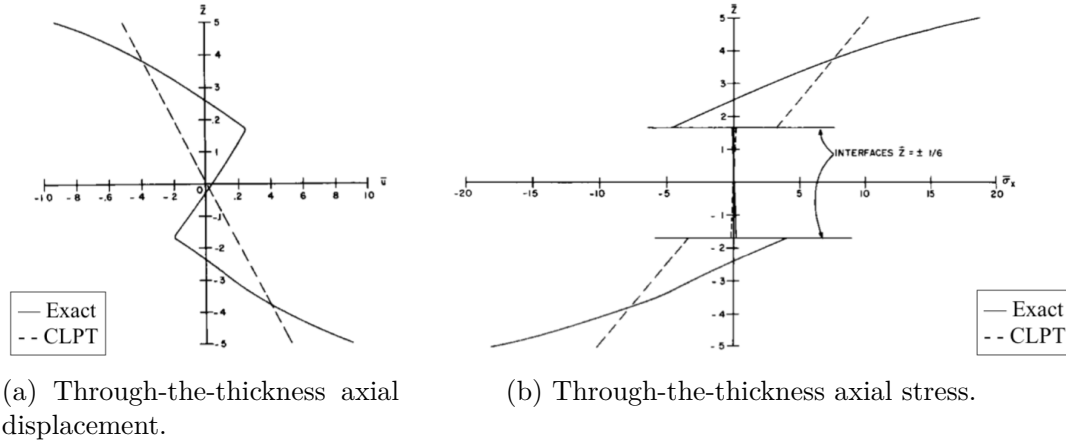
Figure 2.2: Comparison between the Pagano's exact solution and the CLPT for a three-layer, symmetric, [0°/90°/0°], laminate subjected to a sinusoidal-distributed transversal load [21].

Pagano's exact solutions indicated that the trend of the in-plane displacements across the thickness was approximately linear in each layer, with the slope changing at each interface depending on the layer material and fibre orientation.

As the CLPT for the plates, both the BET and the TBT can only reproduce a linear distribution of the in-plane displacement across the thickness of a composite beam and cannot account for any slope variation at the layer interfaces.

Even the adoption of a suitable shear correction factor in TBT, which can lead to better predictions of the transverse-shear strain, does not solve the problem of correct modelling the displacement trend across the thickness of a composite multilayer laminates.

An example of the calculation of a shear correction factor for composite beams was proposed by Madabhusi-Raman and Davalos in [22]. They considered as a shear correction factor the ratio between the transverse-shear strain energy calculated in two different ways: one obtained considering the constant transverse-shear strain across the thickness calculated by TBT, and the other one obtained considering the transverse-shear strain derived from the Cauchy's equilibrium equations. Consequently, the shear correction factor was different for each beam lamination because the energy expressions contained the beam stiffness coefficients of the entire laminate and the reduced stiffness coefficients of the plies.

One of the approaches followed by the researchers to find suitable analytical methods for correctly modelling the composites behaviour is to increase the order of the truncated power series expansion used to express the displacement field components as function of the thickness variable (in the classical theories and in the FSDTs only the first power is considered). The theories derived in this way are called High-order Shear Deformation Theories (HSDTs) or Equivalent Single

Layer (ESL) theories, since one displacement field is assumed for the entire laminate thickness. Various effects can be taken into account by considering higher order terms. As an example, in [23], the assumption of a quadratic dependence of the transversal displacement component on the thickness coordinate allowed the modelling of the transversal normal strain for the analyses of laminated cylindrical shells. In [24], Nelson and Lorch considered a quadratic dependence of all the displacement components on the thickness variable to increase the accuracy of the in-plane displacements distribution along the thickness in orthotropic plates.

A quadratic distribution of the transversal displacement was considered also by Lo et al. in [25]; in addition, they extended the in-plane displacement expansion to the third order for studying the bending of isotropic and laminated plates subjected to a sinusoidal surface load. Compared to lower-order theories, they could get better results. Significant advantages were obtained for laminated plates [26], since the high-order theory was able to describe more accurately the nonlinear pattern of the in-plane displacement across the thickness, but significant differences from the CLPT results were found only for low ratios between the wave length of the sinusoidal load and the plate thickness. Other examples of HSDTs can be found in the review article [27], where different approaches for developing multilayer plate theories are collected.

However, Liu and Li pointed out important limitations of the HSDTs in [28], where they summarised the techniques most commonly used for the analysis of composite laminates. Indeed, the HSDTs assume the continuity across the thickness of both the in-plane displacement functions and their derivatives, but if the first assumption is reasonably true for perfectly bonded layers, the latter is not if the material properties change at the layer interfaces. For this reason, the HSDTs can be inaccurate for highly heterogeneous laminates. A limiting condition is represented by sandwich structures, usually made of a central layer called core that is thick, very light and weaker than the materials used in the external layers, the facesheets. The big difference between the core and the facesheets materials leads to a strong variation of the axial displacements slope at the layer interfaces, which cannot be predicted by the HSDTs.

The Layer-Wise (LW) approach is a technique which overcomes the issues associated to the HSDTs. In the LW theories, the behaviour of each layer is described independently, using an appropriate kinematics for the layer. Reddy [29] proposed a general formulation of a displacement-based, two-dimensional laminate theory; many shear deformation theories can be derived from it by making specific assumptions. In [30], Reddy's theory was successfully employed for the study of 3-layered thick laminates.

In [31–34], Carrera and co-workers explored the Layer-Wise approach for the analyses of composite beams in the framework of the Carrera Unified Formulation (CUF) [35], a method to formulate the finite elements of a theory more efficiently.

Lee and Liu in [36] obtained the exact displacements and stresses distribution

across the thickness of laminated beams. One year later, Robbins and Reddy developed a Layerwise Laminate Plate Theory (LWPT) [37]. All these techniques overcome to the major drawbacks of the HSDTs, and they are accurate also for highly heterogeneous laminations, but they have a number of unknowns dependent on the number of layers. The computational efficiency is then penalised the higher the number of layers of the laminate considered.

A subclass of the general LW theories, the Zigzag (ZZ) theories, are able to describe the piecewise-linear distribution of the in-plane displacements in composite laminates, called zigzag effect. The improvement in the ZZ theories is that the number of kinematic variables is independent of the number of layers.

A first attempt to formulate a theory able to model discontinuities of the in-plane displacement derivatives at the layer interfaces was made by Di Sciuva in [38]. Starting from a particular form of the FSDT, he included an additional function, called zigzag function, in the in-plane displacement expression to model the slope variation at the layer interfaces depending on the material properties. Additional conditions were necessary for the complete determination of the in-plane displacement distribution across the thickness, thus Di Sciuva enforced the constant value of the transverse-shear stress along the entire laminate thickness and assumed that the in-plane displacement (i.e. the zigzag function) vanished across the entire bottom layer, called *fixed layer* (see Fig.[2.3]).
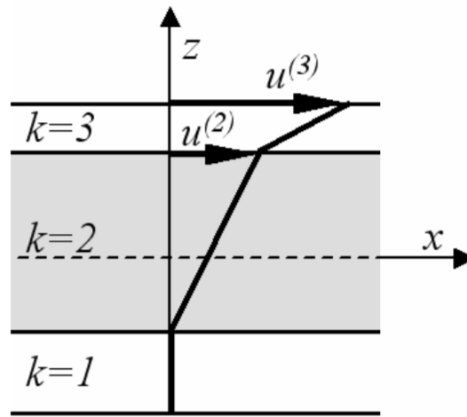
Figure 2.3: Distribution of the Di Sciuva's zigzag function [38] across the thickness of a three layer beam [39].

The result was a theory able to represent both the zigzag pattern of the in-plane displacement guaranteeing the continuity of the transverse-shear stresses at the layer interfaces. In addition, the computational cost was the same as TBT because the kinematic variables were three and independent of the number of layers.

11

One limitation of the Di Sciuva's theory is that the axial components in the displacement field depends on the first derivative of the transversal displacement, w, with respect to the beam longitudinal axis. The consequence of this assumption is that C^1-continuous shape functions are required for a finite element approximation of the variable w. For this reason, Averill [40] formulated his zigzag theory for beams starting from the TBT, so that the bending rotation was a primary variable (see Fig.[2.4] for the zigzag function distribution across the beam thickness). Averill enforced the continuity of just a component of the total transverse-shear stress across the thickness and introduced a penalty term to guarantee the continuity of the total transverse-shear stress component across the thickness in a limiting sense (the limit as a penalty parameter approaches to infinity).
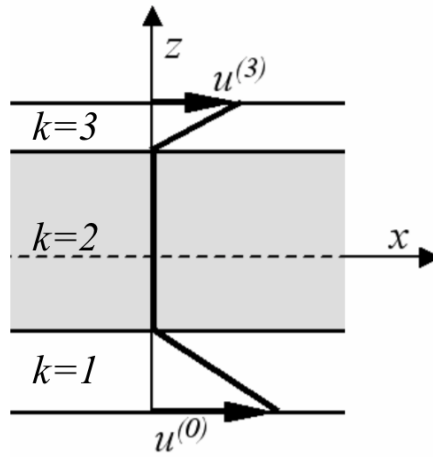
Figure 2.4: Distribution of the Averill's zigzag function [40] across the thickness of a three layer beam [39].

However, both Di Sciuva's and Averill's models have some issues related to the theories formulation. First of all, in Di Sciuva's ZZ theory, the definition of the zigzag function depends on the layer chosen as fixed layer (where the zigzag function is enforced to zero), thus the transverse-shear stiffness depends on the chosen fixed layer. The penalty term in Averill's theory avoids this problem, but in both formulations the cross-sectional integral of the transverse-shear stresses do not correspond to the transverse-shear forces derived from the physical equilibrium equations. Moreover, a major issue appears in case of clamped boundary conditions, where all the kinematic variables have to vanish and consequently the transverse-shear strains and stresses are also null for the way the theories are formulated; this is clearly in contrast to the equilibrium equations.

Few years later, Murakami [41] formulated a new ZZ theory based on the variational principle proposed by Reissner [42]. He introduced in the Reissner variational

model both a transverse stress field and a zigzag C^0 function for the in-plane displacement approximation.The proposed theory predicted very accurately the exact solutions of Pagano [21] for the plate cylindrical bending (see Fig.[2.5]), being also more efficient than smooth nonlinear functions (higher order theories).

(a) Laminate slenderness ratio=4. (b) Laminate slenderness ratio=6.
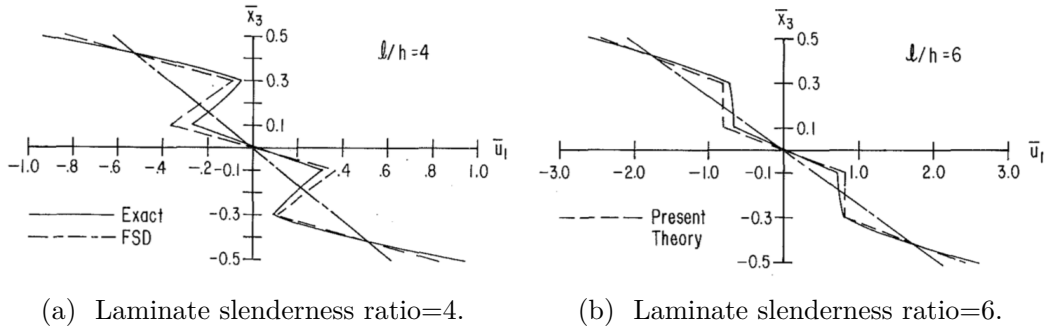
Figure 2.5: Comparison between MZZ, FSDT and Pagano's exact solution (indicated as "Present Theory", "FSD" and "Exact", respectively) for the through-the-thickness variation of the in-plane displacement [41].

The Murakami Zigzag theory (MZZ) has been extensively used by many authors, like Carrera and co-workers who used this zigzg function with the CUF. In [43], Carrera demonstrated the effectiveness of introducing the Murakami's zigzag function in the classical and first-order plate theories to model the zigzag effect instead of using higher order polynomials. De Masi [44], found finite element solutions of the first-, second- and third-order shear deformation theories for plates refined by the inclusion of the Murakami's zigzag function. Both the analytical and the finite element solutions showed that the use of the MZZ led to better predictions of the transversal displacement even for relatively thick composite multilayer plate. Moreover, Brischetto, Carrera and De Masi [45] obtained accurate results also for non-symmetrical sandwich plate analyses.

However, many authors have pointed out that MZZ can be inaccurate in some cases, especially if compared to Di Sciuva's zigzag theory. The main difference between Di Sciuva's and Murakami's approaches is that the definition of Di Sciuva's zigzag function is derived from the physical consideration that the transverse-shear stress has to be continuous across the thickness (physically-based zigzag function), by contrast, Murakami assumes a periodic change of the in-plane displacements slope at the interface independently of the actual physical characteristics of the laminates (kinematic-based zigzag function). In [46, 47], it was demonstrated that the two approaches had the same level of accuracy if the considered laminate had a periodic stacking sequence, while Di Sciuva's zigzag function was more accurate in any other case.

Tessler, Di Sciuva and Gherlone developed the Refined Zigzag Theory (RZT)

13

([48]-[49]) to solve the drawbacks associated to both Di Sciuva's and Averill's theories. As in Averill [40], they started from a first-order shear deformation theory (Timoshenko's theory for beams and Mindlin's theory for plates) and added a piecewise linear zigzag function of the thickness coordinate.

In the RZT, the zigzag function vanishes on both the top and bottom external surfaces, thus its distribution is not null in all layers (see Fig.[2.6]) and this overcomes the problem of the bias towards the transverse-shear stiffness of the fixed layer of Di Sciuva's formulation. The continuity of only a component of the transverse-shear stress is enforced, as in Averill's formulation, but the final shear stress is left discontinuous not considering any penalty term.
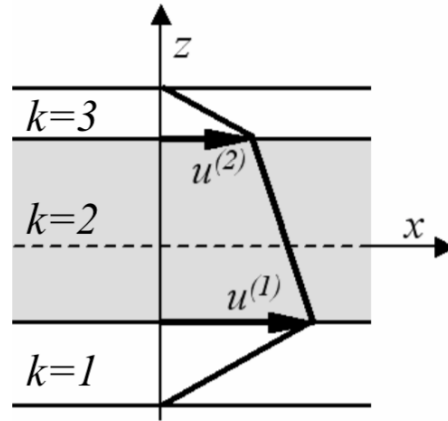
Figure 2.6: Distribution of the RZT zigzag function across the thickness of a three layer beam [39].

Significant consequences of the RZT assumptions are that the shear angle calculated with TBT corresponds to an RZT average shear strain of the cross-section and the magnitude of the zigzag function is a weighted-average shear strain quantity. These two considerations highlight the strong link between the RZT model and the problem physics.

The RZT has four kinematic variables (the axial and transversal displacements, the bending rotation and the zigzag rotation), one more than TBT, but this number is independent of the number of layers. Moreover, it was demonstrated that RZT is extremely accurate and much better than the HSDTs for the analyses of relatively thick beams and plates and also for highly heterogeneous material lay-ups and being also very efficient [48–53].

In addition, in [54] Gherlone compared the RZT to the Murakami's zigzag theory for the analysis of beams with different laminations. First, he recognised that in all previous works the Murakami's assessment was done considering only specific laminations, like cross-ply with alternate orientations, angle-ply with periodic

sequences or three-layer symmetric laminates, whereas the results obtained employing the MZZ for other laminations were not verified. For this reason, Gherlone considered more challenging laminations and assessed both Murakami's and the Refined zigzag functions through a comparison with Pagano's exact elasticity solution. Despite the equivalent results between the two zigzag approaches in case of two-layer, three-layer symmetric, or N-layer periodical stacking sequences, the RZT was more accurate in any other case. In addition, he showed that both theories were inaccurate for laminations that had a weak layer placed on the top and/or bottom of the stacking sequence and proposed a very simple way to correct the zigzag formulation. This technique could be applied only to the RZT, demonstrating that RZT could be very accurate also for lay-ups with external weak layers, whereas MZZ remained highly incorrect.

In [55], Groh and Weaver employed the Hellinger–Reissner mixed variational principle to derive two mixed third-order shear deformation zigzag theories, introducing either the Refined Zigzag or the Murakami Zigzag function in a TSDT. The comparison with Pagano's exact elasticity solution highlighted the superior capabilities of the RZT-based formulation for the bending analysis of thick composite beams. Indeed, the RZT solution was highly accurate for predicting the in-plane and transverse-shear stress distribution across the thickness, even for the most challenging lamination (high heterogeneity and pronounced zigzag effect), whereas Murakami's error reached 10%. The Hellinger–Reissner mixed variational principle was used to get the continuous distribution of the transverse-shear stress directly from the shear strain and with no need of a postprocessing integration. For this same reason, Tessler [56] created a new RZT using the Reissner's mixed variational theorem, called $RZT^{(m)}$, and few years later, he and Groh [57] formulated an efficient shear-locking free beam finite element based on the $RZT^{(m)}$ to study the delamination propagation in composite and sandwich beams.

More recently, Hasim and co-authors [58, 59] developed an isogeomentric finite element based on the RZT for the static analysis of composite and sandwich beams to get more efficient calculation of the transverse-shear stresses through the a-posteriori integration technique (Cauchy's equilibrium equation). Then, they used the isogeometric formulation and the $RZT^{(m)}$ for the study of sandwich beams with embedded delaminations.

In one of the latest works of Weaver and co-authors [60], the RZT was demonstrated to be superior to MZZ also in capturing the 3D stresses of variable-stiffness and sandwich beams, also for highly heterogeneous laminations, being much more computationally efficient than layer-wise models and 3D finite element models.

Compared to other theories, the RZT best performances have been demonstrated for the analyses of relatively thick and highly heterogeneous composite structures, such as sandwich beams. It has been already employed for the static [61, 62] and free-vibration [63] analyses of sandwich beams and assessed for the static, dynamic and buckling analysis of sandwich plates [52]. In addition, the

theory has attracted many authors especially for the possibility of developing very efficient finite elements, highly accurate also for sandwich structures. C^0-continuous beam finite elements based on the classical formulation of the RZT can be found in [51, 64–66], whereas a mixed formulation has been used in [67] to develop beam finite elements based on a third-order Refined Zigzag theory. Other implementations include finite element for beams viscoleastic layers for vibration reduction [68] and RZT-based finite elements for the delamination modelling[69, 70].

It is clear that the choice of a particular kind of RZT-beam finite element depends on the application considered. A field that has not been explored yet is the buckling and postbuckling analyses of composite and sandwich beams using the Refined Zigzag Theory. For the reasons explained above, the use of the RZT for more complex analyses which involve nonlinearities and geometric imperfections, highly heterogeneous laminations and also electro-mechanical effects for the structural control, appears very attractive because of its the remarkable accuracy and efficiency.

2.2 Buckling phenomenon for beams

The buckling phenomenon is related to the instability modes of thin-walled slender structures when subjected to compressive loads which can lead to the failure. In real imperfect structures, the buckling is a nonlinear phenomenon associated to a sudden big increment of the transversal displacements for a small increase of compressive load [71, 72]. The nonlinear mechanics is then required for modelling this kind of nonlinear structural behaviour. From a mathematical point of view, the geometric nonlinearities can be included in the analysis of thin-walled structures by using the kinematic equations of flat plates derived by von Kármán. These equations were extended by Sanders [73] to the case of thin shells of arbitrary shapes, and by these the kinematic equations for beams can be derived through an appropriate specialization.

2.2.1 Buckling of perfect beams

The expression of a critical load for a beam subjected to an axial-compressive force was found for the first time by Euler [74], who studied the equilibrium of a slender column in simply-supported boundary conditions. Euler derived the equilibrium equation of the beam in its deformed configuration obtaining a homogeneous equation that had both the trivial solution, corresponding to the undeformed configuration of the beam, and also an eigenvalue solution, with the eigenvalues corresponding to discrete values of the compressive force. The smallest eigenvalue was called critical buckling load, N_{cr}, defined as

$$N_{cr} = \frac{\pi^2 EI}{L^2} \, . \tag{2.1}$$

Eq.[2.1] is called *Euler column formula* [71] and E is the Young modulus of the material, I is the moment of inertia of the beam cross-section and L is the beam length.

The buckling behaviour of a structure is usually studied representing the possible solutions of the equilibrium equation in a load-displacement plot, reporting the values of the transversal displacement of one point of the structure (on the horizontal axis) for increasing values of applied compressive load (on the vertical axis). The obtained curve is denoted as load-displacement equilibrium path because each point of the curve represents an equilibrium condition for the beam.
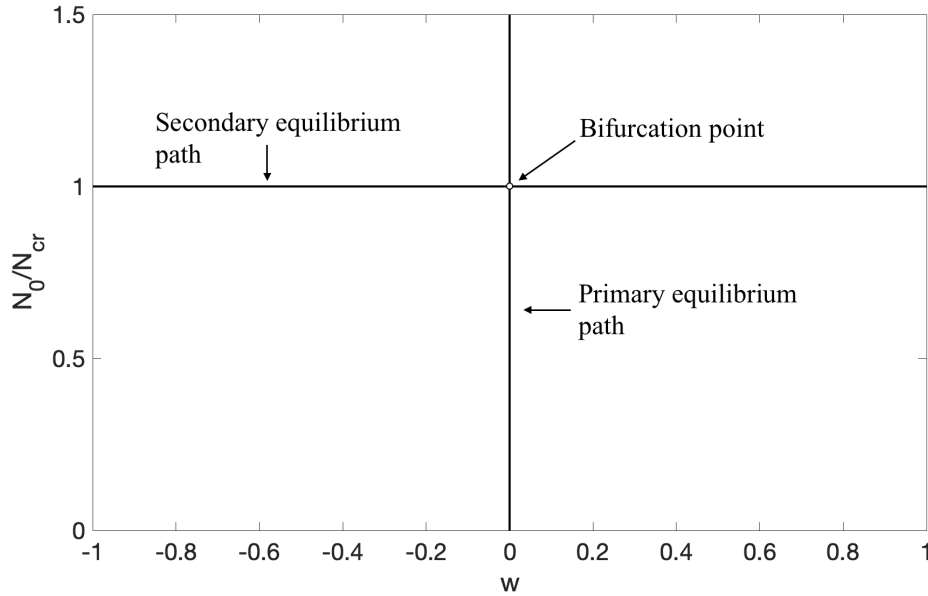
Figure 2.7: Equilibrium paths and the bifurcation point for the Euler's column.

The solutions of the equilibrium equation found by Euler are represented in Fig.[2.7], normalising the load with respect to the critical value given by Eq.[2.1]. The curve corresponding to the homogeneous solution is called *primary equilibrium path*, whereas the solution obtained for a value of the load corresponding to the critical buckling load leads to a *secondary equilibrium path*. The symmetry of the secondary path with respect to the vertical axis indicates that the beam can deflect either upward ($w > 0$) or downward ($w < 0$). The two lines in Fig.[2.7] intersect at the point corresponding to zero displacement and the critical buckling load, meaning that more than one equilibrium state is possible when the beam

is subjected to a compressive force equal to the critical buckling load (*indifferent equilibrium*). The intersection point is called *bifurcation point*. The secondary path in Fig.[2.7] indicates that when $N_0 = N_{cr}$ the beam deflection can be any value, but this is a consequence of the hypothesis of small deflections made by Euler.

In [75], Timoshenko took into account the larger rotations for the analysis of a cantilever column under compression. An important outcome of his study was a more accurate relation between the applied compressive load and the transversal deflection of the beam. As shown in Fig.[2.8], Timoshenko analysis could determine the exact value of deflection for any applied load in the secondary equilibrium path.
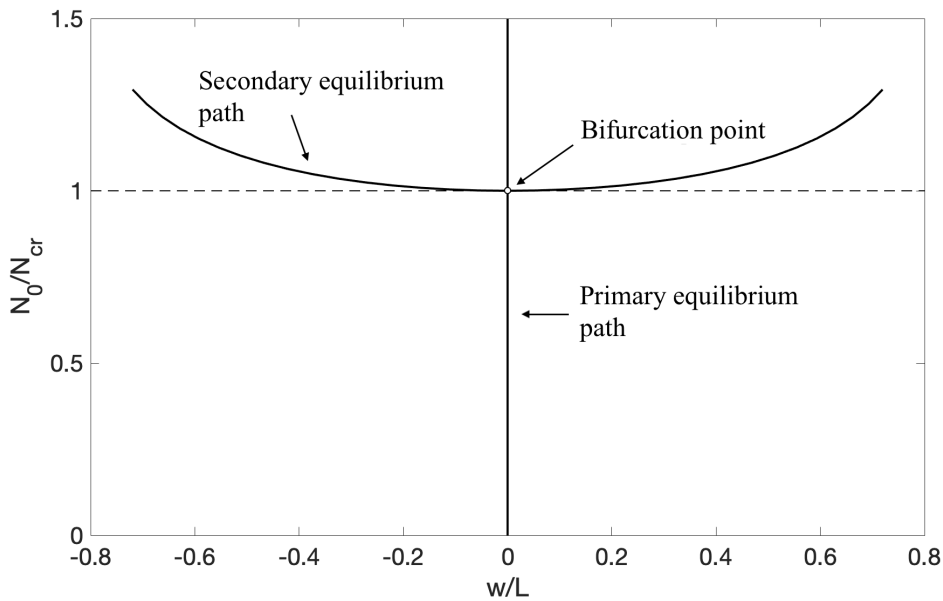
Figure 2.8: Equilibrium paths and the bifurcation point for the Timoshenko's column.

The equilibrium equation found by Euler was linear because the beam he considered (simply-supported and subjected to a concentrate force at the end) had the internal axial force independent of the axial coordinate. In general cases, the equilibrium equation is a nonlinear differential equation and the determination of the equilibrium paths and the bifurcation point is more complicated. The *Euler's method of the adjacent equilibrium configurations* [71] is a technique which allows the determination of the existence of a bifurcation point. This method is based on the research of two possible equilibrium configurations for the same applied load by considering a perturbation of an initial equilibrium configuration. A stability equation is derived from the equilibrium equation and the existence of a solution of the stability equation identifies the presence of more than one equilibrium condition

for the same load. The advantage of this approach is that the stability equation is a linear differential equation. As a consequence, the determination of a bifurcation point and the corresponding value of applied load can be obtained solving a linear differential equation, instead of a nonlinear equation. It is convenient method for evaluating the load corresponding to a bifurcation point, but it does not provide any information about the secondary equilibrium path.

Both Euler and Timoshenko assumed that the beam had a straight centroidal axis, aligned to the load direction. This kind of beams are called *perfect* beams to distinguish them from the case in which geometric imperfections are taken into account and the centroidal axis has an initial deviation from a straight configuration. The nonlinear response of a geometrically imperfect beam subjected to a compressive load is indicated as postbuckling behaviour of the beam.

2.2.2   postbuckling behaviour of imperfect beams

The study of the response of a real beam subjected to a compressive load has to take into account the beam geometric imperfections. As explained in [71], the inclusion of geometric imperfections in the model of a structure makes the equilibrium equation inhomogeneous, thus the solution is a non-null value of transversal displacement for any applied compressive load.
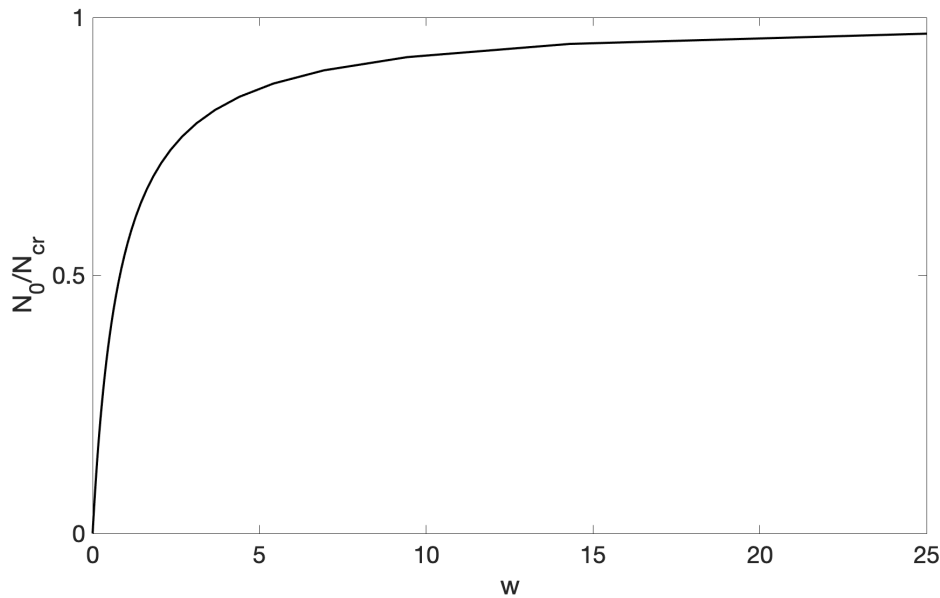
Figure 2.9: Load-displacement equilibrium path of a beam with an initial geometric imperfection.

In this case, there is only one possible load-displacement equilibrium path. The curve representing the equilibrium states of an imperfect beam subjected to an increasing compressive load is linear at the beginning, then the slope progressively reduces approaching the critical buckling load of the beam in its perfect configuration, as shown in Fig.[2.9]. The initial slope of the curve depends on the beam initial deflection: the higher is the imperfection, the lower is the initial slope of the equilibrium path.

In [76], Rivello investigated the influence of the initial imperfection on the nonlinear response of a beam considering a large deflections theory. He also derived the curves indicating the yield stress limits for different geometrical characteristics (beam length and size of the cross-section) of a homogeneous beam made of aluminium alloy, assuming a linearly elastic and perfectly plastic material behaviour. His results showed that the beam started to deflect very fast when the load approached the critical value, but the actual failure happened for a value of load slightly lower the N_{cr}, because the fibres on the concave surface of the deformed beam exceeded the yield stress. In addition, the representation of the yield stress limits in the (w, N_0) plot indicated that the same beam reached the yield stress for a lower value of N_0 the higher was the imperfection.

In general, the determination of the actual postbuckling behaviour of a real beam is obtained by solving a system of nonlinear equilibrium equations taking into account the material characteristics, the geometric imperfections and the loading conditions. The number of equations in the system depends on the number of kinematic variables considered in the theory, thus the complexity of the solution depends on the level of detail of the theory adopted, on the beam physical and material characteristics and on the boundary and loading conditions. It is clear that, if the beam is made of composite materials, the accuracy of a buckling and a postbuckling analyses depends on the ability of the chosen theory to model composites behaviour.

As an example, Sheinman and Adan [77] used a nonlinear TSDT and a variational method to find the nonlinear equilibrium equations of laminated beams. The equilibrium equations were not solved exactly but employing the modification of the Newton's method proposed in [78]. They demonstrated the importance of considering the shear deformation also for the buckling and postbuckling analyses, especially for composites, highlighting the need of employing a higher-order theory for low length-to-thickness ratios.

Barbero and Raftoyiannis [79] instead, used the Euler equation for calculating the critical buckling loads and the failure modes of pultruded composite columns with thin-walled cross-sections, deriving the constitutive equations of the beam from the CLPT. Columns of various lengths were considered to investigate the transition of the first failure mode from global to local buckling when the beam length decreased. They also investigated the nonlinear behaviour of composite beams with geometric imperfections both in pre- and postbuckling regimes.

However, few years later Khedir and Reddy [80] highlighted the inaccuracy of the classical theory for the calculation of the buckling loads of cross-ply laminated beams. The comparison between BE, TBT and other HSDTs showed that BE highly overestimated the buckling loads, whereas the other theories gave similar results for the applications considered.

More than ten years later, Emam and Nayfeh [81] used the Bernoulli–Euler beam theory to develop their model for studying the buckling of composite beams. They found a closed-form solution for the equilibrium configurations of composite beams loaded beyond the critical buckling load and studied both the stability in postbuckling regime and the dynamic behaviour in the buckled state considering various boundary conditions.

In more recent years, Li and Qiao [82] employed the Reddy TSDT to study the pre- and postbuckling of laminated imperfect beams. Firstly they introduced both the geometric nonlinearities and the imperfections in the theory formulation and then they numerically solved the nonlinear equilibrium equations considering several combinations of boundary conditions. They also investigated the effect of the geometric imperfection and the beam lamination on the postbuckling response of the beams.

Many other examples of HSDT employed for the buckling analysis of composite beams [83, 84], for functionally-graded sandwich plates [85] and for the buckling of composite beams with large initial imperfections [86] can be found in the literature.

2.2.3 Experimental buckling

A comprehensive study on the buckling phenomenon involves also the experimental investigation. Extensive material can be found in the literature about the experimental evaluation of the buckling load and the postbuckling behaviour of structures. In [87], Salmon collected the most important studies about columns in compression up to the beginning of the twentieth century, highlighting the importance of linking theory and practice. In his treatise, he also classified the possible eccentricity of load, the initial curvature of the beam and the reduction of material strength (due to defects of non-homogeneity) as column imperfections and all of them had a significant influence on the beam buckling and postbuckling behaviour.

An experimental investigation about the influence of the load eccentricity on the beam postbuckling behaviour was made by von Kármán [88]. He realised compression tests of columns in almost perfect conditions, i.e. very straight specimens and load direction aligned to the beam axis, and compared his results to those obtained by Kirsch [89], characterised by a high load eccentricity, and those of von Tetmajer [90], who made slightly less precise tests than von Kármán [88]. The comparison showed that von Kármán's results were very close to the theoretical load-displacement path of a perfect beam and that the beams with higher load eccentricity reached the yield limit for a significantly lower load.

Important information about the buckling experiments, like the general rules for the experimental setup, the test performance and the analysis of the experimental data can be found in [72]. In the book, it is also highlighted the substantial difference between the buckling tests performed to validate a theory and the tests performed to evaluate the buckling and postbuckling behaviour of a real structure.

If a new theoretical method for calculating the critical buckling load and the load-displacement equilibrium path has to be assessed, then the experiments have to match with the assumptions made in the theory. As an example, the beam tested needs to have the same imperfection considered in the mathematical model, the load has to be perfectly centred if no eccentricity is considered and, very important, the physical boundary conditions must reproduce exactly what is considered in the mathematical model; this is because the postbuckling behaviour of a structure is very sensitive and strongly affected by all these parameters. By contrast, when the aim of the tests is to experimentally investigate the buckling behaviour of a real beam, then the tests have to reproduce the imperfection, the load and the boundary conditions of the real structure.

The most used method to correlate the experiments on real imperfect structures and the theoretical predictions is the Southwell method [91]. The method allows the calculation of the critical buckling load of a beam as the slope of the line obtained plotting the transversal displacement of the beam, w, measured during the test, as function of the ratio between the transversal displacement and the applied load, $\frac{w}{N_0}$.
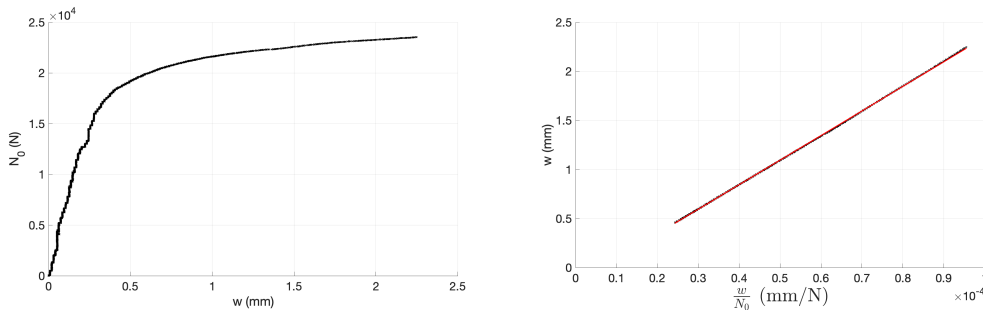
(a) Experimental load-displacement equilibrium path.

(b) Southwell plot.

Figure 2.10: Application of the Southwell method for calculating the critical buckling load of a beam.

The quantities w and N_0 can be plotted in the (w, N_0) plane for representing the equilibrium path obtained experimentally (see Fig.[2.10a]); Southwell developed his method approximating the experimental load-displacement equilibrium path of the imperfect beam by a rectangular hyperbola and then he obtained a line in the

$\left(\frac{w}{N_0}, w\right)$ plane by making a coordinate transformation(see Fig.[2.10b]). The slope of the line in the $\left(\frac{w}{N_0}, w\right)$ plane corresponds to the asymptotic load value of the hyperbola, which is the Euler buckling load.

Lundquist [92] proposed a correction to the Southwell's method to take into account a small pre-load and deflection measured at the beginning of the experiment. Other modifications to the Southwell's method can be found in [93, 94] for particular boundary conditions or for very straight beams, but the original version of the method is still the most preferred one. The method has had a great success not only because of its simplicity but also because it is a non-destructive technique to evaluate the critical buckling load. It has been extended also to more complex structures with suitable adjustments and corrections, but it has also many limitations as in case of large deformations. Further details about the method, its extensions and limitations, and also precise instructions on how to correctly perform a buckling test to verify a theoretical model can be found in [72]. An important warning of the authors is about the kind of boundary conditions to consider in the experimental buckling tests of beams, stating that the fixed ends are much less reliable than simply-supported conditions.

2.2.4 Buckling control and use of piezoelectric actuators

A big concern for aerospace structural applications is the possibility to increase the critical buckling load of the elements subjected to high compressive loads. A possible solution investigated by many authors is the use of piezoelectric actuators to stiffen the structure by reducing the geometric imperfection (see Fig.[2.11]).
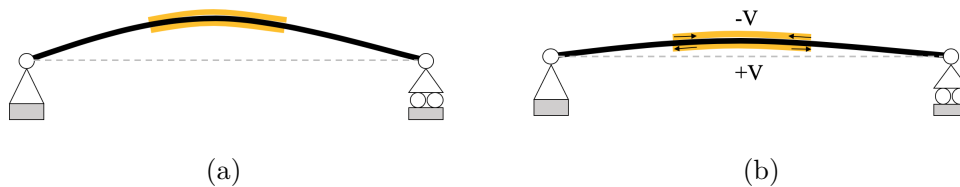
Figure 2.11: Imperfection reduction using piezoelectric actuators: (a) initially imperfect beam; (b) beam deflection after the application of a negative voltage to the top actuator and a positive voltage to the bottom actuator.

In [95], Chandrashekhara and Bhatiat presented their work on the dynamic buckling control of composite plates considering both piezoelectric sensors and actuators. Their formulation was based on the FSDT developing both an analytical and a finite element model able to model piezoelectric patches on plates. The numerical results proved the possibility of increasing the critical buckling load with a closed-loop control system.

The buckling control of beams using piezo-actuators was discussed also by Berlin in his doctoral thesis [96], mainly focusing on civil engineering applications. He made both numerical simulations and experiments to prove that the buckling behaviour of structures could be significantly improved by using piezoelectric actuators. The tests were conducted on a steel beam with piezoelectric patches bonded on the beam external surfaces. By activating the actuators, Berlin was able to increase the load-bearing strength of 5.6 times.

Thomson and Loughlan [97] conducted experiments to demonstrate that it is possible to increase the load-bearing strength of beams by using piezoelectric actuators. They considered carbon/epoxy symmetrically laminated composite beams with piezoelectric actuators on the external surface. The effect was demonstrated comparing the experimental load-displacement equilibrium paths, showing that in case of actuation in the piezoelectric patches the curve was very close to that of a perfect beam.

In De Faria and De Almeida [98], the effect of piezoelectric layers attached to the beam was included in the nonlinear formulation of Bernoulli-Euler beam theory for initially imperfect composite beams under compression. The analysis showed that the nonlinear response of slender composite beams in the pre-buckling regime could be significantly modified by the piezoelectric actuation, obtaining a load-displacement equilibrium path that was close to the ideal solution of perfect beams. Chase [99, 100] conducted multiobjective analysis to find the optimal contollers for the buckling of beams and plates.

Mukherjee and Chaudhuri [101] made a numerical study on the active control of imperfect laminated beams with piezoelectric actuators and sensors subjected to either a static or dynamic axial-compressive load. The composite beam was made of unidirectional orthotropic layers in a symmetrically balanced configuration, with the top and bottom layers made of piezoelectric material. The piezoelectric layers were firstly used as sensors to detect the beam strains, and then as actuator, applying a voltage calculated by a simple control law based on a gain factor for controlling the beam lateral deflection. The deformation caused by the actuator had a stiffening effect on the beam, which almost doubled its critical buckling load in the static analysis and significantly reduced the amplitude of the dynamic response of the first natural frequency in the dynamic analysis.

Abramovich and co-workers conducted many analytical and experimental investigations on the use of piezoelectric actuators to modify the structural response in several applications. For the analytical formulation they always used the FSDT.

In [102], the authors employed the FSDT for the static, free-vibration and buckling analyses of composite laminated beams (symmetric and anti-symmetric laminations) with continuous piezoelectric layers. They also considered the piezoelectric layers as sensor to detect the mechanical strain, and evaluated the voltage to apply to the actuators implementing a control law based on a gain factor. The piezoelectric layers, working as actuators, caused a counteractive bending moment opposite

to the moment due to the mechanical compressive force. The results showed a significant increment of the critical buckling load even for voltages which gave a counteractive bending moment lower than the mechanical bending.

In [103], Waisman and Abramovich studied the stiffening effect due to the actuation of either piezoelectric patches or piezoelectric continuous layers on the free vibrations of non-symmetrically laminated beams. They employed the FSDT to analyse the beams behaviour subjected to axial and lateral tractions, in various boundary conditions. They also verified their results through a comparison to an Ansys finite element model.

The actuation of piezoelectric patches in shear-mode was studied in [104]. The shear actuators were embedded in the foam core of sandwich beams with cross-ply CFRP facesheets considering both symmetric, $[0°/90°/\text{foam}+\text{shear PZT}/90°/0°]$, and anti-symmetric, $[0°/90°/\text{foam}+\text{shear PZT}/0°/90°]$, lay-ups. The aim of the paper was to assess the effectiveness of these configurations with respect to those with extensional piezoelectric patches on the external layers of the beams. The authors performed several analyses for the beams subjected to static lateral and axial forces.

The FSDT was the theory chosen for this kind of applications by many other authors. As an example, Damanpack et al. considered piezoelectric actuators for the active vibration control of sandwich beams [105]. They used the FSDT to model the behaviour of the actuators and beam facesheets, whereas a higher order sandwich theory was used for the core displacements. They also developed a beam finite element for piezo-composite sandwich beams having eighteen nodes for the mechanical degrees of freedom and two electric nodes to include the electric potential as a variable. More recently, the FSDT was used also by Muc, Kędziora and Stawiarski [106] for the buckling analysis of cylindrical shallow panels with piezoelectric actuator patches. They demonstrated that the FSDT was more accurate than CLPT assessing the two theories with a 3D finite element models (Cranes Software, Inc.).

However, as discussed in the previous section, the FSDT has proven not to be the best choice for the static and free-vibration analyses of composite beams that are relatively thick or made of highly heterogeneous materials (see [48, 62, 63]). The reason of its big success for this kind of applications is probably the simplicity of the formulation. Indeed, when piezoelectric elements are considered in the structure, the coupling between the mechanical and the electrical field has to be taken into account in the formulation of the mathematical model [107]. Additional terms corresponding to the electric strains and stresses have to be considered and the final equations will contain more terms the higher the order of the theory adopted, thus the use of a theory with a less complex formulation appears to be very convenient.

25

2.2.5 Buckling of delaminated beams

The complex nature of composite materials, heterogeneous and often highly anisotropic, influences the failure mechanisms of the composite structures. In general, the damages in composites can be classified as *intra-laminar damages* or *inter-laminar damages*. The *intra-laminar damages* refers to the possible fibre breakage, the matrix crack or the debonding between the fibre and the matrix. The *inter-laminar damage*, or delamination, refers to the debonding between two adjacent layers. The presence of manufacturing defects in the structure or impacts can cause delaminations between the layers of a composite laminate or the debonding between the core and the skin of a sandwich. Moreover, under certain circumstances, a composite structure can exhibit intra-laminar damages that can finally result in delaminations because of the loads acting on it. For this reason, the study of the delamination initiation and propagation has got much attention and several methods have been developed for the analysis of delaminated structures.

The delamination can strongly reduce the strength of a beam under compression and the critical buckling load significantly decreases. Many authors attempted to correctly predict the actual buckling loads of delaminated structures and the corresponding buckling modes.

One of the first work about delaminations in structures under compression was conducted by Chai, Babcock and Knauss [108–111]. They studied the delaminations due to impacts on plates subjected to compressive loading. In [112], they considered a pre-delaminated plate and studied the delamination propagation using the energy release rate criterion.

Kardomateas and Schmueser [113] developed an analytical method to study the buckling and postbuckling of composite beams and plates focusing on the effect the transverse-shear stress had on both the value of the critical load and the postbuckling behaviour of the structure. They assumed a mixed-mode buckling instability and used the energy release rate criterion for the delamination growth in postbuckling. They also identified the three possible modes of instability for the compressed delaminated plate: a buckling of the whole structure (*global buckling*), a mixed-buckling where both the two sublaminates buckled, and a *local buckling*, where only one sublaminate in the delaminated area buckled, whereas the base plate remained flat.

Shu [114] presented a model for the buckling of beams with two delaminations. The author based the formulation on the BET and found an exact solution considering the beam as constituted of five independent beams. He also showed how the buckling load diminishes increasing the delamination length and depth.

In [115], Hansen highlighted the difference between the delamination-buckling problem from the debonding-buckling problem in sandwiches, distinguishing the delamination, which could occur in all composites and in sandwiches it was located between the consecutive layers of the facesheets, from the debonding between the

core and the facesheet of a sandwich. The author focused on the debonding between the facesheet and the core performing tests on a FRP sandwich panel. He also made a finite element model using shell elements for the facesheets and solid elements for the core, for calculating the critical buckling load of a perfect structure. Subsequently, he introduced a geometric imperfection and performed the Riks nonlinear analysis. The complex FE model was necessary because of the strong inhomogeneity of the material, thus he tried to reduce the computational time by modelling the core as a discrete set of springs and not as a continuous layer. He got good correlation between experiments and the FE model in the prediction of the critical buckling load of the debonded panel.
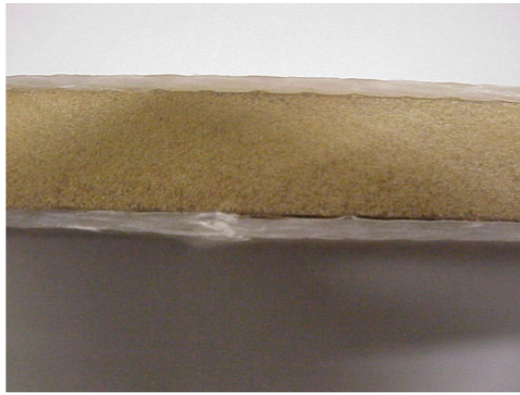
Figure 2.12: Failure of a sandwich panel with a pre-debonding between the core and the bottom facesheet [116].

Mahfuz et al. [116] investigated the effect of the core density on the buckling response of foam core sandwich plates with implanted delaminations, as the panel shown in Fig.[2.12]. They conducted compression tests of four sandwich panels with different core densities, analysing both the effect of the density and the pre-implanted delaminations on the panels load-displacement response and calculating the critical buckling load using the Southwell method. They also realised a FE model in Ansys for the numerical calculation of the buckling load; the model was made using solid elements, uncoupling the nodes of the two sublaminates in the debonded/delaminated parts. The numerical buckling load was calculated solving the conventional eigenvalue problem and a nonlinear analysis was also performed evaluating the buckling load applying the Southwell method to the numerical load-displacement results. However, the latter analysis was made for only one panel because of the *"prolonged running time and memory requirements"*.

Chen and Qiao[117] developed an analytical method for the study of the delamination buckling of bi-layer columns. They modelled both the delaminated and the intact part of the beam as two sub-layers and used the TBT introducing a

flexible-joint model in the formulation, for the deformations at the delamination tips. The model was assessed comparing it to a rigid-joint model, a semi-rigid joint model and a detailed Ansys FE model. The plane-stress FE model realised in Ansys was used as reference solution, highly refining the mesh close to delamination tips. The authors investigated how the critical buckling load was affected by the delamination length, the delamination location along the beam thickness (the ratio between the thicknesses of the two sublayers) and the slenderness ratio of the delaminated sublayer. The results showed that the buckling load decreased the higher the delamination length and the slenderness ratio of the delaminated sublayer. Moreover, it decreased much more rapidly for beams with the two sublayers of different thickness (asymmetric delamination buckling). The model was able to capture the different buckling behaviours for asymmetrically delaminated beams, exhibiting a global buckling for small delamination lengths (with respect to the beam length) or for small slenderness ratio of the delaminated sublayer, whereas the instability became local for higher values of those ratios. The solutions of all models considered tended to converge for high delamination-to-beam length ratio, indicating that the critical buckling load was not substantially influenced by the local deformation at the delamination tip for big delamination length.

In their work, Akbarov and Yahnioglu [118] considered a sandwich plate-strip with piezoelectric facesheets subjected to a compressive axial load. They also assumed a small debonding between the core and the facesheets and studied the crack growth under the applied mechanical load. They carried out the nonlinear equilibrium equations for the electro-mechanical system, also considering geometric imperfections of the facesheets in the debonded area. They highlighted the stiffening effect due to the piezoelectricity, the dependence of the critical buckling load increment on the poling direction and the thickness of the piezoelectric facesheets.

Wang et al. [119] started from determining the critical buckling strain from the beam equilibrium equations (force resultants-strains) assuming an a-priori locally buckled configuration. They calculated the *post-(local-buckling)* energy release rate, partitioning the total value in the two contributions, one for mode I and one for mode II, to predict the consequent delamination propagation.

Juhász and Szekrényes [120] studied, both numerically and experimentally, how the delamination affected the buckling of orthotropic rectangular plates. They created a finite element model extending the FSDT to the analysis of delaminated plates, with asymmetrically located trough-the-width delaminations. The specimens for the tests were manufactured with a pre-induced delamination, inserting a PTFE film between the layers. The tests were performed using an Instron compression-testing machine clamping the plates on two edges. The numerical and experimental results showed both the decreasing value of buckling load increasing the delamination length but also the transition from a global buckling mode to a local buckling.

Li and Shen [121] developed a finite element model based on the LWPT [37]

28

for the static and vibration analyses of composite beams and plates with piezo-electric actuators. They introduced two discrete functions to model, respectively, the discontinuities in the displacement field induced by the delamination and the discontinuities in the strains field due to the material variation along the thickness. The model was assessed through a comparison with data found in the literature and also developing a finite element model in Abaqus. The delamination in the finite element model was obtained uncoupling the nodes in the delaminated area. They investigated the effect of the delamination on the static and vibration response using the piezoelectric layers as sensor to find a correlation between the delamination location and the sensed voltage.

2.3   Conclusion

On the basis of this literature review, it is believed that a new method based on the RZT would be a successful technique for reducing the computational cost of the buckling and postbuckling analyses for composite laminated and sandwich beams geometrically imperfect and with piezoelectric actuators, keeping the same level of accuracy of highly-detailed two- and three-dimensional finite element models.

The extension of this new method to the analysis of beam with piezoelectric actuator patches bonded to the external surfaces (not only piezoelectric continuous layers) would increase the method applicability to real situations.

In addition, the further extension of the method to the modelling of the buckling of pre-delaminated beams would also allow the possibility to investigate the use of piezoelectric actuators for controlling the local buckling. The superior accuracy of the RZT for the analyses of sandwich beams would make this method very attractive for modelling the buckling and postbuckling of sandwich beams with debondings between the core and facesheets, and also for studying the possible usage of piezoelectric actuators on relatively thick structures for static applications.

Chapter 3

The Refined Zigzag Theory for initially imperfect beams with piezoelectric actuators

3.1 Introduction

As highlighted in the previous chapter, the increasing use of composite materials for a broad range of applications and the inadequacy of classical theories to correctly predict the through-the-thickness distribution of the in-plane displacements, led to the development of new analytical approaches specific for composites.

In this chapter, a new analytical model is created for highly accurate and efficient buckling and postbuckling analyses of composite laminated and sandwich beams. The model is based on the Refined Zigzag Theory, which is extended to the nonlinear analysis of geometric imperfect composite beams. The converse piezoelectric effect is also included in the formulation to investigate the possibility of using piezoelectric actuators to control the buckling response (Section 3.2).

The response of initially imperfect composite beams with piezoelectric actuators layers subjected to both distributed and concentrated loads can be calculated solving the nonlinear equilibrium equations based on the RZT, derived applying the Principle of Virtual Work for electro-mechanical systems (Section 3.3).

A finite element formulation is also created (Section 3.4) to accurately and efficiently solve the beam equilibrium problem in more general situations, like anti-symmetric laminations or in case of any boundary conditions. The solution of the nonlinear FE equation is obtained applying the Newton-Raphson method to evaluate the postbuckling nonlinear behaviour of composite beams subjected to compressive forces (Section 3.5). In addition, a strategy based on the Lagrange multipliers method is used to further generalise the new FE model capabilities to the analyses of beams with geometrical discontinuities due to changes in material and geometrical properties, like the presence of piezoelectric patches on a portion

of the beam (Section 3.6).

The new nonlinear RZT-FE model is then extended to the analysis of delaminated composite beams using one-dimensional beam finite elements to evaluate the buckling and the nonlinear response in the presence of delaminations (Section 3.6.1). This new method is much more general than other analytical models which require a symmetric lamination hypothesis. In addition, the use of one-dimensional finite elements results in less computational cost than the FE commercial codes, where two- or three-dimensional models are necessary for this kind of problem. Moreover, the presence of the converse piezoelectric effect in the model allows the possibility to investigate the usage of piezoelectric actuators to control the local buckling of delaminated sandwich beams.

3.2 Nonlinear RZT for composite beams with piezoelectric layers: basic assumptions

The basic assumptions of the Refined Zigzag Theory for beams are here recalled [48] and a nonlinear strain field based on the RZT is derived to extend the theory to the analysis of composite beams with geometric nonlinearities and geometric imperfections.

The beam reference system (x, y, z) is oriented in the way that the coordinate $x \in [x_a, x_b]$ corresponds to the beam longitudinal axis and the coordinate $z \in [-h, h]$ corresponds to the beam thickness (see Fig.[3.1]). The length of the beam is L and the cross-sectional area $A = 2h \times b$ lays in the (y, z) plane. The beam lamination is constituted of N orthotropic material layers, including piezoelectric materials, with the orthotropy axes corresponding to the Cartesian coordinates[1]. The thickness of each layer is $2h^{(k)}$, where the superscript (k) indicates the kth material layer. The beam presents an initial geometric imperfection described by the function $w^*(x)$ indicating the initial (stress-free) transversal deviations of the beam from a straight axis configuration.

---

[1]The assumption of having layers with the orthotropy axes corresponding to the Cartesian coordinates is a consequence of the fact that the RZT model considers beams in cylindrical bending in the (x, z) plane; any other orientation of the layers would cause an out-of-plane displacement.
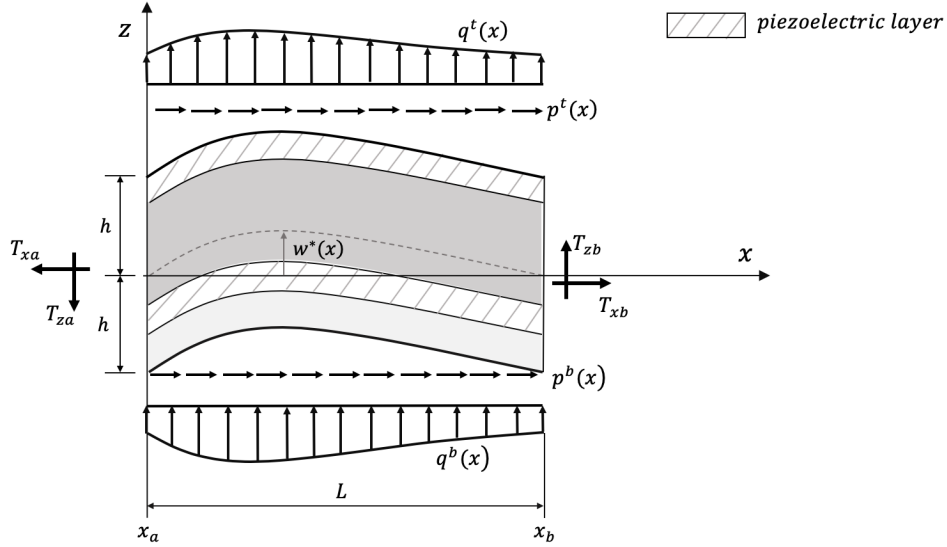
Figure 3.1: Notation for beam geometry and applied loads.

The mechanical loads applied to the bottom $(z = -h)$ and the top $(z = +h)$ beam surfaces are the distributed axial loads, $p^b(x)$ and $p^t(x)$, and the distributed transverse loads, $q^b(x)$ and $q^t(x)$ (units of force/ length). In addition, the end cross-sections are subjected to the prescribed axial (T_{xa}, T_{xb}) and transverse-shear (T_{za}, T_{zb}) tractions. Only planar deformations in the (x, z) plane are considered under the assigned load system.

The orthogonal displacement vector **s** in the Refined Zigzag Theory [51] is defined as

$$\mathbf{s} \equiv \begin{Bmatrix} u_x^{(k)}(x,z) \\ u_z(x,z) \end{Bmatrix} = \begin{bmatrix} 1 & 0 & z & \phi^{(k)} \\ 0 & 1 & 0 & 0 \end{bmatrix} \begin{Bmatrix} u(x) \\ w(x) \\ \theta(x) \\ \psi(x) \end{Bmatrix} \equiv \mathbf{Z_u u} \,, \tag{3.1}$$

where $u_x^{(k)}$ and u_z are the displacements in the directions of the $x-$ and $z-$axis, respectively. The transverse displacement $u_z \equiv w$ is assumed to be uniform along the beam thickness, thus it is independent of the kth layer characteristics. The vector **u** contains the four kinematic variables of the theory: the uniform axial displacement, $u(x)$, the deflection, $w(x)$, the average cross-sectional (bending) rotation, $\theta(x)$, and the zigzag rotation, $\psi(x)$. This variable was introduced to model the through-the-thickness zigzag trend of the axial displacement. The total zigzag displacement is obtained multiplying $\psi(x)$ and the zigzag function, $\phi^{(k)}$. A subscript (i) is used to indicate the interface between consecutive layers $(i = 0,1, \cdots, N)$, as shown in Fig.[3.2].
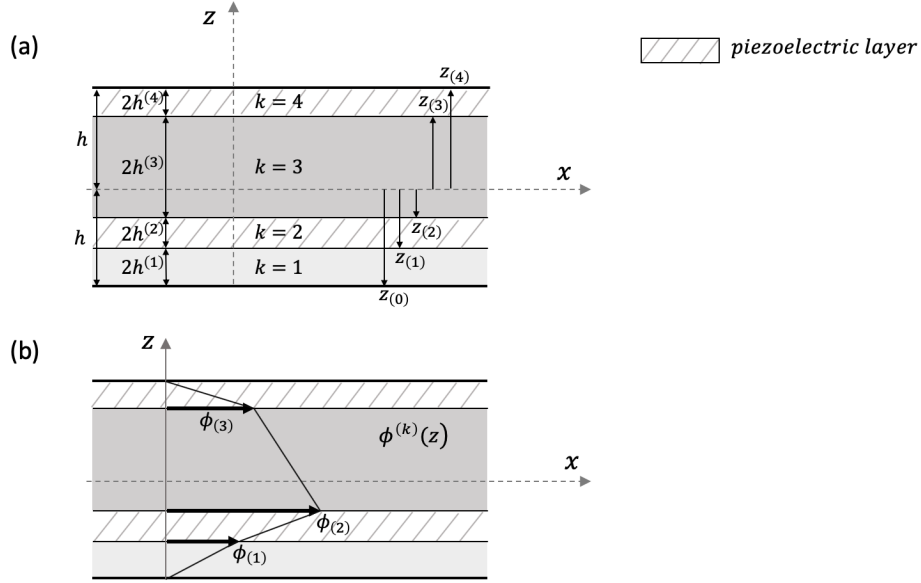
Figure 3.2: Through-thickness layer notation and zigzag function of the Refined Zigzag Theory for a four-layered piezo-composite laminate: (a) layer notation and (b) zigzag function.

The first interface layer, $i = 0$, is at $z \equiv z_{(0)} = -h$, and the last interface, $i = N$, is at $z \equiv z_{(N)} = h$; the axial displacement, $u_x^{(k)}(x, z)$, and the zigzag function, $\phi^{(k)}$, vanish on both the top and the bottom surfaces of the beam:

$$\phi_{(0)} = \phi^{(1)}(-h) = 0 \qquad \text{and} \qquad \phi_{(N)} = \phi^{(N)}(+h) = 0, \qquad (3.2)$$

$$u_{(0)} = u(x, -h) = 0 \qquad \text{and} \qquad u_{(N)} = u(x, h) = 0. \qquad (3.3)$$

Within the layer, the function $\phi^{(k)}$ is piecewise linear, C^0-continuous, and it is also lamination and material dependent (see Fig.[3.2]). At the i-th layer interface, the zigzag function is

$$\phi_{(i)} = \phi_{(i-1)} + 2h^{(i)}\beta^{(i)}, \qquad i = 1, \cdots, N - 1, \qquad (3.4)$$

where $\beta^{(i)} \equiv \phi_{,z}^{(i)}$ and it is piecewise-constant along the thickness. $\beta^{(k)}$ ($k = 1, \cdots, N$) can be expressed in terms of the displacements at the top and the bottom interfaces of the kth layer:

$$\beta^{(k)} = \frac{u_{(k)} - u_{(k-1)}}{2h^{(k)}}, \qquad k = 1, \cdots, N. \qquad (3.5)$$

Taking into account Eq.[3.3], the following property can be derived from Eq.[3.5]:

$$\int_A \beta^{(k)} dA \equiv b \sum_{k=1}^{N} \left(u_{(k)} - u_{(k-1)} \right) = b(u_{(N)} - u_{(0)}) = 0 \,. \qquad (3.6)$$

As shown in [48], the enforcement of the continuity of a transversal shear stress component in the Refined Zigzag model leads to

$$G_{xz}^{(k)}(1 + \beta^{(k)}) = G_{xz}^{(k+1)}(1 + \beta^{(k+1)}) \,, \qquad k = 1, \cdots, N-1, \qquad (3.7)$$

where $G_{xz}^{(k)}$ is the transverse-shear modulus of the kth layer. The quantity $G \equiv G_{xz}^{(k)}(1 + \beta^{(k)})$ is then constant along the beam thickness and the function $\beta^{(k)}$ can be expressed as

$$\beta^{(k)} = \frac{G}{G_{xz}^{(k)}} - 1 \,, \qquad k = 1, \cdots, N. \qquad (3.8)$$

Integrating Eq.[3.8] over the beam cross-section and considering Eq.[3.6], G is defined in terms of the transverse-shear moduli of all the layers:

$$G = \frac{2h}{\int_{-h}^{h} \left(1/G_{xz}^{(k)} \right) dz} = \frac{2h}{\sum_{k=1}^{N} \left(h^{(k)}/G_{xz}^{(k)} \right)} \,, \qquad (3.9)$$

Eqs.[3.4-3.8] show that the slope of the zigzag function along the thickness of each layer depends on the transverse-shear modulus of the layer, $G_{xz}^{(k)}$. However, in case of an anti-symmetric lamination and an external layer with a transverse-shear rigidity weaker than the adjacent one, the external layer behaviour is driven by the internal layer and, consequently, the slope of the axial displacement function $(u(x,z))$ along z is continuous at the interface. This means that also the zigzag function slope has to be the same in the two consecutive layers. In [54], Gherlone proved that the correct calculation of the zigzag function is obtained taking the transverse-shear modulus of the inner layer as the value of the transverse-shear modulus for the external weaker layer (only for defining the zigzag function).

A layer thickness coordinate, $\zeta^{(k)} \in [-1,1]$, is introduced to completely define the linear distribution of $\phi^{(k)}$ in the kth material layer located in the range $[z_{(k-1)}, z_{(k)}]$:

$$\zeta^{(k)} = [(z - z_{(k-1)})/h^{(k)} - 1] \,, \qquad k = 1, \cdots, N \,.$$

The full expression of $\phi^{(k)}$ along the thickness of the kth material layer is

$$\phi^{(k)} \equiv \frac{1}{2}(1 - \zeta^{(k)})\phi_{(k-1)} + \frac{1}{2}(1 + \zeta^{(k)})\phi_{(k)} \,.$$

The nonlinear axial strain is considered in the RZT formulation using the von Kármán kinematic equations particularised to beam structures. Moreover, the

RZT is here extended introducing also the geometric imperfections in the nonlinear relations (it has never been done for the RZT in any other work):

$$\epsilon_x = u_{x,x} + \frac{1}{2}u_{z,x}^2 + u_{z,x}w_{,x}^*\,,$$
$$\gamma_{xz} = \frac{1}{2}\big(u_{x,z} + u_{z,x}\big)\,.\tag{3.10}$$

Substituting the derivatives of the displacement components of Eq.[3.1] in Eq.[3.10], the RZT nonlinear axial strain, $\epsilon_x^{(k)}$, and shear strain, $\gamma_{xz}^{(k)}$, are obtained:

$$\epsilon_x^{(k)} = u_{,x} + z\theta_{,x} + \phi^{(k)}\psi_{,x} + \frac{1}{2}w_{,x}^2 + w_{,x}w_{,x}^*\,,$$
$$\gamma_{xz}^{(k)} = w_{,x} + \theta + \beta^{(k)}\psi\,.\tag{3.11}$$

In matrix form,

$$\epsilon_x^{(k)} = \mathbf{Z}_\epsilon^{(\mathbf{k})}\boldsymbol{\omega} + \frac{1}{2}\boldsymbol{\omega}^T\mathbf{H}\boldsymbol{\omega} + \boldsymbol{\omega}^{*T}\boldsymbol{\omega}\,,$$
$$\gamma_{xz}^{(k)} = \mathbf{Z}_\gamma^{(\mathbf{k})}\boldsymbol{\omega}\,.\tag{3.12}$$

The vectors $\boldsymbol{\omega}$ and $\boldsymbol{\omega}^*$ contain, respectively, the derivative with respect to the x-coordinate of the kinematic variables of the theory and of the initial imperfection function, $w^*(x)$,

$$\boldsymbol{\omega} \equiv \begin{bmatrix} u_{,x} & w_{,x} & \theta & \psi & \theta_{,x} & \psi_{,x} \end{bmatrix}^T,\tag{3.13}$$
$$\boldsymbol{\omega}^* \equiv \begin{bmatrix} 0 & w_{,x}^* & 0 & 0 & 0 & 0 \end{bmatrix}^T.\tag{3.14}$$

The matrices $\mathbf{Z}_\epsilon^{(\mathbf{k})}$ and $\mathbf{Z}_\gamma^{(\mathbf{k})}$ contain the terms of Eq.[3.11] dependent on the z-coordinate:

$$\mathbf{Z}_\epsilon{}^{(k)} = \begin{bmatrix} 1 & 0 & 0 & 0 & z & \phi^{(k)} \end{bmatrix},\tag{3.15}$$
$$\mathbf{Z}_\gamma{}^{(k)} = \begin{bmatrix} 0 & 1 & 1 & \beta^{(k)} & 0 & 0 \end{bmatrix},\tag{3.16}$$

and $\mathbf{H}$ is a zero-one matrix which selects the suitable component of the vector $\boldsymbol{\omega}$ to express the quadratic term of $\epsilon_x^{(k)}$,

$$\mathbf{H} = \begin{bmatrix} 0 & 0 & 0 & 0 & 0 & 0 \\ 0 & 1 & 0 & 0 & 0 & 0 \\ 0 & 0 & 0 & 0 & 0 & 0 \\ 0 & 0 & 0 & 0 & 0 & 0 \\ 0 & 0 & 0 & 0 & 0 & 0 \\ 0 & 0 & 0 & 0 & 0 & 0 \end{bmatrix}.\tag{3.17}$$

3.2.1 Constitutive relations for electro-mechanical fields

The converse piezoelectric effect has been modelled for the piezoelectric layers of the beam in Fig.[3.1] to work as actuators. The poling direction in each piezoelectric layer is parallel to the $z-$coordinates, as indicated in Fig.[3.3].
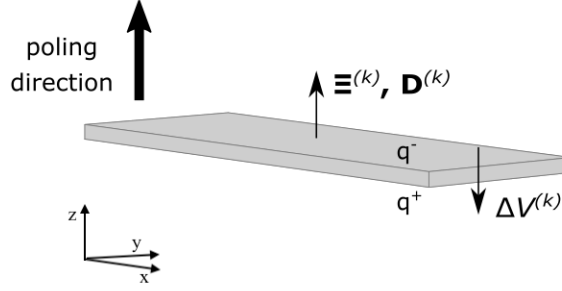
Figure 3.3: Piezoelectric layers characteristics.

The top and the bottom surfaces have two different electric charges, q^- and q^+, giving an electric potential difference $\Delta V^{(k)}$ parallel to the poling direction. For the assumptions made, the electric field vector, $\mathbf{\Xi}^{(k)}$, and the electric displacement vector, $\mathbf{D}^{(k)}$, are

$$\mathbf{\Xi}^{(k)} = \begin{Bmatrix} 0 \\ 0 \\ \Xi^{(k)} \end{Bmatrix} , \qquad \mathbf{D}^{(k)} = \begin{Bmatrix} 0 \\ 0 \\ D_z^{(k)} \end{Bmatrix} . \tag{3.18}$$

The electrostatic behaviour of the piezoelectric layers is assumed to be linear, thus the dielectric properties are not dependent on the electrostatic field intensity.

Making the hypotheses that the beam exhibits a plane-stress behavior in the (x, z) plane and the transverse normal stress $\sigma_z^{(k)}$ is negligibly small compared to the axial and transverse-shear stresses, the constitutive relations of the beam for a linearly coupled electro-mechanical field are

$$\sigma_x^{(k)} = E_x^{(k)}\epsilon_x^{(k)} - e_{31}^{(k)}\Xi_z^{(k)} ,$$
$$\tau_{xz}^{(k)} = G_{xz}^{(k)}\gamma_{xz}^{(k)} , \tag{3.19}$$

$$D_z^{(k)} = e_{31}^{(k)}\epsilon_x^{(k)} + \chi_{33}^{(k)}\Xi_z^{(k)} . \tag{3.20}$$

where $E_x^{(k)}$ and $G_{xz}^{(k)}$ are, respectively, the axial and the transverse-shear moduli of the kth layer, and $e_{31}^{(k)}$ and $\chi_{33}^{(k)}$ are the piezoelectric stress coefficient and the

dielectric permittivity of the material. All the mechanical and electrical properties are assumed to be constant in time and within each layer.

The constitutive relations are particularised to the RZT-beam substituting Eq.[3.11] in Eqs.[3.19 - 3.20], obtaining

$$
\sigma_x^{(k)} = E_x^{(k)} \left(u_{,x} + z\theta_{,x} + \phi^{(k)}\psi_{,x} + \frac{1}{2}w_{,x}^2 + w_{,x}w_{,x}^* \right) - e_{31}^{(k)}\Xi_z^{(k)} \,,
$$

$$
\tau_{xz}^{(k)} = G_{xz}^{(k)} \left(w_{,x} + \theta + \beta^{(k)}\psi \right) \,, \tag{3.21}
$$

$$
D_z^{(k)} = e_{31}^{(k)} \left(u_{,x} + z\theta_{,x} + \phi^{(k)}\psi_{,x} + \frac{1}{2}w_{,x}^2 + w_{,x}w_{,x}^* \right) + \chi_{33}^{(k)}\Xi_z^{(k)} \,. \tag{3.22}
$$

3.3 Nonlinear equilibrium equations for composite beams with piezoelectric actuators based on the RZT

In this section, the Principle of Virtual Work (PVW) is employed in the form of the electrical enthalpy to express the coupling between the mechanical and electrical fields and derive the Euler-Lagrange equilibrium equations for imperfect beams with piezoelectric actuator layers. Firstly, the electrical enthalpy and the work of the external forces and charges are particularised to the nonlinear RZT for beams and subsequently the nonlinear equilibrium equations and a set of consistent boundary conditions are obtained assuming that the total virtual work vanishes.

3.3.1 The Principle of Virtual Work for electro-mechanical applications

The PVW for electro-mechanical systems can be formulated as the equality of the virtual variation of the electrical enthalpy, δH_e, and the virtual work of the external forces and electrical charges, δL_E [107]:

$$
\delta H_E - \delta L = 0 \qquad \rightarrow \qquad \delta H_E = \delta L \,. \tag{3.23}
$$

The virtual variation of the electrical enthalpy

By definition, the electrical enthalpy is related to the internal energy, U, and to the work of the internal charges, U_e, as follows [107]:

$$
H_E = U - U_E \,, \tag{3.24}
$$

37

where

$$U_E = \int_V \mathbf{\Xi}^T \mathbf{D} dV \, . \tag{3.25}$$

Since for an adiabatic process the virtual variation of the internal energy is [122]

$$\delta U = \int_V \delta \boldsymbol{\epsilon}^T \boldsymbol{\sigma} dV + \int_V \delta \mathbf{D}^T \mathbf{\Xi} dV \, , \tag{3.26}$$

the virtual variation of the electric enthalpy is

$$\delta H_E = \int_V \delta \boldsymbol{\epsilon}^T \boldsymbol{\sigma} dV - \int_V \delta \mathbf{\Xi}^T \mathbf{D} dV \, , \tag{3.27}$$

where the quantities $\boldsymbol{\epsilon}$ and $\boldsymbol{\sigma}$ are the strain and stress tensors.

Considering the assumptions made in the previous sections, the products in the integrals of the Eq.[3.27] can be simplified as follows:

$$\delta H_E = \int_{x_a}^{x_b} \int_A \left[\delta \epsilon_x^{(k)} \sigma_x^{(k)} + \delta \gamma_{xz}^{(k)} \tau_{xz}^{(k)} \right] dA dx - \int_V \delta \Xi_z^{(k)T} D_z^{(k)} dV \, . \tag{3.28}$$

A voltage source is assumed as electric power supplier of the piezoelectric actuator layers. This means that the electric potential on each electrode of the generic piezoelectric layer, and thus the electric field $\Xi_z^{(k)}$ in the layer, is prescribed. For this reason, the virtual variation $\delta \Xi_z^{(k)}$ vanishes.

Using the nonlinear strain-displacement relations for the RZT of Eq.[3.11], δH_E becomes

$$\delta H_E = \int_{x_a}^{x_b} \int_A \left[\delta \left(u_{,x} + z\theta_{,x} + \phi^{(k)}\psi_{,x} + \frac{1}{2}w_{,x}^2 + w_{,x}w_{,x}^* \right) \sigma_x^{(k)} + \right.$$
$$\left. + \delta \left(w_{,x} + \theta + \beta^{(k)}\psi \right) \tau_{xz}^{(k)} \right] dA dx \, . \tag{3.29}$$

Defining the internal forces and moments as

$$[N_x, M_x, M_\phi] \equiv \int_A (1, z, \phi^{(k)})\sigma_x^{(k)} dA \, ,$$
$$[V_x, V_\phi] \equiv \int_A (1, \beta^{(k)})\tau_{xz}^{(k)} dA \, , \tag{3.30}$$

and integrating over the beam cross-section, Eq.[3.29] is reduced to

$$\delta H_E = \int_{x_a}^{x_b} \left[N_x \delta u_{,x} + M_x \delta \theta_{,x} + M_\phi \delta \psi_{,x} + N_x (w_{,x} + w_{,x}^*)\delta w_{,x} + V_x \delta w_{,x} + V_x \delta \theta + \right.$$
$$\left. + V_\phi \delta \psi \right] dx \, . \tag{3.31}$$

38

Integrating by parts, the expression of the electrical enthalpy virtual variation for the nonlinear RZT for beams is obtained:

$$
\delta H_E = \int_{x_a}^{x_b} \Big[-N_{x,x}\delta u - M_{x,x}\delta\theta - M_{\phi,x}\delta\psi - [N_x(w_{,x} + w^*_{,x}) + V_x]_{,x}\delta w + V_x\delta\theta +
$$
$$
+ V_\phi\delta\psi \Big] dx + [N_x\delta u]_{x_a}^{x_b} + [M_x\delta\theta]_{x_a}^{x_b} + [M_\phi\delta\psi]_{x_a}^{x_b} + [(N_x(w_{,x} + w^*_{,x}) + V_x)\delta w]_{x_a}^{x_b} .
$$

$$(3.32)$$

The virtual work of the external forces and charges

The external action to be considered in the PVW for an electro-mechanical system is the sum of the virtual work done by the external mechanical forces for an arbitrary admissible virtual displacement field, δL_m, and the virtual work done by external charges for an arbitrary admissible virtual electric potential, δL_E [107]:

$$
\delta L = \delta L_m + \delta L_E .
$$

$$(3.33)$$

The quantity $\delta L_E = 0$ because the electric potential is prescribed, thus δL corresponds to δL_m. For the load system represented in Fig.[3.1],

$$
\delta L = \int_{x_a}^{x_b} \Big[p^b\delta u_x^{(1)}(-h) + p^t\delta u_x^{(N)}(+h) + q^b\delta u_z^{(1)}(-h) + q^t\delta u_z^{(N)}(+h) \Big] dx +
$$
$$
- \int_A \Big[T_{xa}\delta u_x^{(k)}(x_a,z) + T_{za}\delta u_z^{(k)}(x_a,z) \Big] dA + \int_A \Big[T_{xb}\delta u_x^{(k)}(x_b,z) + T_{zb}\delta u_z^{(k)}(x_b,z) \Big] dA .
$$

$$(3.34)$$

Considering the displacement field for the RZT-beam (Eq.[3.1]),

$$
\delta L = \int_{x_a}^{x_b} \Big[p^b \cdot (\delta u - h\delta\theta) + p^t \cdot (\delta u + h\delta\theta) + q^b \cdot \delta w + q^t \cdot \delta w \Big] dx +
$$
$$
- \int_A [T_{xa} \cdot (\delta u(x_a) + z\delta\theta(x_a) + \phi\delta\psi(x_a)) + T_{za} \cdot \delta w(x_a)] dA + \quad (3.35)
$$
$$
+ \int_A [T_{xb} \cdot (\delta u(x_b) + z\delta\theta(x_b) + \phi\delta\psi(x_b)) + T_{zb} \cdot w(x_b)] dA .
$$

It can be rearranged as

$$
\delta L = \int_{x_a}^{x_b} \Big[(p^b + p^t) \cdot \delta u + h(p^t - p^b) \cdot \delta\theta + (q^b + q^t) \cdot \delta w \Big] dx +
$$
$$
- \int_A [T_{xa} \cdot \delta u(x_a) + zT_{xa} \cdot \delta\theta(x_a) + \phi T_{xa} \cdot \delta\psi(x_a) + T_{za} \cdot \delta w(x_a)] dA + \quad (3.36)
$$
$$
+ \int_A [T_{xb} \cdot \delta u(x_b) + zT_{xb} \cdot \delta\theta(x_b) + \phi T_{xb} \cdot \delta\psi(x_b) + T_{zb} \cdot w(x_b)] dA .
$$

The applied concentrated forces and moments are defined as

$$[\bar{N}_{x\alpha}, \bar{M}_{x\alpha}, \bar{M}_{\phi\alpha}, \bar{V}_{x\alpha}] \equiv \int_A [T_{x\alpha}, zT_{x\alpha}, \phi^{(k)}T_{x\alpha}, T_{z\alpha}]dA\,, \qquad (\alpha = a, b), \quad (3.37)$$

while

$$[\bar{p}, \bar{q}, \bar{m}] \equiv [p^b + p^t, q^b + q^t, h(p^t - p^b)] \quad (3.38)$$

are the total distributed axial ($\bar{p}$) and transverse ($\bar{q}$) loads and the distributed bending moment ($\bar{m}$).

Simplifying Eq.[3.36], the expression of the virtual work of the external forces is obtained:

$$\delta L = \int_{x_a}^{x_b} [\bar{p} \cdot \delta u + \bar{m} \cdot \delta\theta + \bar{q} \cdot \delta w]\,dx - \bar{N}_{xa} \cdot \delta u(x_a) - \bar{M}_{xa} \cdot \delta\theta(x_a) - \bar{M}_{\phi a} \cdot \delta\psi(x_a)+$$
$$- \bar{V}_{xa} \cdot \delta w(x_a) + \bar{N}_{xb} \cdot \delta u(x_b) + \bar{M}_{xb} \cdot \delta\theta(x_b) + \bar{M}_{\phi b} \cdot \delta\psi(x_b) + \bar{V}_{xb} \cdot \delta w(x_b)\,.$$
$$(3.39)$$

3.3.2 Nonlinear equilibrium equations based on the RZT

The PVW of Eq.[3.23] is particularised to the nonlinear RZT for beams considering the expression of the virtual variation of the electrical enthalpy of Eq.[3.32] and the virtual work of Eq.[3.39]:

$$\int_{x_a}^{x_b} \left\{ [N_{x,x} + \bar{p}] \cdot \delta u + [N_{x,x}(w_{,x} + w^*_{,x}) + N_x(w_{,xx} + w^*_{,xx}) + V_{x,x} + \bar{q}] \cdot \delta w + \right.$$
$$+ [M_{x,x} - V_x + \bar{m}] \cdot \delta\theta + [M_{\phi,x} - V_\phi] \cdot \delta\psi \right\}dx = \bar{N}_{xa} \cdot \delta u(x_a) + \bar{M}_{xa} \cdot \delta\theta(x_a)+$$
$$+ \bar{M}_{\phi a} \cdot \delta\psi(x_a) + \bar{V}_{xa} \cdot \delta w(x_a) - \bar{N}_{xb} \cdot \delta u(x_b) - \bar{M}_{xb} \cdot \delta\theta(x_b) - \bar{M}_{\phi b} \cdot \delta\psi(x_b)+$$
$$- \bar{V}_{xb} \cdot \delta w(x_b) + [N_x \delta u]_{x_a}^{x_b} + [M_x \delta\theta]_{x_a}^{x_b} + [M_\phi \delta\psi]_{x_a}^{x_b} + [(N_x(w_{,x} + w^*_{,x}) + V_x)\delta w]_{x_a}^{x_b}\,.$$
$$(3.40)$$

The first term of the equation gives the nonlinear equilibrium equations for RZT:

$$N_{x,x} + \bar{p} = 0\,,$$
$$N_{x,x}(w_{,x} + w^*_{,x}) + N_x(w_{,xx} + w^*_{,xx}) + V_{x,x} + \bar{q} = 0\,,$$
$$M_{x,x} - V_x + \bar{m} = 0\,,$$
$$M_{\phi,x} - V_\phi = 0\,, \qquad (3.41)$$

and the second term yields the boundary conditions:

$$
\begin{aligned}
u(x_\alpha) &= \bar{u}_\alpha\,, &\quad \text{or} \quad& & N_x(x_\alpha) &= \bar{N}_{x_\alpha}\,, \\
w(x_\alpha) &= \bar{w}_\alpha\,, &\quad \text{or} \quad& & V_x(x_\alpha) &= \bar{V}_{x_\alpha}\,, \\
\theta(x_\alpha) &= \bar{\theta}_\alpha\,, &\quad \text{or} \quad& & M_x(x_\alpha) &= \bar{M}_{x_\alpha}\,, \\
\psi(x_\alpha) &= \bar{\psi}_\alpha\,, &\quad \text{or} \quad& & M_\phi(x_\alpha) &= \bar{M}_{\phi_\alpha}\,,
\end{aligned}
\tag{3.42}
$$

where the bar superscript indicates prescribed quantities (either displacements and rotations or forces and moments) at the beam edges for $\alpha = a, b$.

Equilibrium equations in terms of displacement components

The nonlinear constitutive equations relate the stress resultants to the derivative of the displacement components. They are obtained expressing the stresses in Eqs.[3.30] as in Eqs.[3.19], and the strains as in Eqs.[3.12]. The resulting relations can be written in matrix form as

$$
\mathbf{R} = \boldsymbol{\Delta}\boldsymbol{\omega} + \bar{\boldsymbol{\Delta}}\left(\frac{1}{2}\boldsymbol{\omega}^T\boldsymbol{H}\boldsymbol{\omega} + \boldsymbol{\omega}^{*T}\boldsymbol{\omega}\right) - \mathbf{F^{ind}}\,.
\tag{3.43}
$$

The vector $\mathbf{R} \equiv [N_x \quad V_x \quad V_\phi \quad M_x \quad M_\phi]^T$ contains the stress resultants and $\boldsymbol{\Delta}$ is the matrix defined as

$$
\boldsymbol{\Delta} =
\begin{bmatrix}
A_{11} & 0 & 0 & 0 & B_{12} & B_{13} \\
0 & \bar{G}A & \bar{G}A & (G-\bar{G})A & 0 & 0 \\
0 & (G-\bar{G})A & (G-\bar{G})A & (\bar{G}-G)A & 0 & 0 \\
B_{12} & 0 & 0 & 0 & D_{11} & D_{12} \\
B_{13} & 0 & 0 & 0 & D_{12} & D_{22}
\end{bmatrix}\,,
\tag{3.44}
$$

where the stiffness coefficients are

$$
\begin{aligned}
[A_{11}, B_{12}, D_{11}] &\equiv \int_A E_x^{(k)}[1, z, z^2]dA\,, \\
[B_{13}, D_{12}, D_{22}] &\equiv \int_A E_x^{(k)}\phi^{(k)}[1, z, \phi^{(k)}]dA\,,
\end{aligned}
\tag{3.45}
$$

and

$$
\bar{G} \equiv \frac{1}{2h}\int_{-h}^{+h} G_{xz}^{(k)}dz\,,
\tag{3.46}
$$

is the average thickness-weighted transverse-shear modulus of the total laminate.

The vector $\bar{\boldsymbol{\Delta}}$ in Eq.[3.43] corresponds to the first column of the matrix $\boldsymbol{\Delta}$, and $\mathbf{F^{ind}}$ contains the induced axial force and moments due to the piezoelectric actuation,

$$\mathbf{F^{ind}} \equiv [N_x^{ind} \quad 0 \quad 0 \quad M_x^{ind} \quad M_\phi^{ind}]^T \equiv \int_A e_{31}^{(k)} \Xi_z^{(k)} [1,0,0,z,\phi^{(k)}]^T dA \,. \tag{3.47}$$

The Equilibrium equations in terms of displacement components can be obtained substituting the stress resultant of Eq.[3.43] into Eq.[3.41]:

$$A_{11} \left[u_{,xx} + \left(\frac{1}{2} w_{,x}^2 + w_{,x} w_{,x}^* \right)_{,x} \right] + B_{12} \theta_{,xx} + B_{13} \psi_{,xx} + \bar{p} - N_{x,x}^{ind} = 0 \,,$$

$$\left\{ \left[A_{11} \left(u_{,x} + \frac{1}{2} w_{,x}^2 + w_{,x} w_{,x}^* \right) + B_{12} \theta_{,x} + B_{13} \psi_{,x} - N_x^{ind} \right] (w_{,x} + w_{,x}^*) \right\}_{,x} +$$

$$+ \bar{G} A (w_{,xx} + \theta_{,x}) + (G - \bar{G}) A \psi_{,x} + \bar{q} = 0 \,,$$

$$B_{12} \left[u_{,xx} + \left(\frac{1}{2} w_{,x}^2 + w_{,x} w_{,x}^* \right)_{,x} \right] + D_{11} \theta_{,xx} + D_{12} \psi_{,xx} - \bar{G} A (w_{,x} + \theta) - (G - \bar{G}) A \psi +$$

$$+ \bar{m} - M_{x,x}^{ind} = 0 \,,$$

$$B_{13} \left[u_{,xx} + \left(\frac{1}{2} w_{,x}^2 + w_{,x} w_{,x}^* \right)_{,x} \right] + D_{12} \theta_{,xx} + D_{22} \psi_{,xx} - (G - \bar{G}) A (w_{,x} + \theta) +$$

$$- (\bar{G} - G) A \psi - M_{\phi,x}^{ind} = 0 \,. \tag{3.48}$$

It is worth noticing that the electric field in the kth piezoelectric layer can be expressed as the ratio between the applied voltage, $V^{(k)}$, and the layer thickness, $2h^{(k)}$,

$$\Xi_z^{(k)} = \frac{V^{(k)}}{2h^{(k)}} \,, \tag{3.49}$$

thus the induced resultant force and moments of Eq.[3.47] can be also written as

$$[N_x^{ind}, 0, 0, M_x^{ind}, M_\phi^{ind}]^T = \int_A \frac{e_{31}^{(k)}}{2h^{(k)}} V^{(k)} [1,0,0,z,\phi^{(k)}]^T dA \,. \tag{3.50}$$

The electrical quantities $e_{31}^{(k)}$ and $V^{(k)}$ are constant within the layer so they can be taken out of the integral. In addition, the electrical stiffness coefficients per unit of voltage in the kth layer can be defined as

$$\left[a_E^{(k)}, d_E^{(k)}, c_E^{(k)} \right] \equiv b \frac{e_{31}^{(k)}}{2h^{(k)}} \int_{z^{k-}}^{z^{k+}} \left(1, z, \phi^{(k)} \right) dz \,, \tag{3.51}$$

and consequently Eq.[3.50] becomes

$$[N_x^{ind}, 0, 0, M_x^{ind}, M_\phi^{ind}]^T = \sum_{k=1}^{N} [a_E^{(k)}, 0, 0, d_E^{(k)}, c_E^{(k)}]^T V^{(k)} . \tag{3.52}$$

3.3.3 Example of an analytical solution of the RZT nonlinear equilibrium equations

The equilibrium problem for a composite beam with piezoelectric layers and geometric imperfections can be solved using Eqs.[3.41]. In general cases, it is not easy or even possible to find a solution of the equilibrium equations. One case for which a solution exists is when a simply-supported, symmetric laminated beam is considered in the following conditions (refer to Fig.[3.4]):

- the initial imperfection function has a sinusoidal distribution along the beam length, $w^* = w_0^* \cdot sin(\pi x/L)$;

- the distributed axial load and the distributed bending moment are equal to zero, $\bar{p} = \bar{m} = 0$;

- the beam is subjected to a sinusoidal distributed transverse load, $\bar{q} = q_0 \cdot sin(\pi x/L)$, and to a compressive axial load λN_0 at the supported edge (λ is constant and N_0 is a reference load);

- two piezoelectric-actuator layers are uniformly distributed on the top and the bottom beam surfaces with a constant voltage, $\bar{V}$, applied to both layers.
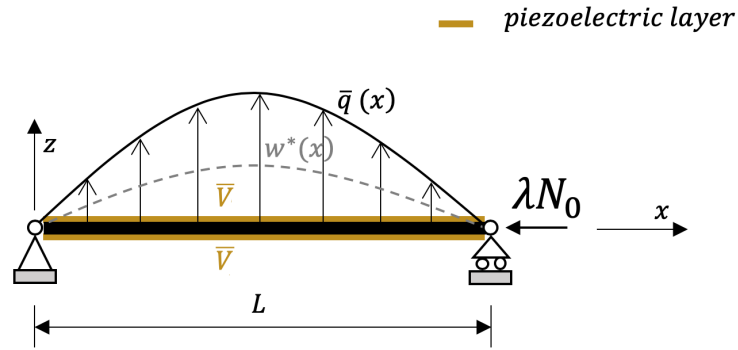
Figure 3.4: Geometrically imperfect beam with two piezoelectric actuator layers subjected to a sinusoidal transverse load, $\bar{q}$, and a compressive force, λN_0, in simply-supported boundary conditions.

For the assumptions made, Eqs.[3.41] become

$$
\begin{aligned}
N_{x,x} &= 0 \,, \\
N_{x,x}(w_{,x} + w^*_{,x}) + N_x(w_{,xx} + w^*_{,xx}) + V_{x,x} + \bar{q} &= 0 \,, \\
M_{x,x} - V_x &= 0 \,, \\
M_{\phi,x} - V_\phi &= 0 \,,
\end{aligned}
\tag{3.53}
$$

and the boundary conditions at the beam edges, x=0 and x=L, are

$$
\begin{cases}
u(0) = 0 \,, \\
w(0) = 0 \,, \\
M_x(0) = 0 \,, \\
M_\phi(0) = 0
\end{cases}
\quad \text{and} \quad
\begin{cases}
N_x(L) = -\lambda N_0 \,, \\
w(L) = 0 \,, \\
M_x(L) = 0 \,, \\
M_\phi(L) = 0 \,.
\end{cases}
\tag{3.54}
$$

The first equation of Eqs.[3.53] implies that N_x is constant with respect to x. For the assumed boundary and loading conditions, $N_x(x) = -\lambda N_0$, thus the system of equations Eqs.[3.53] can be simplified as

$$
\begin{cases}
N_x(x) = -\lambda N_0 \qquad \forall x \in [0, L], \\
-\lambda N_0(w_{,xx} + w^*_{,xx}) + V_{x,x} + \bar{q} = 0 \,, \\
M_{x,x} - V_x = 0 \,, \\
M_{\phi,x} - V_\phi = 0 \,.
\end{cases}
\tag{3.55}
$$

Considering the constitutive equations for the nonlinear RZT for beams (Eqs.[3.43]) and the hypothesis of symmetric lamination ($B_{12} = B_{13} = 0$), the quantities in the previous equations can be expressed in terms of the derivative of the kinematic variables:

$$
\begin{aligned}
N_x &= A_{11}\left(u_{,x} + \frac{1}{2}w_{,x}^2 + w_{,x}w^*_{,x}\right) - N_x^{ind} \,, \\
V_x &= \bar{G}Aw_{,x} + \bar{G}A\theta + (G - \bar{G})A\psi \,, \\
V_\phi &= (G - \bar{G})Aw_{,x} + (G - \bar{G})A\theta + (\bar{G} - G)A\psi \,, \\
M_x &= D_{11}\theta_{,x} + D_{12}\psi_{,x} - M_x^{ind} \,, \\
M_\phi &= D_{12}\theta_{,x} + D_{22}\psi_{,x} - M_\phi^{ind} \,.
\end{aligned}
\tag{3.56}
$$

The induced force and moments are calculated using Eq.[3.52]:

44

$$N_x^{ind} = a_E^{(1)}\bar{V} + a_E^{(N)}\bar{V} = 2a_E\bar{V}\,,$$
$$M_x^{ind} = d_E^{(1)}\bar{V} + d_E^{(N)}\bar{V} = 0\,, \tag{3.57}$$
$$M_\phi^{ind} = c_E^{(1)}\bar{V} + c_E^{(N)}\bar{V} = 0\,,$$

because $a_E = a_E^{(1)} = a_E^{(N)}$, $d_E = -d_E^{(1)} = d_E^{(N)}$ and $c_E = -c_E^{(1)} = c_E^{(N)}$ for the hypothesis of symmetric lamination.
Substituting Eqs.[3.56] in Eqs.[3.55],

$$\begin{cases} A_{11}\left(u_{,x} + \dfrac{1}{2}w_{,x}^2 + w_{,x}w_{,x}^*\right) - N_x^{ind} = -\lambda N_0\,, \\[2mm] (\bar{G}A - \lambda N_0)w_{,xx} + \bar{G}A\theta_{,x} + (G - \bar{G})A\psi_{,x} = \lambda N_0 w_{,xx}^* - \bar{q}\,, \\[2mm] \bar{G}Aw_{,x} + \bar{G}A\theta - D_{11}\theta_{,xx} + (G - \bar{G})A\psi - D_{12}\psi_{,xx} = 0\,, \\[2mm] (G - \bar{G})Aw_{,x} + (G - \bar{G})A\theta - D_{12}\theta_{,xx} + (\bar{G} - G)A\psi - D_{22}\psi_{,xx} = 0\,. \end{cases} \tag{3.58}$$

Note that the derivatives of the induced moments vanish because M_x^{ind} and M_ϕ^{ind} are constant along x and also equal to zero.

The following expressions of the kinematic variables represent the solution of the system and satisfy the boundary conditions:

$$\begin{cases} u(x) &= u_0 \cdot sin(2\pi x/L) + Cx\,, \\ w(x) &= w_0 \cdot sin(\pi x/L)\,, \\ \theta(x) &= \theta_0 \cdot cos(\pi x/L)\,, \\ \psi(x) &= \psi_0 \cdot cos(\pi x/L)\,. \end{cases} \tag{3.59}$$

The amplitudes of the kinematic variables $w(x)$, $\theta(x)$ and $\psi(x)$ are determined solving the linear system obtained substituting the derivatives of Eqs.[3.59] in the last three equations of Eqs.[3.58]:

$$\begin{cases} (\bar{G}A - \lambda N_0)\dfrac{\pi}{L}w_0 + \bar{G}A\theta_0 + (G - \bar{G})A\psi_0 = \lambda N_0\dfrac{\pi}{L}w_0^* + q_0\,, \\[3mm] \bar{G}A\dfrac{\pi}{L}w_0 + \left(\bar{G}A + D_{11}\left(\dfrac{\pi}{L}\right)^2\right)\theta_0 + \left((G - \bar{G})A + D_{12}\left(\dfrac{\pi}{L}\right)^2\right)\psi_0 = 0\,, \\[3mm] (G - \bar{G})A\dfrac{\pi}{L}w_0 + \left((G - \bar{G})A + D_{12}\left(\dfrac{\pi}{L}\right)^2\right)\theta_0 + \left((\bar{G} - G)A + D_{22}\left(\dfrac{\pi}{L}\right)^2\right)\psi_0 = 0\,. \end{cases} \tag{3.60}$$

The constants u_0 and C of the $u(x)$ solution in Eqs.[3.59] can be found substituting the derivative of $u(x)$ and $w(x)$ in the expression of $N(x)$ of Eqs.[3.56]. After some operations it becomes

$$N(x) = A_{11}C - 2A_{11}\frac{\pi}{L}u_0 + A_{11}\frac{\pi}{L}\left[4u_0 + \frac{\pi}{L}\left(\frac{1}{2}w_0^2 + w_0 w_0^*\right)\right]cos^2(\frac{\pi x}{L}) - N_x^{ind}, \tag{3.61}$$

where w_0^* is the amplitude of the geometric imperfection function previously defined. In order to satisfy the first equation in Eqs.[3.55], u_0 and C must be

$$u_0 = -\frac{\pi}{8L}\left(w_0^2 + 2w_0 w_0^*\right), \tag{3.62}$$

$$C = -\left(\frac{\pi}{2L}\right)^2\left(w_0^2 + 2w_0 w_0^*\right) + \frac{N_x^{ind} - \lambda N_0}{A_{11}}. \tag{3.63}$$

3.4 Finite element formulation of the nonlinear RZT for imperfect beams with piezoelectric actuators

The analytical solution shown in the previous section has been obtained for a very particular beam which has a symmetric lamination and geometric imperfection. Nevertheless, the aim of this work is not to find the exact solution of the equilibrium equations (Eqs.[3.48]) but to create a finite element formulation based on the nonlinear RZT for piezo-composite imperfect beams able to solve the equations in an approximate way, for any kind of beam lamination, boundary and loading conditions.

Starting from the definition in Eq.[3.28], and using Eq.[3.12] and Eq.[3.21], the electrical enthalpy is written in matrix form as

$$\delta H_E = \int_{x_a}^{x_b} \int_A \left[\delta \boldsymbol{\omega}^T \mathbf{Z}_\epsilon^{(k)T} E_x^{(k)} \mathbf{Z}_\epsilon^{(k)} \boldsymbol{\omega} \right] dAdx + \frac{1}{2} \int_{x_a}^{x_b} \int_A \left[\delta \boldsymbol{\omega}^T \mathbf{Z}_\epsilon^{(k)T} E_x^{(k)} \boldsymbol{\omega}^T \boldsymbol{H} \boldsymbol{\omega} \right] dAdx +$$

$$+ \int_{x_a}^{x_b} \int_A \left[\delta \boldsymbol{\omega}^T \mathbf{Z}_\epsilon^{(k)T} E_x^{(k)} \boldsymbol{\omega}^{*T} \boldsymbol{\omega} \right] dAdx + \int_{x_a}^{x_b} \int_A \left[\delta \boldsymbol{\omega}^T \boldsymbol{H} \boldsymbol{\omega} E_x^{(k)} \mathbf{Z}_\epsilon^{(k)} \boldsymbol{\omega} \right] dAdx +$$

$$+ \int_{x_a}^{x_b} \int_A \left[\delta \boldsymbol{\omega}^T \boldsymbol{H} \boldsymbol{\omega} E_x^{(k)} \left(\frac{1}{2} \boldsymbol{\omega}^T \boldsymbol{H} \boldsymbol{\omega} \right) \right] dAdx + \int_{x_a}^{x_b} \int_A \left[\delta \boldsymbol{\omega}^T \boldsymbol{H} \boldsymbol{\omega} E_x^{(k)} \left(\boldsymbol{\omega}^{*T} \boldsymbol{\omega} \right) \right] dAdx +$$

$$+ \int_{x_a}^{x_b} \int_A \left[\delta \boldsymbol{\omega}^T \boldsymbol{\omega}^* E_x^{(k)} \mathbf{Z}_\epsilon^{(k)} \boldsymbol{\omega} \right] dAdx + \int_{x_a}^{x_b} \int_A \left[\delta \boldsymbol{\omega}^T \boldsymbol{\omega}^* E_x^{(k)} \left(\frac{1}{2} \boldsymbol{\omega}^T \boldsymbol{H} \boldsymbol{\omega} \right) \right] dAdx +$$

$$+ \int_{x_a}^{x_b} \int_A \left[\delta \boldsymbol{\omega}^T \boldsymbol{\omega}^* E_x^{(k)} \left(\boldsymbol{\omega}^{*T} \boldsymbol{\omega} \right) \right] dAdx - \int_{x_a}^{x_b} \int_A \left[\delta \boldsymbol{\omega}^T \mathbf{Z}_\epsilon^{(k)T} e_{31}^{(k)} \Xi_z^{(k)} \right] dAdx +$$

$$- \int_{x_a}^{x_b} \int_A \left[\delta \boldsymbol{\omega}^T \boldsymbol{H} \boldsymbol{\omega} e_{31}^{(k)} \Xi_z^{(k)} \right] dAdx - \int_{x_a}^{x_b} \int_A \left[\delta \boldsymbol{\omega}^T \boldsymbol{\omega}^* e_{31}^{(k)} \Xi_z^{(k)} \right] dAdx +$$

$$+ \int_{x_a}^{x_b} \int_A \left[\delta \boldsymbol{\omega}^T \mathbf{Z}_\gamma^{(k)T} G_{xz}^{(k)} \mathbf{Z}_\gamma^{(k)} \boldsymbol{\omega} \right] dAdx \,.$$

$$(3.64)$$

In Eq.[3.64], the kinematic variables appear in the vector $\boldsymbol{\omega}$ with the highest order of the derivatives, with respect to the spatial coordinate x, corresponding to the first order, thus C^0-continuous shape functions can be used for the finite element approximation. The linear Lagrange polynomials could be used as shape functions for the approximation of all the RZT kinematic variables (*isoparametric interpolation*), as for the standard formulation of the beam element based on the Timoshenko Beam Theory. However, in [5] it was proven that the use of the same polynomials degree for the shape functions approximating $u(x)$, $w(x)$ and $\theta(x)$, is the cause of the shear-locking phenomenon [4] in the TBT FE models, and to avoid this, the polynomial approximating $w(x)$ has to be one degree higher than the one used for $\theta(x)$. In this way, the condition of zero transverse-shear strain γ_{xz} for the thin-beam limit ($L/2h \to \infty$) can be guaranteed.

For this reason, the linear Lagrange polynomials, N_i^L, are here used for the variables $u(x)$, $\theta(x)$ and $\psi(x)$ whereas the quadratic Lagrange polynomials, N_j^Q, are used for the variable $w(x)$. This kind of interpolation is called *anisoparametric interpolation* because $w(x)$ and $\theta(x)$ have different polynomial degrees. A non-dimensional axial coordinate $\xi \equiv 2x/L^e - 1 \in [-1,1]$ is introduced to define the polynomials N_i^L and N_i^Q:

$$[N_1^L, N_2^L] = \left[\frac{1}{2}(1 - \xi), \frac{1}{2}(1 + \xi) \right], \tag{3.65}$$

$$[N_1^Q, N_m^Q, N_2^Q] = \left[\frac{1}{2}\xi(\xi - 1), (1 - \xi^2), \frac{1}{2}\xi(\xi + 1) \right]. \tag{3.66}$$

The anisoparametric interpolation results in a three-node finite element with four degrees of freedom at each external node and one degree of freedom, w_m, at the internal node, as shown in Fig.[3.5].
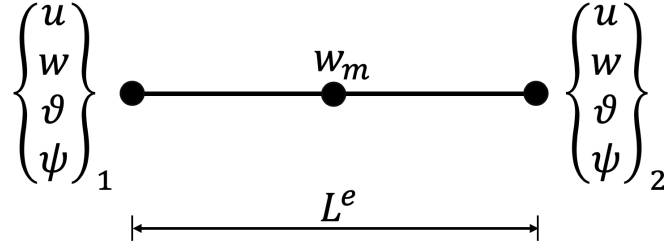
Figure 3.5: Three-node anisoparametric element based on the Refined Zigzag Theory for beams.

The vector of the nodal degrees of freedom of the three-node anisoparametric element is $\mathbf{u_{au}^e} \equiv \begin{bmatrix} u_1 & w_1 & \theta_1 & \psi_1 & w_m & u_2 & w_2 & \theta_2 & \psi_2 \end{bmatrix}^T$, thus the corresponding finite element approximation of the kinematic variable vector, $\mathbf{u}$, is

$$\mathbf{u} = \begin{Bmatrix} u(x) \\ w(x) \\ \theta(x) \\ \psi(x) \end{Bmatrix} \simeq \mathbf{N_{au}} \mathbf{u_{au}^e} \,, \tag{3.67}$$

where the shape function matrix $\mathbf{N_{au}}$ is

$$\mathbf{N_{au}} \equiv \begin{bmatrix} N_1^L & 0 & 0 & 0 & 0 & N_2^L & 0 & 0 & 0 \\ 0 & N_1^Q & 0 & 0 & N_m^Q & 0 & N_2^Q & 0 & 0 \\ 0 & 0 & N_1^L & 0 & 0 & 0 & 0 & N_2^L & 0 \\ 0 & 0 & 0 & N_1^L & 0 & 0 & 0 & 0 & N_2^L \end{bmatrix} \,. \tag{3.68}$$

As shown in [51], the topology of the three-node finite element can be simplified to obtain a two-node finite element with four degrees of freedom per node by imposing a constraint condition on the transverse-shear force resultant V_x. The definition of V_x of Eq.[3.30] can be rewritten as

$$V_x = \bar{G} A \left[w_{,x}(x) + \theta(x) + r\psi(x) \right] \,, \tag{3.69}$$

where $r \in [-1,0]$ is a transverse-shear parameter depending on the materials of the beam. The parameter is defined as

$$r \equiv -\frac{\bar{G} - G}{\bar{G}} \,. \tag{3.70}$$

Introducing the anisoparametric interpolation of the kinematic variables of Eq.[3.67] in Eq.[3.69]:

$$V_x \simeq \bar{G}A \left[N_{1,x}^Q w_1 + N_{m,x}^Q w_m + N_{2,x}^Q w_2 + N_1^L \left(\theta_1 + r\psi_1 \right) + N_2^L \left(\theta_2 + r\psi_2 \right) \right] . \quad (3.71)$$

Eq.[3.71] indicates that V_x has a linear distribution along the x-coordinate of a three-node anisoparametric finite element. Imposing the constraint condition $V_{x,x} = 0$ (V_x constant along x), the degree of freedom w_m can be expressed as a function of the degrees of freedom of the external nodes:

$$w_m = -\frac{N_{1,xx}^Q}{N_{m,xx}^Q} w_1 - \frac{N_{2,xx}^Q}{N_{m,xx}^Q} w_2 - \frac{N_{1,x}^L}{N_{m,xx}^Q} \left(\theta_1 + r\psi_1 \right) - \frac{N_{2,x}^L}{N_{m,xx}^Q} \left(\theta_2 + r\psi_2 \right) . \quad (3.72)$$

Substituting the derivative of the Lagrange polynomials of Eq.[3.66] in Eq.[3.72]:

$$w_m = \frac{w_1 + w_2}{2} + \frac{L^e}{8} \left[\left(\theta_2 + r\psi_2 \right) - \left(\theta_1 + r\psi_1 \right) \right] . \quad (3.73)$$

The *anisoparametric-constrained* approximation of the kinematic variable vector **u** is obtained substituting Eq.[3.73] in Eq.[3.67]:

$$\mathbf{u} = \begin{Bmatrix} u(x) \\ w(x) \\ \theta(x) \\ \psi(x) \end{Bmatrix} \simeq \mathbf{N}\mathbf{u}^\mathbf{e} , \quad (3.74)$$

where $\mathbf{u}^\mathbf{e}$ is a vector containing the degrees of freedom of the external nodes only,

$$\mathbf{u}^\mathbf{e} \equiv \begin{bmatrix} u_1 & w_1 & \theta_1 & \psi_1 & u_2 & w_2 & \theta_2 & \psi_2 \end{bmatrix}^T , \quad (3.75)$$

and the shape function matrix, **N**, is

$$\mathbf{N} \equiv \begin{bmatrix} N_1^L & 0 & 0 & 0 & N_2^L & 0 & 0 & 0 \\ 0 & N_1^L & -l^e N_m^Q & -l^e r N_m^Q & 0 & N_2^L & l^e N_m^Q & l^e r N_m^Q \\ 0 & 0 & N_1^L & 0 & 0 & 0 & N_2^L & 0 \\ 0 & 0 & 0 & N_1^L & 0 & 0 & 0 & N_2^L \end{bmatrix} , \quad (3.76)$$

where $l^e = L^e/8$.

The finite element corresponding to the anisoparametric-constrained approximation has only two nodes and eight degrees of freedom, as shown in Fig.[3.6]. The complete derivation of the anisoparametric-constrained finite element based on the RZT for beams and further details on the constraint condition can be found in [51].
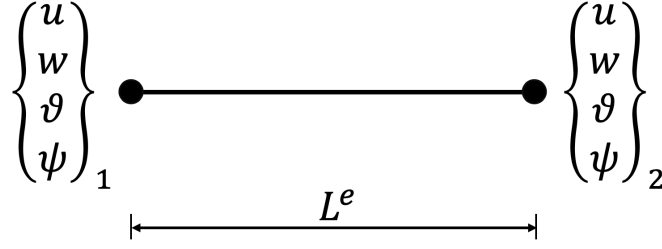
Figure 3.6: Two-node constrained anisoparametric element based on the Refined Zigzag Theory for beams.

The vector of the derivative of the kinematic variables, $\boldsymbol{\omega}$, can be approximated as

$$\boldsymbol{\omega} \simeq \mathbf{B^e u^e}, \tag{3.77}$$

where the matrix $\mathbf{B^e}$ contains the derivative of the shape functions with respect to the x coordinate,

$$\mathbf{B^e} \equiv \begin{bmatrix} N_{1,\xi}^L & 0 & 0 & 0 & N_{2,\xi}^L & 0 & 0 & 0 \\ 0 & N_{1,\xi}^L & -l^e N_{m,\xi}^Q & -l^e c N_{m,\xi}^Q & 0 & N_{2,\xi}^L & l^e N_{m,\xi}^Q & l^e c N_{m,\xi}^Q \\ 0 & 0 & L^e N_1^L & 0 & 0 & 0 & L^e N_2^L & 0 \\ 0 & 0 & 0 & L^e N_1^L & 0 & 0 & 0 & L^e N_2^L \\ 0 & 0 & N_{1,\xi}^L & 0 & 0 & 0 & N_{2,\xi}^L & 0 \\ 0 & 0 & 0 & N_{1,\xi}^L & 0 & 0 & 0 & N_{2,\xi}^L \end{bmatrix}. \tag{3.78}$$

The initial imperfection function, $w^*(x)$, is approximated within the finite element using the quadratic Lagrange polynomials (see Fig.[3.7]):

$$w^*(x) \simeq \begin{bmatrix} N_1^Q & N_m^Q & N_2^Q \end{bmatrix} \begin{Bmatrix} w_1^* \\ w_m^* \\ w_2^* \end{Bmatrix} \equiv \mathbf{N^* u^{*e}}. \tag{3.79}$$

The values of $w^*(x)$ at the finite element edges, w_1^* and w_2^*, and at the mid-point, w_m^*, correspond to the real (measured) values of the imperfection in the x-locations, thus they are prescribed quantities.
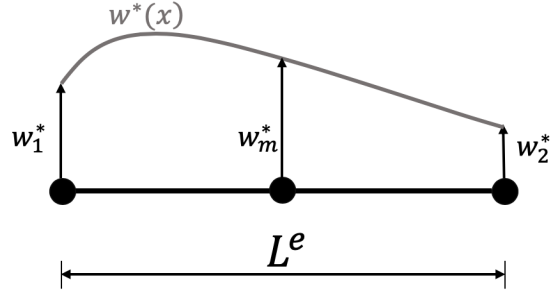
Figure 3.7: Parabolic approximation of the initial imperfection in the finite element.

The finite element approximation of the vector $\boldsymbol{\omega}^*$ is then

$$\boldsymbol{\omega}^* \simeq \mathbf{B}^{*\mathbf{e}}\mathbf{u}^{*\mathbf{e}} = \frac{1}{L^e}\begin{bmatrix} 0 & 0 & 0 \\ N_{1,\xi}^Q & N_{m,\xi}^Q & N_{2,\xi}^Q \\ 0 & 0 & 0 \\ 0 & 0 & 0 \\ 0 & 0 & 0 \\ 0 & 0 & 0 \end{bmatrix}\begin{Bmatrix} w_1^* \\ w_m^* \\ w_2^* \end{Bmatrix}. \tag{3.80}$$

Introducing the finite element approximation for $\boldsymbol{\omega}$ (Eq.[3.77]) and $\boldsymbol{\omega}^*$ (Eq.[3.80]) in Eq.[3.64], and considering that $\mathbf{B^e}$ and $\mathbf{H}$ are not dependent on the cross-sectional variables, the virtual variation of the electrical enthalpy in the finite element approximation is

$$\delta H_E^e \simeq \delta \mathbf{u}^{\mathbf{e}T} \int_{x_a}^{x_b} \mathbf{B}^{\mathbf{e}T} \left[\int_A \mathbf{Z}_\epsilon^{(k)T} E_x^{(k)} \mathbf{Z}_\epsilon^{(k)} dA \right] \mathbf{B}^{\mathbf{e}} dx \mathbf{u}^{\mathbf{e}} +$$

$$+ \frac{1}{2} \delta \mathbf{u}^{\mathbf{e}T} \int_{x_a}^{x_b} \mathbf{B}^{\mathbf{e}T} \left[\int_A \mathbf{Z}_\epsilon^{(k)T} E_x^{(k)} dA \right] \mathbf{u}^{\mathbf{e}T} \mathbf{B}^{\mathbf{e}T} \mathbf{H} \mathbf{B}^{\mathbf{e}} dx \mathbf{u}^{\mathbf{e}} +$$

$$+ \delta \mathbf{u}^{\mathbf{e}T} \int_{x_a}^{x_b} \mathbf{B}^{\mathbf{e}T} \left[\int_A \mathbf{Z}_\epsilon^{(k)T} E_x^{(k)} dA \right] \mathbf{u}^{*\mathbf{e}T} \mathbf{B}^{*\mathbf{e}T} \mathbf{B}^{\mathbf{e}} dx \mathbf{u}^{\mathbf{e}} +$$

$$+ \delta \mathbf{u}^{\mathbf{e}T} \int_{x_a}^{x_b} \mathbf{B}^{\mathbf{e}T} \mathbf{H} \mathbf{B}^{\mathbf{e}} \mathbf{u}^{\mathbf{e}} \left[\int_A E_x^{(k)} \mathbf{Z}_\epsilon^{(k)} dA \right] \mathbf{B}^{\mathbf{e}} dx \mathbf{u}^{\mathbf{e}} +$$

$$+ \frac{1}{2} \delta \mathbf{u}^{\mathbf{e}T} \int_{x_a}^{x_b} \mathbf{B}^{\mathbf{e}T} \mathbf{H} \mathbf{B}^{\mathbf{e}} \mathbf{u}^{\mathbf{e}} \left[\int_A E_x^{(k)} dA \right] \mathbf{u}^{\mathbf{e}T} \mathbf{B}^{\mathbf{e}T} \mathbf{H} \mathbf{B}^{\mathbf{e}} dx \mathbf{u}^{\mathbf{e}} +$$

$$+ \delta \mathbf{u}^{\mathbf{e}T} \int_{x_a}^{x_b} \mathbf{B}^{\mathbf{e}T} \mathbf{H} \mathbf{B}^{\mathbf{e}} \mathbf{u}^{\mathbf{e}} \left[\int_A E_x^{(k)} dA \right] \mathbf{u}^{*\mathbf{e}T} \mathbf{B}^{*\mathbf{e}T} \mathbf{B}^{\mathbf{e}} dx \mathbf{u}^{\mathbf{e}} +$$

$$+ \delta \mathbf{u}^{\mathbf{e}T} \int_{x_a}^{x_b} \mathbf{B}^{\mathbf{e}T} \mathbf{B}^{*\mathbf{e}} \mathbf{u}^{*\mathbf{e}} \left[\int_A E_x^{(k)} \mathbf{Z}_\epsilon^{(k)} dA \right] \mathbf{B}^{\mathbf{e}} dx \mathbf{u}^{\mathbf{e}} + \qquad (3.81)$$

$$+ \frac{1}{2} \delta \mathbf{u}^{\mathbf{e}T} \int_{x_a}^{x_b} \mathbf{B}^{\mathbf{e}T} \mathbf{B}^{*\mathbf{e}} \mathbf{u}^{*\mathbf{e}} \left[\int_A E_x^{(k)} dA \right] \mathbf{u}^{\mathbf{e}T} \mathbf{B}^{\mathbf{e}T} \mathbf{H} \mathbf{B}^{\mathbf{e}} dx \mathbf{u}^{\mathbf{e}} +$$

$$+ \delta \mathbf{u}^{\mathbf{e}T} \int_{x_a}^{x_b} \mathbf{B}^{\mathbf{e}T} \mathbf{B}^{*\mathbf{e}} \mathbf{u}^{*\mathbf{e}} \left[\int_A E_x^{(k)} dA \right] \mathbf{u}^{*\mathbf{e}T} \mathbf{B}^{*\mathbf{e}T} \mathbf{B}^{\mathbf{e}} dx \mathbf{u}^{\mathbf{e}} +$$

$$- \delta \mathbf{u}^{\mathbf{e}T} \int_{x_a}^{x_b} \mathbf{B}^{\mathbf{e}T} \left[\int_A \mathbf{Z}_\epsilon^{(k)T} e_{31}^{(k)} \Xi_z^{(k)} dA \right] dx +$$

$$- \delta \mathbf{u}^{\mathbf{e}T} \int_{x_a}^{x_b} \mathbf{B}^{\mathbf{e}T} \mathbf{H} \mathbf{B}^{\mathbf{e}} \mathbf{u}^{\mathbf{e}} \left[\int_A e_{31}^{(k)} \Xi_z^{(k)} dA \right] dx +$$

$$- \delta \mathbf{u}^{\mathbf{e}T} \int_{x_a}^{x_b} \mathbf{B}^{\mathbf{e}T} \mathbf{B}^{*\mathbf{e}} \mathbf{u}^{*\mathbf{e}} \left[\int_A e_{31}^{(k)} \Xi_z^{(k)} dA \right] dx +$$

$$+ \delta \mathbf{u}^{\mathbf{e}T} \int_{x_a}^{x_b} \mathbf{B}^{\mathbf{e}T} \left[\int_A \mathbf{Z}_\gamma^{(k)T} G_{xz}^{(k)} \mathbf{Z}_\gamma^{(k)} dA \right] \mathbf{B}^{\mathbf{e}} dx \mathbf{u}^{\mathbf{e}} .$$

Collecting $\delta \mathbf{u}^{\mathbf{e}T}$, Eq.[3.81] becomes

$$
\begin{aligned}
\delta H_E^e \simeq \delta \mathbf{u^{e}}^T \cdot \Bigg\{ \Bigg[& \int_{x_a}^{x_b} \mathbf{B^e}^T \left(\int_A \mathbf{Z}_\epsilon^{(k)T} E_x^{(k)} \mathbf{Z}_\epsilon^{(k)} dA \right) \mathbf{B^e} dx + \\
+ & \int_{x_a}^{x_b} \mathbf{B^e}^T \left(\int_A \mathbf{Z}_\gamma^{(k)T} G_{xz}^{(k)} \mathbf{Z}_\gamma^{(k)} dA \right) \mathbf{B^e} dx + \frac{1}{2} \int_{x_a}^{x_b} \mathbf{B^e}^T \left(\int_A \mathbf{Z}_\epsilon^{(k)T} E_x^{(k)} dA \right) \mathbf{u^e}^T \mathbf{B^e}^T \mathbf{HB^e} dx + \\
+ & \int_{x_a}^{x_b} \mathbf{B^e}^T \left(\int_A \mathbf{Z}_\epsilon^{(k)T} E_x^{(k)} dA \right) \mathbf{u^{*e}}^T \mathbf{B^{*e}}^T \mathbf{B^e} dx + \frac{1}{2} \int_{x_a}^{x_b} \mathbf{B^e}^T \mathbf{HB^e u^e} \left(\int_A E_x^{(k)} dA \right) \mathbf{u^e}^T \mathbf{B^e}^T \mathbf{HB^e} dx + \\
+ & \int_{x_a}^{x_b} \mathbf{B^e}^T \mathbf{HB^e u^e} \left(\int_A E_x^{(k)} \mathbf{Z}_\epsilon^{(k)} dA \right) \mathbf{B^e} dx + \int_{x_a}^{x_b} \mathbf{B^e}^T \mathbf{HB^e u^e} \left(\int_A E_x^{(k)} dA \right) \mathbf{u^{*e}}^T \mathbf{B^{*e}}^T \mathbf{B^e} dx + \\
+ & \int_{x_a}^{x_b} \mathbf{B^e}^T \mathbf{B^{*e} u^{*e}} \left(\int_A E_x^{(k)} dA \right) \mathbf{u^{*e}}^T \mathbf{B^{*e}}^T \mathbf{B^e} dx + \int_{x_a}^{x_b} \mathbf{B^e}^T \mathbf{B^{*e} u^{*e}} \left(\int_A E_x^{(k)} \mathbf{Z}_\epsilon^{(k)} dA \right) \mathbf{B^e} dx + \\
+ & \frac{1}{2} \int_{x_a}^{x_b} \mathbf{B^e}^T \mathbf{B^{*e} u^{*e}} \left(\int_A E_x^{(k)} dA \right) \mathbf{u^e}^T \mathbf{B^e}^T \mathbf{HB^e} dx - \int_{x_a}^{x_b} \left(\int_A e_{31}^{(k)} \Xi_z^{(k)} dA \right) \mathbf{B^e}^T \mathbf{HB^e u^e} dx \Bigg] \cdot \mathbf{u^e} + \\
- & \int_{x_a}^{x_b} \mathbf{B^e}^T \left(\int_A \mathbf{Z}_\epsilon^{(k)T} e_{31}^{(k)} \Xi_z^{(k)} dA \right) dx - \int_{x_a}^{x_b} \left(\int_A e_{31}^{(k)} \Xi_z^{(k)} dA \right) \mathbf{B^e}^T \mathbf{B^{*e}} dx \cdot \mathbf{u^{*e}} \Bigg\} .
\end{aligned}
\tag{3.82}
$$

It is convenient to define a vector $\mathbf{V_P^e}$ containing the values V_P^{ek} of the voltage applied in kth layer of the finite element ($V_P^{ek} = 0$ if the layer is not made of piezoelectric material or if the applied voltage is zero):

$$
\mathbf{V_P^e} \equiv \begin{bmatrix} V_P^{e1} & ... & V_P^{ek} & ... & V_P^{eN} \end{bmatrix}^T .
\tag{3.83}
$$

Considering Eqs.[3.49-3.52], after some operations, the integrals related to the piezoelectric contribution in Eq.[3.82] can be simplified as follows:

$$
\int_A e_{31}^{(k)} \Xi_z^{(k)} dA \equiv N_x^{inde} , \qquad \int_A \mathbf{Z}_\epsilon^{(k)T} e_{31}^{(k)} \Xi_z^{(k)} dA \equiv \mathbf{Z_P^e V_P^e} ,
\tag{3.84}
$$

where

$$
\mathbf{Z_P^e} \equiv \begin{bmatrix}
a_E^1 & ... & a_E^k & ... & a_E^N \\
0 & & 0 & & 0 \\
0 & & 0 & & 0 \\
0 & ... & 0 & ... & 0 \\
d_E^1 & & d_E^k & & d_E^N \\
c_E^1 & ... & c_E^k & ... & c_E^N
\end{bmatrix} .
\tag{3.85}
$$

In addition, it is useful to introduce a matrix $\mathbf{Z_N^e}$:

$$
\mathbf{Z_N^e} \equiv \int_A [E_x^{(k)} \mathbf{Z}_\epsilon^{(k)}] dA ,
\tag{3.86}
$$

which can be written in terms of the stiffness coefficients A_{11}^e, B_{12}^e and B_{13}^e of the finite element, e, using Eqs.[3.15]-[3.45]:

$$\mathbf{Z_N^e} = \begin{bmatrix} A_{11}^e & 0 & 0 & 0 & B_{12}^e & B_{13}^e \end{bmatrix}. \tag{3.87}$$

The finite element approximation of the electrical enthalpy virtual variation is then

$$
\begin{aligned}
\delta H_E^e \simeq \delta \mathbf{u^{e}}^T \cdot \Bigg\{ & \Bigg[\int_{x_a}^{x_b} \mathbf{B^{e}}^T \left(\int_A \mathbf{Z}_\epsilon^{(k)T} E_x^{(k)} \mathbf{Z}_\epsilon^{(k)} dA \right) \mathbf{B^e} dx + \\
& + \int_{x_a}^{x_b} \mathbf{B^{e}}^T \left(\int_A \mathbf{Z}_\gamma^{(k)T} G_{xz}^{(k)} \mathbf{Z}_\gamma^{(k)} dA \right) \mathbf{B^e} dx + \frac{1}{2} \int_{x_a}^{x_b} \mathbf{B^{e}}^T \mathbf{Z_N^{e}}^T \mathbf{u^{e}}^T \mathbf{B^{e}}^T \mathbf{HB^e} dx + \\
& + \int_{x_a}^{x_b} \mathbf{B^{e}}^T \mathbf{Z_N^{e}}^T \mathbf{u^{*e}}^T \mathbf{B^{*e}}^T \mathbf{B^e} dx + \frac{1}{2} \int_{x_a}^{x_b} \mathbf{B^{e}}^T \mathbf{HB^e} \mathbf{u^e} A_{11}^e \mathbf{u^{e}}^T \mathbf{B^{e}}^T \mathbf{HB^e} dx + \\
& + \int_{x_a}^{x_b} \mathbf{B^{e}}^T \mathbf{HB^e} \mathbf{u^e} \mathbf{Z_N^e} \mathbf{B^e} dx + \int_{x_a}^{x_b} \mathbf{B^{e}}^T \mathbf{HB^e} \mathbf{u^e} A_{11}^e \mathbf{u^{*e}}^T \mathbf{B^{*e}}^T \mathbf{B^e} dx + \\
& + \int_{x_a}^{x_b} \mathbf{B^{e}}^T \mathbf{B^{*e}} \mathbf{u^{*e}} A_{11}^e \mathbf{u^{*e}}^T \mathbf{B^{*e}}^T \mathbf{B^e} dx + \int_{x_a}^{x_b} \mathbf{B^{e}}^T \mathbf{B^{*e}} \mathbf{u^{*e}} \mathbf{Z_N^e} \mathbf{B^e} dx + \\
& + \frac{1}{2} \int_{x_a}^{x_b} \mathbf{B^{e}}^T \mathbf{B^{*e}} \mathbf{u^{*e}} A_{11}^e \mathbf{u^{e}}^T \mathbf{B^{e}}^T \mathbf{HB^e} dx - N_x^{inde} \int_{x_a}^{x_b} \mathbf{B^{e}}^T \mathbf{HB^e} dx \Bigg] \cdot \mathbf{u^e} + \\
& - \int_{x_a}^{x_b} \mathbf{B^{e}}^T dx \cdot \mathbf{Z_P^e} \mathbf{V_P^e} - N_x^{inde} \int_{x_a}^{x_b} \mathbf{B^{e}}^T \mathbf{B^{*e}} dx \cdot \mathbf{u^{*e}} \Bigg\}.
\end{aligned}
\tag{3.88}
$$

The following stiffness matrices can be defined, indicating those dependent on $\mathbf{u^e}$ with an overbar:

$$\mathbf{K^e} \equiv \int_{x_a}^{x_b} \mathbf{B^{e}}^T \left[\int_A \left(\mathbf{Z}_\epsilon^{(k)T} E_x^{(k)} \mathbf{Z}_\epsilon^{(k)} + \mathbf{Z}_\gamma^{(k)T} G_{xz}^{(k)} \mathbf{Z}_\gamma^{(k)} \right) dA \right] \mathbf{B^e} dx \,, \qquad (3.89)$$

$$\mathbf{\bar{K}^e_{GI}}(\mathbf{u^e}) \equiv \int_{x_a}^{x_b} \mathbf{B}^{eT} \mathbf{HB^e} \mathbf{u^e} \mathbf{Z^e_N} \mathbf{B^e} dx \,, \qquad (3.90)$$

$$\mathbf{\bar{K}^e_{GII}}(\mathbf{u^e}) \equiv \int_{x_a}^{x_b} \mathbf{B}^{eT} \mathbf{HB^e} \mathbf{u^e} A_{11}^e \mathbf{u}^{eT} \mathbf{B}^{eT} \mathbf{HB^e} dx \,, \qquad (3.91)$$

$$\mathbf{\bar{K}^e_{GM}}(\mathbf{u^e}, \mathbf{u^{*e}}) \equiv \int_{x_a}^{x_b} \mathbf{B}^{eT} \mathbf{HB^e} \mathbf{u^e} A_{11}^e \mathbf{u}^{*eT} \mathbf{B^{*e}}^T \mathbf{B^e} dx \,, \qquad (3.92)$$

$$\mathbf{K^{*e}_{GI}}(\mathbf{u^{*e}}) \equiv \int_{x_a}^{x_b} \mathbf{B}^{eT} \mathbf{B^{*e}} \mathbf{u^{*e}} \mathbf{Z^e_N} \mathbf{B^e} dx \,, \qquad (3.93)$$

$$\mathbf{K^{*e}_{GII}}(\mathbf{u^{*e}}) \equiv \int_{x_a}^{x_b} \mathbf{B}^{eT} \mathbf{B^{*e}} \mathbf{u^{*e}} A_{11}^e \mathbf{u}^{*eT} \mathbf{B^{*e}}^T \mathbf{B^e} dx \,, \qquad (3.94)$$

$$\mathbf{K^e_G} \equiv \int_{x_a}^{x_b} \mathbf{B}^{eT} \mathbf{HB^e} dx \,, \qquad (3.95)$$

$$\mathbf{K^{*e}_G} \equiv \int_{x_a}^{x_b} \mathbf{B}^{eT} \mathbf{B^{*e}} dx \,, \qquad (3.96)$$

$$\mathbf{K^e_P} \equiv \int_{x_a}^{x_b} \mathbf{B}^{eT} dx \cdot \mathbf{Z^e_P} \,. \qquad (3.97)$$

Eq.[3.88] is simplified as

$$\begin{aligned} \delta H_E^e \simeq & \delta \mathbf{u}^{eT} \cdot \left[\left(\mathbf{K^e} + \frac{1}{2}\mathbf{\bar{K}^e_{GI}}^T + \mathbf{\bar{K}^e_{GI}} + \mathbf{K^{*e}_{GI}}^T + \mathbf{K^{*e}_{GI}} + \frac{1}{2}\mathbf{\bar{K}^e_{GII}} + \mathbf{K^{*e}_{GII}} + \right. \right. \\ & \left. \left. + \frac{1}{2}\mathbf{\bar{K}^e_{GM}}^T + \mathbf{\bar{K}^e_{GM}} - N_x^{inde}\mathbf{K^e_G} \right) \cdot \mathbf{u^e} - N_x^{inde}\mathbf{K^{*e}_G}\mathbf{u^{*e}} - \mathbf{K^e_P}\mathbf{V^e_P} \right] \,. \end{aligned} \qquad (3.98)$$

Indicating with $\mathbf{F^e}$ the vector of nodal forces equivalent to the applied mechanical forces, the virtual work done by the external forces in the finite element approximation is

$$\delta L^e \simeq \delta \mathbf{u}^{eT} \mathbf{F^e} \,. \qquad (3.99)$$

Applying the Principle of Virtual Work (Eq.[3.23]) using Eq.[3.98] and Eq.[3.99], the problem of the equilibrium is reduced to the solution of the following nonlinear matrix equation:

$$\begin{aligned} & \left(\mathbf{K^e} + \frac{1}{2}\mathbf{\bar{K}^e_{GI}}^T + \mathbf{\bar{K}^e_{GI}} + \mathbf{K^{*e}_{GI}}^T + \mathbf{K^{*e}_{GI}} + \frac{1}{2}\mathbf{\bar{K}^e_{GII}} + \mathbf{K^{*e}_{GII}} + \frac{1}{2}\mathbf{\bar{K}^e_{GM}}^T + \mathbf{\bar{K}^e_{GM}} + \right. \\ & \left. - N_x^{inde}\mathbf{K^e_G} \right) \cdot \mathbf{u^e} = \mathbf{F^e} + N_x^{inde}\mathbf{K^{*e}_G}\mathbf{u^{*e}} + \mathbf{K^e_P}\mathbf{V^e_P} \,. \end{aligned}$$

$$(3.100)$$

3.4.1 Constant axial force

It is here shown that for particular boundary and loading conditions the beam axial force is independent of the degrees of freedom and Eq.[3.100] is reduced to a linear relation.

The general definition of the normal force is

$$N_x = \int_A \sigma_{\mathbf{x}} dA \,. \tag{3.101}$$

Substituting Eq.[3.12] in the axial stress definition of Eq.[3.19] and then in Eq.[3.101]:

$$N_x = \int_A \left[E_x^{(k)} \left(\mathbf{Z}_\epsilon^{(\mathbf{k})} \boldsymbol{\omega} + \frac{1}{2} \boldsymbol{\omega}^T \mathbf{H} \boldsymbol{\omega} + \boldsymbol{\omega}^{*T} \boldsymbol{\omega} \right) - e_{31}^{(k)} \Xi_z^{(k)} \right] dA \,. \tag{3.102}$$

In the finite element approximation (Eq.[3.77] and Eq.[3.80]), it is

$$N_x \simeq \int_A \left[E_x^{(k)} \left(\mathbf{Z}_\epsilon^{(\mathbf{k})} \mathbf{B^e u^e} + \frac{1}{2} \mathbf{u}^{\mathbf{e}T} \mathbf{B^e}^T \mathbf{H} \mathbf{B^e u^e} + \mathbf{u}^{*\mathbf{e}T} \mathbf{B}^{*\mathbf{e}T} \mathbf{B^e u^e} \right) - e_{31}^{(k)} \Xi_z^{(k)} \right] dA \,. \tag{3.103}$$

The virtual variation of the normal force due to a virtual variation of the vector $\mathbf{u^e}$ is

$$\delta N_x \simeq \int_A \left[E_x^{(k)} \left(\mathbf{Z}_\epsilon^{(\mathbf{k})} \mathbf{B^e} \cdot \delta \mathbf{u^e} + \mathbf{u}^{\mathbf{e}T} \mathbf{B^e}^T \mathbf{H} \mathbf{B^e} \cdot \delta \mathbf{u^e} + \mathbf{u}^{*\mathbf{e}T} \mathbf{B}^{*\mathbf{e}T} \mathbf{B^e} \cdot \delta \mathbf{u^e} \right) \right] dA$$
$$= \mathbf{Z_N B^e} \cdot \delta \mathbf{u^e} + A_{11}^e \mathbf{u}^{\mathbf{e}T} \mathbf{B^e}^T \mathbf{H} \mathbf{B^e} \cdot \delta \mathbf{u^e} + A_{11}^e \mathbf{u}^{*\mathbf{e}T} \mathbf{B}^{*\mathbf{e}T} \mathbf{B^e} \cdot \delta \mathbf{u^e} \,. \tag{3.104}$$

Collecting the appropriate terms in the electrical enthalpy virtual variation (Eq.[3.88]), δN_x appears in the two terms at the end of the following equation:

$$\delta H_E^e = \delta \mathbf{u^e}^T \cdot \left[\int_{x_a}^{x_b} \mathbf{B^e}^T \left(\int_A \mathbf{Z}_\epsilon^{(k)T} E_x^{(k)} \mathbf{Z}_\epsilon^{(k)} dA \right) \mathbf{B^e} dx + \right.$$
$$+ \int_{x_a}^{x_b} \mathbf{B^e}^T \left(\int_A \mathbf{Z}_\gamma^{(k)T} G_{xz}^{(k)} \mathbf{Z}_\gamma^{(k)} dA \right) \mathbf{B^e} dx + \int_{x_a}^{x_b} \mathbf{B^e}^T \mathbf{B}^{*\mathbf{e}} \mathbf{u}^{*\mathbf{e}} \mathbf{Z_N^e B^e} dx +$$
$$\left. + \int_{x_a}^{x_b} \mathbf{B^e}^T \mathbf{H} \mathbf{B^e} \mathbf{u^e} \mathbf{Z_N^e B^e} dx - N_x^{inde} \int_{x_a}^{x_b} \mathbf{B^e}^T \mathbf{H} \mathbf{B^e} dx \right] \cdot \mathbf{u^e} + \tag{3.105}$$
$$- \delta \mathbf{u^e}^T \cdot \left[\int_{x_a}^{x_b} \mathbf{B^e}^T dx \cdot \mathbf{Z_P^e V_P^e} + \delta \mathbf{u^e}^T N_x^{inde} \int_{x_a}^{x_b} \mathbf{B^e}^T \mathbf{B}^{*\mathbf{e}} dx \cdot \mathbf{u}^{*\mathbf{e}} \right] +$$
$$+ \frac{1}{2} \int_{x_a}^{x_b} \delta N_x \mathbf{u^e}^T \mathbf{B^e}^T \mathbf{H} \mathbf{B^e} dx \cdot \mathbf{u^e} + \int_{x_a}^{x_b} \delta N_x \mathbf{u}^{*\mathbf{e}T} \mathbf{B^e}^T \mathbf{B^e} dx \cdot \mathbf{u^e} \,.$$

Moreover, the term linearly dependent on $\mathbf{u^e}$ in the axial force expression (Eq.[3.102]) can be defined as follows:

$$N_{xc}^e \equiv \mathbf{Z_N^e} \mathbf{B^e} \mathbf{u^e} \,. \tag{3.106}$$

The quantity N_{xc}^e is constant within the beam element because the matrix $\mathbf{Z_N^e}$ (Eq.[3.86]) selects only constant terms of $\mathbf{B^e}$, thus N_{xc}^e can be taken out of the integrals. Rearranging,

$$
\begin{aligned}
\delta H_E^e = \delta \mathbf{u^e}^T \cdot &\left[\int_{x_a}^{x_b} \mathbf{B^e}^T \left(\int_A \mathbf{Z_\epsilon}^{(k)T} E_x^{(k)} \mathbf{Z_\epsilon}^{(k)} dA \right) \mathbf{B^e} dx + \right. \\
&+ \int_{x_a}^{x_b} \mathbf{B^e}^T \left(\int_A \mathbf{Z_\gamma}^{(k)T} G_{xz}^{(k)} \mathbf{Z_\gamma}^{(k)} dA \right) \mathbf{B^e} dx + N_{xc}^e \int_{x_a}^{x_b} \mathbf{B^e}^T \mathbf{H} \mathbf{B^e} dx + \\
&\left. - N_x^{inde} \int_{x_a}^{x_b} \mathbf{B^e}^T \mathbf{H} \mathbf{B^e} dx \right] \cdot \mathbf{u^e} + N_{xc}^e \int_{x_a}^{x_b} \mathbf{B^e}^T \mathbf{B^{*e}} dx \cdot \mathbf{u^{*e}} + \\
&+ \frac{1}{2} \int_{x_a}^{x_b} \delta N_x \mathbf{u^e}^T \mathbf{B^e}^T \mathbf{H} \mathbf{B^e} dx \cdot \mathbf{u^e} + \int_{x_a}^{x_b} \delta N_x \mathbf{u^{*e}}^T \mathbf{B^{*e}}^T \mathbf{B^e} dx \cdot \mathbf{u^e} + \\
&- \delta \mathbf{u^e}^T \cdot \left[\int_{x_a}^{x_b} \mathbf{B^e}^T dx \cdot \mathbf{Z_P^e} \mathbf{V_P^e} + N_x^{inde} \int_{x_a}^{x_b} \mathbf{B^e}^T \mathbf{B^{*e}} dx \cdot \mathbf{u^{*e}} \right] .
\end{aligned}
\tag{3.107}
$$

When the axial force is assigned as boundary condition of the beam (e.g. the applied axial force at the supported edge of a simply-supported beam), N_x is independent of $\mathbf{u^e}$, thus the virtual variation $\delta N_x = 0$ and Eq.[3.107] is simplified as

$$
\begin{aligned}
\delta H_E^e = \delta \mathbf{u^e}^T \cdot &\left[\int_{x_a}^{x_b} \mathbf{B^e}^T \left(\int_A \mathbf{Z_\epsilon}^{(k)T} E_x^{(k)} \mathbf{Z_\epsilon}^{(k)} dA \right) \mathbf{B^e} dx + \right. \\
&+ \int_{x_a}^{x_b} \mathbf{B^e}^T \left(\int_A \mathbf{Z_\gamma}^{(k)T} G_{xz}^{(k)} \mathbf{Z_\gamma}^{(k)} dA \right) \mathbf{B^e} dx + N_{xc}^e \int_{x_a}^{x_b} \mathbf{B^e}^T \mathbf{H} \mathbf{B^e} dx + \\
&\left. - N_x^{inde} \int_{x_a}^{x_b} \mathbf{B^e}^T \mathbf{H} \mathbf{B^e} dx \right] \cdot \mathbf{u^e} + N_{xc}^e \int_{x_a}^{x_b} \mathbf{B^e}^T \mathbf{B^{*e}} dx \cdot \mathbf{u^{*e}} + \\
&- \delta \mathbf{u^e}^T \cdot \left[\int_{x_a}^{x_b} \mathbf{B^e}^T dx \cdot \mathbf{Z_P^e} \mathbf{V_P^e} + N_x^{inde} \int_{x_a}^{x_b} \mathbf{B^e}^T \mathbf{B^{*e}} dx \cdot \mathbf{u^{*e}} \right] .
\end{aligned}
\tag{3.108}
$$

Considering Eqs.[3.89, 3.95-3.99], Eq.[3.23] becomes

$$\left[\mathbf{K^e} - \left(N_x^{inde} - N_{xc}^e \right) \mathbf{K_G^e} \right] \cdot \mathbf{u^e} = \mathbf{F^e} + \left(N_x^{inde} - N_{xc}^e \right) \mathbf{K_G^{*e}} \mathbf{u^{*e}} + \mathbf{K_P^e} \mathbf{V_P^e} \,. \tag{3.109}$$

All the matrices in Eq.[3.109] are independent of the degrees-of freedom vector, thus, the equation can be solved in the conventional way without using the Newton-Raphson method. Eq.[3.109] and, in general, Eq.[3.100] can be used to find the equilibrium condition of a composite beam for any applied mechanical load and electrical voltage. The entire nonlinear load-displacement equilibrium path of axially-compressed beams can be reconstructed by iteratively solving the equation increasing the load from zero to the desired value.

In addition, Eq.[3.109] can be used to find the critical buckling loads of a simply-supported beam solving the eigenvalue problem:

$$(\mathbf{K^e} - P_i^e \mathbf{K_G^e}) \cdot \hat{\mathbf{u}}^\mathbf{e} = 0 \,, \tag{3.110}$$

where the eigenvalues $P_i^e = N_x^{inde} - N_{xc}^e$ are the buckling loads and the eigenvectors $\hat{\mathbf{u}}_\mathbf{i}^\mathbf{e}$ are the buckling mode shapes.

3.5 The Newton-Raphson method for solving the nonlinear RZT-FE equation

In the FE equilibrium equation (Eq.[3.100]), the matrices with a bar superscript are function of the degrees of freedom vector $\mathbf{u^e}$, thus the resulting nonlinear equation is solved using an incremental-iterative technique based on the Newton-Raphson method, as shown in [123]. The nonlinear equation for the beam structure is obtained assembling the matrices and vectors of all the finite elements of the model:

$$\left(\mathbf{K} + \frac{1}{2}\bar{\mathbf{K}}_{\mathbf{GI}}{}^T + \bar{\mathbf{K}}_{\mathbf{GI}} + \mathbf{K}_{\mathbf{GI}}^*{}^T + \mathbf{K}_{\mathbf{GI}}^* + \frac{1}{2}\bar{\mathbf{K}}_{\mathbf{GII}} + \mathbf{K}_{\mathbf{GII}}^* + \frac{1}{2}\bar{\mathbf{K}}_{\mathbf{GM}}{}^T + \bar{\mathbf{K}}_{\mathbf{GM}} + \right.$$
$$\left. - \mathbf{K}_{\mathbf{GAe}}\right) \cdot \mathbf{u} - \mathbf{F} - \mathbf{K}_{\mathbf{GAe}}^* \mathbf{u}^* - \mathbf{K_P V_P} = 0 \,,$$
$$\tag{3.111}$$

where $\mathbf{K_{GAe}}$ and $\mathbf{K_{GAe}^*}$ are obtained assembling the element-based matrices $N_x^{inde}\mathbf{K_G^e}$ and $N_x^{inde}\mathbf{K_G^{*e}}$.

Using a vectorial function $\mathbf{g}(\mathbf{u}, \lambda)$, Eq.[3.111] can be written as

$$\mathbf{g}(\mathbf{u}, \lambda) = \mathbf{q_i}(\mathbf{u}, \lambda) - \lambda \mathbf{q_e} = 0 \,. \tag{3.112}$$

The vector $\mathbf{q_i}(\mathbf{u}, \lambda)$ is the internal forces vector and it is a function of both the degrees of freedom vector $\mathbf{u}$ and the increment factor, λ. The external forces vector, $\mathbf{q_e}$, increases by λ at each increment.

The applications presented in this work can be classified as *electrical-forces-only* or *mechanical-forces-only* because the mechanical and the electrical load increments

have never been applied at the same time. These two conditions can be described as follows:

1. *Electrical forces only*: no mechanical loads are applied and the voltage vector V_P is increased. At the i-th increment, the applied voltage is $V_{Pi} = \lambda_i V_{P1}$, where V_{P1} is the initial reference voltage vector.

   Note that the quantity N_x^{inde} contains the voltage, thus the matrices $\mathbf{K_{GAe}}$ and $\mathbf{K_{GAe}^*}$ change with λ. For $V_P = V_{P1}$, $\mathbf{K_{GAe}} = \mathbf{K_{GAe1}}$ and $\mathbf{K_{GAe}^*} = \mathbf{K_{GAe1}^*}$, thus:

$$
\mathbf{q_i} = \left(\mathbf{K} + \frac{1}{2}\bar{\mathbf{K}}_{\mathbf{GI}}^T + \bar{\mathbf{K}}_{\mathbf{GI}} + \mathbf{K_{GI}^*}^T + \mathbf{K_{GI}^*} + \frac{1}{2}\bar{\mathbf{K}}_{\mathbf{GII}} + \mathbf{K_{GII}^*} + \right.
$$
$$
\left. + \frac{1}{2}\bar{\mathbf{K}}_{\mathbf{GM}}^T + \bar{\mathbf{K}}_{\mathbf{GM}} - \lambda \mathbf{K_{GAe1}} \right) \cdot \mathbf{u}, \tag{3.113}
$$

$$
\mathbf{q_e} = \mathbf{K_{GAe1}^*} \mathbf{u^*} + \mathbf{K_P} \mathbf{V_{P1}}. \tag{3.114}
$$

2. *Mechanical forces only*: the voltage in the actuators has a constant value and the incremental-iterative solution is related only to the applied mechanical forces. This means that the matrices $\mathbf{K_{GAe}}$ and $\mathbf{K_{GAe}^*}$ are independent of λ and the internal forces vector is a function of $\mathbf{u}$ only.

   Indicating with $\mathbf{F_1}$ the initial reference mechanical load vector,

$$
\mathbf{q_i} = \left(\mathbf{K} + \frac{1}{2}\bar{\mathbf{K}}_{\mathbf{GI}}^T + \bar{\mathbf{K}}_{\mathbf{GI}} + \mathbf{K_{GI}^*}^T + \mathbf{K_{GI}^*} + \frac{1}{2}\bar{\mathbf{K}}_{\mathbf{GII}} + \mathbf{K_{GII}^*} + \right.
$$
$$
\left. + \frac{1}{2}\bar{\mathbf{K}}_{\mathbf{GM}}^T + \bar{\mathbf{K}}_{\mathbf{GM}} - \mathbf{K_{GAe}} \right) \cdot \mathbf{u} - \mathbf{K_{GAe}^*} \mathbf{u^*} - \mathbf{K_P} \mathbf{V_P}, \tag{3.115}
$$

$$
\mathbf{q_e} = \mathbf{F_1}. \tag{3.116}
$$

The solution procedure at each step combines an incremental solution, that is the tangential increment of $\mathbf{u}$ corresponding to the load increment of the step, used as predictive starting solution point (*predictor*) and Newton-Raphson iterations (*corrector*), which find a convergent value of $\mathbf{u}$ for the assigned load. The procedure is briefly described below using a superscript for the increments and a subscript for the iterations:

1. the starting equilibrium point is the homogeneous condition, because $\mathbf{u} = 0$ when no loads are applied. It is indicated by the superscript (0), thus:

$$
(\mathbf{u}^{(0)} = 0, \lambda^{(0)} = 0) \qquad \text{and} \qquad \mathbf{g}^{(0)} = \mathbf{g}(\mathbf{u}^{(0)}, \lambda^{(0)}) = 0 \,;
$$

2. the tangent stiffness matrix is calculated for the initial condition:

$$\mathbf{K_T}^{(0)} = \left(\frac{\mathrm{d}\mathbf{g}}{\mathrm{d}\mathbf{u}}\right)^{(0)} ;$$

3. the first incremental solution (*predictor*) is calculated as

$$\mathbf{u}_0^{(1)} = \mathbf{u}^{(0)} + \left(\mathbf{K_T}^{(0)}\right)^{-1} \mathbf{\Delta q_e}^{(1)} ,$$

where $\mathbf{\Delta q_e}^{(1)} = \lambda^{(1)}\mathbf{q_{e1}}$ and $\mathbf{q_{e1}}$ is unitary reference load vector;

4. the function $\mathbf{g}$ is calculated in the $(\mathbf{u}_0^{(1)}, \lambda^{(1)})$ condition,

$$\mathbf{g}_0^{(1)} = \mathbf{g}(\mathbf{u}^{(1)}, \lambda^{(1)}) .$$

If $\mathbf{g}_0^{(1)} \neq 0$ and does not satisfy the convergence criterion of the predictor, the Newton-Raphson iterations begin for the load factor increment $\lambda^{(1)}$

(a) the tangent stiffness matrix is calculated for $(\mathbf{u}_0^{(1)}, \lambda^{(1)})$:

$$\mathbf{K_{T0}}^{(1)} = \left(\frac{\mathrm{d}\mathbf{g}}{\mathrm{d}\mathbf{u}}\right)_0^{(1)} ;$$

(b) the increment at the first iteration is then

$$\delta\mathbf{u}_1^{(1)} = - \left(\mathbf{K_{T0}}^{(1)}\right)^{-1} \mathbf{g}_0^{(1)} ;$$

(c) the solution at the first iteration is

$$\mathbf{u}_1^{(1)} = \mathbf{u}_0^{(1)} + \delta\mathbf{u}_1^{(1)} ;$$

(d) if the function $\mathbf{g}_1^{(1)} = \mathbf{g}(\mathbf{u}_1^{(1)}, \lambda^{(1)}) \neq 0$ and does not satisfy the convergence criterion for the corrector, another iteration is needed;

(e) the tangent stiffness matrix is calculated for $(\mathbf{u}_1^{(1)}, \lambda^{(1)})$:

$$\mathbf{K_{T1}}^{(1)} = \left(\frac{\mathrm{d}\mathbf{g}}{\mathrm{d}\mathbf{u}}\right)_1^{(1)} ;$$

(f) the increment at the second iteration is

$$\delta\mathbf{u}_2^{(1)} = - \left(\mathbf{K_{T1}}^{(1)}\right)^{-1} \mathbf{g}_1^{(1)} ;$$

(g) the solution at the second iteration is

$$\mathbf{u}_1^{(1)} = \mathbf{u}_1^{(1)} + \delta\mathbf{u}_2^{(1)} \, ;$$

(h) the function $\mathbf{g}_2^{(1)} = \mathbf{g}(\mathbf{u}_2^{(1)}, \lambda^{(1)})$ is calculated to check the convergence. The last nth iteration is the one for which $\mathbf{g}_n^{(1)}$ satisfies the corrector convergence criterion.

The second equilibrium point is then $(\mathbf{u}^{(1)}, \lambda^{(1)})$, where $\mathbf{u}^{(1)} = \mathbf{u}_n^{(1)}$. The procedure continues starting from point 1, but with $(\mathbf{u}^{(1)}, \lambda^{(1)})$ as initial condition and the load factor $\lambda = \lambda^{(2)}$.

The convergence criterion adopted for both the predictor increments and the corrector iterations is based on the calculation of a parameter indicated as *coit* [123],

$$coit(\mathbf{g}, \mathbf{q_e}) = \left(\mathbf{g}^T \cdot \mathbf{g}\right)^{0.5} - 0.01 \left(\mathbf{q_e}^T \cdot \mathbf{q_e}\right)^{0.5} \, .$$

The nth predictor increment converges if $coit(\mathbf{g} = \mathbf{g}^{(n)}, \mathbf{q_e} = \mathbf{q_e}^{(n)}) < 0$ and the ith corrector iteration of the m-th predictor increment converges if $coit(\mathbf{g} = \mathbf{g}_i^{(m)}, \mathbf{q_e} = \mathbf{q_e}_i^{(m)}) < 0$.

The load factor changes at each increment and is calculated as

$$\lambda^{(n)} = \lambda^{(n-1)}\sqrt{\frac{I^{ref}}{I^{n-1}}} \, , \tag{3.117}$$

where λ^{n-1} is the previous increment factor for which I^{n-1} iterations were required and I^{ref} is a reference number of desired iterations.

3.5.1 Tangent stiffness matrix calculation for the RZT model

The element-based tangent stiffness matrix is defined as

$$\mathbf{K_T^e}(\mathbf{u^e}) = \frac{\mathrm{d}\mathbf{g^e}}{\mathrm{d}\mathbf{u^e}} \, . \tag{3.118}$$

The definition of the vectorial function $\mathbf{g}$ in Eq.[3.112] shows that only the internal forces vector $\mathbf{q_i}$ depends on the degrees of freedom vector $\mathbf{u}$, thus for the finite element e:

$$\frac{\mathrm{d}\mathbf{g^e}}{\mathrm{d}\mathbf{u^e}} = \frac{\mathrm{d}\mathbf{q_i^e}}{\mathrm{d}\mathbf{u^e}} \, . \tag{3.119}$$

For the *mechanical forces only* case the derivative $\mathrm{d}\mathbf{q_i^e}/\mathrm{d}\mathbf{u^e}$ is (refer to Eq.[3.115])

$$\frac{d\mathbf{q_i^e}}{d\mathbf{u^e}} = \mathbf{K^e} + \mathbf{K_{GI}^{*e}}^T + \mathbf{K_{GI}^{*e}} + \frac{1}{2}\bar{\mathbf{K}}_{\mathbf{GII}}^{\mathbf{e}} + \mathbf{K_{GII}^{*e}} - \mathbf{K_{GAe}^e} +$$
$$+ \frac{d}{d\mathbf{u^e}}\left(\frac{1}{2}\bar{\mathbf{K}}_{\mathbf{GI}}^{\mathbf{e}}{}^T\mathbf{u^e} + \bar{\mathbf{K}}_{\mathbf{GI}}^{\mathbf{e}}\mathbf{u^e} + \frac{1}{2}\bar{\mathbf{K}}_{\mathbf{GM}}^{\mathbf{e}}{}^T\mathbf{u^e} + \bar{\mathbf{K}}_{\mathbf{GM}}^{\mathbf{e}}\mathbf{u^e}\right). \tag{3.120}$$

The matrices with the overbar are a function of the degrees of freedom vector $\mathbf{u^e}$, thus it is useful to introduce the following derivatives:

$$\frac{d}{d\mathbf{u^e}}\left[\bar{\mathbf{K}}_{\mathbf{GI}}^{\mathbf{e}}\cdot\mathbf{u^e}\right] = \bar{\mathbf{K}}_{\mathbf{GI}}^{\mathbf{e}} + \bar{\mathbf{K}}_{\mathbf{GI2}}^{\mathbf{e}}, \tag{3.121}$$

$$\frac{d}{d\mathbf{u^e}}\left[\bar{\mathbf{K}}^{\mathbf{e}}{}_{\mathbf{GI}}^T\cdot\mathbf{u^e}\right] = 2\bar{\mathbf{K}}^{\mathbf{e}}{}_{\mathbf{GI}}^T, \tag{3.122}$$

$$\frac{d}{d\mathbf{u^e}}\left[\bar{\mathbf{K}}_{\mathbf{GII}}^{\mathbf{e}}\cdot\mathbf{u^e}\right] = 2\bar{\mathbf{K}}_{\mathbf{GII}}^{\mathbf{e}} + \bar{\mathbf{K}}_{\mathbf{GII2}}^{\mathbf{e}}, \tag{3.123}$$

$$\frac{d}{d\mathbf{u^e}}\left[\bar{\mathbf{K}}_{\mathbf{GM}}^{\mathbf{e}}\cdot\mathbf{u^e}\right] = \bar{\mathbf{K}}_{\mathbf{GM}}^{\mathbf{e}} + \bar{\mathbf{K}}_{\mathbf{GM2}}^{\mathbf{e}}, \tag{3.124}$$

$$\frac{d}{d\mathbf{u^e}}\left[\bar{\mathbf{K}}^{\mathbf{e}}{}_{\mathbf{GM}}^T\cdot\mathbf{u^e}\right] = 2\bar{\mathbf{K}}^{\mathbf{e}}{}_{\mathbf{GM}}^T, \tag{3.125}$$

where

$$\bar{\mathbf{K}}_{\mathbf{GI2}}^{\mathbf{e}} \equiv \int_{x_a}^{x_b} \mathbf{B}^{\mathbf{e}T}\mathbf{H}\mathbf{B}^{\mathbf{e}}\mathbf{Z}_{\mathbf{N}}^{\mathbf{e}}\mathbf{B}^{\mathbf{e}}\mathbf{u^e}dx,$$

$$\bar{\mathbf{K}}_{\mathbf{GII2}}^{\mathbf{e}} \equiv A_{11}^e\int_{x_a}^{x_b} \mathbf{B}^{\mathbf{e}T}\mathbf{H}\mathbf{B}^{\mathbf{e}}\mathbf{u}^{\mathbf{e}T}\mathbf{B}^{\mathbf{e}T}\mathbf{H}\mathbf{B}^{\mathbf{e}}\mathbf{u^e}dx, \tag{3.126}$$

$$\bar{\mathbf{K}}_{\mathbf{GM2}}^{\mathbf{e}} \equiv A_{11}^e\int_{x_a}^{x_b} \mathbf{B}^{\mathbf{e}T}\mathbf{H}\mathbf{B}^{\mathbf{e}}\mathbf{u}^{*\mathbf{e}T}\mathbf{B}^{*\mathbf{e}T}\mathbf{B}^{\mathbf{e}}\mathbf{u^e}dx.$$

The full expression of the tangent stiffness matrix for the nonlinear RZT model is then

$$\mathbf{K_T^e}(\mathbf{u^e}) = \mathbf{K^e} + \bar{\mathbf{K}}^{\mathbf{e}}{}_{\mathbf{GI}}^T + \bar{\mathbf{K}}_{\mathbf{GI}}^{\mathbf{e}} + \bar{\mathbf{K}}_{\mathbf{GI2}}^{\mathbf{e}} + \mathbf{K_{GI}^{*e}}^T + \mathbf{K_{GI}^{*e}} + \bar{\mathbf{K}}_{\mathbf{GII}}^{\mathbf{e}} +$$
$$+ \frac{1}{2}\bar{\mathbf{K}}_{\mathbf{GII2}}^{\mathbf{e}} + \mathbf{K_{GII}^{*e}} + \bar{\mathbf{K}}^{\mathbf{e}}{}_{\mathbf{GM}}^T + \bar{\mathbf{K}}_{\mathbf{GM}}^{\mathbf{e}} + \bar{\mathbf{K}}_{\mathbf{GM2}}^{\mathbf{e}} - \mathbf{K_{GAe}^e}. \tag{3.127}$$

3.6 Interfaces between beam finite elements

The finite element formulation presented in the previous sections provides the equilibrium solution of axially-loaded composite beams with geometric imperfections and piezoelectric actuators for any kind of boundary conditions. However, the formulation needs to be further generalised to correctly model beams with discontinuities in the material or geometrical properties (e.g. the finite elements have different material or geometrical characteristics). In general, two kinds of discontinuity, or interface, can occur between two consecutive finite elements:

- an *analytical interface*, when different analytical models are used for the two elements (Fig.[3.8a]).

- a *physical interface*, when the elements have either different material properties (Fig.[3.8b]) and/or there is an offset between the axes of the two elements (one element is thicker or the two elements are misaligned, Figs.[3.8c-3.8d]);
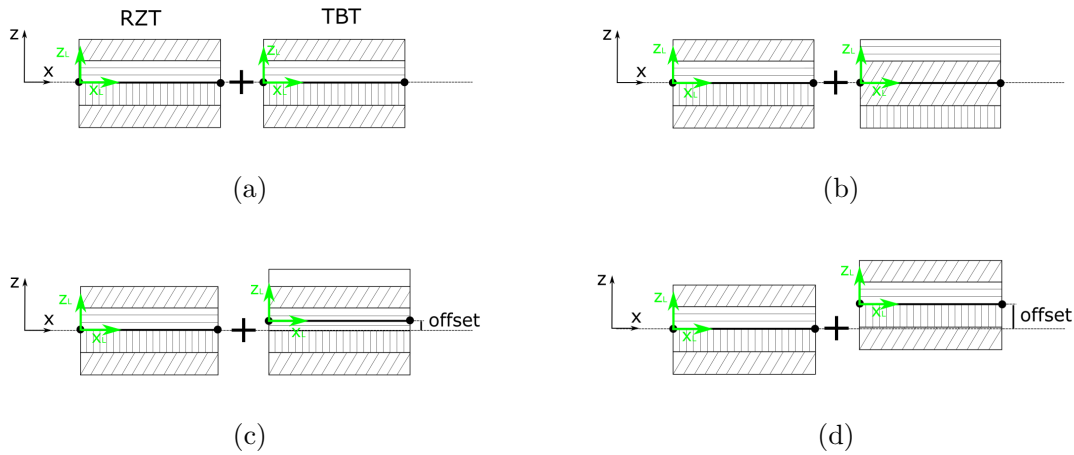
Figure 3.8: Interfaces between two consecutive finite elements: (a) analytical interface; geometrical interfaces due to (b) a change of the material layers, (c) an additional layer in the second element and (d) a misalignment between the elements.

In these cases, the displacement field vectors of the two elements at the interface are different because either the mathematical model or the geometric and material characteristics change. This inconsistency can be solved minimising the difference between the displacements fields by using a strategy based on the Lagrange multipliers method.
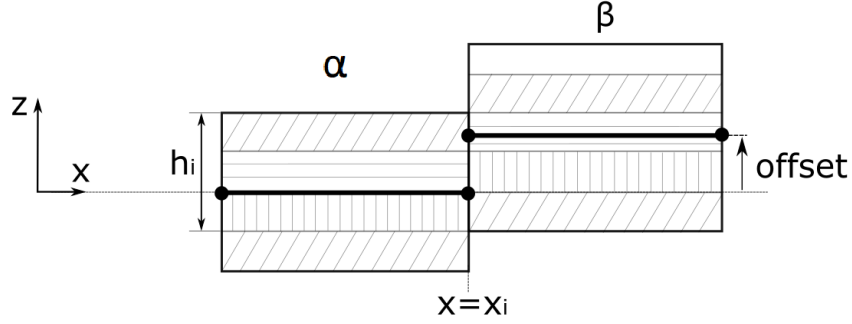
Figure 3.9: Geometrical interface between the elements α an β.

Considering a beam modelled using two finite elements, α and β, with an interface at $x = x_i$ (see Fig.[3.9]), the total potential energy of the system is the sum of the total potential energy of the first element and the total potential energy of the second element:

$$\Pi = \Pi^\alpha + \Pi^\beta \,. \tag{3.128}$$

The problem of the beam equilibrium can be solved finding the minimum of the total potential energy subjected to the constraint condition that the work done by fictitious forces on the difference between the two displacement fields at the interface, $\mathbf{s_i^\alpha}$ and $\mathbf{s_i^\beta}$, is zero. The physical meaning of this constraint condition is that, since the two elements are joint at the interface, the two displacement fields have to be the same, thus the beam cannot be deformed as if it was split in that location [124]. The total potential energy of the generic finite element j ($j = \alpha, \beta$) is the difference between the strain energy, U^j, and the work done by the external forces L_m^j:

$$\Pi^j = U^j - L_m^j \,. \tag{3.129}$$

Considering the finite element approximation for nonlinear and geometric imperfect beams (for the sake of simplicity, the condition of constant normal force and no electrical contribution is shown), the total potential energy of the element j is

$$\Pi^j = \frac{1}{2}\mathbf{u^j}^T\mathbf{K^j}\mathbf{u^j} + N_{xc}^j\frac{1}{2}\mathbf{u^j}^T\mathbf{K_G^j}\mathbf{u^j} + N_{xc}^j\mathbf{u^j}^T\mathbf{K_G^{*j}}\mathbf{u^{*j}} - \mathbf{u^j}^T\mathbf{F^j}\,, \tag{3.130}$$

thus the total potential energy Π is a function of the degrees of freedom vectors of the two elements, $\Pi = \Pi(\mathbf{u}^\alpha, \mathbf{u}^\beta)$.

The Langrange function is introduced to transform a constrained minimum problem of the function $\Pi = \Pi(\mathbf{u}^\alpha, \mathbf{u}^\beta)$, to an unconstrained minimum problem of a function, $\Pi_i = \Pi_i(\mathbf{u}^\alpha, \mathbf{u}^\beta, \lambda)$, which depends also on the Lagrange multipliers vector, $\boldsymbol{\lambda}$,

64

$$\Pi_i = \Pi^\alpha + \Pi^\beta + \int_{A_i} \boldsymbol{\lambda}^T \cdot \left(\mathbf{s_i^\alpha} - \mathbf{s_i^\beta} \right) dA \,. \tag{3.131}$$

The additional term in Π_i is the fictitious work given by the integral over the interface cross-section, $A_i = h_i \times b$, of the product between the fictitious stresses $\boldsymbol{\lambda}$ and the difference between the displacement fields of the two elements at the interface. Note that h_i is the thickness shared by the two elements indicated in Fig.[3.9].

The function Π_i of Eq.[3.131], can be then written taking into account also Eq.[3.1] and Eq.[3.74]:

$$
\begin{aligned}
\Pi_i(\mathbf{u}^\alpha, \mathbf{u}^\beta, \boldsymbol{\lambda}) = {} & \left[\frac{1}{2} \mathbf{u}^{\alpha T} \left(\mathbf{K}^\alpha + N_{xc}^\alpha \mathbf{K_G}^\alpha \right) \mathbf{u}^\alpha + N_{xc}^\alpha \mathbf{u}^{\alpha T} \mathbf{K_G^{*\alpha}} \mathbf{u}^{*\alpha} - \mathbf{u}^{\alpha T} \mathbf{F}^\alpha \right] \\
& + \left[\frac{1}{2} \mathbf{u}^{\beta T} \left(\mathbf{K}^\beta + N_{xc}^\beta \mathbf{K_G}^\beta \right) \mathbf{u}^\beta + N_{xc}^\beta \mathbf{u}^{\beta T} \mathbf{K_G^{*\beta}} \mathbf{u}^{*\beta} - \mathbf{u}^{\beta T} \mathbf{F}^\beta \right] \\
& + \int_{A_i} \boldsymbol{\lambda}^T \cdot \left(\mathbf{Z_u^\alpha} \mathbf{N}^\alpha(x_i) \mathbf{u}^\alpha - \mathbf{Z_u^\beta} \mathbf{N}^\beta(x_i) \mathbf{u}^\beta \right) dA \,.
\end{aligned}
\tag{3.132}
$$

Note that the shape function matrices of both elements $\mathbf{N^j}$ are evaluated at $x = x_i$, $i = \alpha, \beta$.

The Lagrange multipliers vector has two components, λ_u and λ_w, one for each displacement variable. The through-the-thickness distribution of the Lagrange multipliers at the interface is defined using the variables $\bar{\lambda}_{u1}$, $\bar{\lambda}_{u2}$ and $\bar{\lambda}_w$, because a linear distribution is assumed for λ_u, whereas λ_w is constant over the beam cross-section:

$$\boldsymbol{\lambda} = \begin{Bmatrix} \lambda_u \\ \lambda_w \end{Bmatrix} = \begin{bmatrix} N_1^L & N_2^L & 0 \\ 0 & 0 & 1 \end{bmatrix} \begin{Bmatrix} \bar{\lambda}_{u1} \\ \bar{\lambda}_{u2} \\ \bar{\lambda}_w \end{Bmatrix} \equiv \mathbf{N}_\lambda \bar{\boldsymbol{\lambda}} \,. \tag{3.133}$$

N_1^L and N_2^L are the linear Lagrange polynomials defined in Eq.[3.65], but in this case they are function of the thickness coordinate z.

Defining the matrix $\mathbf{H}^j$ for the element j,

$$\mathbf{H}^j = b^j \int_{h_i} \mathbf{N}_\lambda{}^T \mathbf{Z_u^j} dz \, \mathbf{N}^j(x_i) \,, \tag{3.134}$$

the function Π_i is then

$$
\begin{aligned}
\Pi_i(\mathbf{u}^\alpha, \mathbf{u}^\beta, \boldsymbol{\lambda}) = {} & \left[\frac{1}{2} \mathbf{u}^{\alpha T} \left(\mathbf{K}^\alpha + N_{xc}^\alpha \mathbf{K_G}^\alpha \right) \mathbf{u}^\alpha + N_{xc}^\alpha \mathbf{u}^{\alpha T} \mathbf{K_G^{*\alpha}} \mathbf{u}^{*\alpha} - \mathbf{u}^{\alpha T} \mathbf{F}^\alpha \right] \\
& + \left[\frac{1}{2} \mathbf{u}^{\beta T} \left(\mathbf{K}^\beta + N_{xc}^\beta \mathbf{K_G}^\beta \right) \mathbf{u}^\beta + N_{xc}^\beta \mathbf{u}^{\beta T} \mathbf{K_G^{*\beta}} \mathbf{u}^{*\beta} - \mathbf{u}^{\beta T} \mathbf{F}^\beta \right] \\
& + \bar{\boldsymbol{\lambda}}^T \mathbf{H}^\alpha \mathbf{u}^\alpha - \bar{\boldsymbol{\lambda}}^T \mathbf{H}^\beta \mathbf{u}^\beta \,.
\end{aligned}
\tag{3.135}
$$

65

The minimum of the function Π_i can be found solving the system:

$$
\begin{cases}
\dfrac{\delta\Pi_i}{\delta\mathbf{u}^\alpha} = 0\,, \\[2mm]
\dfrac{\delta\Pi_i}{\delta\mathbf{u}^\beta} = 0\,, \\[2mm]
\dfrac{\delta\Pi_i}{\delta\bar{\boldsymbol{\lambda}}} = 0\,,
\end{cases}
\tag{3.136}
$$

that is

$$
\begin{cases}
\left(\mathbf{K}^\alpha + N_{xc}^\alpha \mathbf{K_G^\alpha}\right)\mathbf{u}^\alpha + N_{xc}^\alpha \mathbf{K_G^*}^\alpha \mathbf{u}^{*\alpha} - \mathbf{F}^\alpha + \mathbf{H}^{\alpha T}\bar{\boldsymbol{\lambda}} = 0\,, \\[2mm]
\left(\mathbf{K}^\beta + N_{xc}^\beta \mathbf{K_G}^\beta\right)\mathbf{u}^\beta + N_{xc}^\beta \mathbf{K_G^*}^\beta \mathbf{u}^{*\beta} - \mathbf{F}^\beta - \mathbf{H}^{\beta T}\bar{\boldsymbol{\lambda}} = 0\,, \\[2mm]
\mathbf{H}^\alpha \mathbf{u}^\alpha - \mathbf{H}^\beta \mathbf{u}^\beta = 0\,.
\end{cases}
\tag{3.137}
$$

In matrix form, the degrees of freedom and the Lagrange multipliers can be collected in one vector because they are the variables of the system,

$$
\begin{aligned}
\left(\begin{bmatrix} \mathbf{K}^\alpha & \mathbf{0} & \mathbf{H}^{\alpha T} \\ \mathbf{0} & \mathbf{K}^\beta & -\mathbf{H}^{\beta T} \\ \mathbf{H}^\alpha & -\mathbf{H}^\beta & \mathbf{0} \end{bmatrix} + \begin{bmatrix} N_{xc}^\alpha \mathbf{K_G^{e\alpha}} & \mathbf{0} & \mathbf{0} \\ \mathbf{0} & N_{xc}^\beta \mathbf{K_G^\beta} & \mathbf{0} \\ \mathbf{0} & \mathbf{0} & \mathbf{0} \end{bmatrix}\right) \begin{Bmatrix} \mathbf{u}^\alpha \\ \mathbf{u}^\beta \\ \bar{\boldsymbol{\lambda}} \end{Bmatrix} = \\[2mm]
- \begin{bmatrix} N_{xc}^\alpha \mathbf{K_G^{*e\alpha}} & \mathbf{0} \\ \mathbf{0} & N_{xc}^\beta \mathbf{K_G^{*e\beta}} \\ \mathbf{0} & \mathbf{0} \end{bmatrix} \begin{Bmatrix} \mathbf{u}^{*\alpha} \\ \mathbf{u}^{*\beta} \end{Bmatrix} + \begin{Bmatrix} \mathbf{F}^\alpha \\ \mathbf{F}^\beta \\ \mathbf{0} \end{Bmatrix}\,,
\end{aligned}
\tag{3.138}
$$

that is

$$
\left(\mathbf{K} + \mathbf{K_{GN}}\right)\mathbf{u} = -\mathbf{K_{GN}^*}\mathbf{u}^* + \mathbf{F}\,,
\tag{3.139}
$$

where the vector $\mathbf{u}$ contains both the degrees of freedom of the beam and the Lagrange multipliers variables.

It can be seen that the stiffness matrix $\mathbf{K}$ of a beam with an interface has additional rows and columns for the new degrees of freedom at the interface but also other terms related to the variables of the Lagrange multipliers. The geometric stiffness matrices of the beam, $\mathbf{K_{GN}}$ and $\mathbf{K_{GN}^*}$, contain the geometric stiffness matrices of each element multiplied by the normal force acting on the element. $\mathbf{K_{GN}}$, $\mathbf{K_{GN}^*}$ and the vector $\mathbf{F}$ have additional rows and columns of zero-elements corresponding to the Lagrange multipliers variables.

3.6.1 Modelling delaminated composite beams using RZT-beam finite elements

The strategy based on the Lagrange Multipliers method can be employed also for modelling beams with delaminations, like the six-layer beam shown in Fig.[3.10]. The fourth and the fifth layers of the beam are separated between $x = x_m$ and $x = x_n$, thus the laminate is divided in two sublaminates along $L_d = x_n - x_m$.
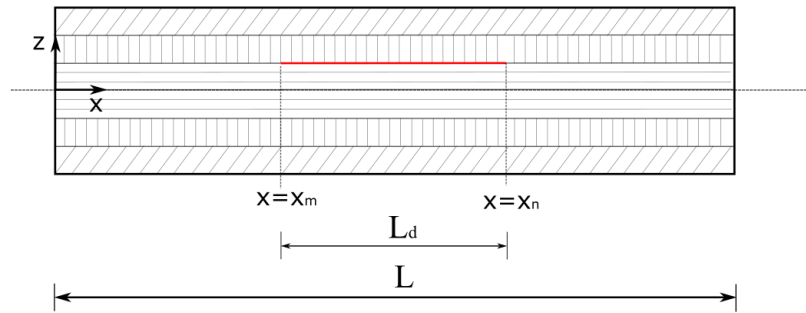
Figure 3.10: Six-layer composite beam with a delamination.

In order to model the behaviour of each sublaminate, two RZT-beam finite elements have to be employed along the thickness in the delaminated part. The minimum number of RZT-beam finite elements required to model the delaminated beam in Fig.[3.10] is four, and they are indicated as a, b, c and d in Fig.[3.11].
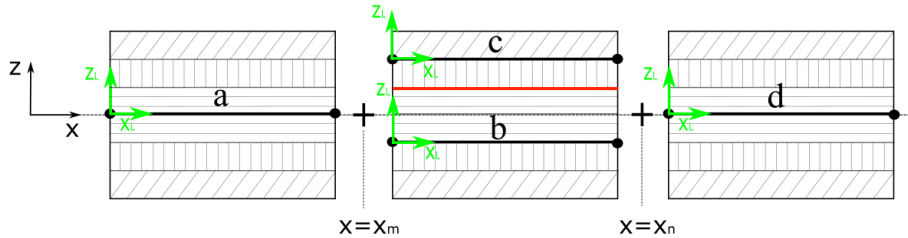
Figure 3.11: FE model of a delaminated composite beam using beam-RZT finite elements.

At $x = x_m$ and $x = x_n$ the finite elements of the non-delaminated parts (a and d respectively) have to be linked to the two finite elements of the delaminated part (b and c). The elements in the delaminated part have a different thickness and their axes are not aligned to those of the elements in the non-delaminated parts. This means that to link the element a to both the elements b and c, the Lagrange multipliers method can be employed as shown in the previous section, but

considering that there are two interfaces at the same point $(x = x_m)$, one interface is between a and b and the other interface is between a and c. The same happens at $x = x_n$, where both the elements b and c have to be linked to the element d. The resulting number of interfaces is then four. Introducing a vector of Lagrange multipliers for each interface, the function Π_i for the delaminated beam model of Fig.[3.11] is

$$\Pi_i = \Pi^a + \Pi^b + \Pi^c + \Pi^d + \int_{A_{m1}} \boldsymbol{\lambda_1}^T \cdot \left(\mathbf{s_m^a} - \mathbf{s_m^b}\right) dA + \int_{A_{m2}} \boldsymbol{\lambda_2}^T \cdot (\mathbf{s_m^a} - \mathbf{s_m^c}) \, dA +$$
$$+ \int_{A_{n1}} \boldsymbol{\lambda_3}^T \cdot \left(\mathbf{s_n^b} - \mathbf{s_n^d}\right) dA + \int_{A_{n2}} \boldsymbol{\lambda_4}^T \cdot \left(\mathbf{s_n^c} - \mathbf{s_n^d}\right) dA \,,$$

(3.140)

where s_i^j is the displacement vector of the element j at the interface $x = x_i$.

Considering Eq.[3.133], the finite element formulation of Π_i for the delaminated beam is

$$\Pi_i = \left[\frac{1}{2}\mathbf{u}^{aT} \left(\mathbf{K}^a + N_{xc}^a \mathbf{K_G}^a\right) \mathbf{u}^a - \mathbf{u}^{aT}\mathbf{F}^a\right] + \left[\frac{1}{2}\mathbf{u}^{bT} \left(\mathbf{K}^b + N_{xc}^b \mathbf{K_G}^b\right) \mathbf{u}^b - \mathbf{u}^{bT}\mathbf{F}^b\right] +$$
$$+ \left[\frac{1}{2}\mathbf{u}^{cT} \left(\mathbf{K}^c + N_{xc}^c \mathbf{K_G}^c\right) \mathbf{u}^c - \mathbf{u}^{cT}\mathbf{F}^c\right] + \left[\frac{1}{2}\mathbf{u}^{dT} \left(\mathbf{K}^d + N_{xc}^d \mathbf{K_G}^d\right) \mathbf{u}^d - \mathbf{u}^{dT}\mathbf{F}^d\right] +$$
$$+ \bar{\boldsymbol{\lambda}}_\mathbf{1}^T \left(\mathbf{H_{m1}^a}\mathbf{u}^a - \mathbf{H_{m1}^b}\mathbf{u}^b\right) + \bar{\boldsymbol{\lambda}}_\mathbf{2}^T \left(\mathbf{H_{m2}^a}\mathbf{u}^a - \mathbf{H_{m2}^c}\mathbf{u}^c\right) +$$
$$+ \bar{\boldsymbol{\lambda}}_\mathbf{3}^T \left(\mathbf{H_{n1}^b}\mathbf{u}^b - \mathbf{H_{n1}^d}\mathbf{u}^d\right) + \bar{\boldsymbol{\lambda}}_\mathbf{4}^T \left(\mathbf{H_{n2}^c}\mathbf{u}^c - \mathbf{H_{n2}^d}\mathbf{u}^d\right) \,.$$

(3.141)

The matrix $\mathbf{H_{il}^j}$ is defined for the interface l $(l = 1,2)$ of the element j at $x = x_i$, as

$$\mathbf{H_{il}^j} = \int_{A_{il}} \mathbf{N}_\lambda{}^T \mathbf{Z_u^j} dz \, \mathbf{N^j}(x_i) \,.$$

(3.142)

The condition that the partial derivatives of the function Π_i with respect to its variables $\mathbf{u}^a$, $\mathbf{u}^b$, $\mathbf{u}^c$, $\mathbf{u}^d$, $\bar{\boldsymbol{\lambda}}_\mathbf{1}$, $\bar{\boldsymbol{\lambda}}_\mathbf{2}$, $\bar{\boldsymbol{\lambda}}_\mathbf{3}$, $\bar{\boldsymbol{\lambda}}_\mathbf{4}$, have to vanish leads to the following matrix equation (for the sake of simplicity, the condition of constant normal force and the absence of electrical forces and geometric imperfections is considered):

$$\left(\mathbf{K} + \mathbf{K_{GN}}\right) \mathbf{u} = \mathbf{F} \,,$$

(3.143)

where the vector of the unknowns contains both the degrees of freedom and the four vectors of Lagrange multipliers variables,

$$\mathbf{u} = \begin{Bmatrix} \mathbf{u}^a \\ \mathbf{u}^b \\ \mathbf{u}^c \\ \mathbf{u}^d \\ \bar{\lambda}_1 \\ \bar{\lambda}_2 \\ \bar{\lambda}_3 \\ \bar{\lambda}_4 \end{Bmatrix} . \tag{3.144}$$

The stiffness matrix of the beam, $\mathbf{K}$, contains the terms related to the interfaces $(\mathbf{H_{il}^j})$ as follows:

$$\mathbf{K} = \begin{bmatrix} \mathbf{K}^a & \mathbf{0} & \mathbf{0} & \mathbf{0} & \mathbf{H}_{\mathbf{m1}}^{aT} & \mathbf{H}_{\mathbf{m2}}^{aT} & \mathbf{0} & \mathbf{0} \\ \mathbf{0} & \mathbf{K}^b & \mathbf{0} & \mathbf{0} & -\mathbf{H}_{\mathbf{m1}}^{bT} & \mathbf{0} & \mathbf{H}_{\mathbf{n1}}^{bT} & \mathbf{0} \\ \mathbf{0} & \mathbf{0} & \mathbf{K}^c & \mathbf{0} & \mathbf{0} & -\mathbf{H}_{\mathbf{m2}}^{cT} & \mathbf{0} & \mathbf{H}_{\mathbf{n2}}^{cT} \\ \mathbf{0} & \mathbf{0} & \mathbf{0} & \mathbf{K}^d & \mathbf{0} & \mathbf{0} & -\mathbf{H}_{\mathbf{n1}}^{dT} & -\mathbf{H}_{\mathbf{n2}}^{dT} \\ \mathbf{H}_{\mathbf{m1}}^a & -\mathbf{H}_{\mathbf{m1}}^b & \mathbf{0} & \mathbf{0} & \mathbf{0} & \mathbf{0} & \mathbf{0} & \mathbf{0} \\ \mathbf{H}_{\mathbf{m2}}^a & \mathbf{0} & -\mathbf{H}_{\mathbf{m2}}^c & \mathbf{0} & \mathbf{0} & \mathbf{0} & \mathbf{0} & \mathbf{0} \\ \mathbf{0} & \mathbf{H}_{\mathbf{n1}}^b & \mathbf{0} & -\mathbf{H}_{\mathbf{n1}}^d & \mathbf{0} & \mathbf{0} & \mathbf{0} & \mathbf{0} \\ \mathbf{0} & \mathbf{0} & \mathbf{H}_{\mathbf{n2}}^c & -\mathbf{H}_{\mathbf{n2}}^d & \mathbf{0} & \mathbf{0} & \mathbf{0} & \mathbf{0} \end{bmatrix} , \tag{3.145}$$

while the geometric stiffness matrix and the force vector have additional zero-element terms

$$\mathbf{K_{GN}} = \begin{bmatrix} N_{xc}^a \mathbf{K_G^{ea}} & \mathbf{0} & \mathbf{0} & \mathbf{0} & \mathbf{0} & \mathbf{0} & \mathbf{0} & \mathbf{0} \\ \mathbf{0} & N_{xc}^b \mathbf{K_G^{eb}} & \mathbf{0} & \mathbf{0} & \mathbf{0} & \mathbf{0} & \mathbf{0} & \mathbf{0} \\ \mathbf{0} & \mathbf{0} & N_{xc}^c \mathbf{K_G^{ec}} & \mathbf{0} & \mathbf{0} & \mathbf{0} & \mathbf{0} & \mathbf{0} \\ \mathbf{0} & \mathbf{0} & \mathbf{0} & N_{xc}^d \mathbf{K_G^{ed}} & \mathbf{0} & \mathbf{0} & \mathbf{0} & \mathbf{0} \\ \mathbf{0} & \mathbf{0} & \mathbf{0} & \mathbf{0} & \mathbf{0} & \mathbf{0} & \mathbf{0} & \mathbf{0} \\ \mathbf{0} & \mathbf{0} & \mathbf{0} & \mathbf{0} & \mathbf{0} & \mathbf{0} & \mathbf{0} & \mathbf{0} \\ \mathbf{0} & \mathbf{0} & \mathbf{0} & \mathbf{0} & \mathbf{0} & \mathbf{0} & \mathbf{0} & \mathbf{0} \\ \mathbf{0} & \mathbf{0} & \mathbf{0} & \mathbf{0} & \mathbf{0} & \mathbf{0} & \mathbf{0} & \mathbf{0} \end{bmatrix} , \tag{3.146}$$

$$\mathbf{F} = \begin{Bmatrix} \mathbf{F}^a \\ \mathbf{F}^b \\ \mathbf{F}^c \\ \mathbf{F}^d \\ \mathbf{0} \\ \mathbf{0} \\ \mathbf{0} \\ \mathbf{0} \end{Bmatrix} . \tag{3.147}$$

3.7 Conclusion

A new analytical model based on the Refined Zigzag Theory has been created for the buckling and postbuckling analyses of composite laminated and sandwich beams subjected to axial compressive loads. The geometric nonlinearities and the geometric imperfections have been introduced for the first time in the RZT formulation in order to generate a model able to evaluate the buckling loads and the nonlinear response of geometrically imperfect composite beams.

In addition, one of the capabilities of the model is that the beam layers can be made of piezoelectric material. The converse piezoelectric effect has been considered in the formulation to investigate the possibility to control the buckling response with piezoelectric actuators using a theory as efficient as the Timoshenko Beam Theory but suitable for composites.

Firstly, the equilibrium equations based on the nonlinear RZT have been derived to find the response of initially imperfect composite beams with piezoelectric actuator layers subjected to both distributed and concentrated loads. An example of the analytical solution has been shown for a symmetric, piezo-composite laminated beam, with an initial deflection approximated by a sinusoidal function, with simply-supported boundary conditions and subjected to an axial-compressive force and a sinusoidal-distributed transverse load.

Subsequently, a finite element formulation based on C^0 RZT-beam finite elements has been created to solve the buckling and the nonlinear equilibrium problem of composite beams for any lamination, load system, boundary conditions and geometric imperfection. In addition, a strategy based on the Lagrange multipliers method has been employed to correctly model any kind of discontinuity in the beam lamination. As a consequence, the new RZT-FE model can be used for the analysis of beams with local thickness and material changes due to piezoelectric actuator patches on the beam surfaces. The actuators for the buckling control can be then either continuous piezoelectric layers (internal or external) or patches externally bonded to the beam.

A further application of the model is the analysis of delaminated composite beams. The new RZT-FE model is extended to the buckling and postbuckling analyses of delaminated composite and sandwich beams, with the possibility to investigate the local buckling control using piezoelectric actuator patches.

The new RZT-FE model is very attractive because it is based on a theory suitable for composites and sandwiches with a very simple formulation, characterised by only one additional degree of freedom per node with respect to the Bernoulli-Euler and Timoshenko beam theories, and it can be employed for various and general applications, for both symmetrically and anti-symmetrically laminated beams. It combines accuracy and efficiency and it can be used to study the control of both the global and the local buckling of composite and sandwich beams.

Chapter 4

Numerical verification

4.1 Introduction

The new nonlinear RZT-FE model is implemented in a Matlab routine to perform the buckling and postbuckling analyses of composite beams with and without pizoelectric actuators. In this chapter, the model is numerically assessed for the buckling and the nonlinear static (postbuckling) analyses of both sandwich beams and composite laminated beams with piezoelectric actuators.

Firstly, three sandwich beams with aluminium facesheets and a foam core, with various slenderness and face-to-core thickness ratios, are considered (Section 4.2). Two different structural foams are taken into account in order to study the influence of the face-to-core stiffness ratio on the numerical predictions. The buckling loads and the nonlinear response to a compressive force are calculated for each beam and the RZT results are compared to those obtained by both one-dimensional models based on Timoshenko beam finite elements and two-dimensional, highly-detailed, finite element models realised either in Abaqus or in Nastran. The high-fidelity Abaqus and Nastran solutions are taken as a reference to demonstrate that the RZT is very accurate and also more efficient than the commercial codes. In addition, it is shown that the Timoshenko FE models are not able to correctly predict the buckling loads and the nonlinear response of sandwich beams with low slenderness ratios and highly heterogeneous materials.

Subsequently, the RZT model is employed for the analysis of five composite multilayer beams with piezoelectric actuator patches bonded to the external surfaces considering various geometries and actuator locations (Section 4.3). In Abaqus, the piezoelectric properties can be assigned only to solid elements, thus the reference models are realised using three-dimensional finite elements. The buckling analysis is performed and then the buckling modes are used to introduce the geometric imperfections in each model to calculate the nonlinear static response of the imperfect beams subjected to an axial compressive load. For both these analyses the piezoelectric effect is not considered and the actuators are just geometric entities which

introduce geometric and material discontinuities to assess the RZT in this condition. The piezoelectric actuation is then taken into account applying a voltage to the actuators. The nonlinear static response of the imperfect beams is calculated in terms of transversal deflection; the RZT and Abaqus predictions are compared to demonstrate that RZT is very accurate also for high voltages and it is a more efficient and convenient way to perform these analyses.

4.2 Nonlinear static and buckling analyses of sandwich beams

Three sandwich beams with different material and geometrical properties have been considered for the numerical validation of the nonlinear FE model based on the RZT, with a focus on highly heterogeneous materials and low slenderness ratios. All the beams have a foam core and aluminium facesheets; two of them, the IG-32-5 and the WF-32-5, have the same geometry (length and thicknesses) but the material of the core is the Rohacell® IG31 for the IG-32-5 and the Rohacell® WF110 for the WF-32-5. The third beam, named IG-96-2, has a Rohacell® IG31 core but it is longer than the other two beams. Moreover, the IG-32-5 and the WF-32-5 have a slenderness ratio of 20 and a core-to-face thickness ratio of 1.2, whereas the slenderness ratio of the IG-96-2 is 40 and its core-to-face thickness ratio is 10. These beams were realised for the experimental assessments of the RZT for the static and dynamic analyses ([62]-[63]) and their material properties and dimensions can be found in Tables [4.1-4.2]. Figs.[4.1] show the IG-32-5 and the IG-96-2 in the configuration used in a previous work for the free-vibration analysis.

(a) *IG-32-5*   (b) *IG-96-2*
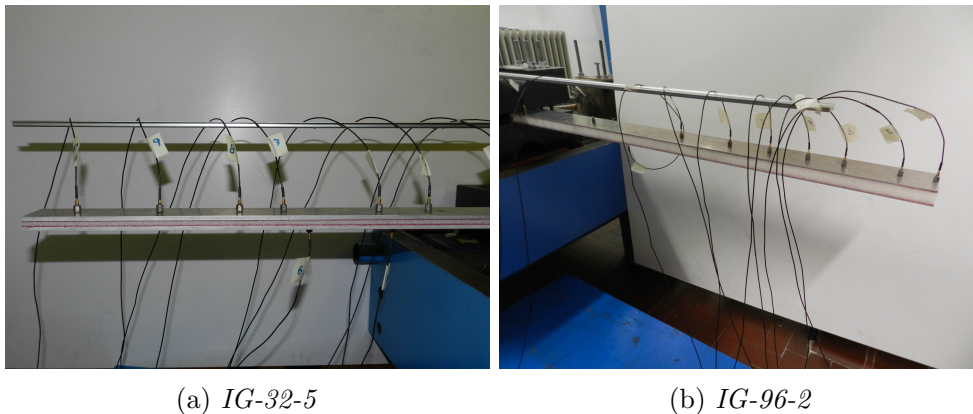
Figure 4.1: The IG-32-5 and the IG-96-2 sandwich beams employed to validate the RZT for the free-vibration analysis [63].

	Ergal®	Rohacell®IG31	Rohacell®WF110
E (MPa)	69,570	40.3	196
G (MPa)	25,766	12.4	65.4

Table 4.1: Material properties of the sandwich beams for the numerical validation.

Beam	L	b	h_c	h_f
IG-32-5	320	48.53	6.07	5
WF-32-5	320	48.18	6.10	5
IG-96-2	960	72.40	19.93	2

Table 4.2: Geometrical properties of the sandwich beams for the numerical validation (mm).

The buckling and the nonlinear static analyses have been conducted for each beam in both simply-supported and cantilever boundary conditions (see Fig.[4.2]).

Figure 4.2: Load and boundary conditions: (a) simply-supported- (b) clamped-free-beam subjected to an axial-compressive force.

4.2.1 Finite element models of the sandwich beams

Each beam has been analysed using three different finite element models: a high-fidelity two-dimensional model realised either in Abaqus® or in MSC/Nastran®, a one-dimensional model based on RZT-beam finite elements and a one-dimensional model based on TBT-beam finite elements.

The 2D models were experimentally validated in previous works for the static and free-vibration analyses of sandwich beams, thus they are taken as the reference solution. Four-node 2D finite elements (S4R for Abaqus and QUAD4 for Nastran) have been used in the (x, z) plane for a plane stress model of the beams oriented as in Fig.[3.1]. A suitable element dimension has been chosen to guarantee the presence of at least two elements along the thickness in each layer, as shown in Fig.[4.3]. The exact numbers of nodes and elements of the 2D meshes are reported in Table [4.3].

73

(a) (IG-WF)-32-5.

(b) IG-96-2.
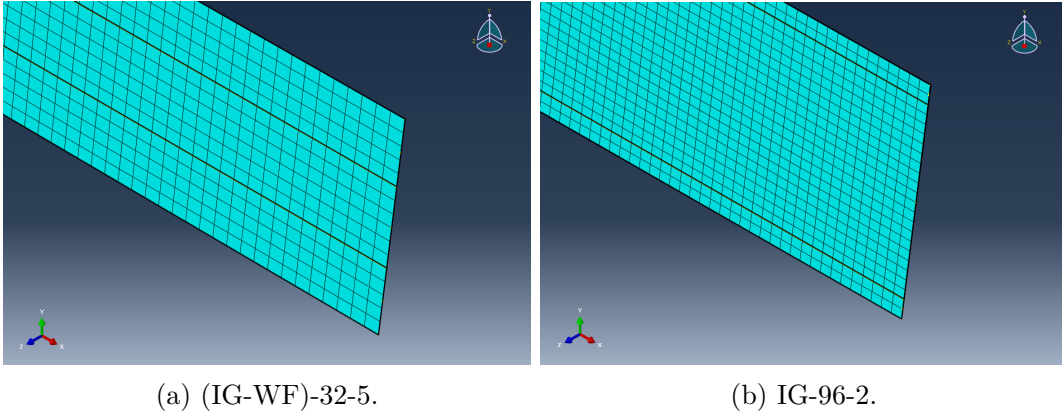
Figure 4.3: Two-dimensional models of the beams using four-node 2D finite elements.

The usual way for modelling beam-like structures in the finite element commercial codes is using 1D-beam elements. These elements are based on the Timoshenko Beam Theory and have only two nodes, thus the resulting finite element model of a beam has a considerably lower number of degrees of freedom than a 2D model. For this reason, the analyses have been conducted also for 1D models based on the TBT to show that, despite the lower computational cost, possible issues can occur for particular beam geometries and material characteristics, even using an ad-hoc shear correction factor k based on the transverse-shear strain energy [22].

	No. of nodes	No. of elements			
		along L	along h_f	along h_c	total
(IG/WF)-32-5	5,457	320	5	6	5,120
IG-96-2	25,947	960	2	20	23,040

Table 4.3: Number of nodes and finite elements of the two-dimensional models in Nastran and Abaqus.

The RZT and the TBT finite element models have been implemented in Matlab, and the inputs needed in the routine are the beam geometrical and material characteristics, the load and boundary conditions and the desired number of finite elements.

To set the number of finite elements of the one-dimensional models, the buckling and postbuckling analyses of the beams have been performed several times for an increasing the number elements. The minimum number of elements which did not give appreciable differences comparing the solutions to those obtained with a higher number of elements was 40 for the shortest beams, thus a mesh of 40 finite elements has been considered for both the TBT and the RZT models of all the beams.

4.2.2 Buckling analysis of the sandwich beams

The buckling loads of the beams modelled with RZT finite elements have been calculated solving the eigenvalue problem of Eq.[3.110] in 3.4.1. An equivalent equation has been solved for the models based on the TBT, considering a specific shear correction factor, k, calculated for each beam: $k^2 = 1.1163 \times 10^{-3}$ for the IG-32-5, $k^2 = 5.1762 \times 10^{-3}$ for the WF-32-5 and $k^2 = 1.4914 \times 10^{-2}$ for the IG-96-2[1]. In Abaqus, the buckling analysis has been performed applying a distributed piecewise constant load along the thickness at the supported edge. The load magnitude in each layer is proportional to the Young modulus of the corresponding material to guarantee a constant axial strain in the cross-section and to avoid local effects (that cannot be modelled by RZT and TBT).

The values of the first two buckling loads for each beam are reported in Table [4.4] for the cantilever boundary conditions, and in Table [4.5] for the simply-supported conditions, indicating the percentage deviation, Δ, of RZT and TBT from the Abaqus solution.

Beam	ABAQUS (N)	RZT (N)	Δ %	TBT (N)	Δ %
IG-32-5	9,850	9,905	0.56	9,159	-7.02
	26,292	26,856	2.15	13,196	-49.81
WF-32-5	19,498	19,540	0.22	19,409	-0.46
	63,985	64,303	0.50	55,153	-13.8
IG-96-2	5,017	5,026	0.18	5,025	0.16
	15,973	16,076	0.64	15,994	0.13

Table 4.4: Buckling loads for cantilever boundary conditions.

It can be noticed that the RZT and TBT percentage deviations in Table [4.5] for the simply-supported boundary conditions are higher than the corresponding values in Table [4.4] for the cantilever configuration, but the RZT deviations are generally much lower than the TBT in both cases. The RZT deviation on the first buckling load is higher than 1% only for the shortest and most heterogeneous beam, the IG-32-5, reaching 1.84% in simply-supported boundary conditions. The RZT predictions are very accurate also for the second buckling load, with the deviation up to 3.27% only for the IG-32-5 and lower than 2% in all other cases. On the other

---

[1]As explained in the literature review, the method proposed in [22] is based on the calculation of the transverse-shear strain energy in two different ways. The final expression of the shear correction factor depends on the stiffness coefficients of the beam, thus different laminations and thicknesses lead to different values of the coefficient.

hand, the TBT is accurate only for the IG-96-2, which has the highest slenderness ratio, and for the first buckling load of the WF-32-5 in cantilever configuration, but when simply-supported boundary conditions are considered, the deviation is almost 5%. In any other case TBT is inaccurate, especially for the simply-supported boundary conditions, where the values reach almost 30% and 65% for the first and second buckling loads of the IG-32-5.

These results point out that, in the FE commercial codes, the model of a composite beam has to be at least two-dimensional to guarantee the right solution for any kind of beam geometry and material properties, because the one-dimensional models can give incorrect results as they are based on the TBT. However, the major drawback of the two-dimensional FE models is the computational cost. The time for the RZT and TBT buckling analyses is always less than one second, while the time needed by Abaqus to perform the same analyses is one (for the (IG/WF)-32-5) or two (for the IG-96-2) orders of magnitude higher. For this reason, the RZT is an excellent compromise between accuracy and computational effort.

Beam	ABAQUS (N)	RZT (N)	Δ %	TBT (N)	Δ %
IG-32-5	17,361	17,681	1.84	12,346	-28,89
	37,745	38,980	3.27	13,522	-64.18
WF-32-5	45,005	45,311	0.68	42,828	-4.84
	80,009	81,329	1.65	61,332	-23.34
IG-96-2	11,894	11,946	0.44	11,926	0.27
	18,172	18,354	1.00	18,162	-0.06

Table 4.5: Buckling loads for simply-supported boundary conditions.

4.2.3 Nonlinear response of the sandwich beams subjected to a compressive force

The nonlinear response of the beams has been obtained for various initial imperfection configurations and in both simply-supported and cantilever boundary conditions. A compressive force N_0 has been applied at the supported edge and the RZT beam response has been evaluated solving Eq.[3.109] with $N_{xc}^e = -N_0$, and with $N_x^{inde} = 0$ and $\mathbf{V_P^e} = \mathbf{0}$ because no piezoelectric actuators are considered:

$$[\mathbf{K^e} - N_0 \mathbf{K_G^e}] \cdot \mathbf{u^e} = \mathbf{F^e} + N_0 \mathbf{K_G^{*e}} \mathbf{u^{*e}}. \tag{4.1}$$

Eq.[4.1] has been solved for 20 values of N_0, with constant increments of load from $N_0 = 0$ to $N_0 = 0.99 N_{cr}$. For each value of N_0, the equation has been solved

76

in the conventional way since the stiffness matrices in the equation are independent of the degrees of freedom. A formally equivalent equation has been solved for the TBT FE models.

A first analysis has been conducted for the IG-32-5 in cantilever configuration and the geometric imperfection is described by the following relation:

$$w^*(x) = \frac{L^2 + \mu^2 - \sqrt{(L^2 + \mu^2)^2 - 4\mu^2 x^2}}{2\mu} \ . \tag{4.2}$$

The parameter μ indicates the maximum deflection at the tip and the value chosen is $\mu = w^*(L) = 1$ mm.

The reference 2D model has been realised in MSC/Patran with the geometry reproducing the beam in its imperfect configuration (see Fig.[4.4]).
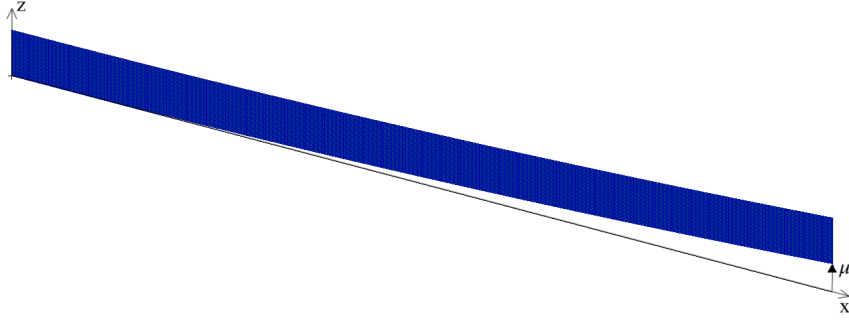
Figure 4.4: Nastran model of a cantilever beam with an initial geometric imperfection function defined in Eq.[4.2].

The geometric imperfection can be easily introduced in the 1D models (RZT and TBT) indicating the expression of the function $w^*(x)$, which is approximated in the finite element method as explained in 3.4.

The nonlinear response of the beam has been calculated[2] for the three models increasing the applied load N_0 from 0 to 99% of the critical buckling load calculated in the previous section. The load-transversal displacement equilibrium path of the node at the beam tip is reported in Fig.[4.5].

---

[2]In Nastran, to perform a nonlinear static analysis, the modified Newton-Raphson method has been used with a number of load increments of 10 and a maximum iteration number of 25 [19].
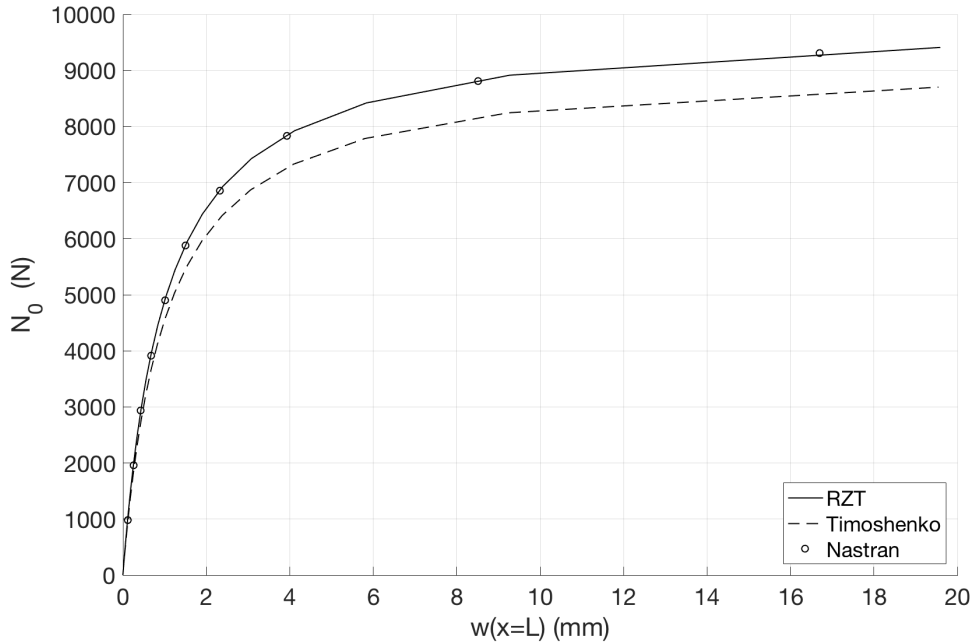
Figure 4.5: Load–deflection curves for the cantilevered IG-32-5 beam with initial imperfection.

The main disadvantage of Nastran is that the imperfections can be taken into account only if the model geometry has the actual initial deformed shape.

In Abaqus, the imperfection can be optionally introduced in the model of a perfect beam as a linear combination of the buckling modes. For this reason, Abaqus has been used to validate the RZT predictions for various imperfections. Moreover, for each beam, three different configurations have been chosen as initial deflection, described by the following combinations of buckling modes:

1. imperfection corresponding to the first buckling mode

2. imperfection corresponding to the second buckling mode

3. imperfection corresponding to a linear combination of the first and the second buckling mode, 70% and 30% respectively.

In each case, the actual initial deflection has been obtained setting to 1 mm the maximum deflection of the deformed shape[3].

---

[3]The method used in Abaqus for the nonlinear static analysis is the arc-length method. The first increment has been set at 10% of the maximum applied load (corresponding to the buckling

The nonlinear response of the beams is calculated for both simply-supported and cantilever boundary conditions and considering all the imperfection combinations described above. The results of RZT, TBT and Abaqus are compared in Figs.[4.6-4.14].

As expected, the load-deflection curves of the beams with the geometric imperfection described by either a generic function (Fig.[4.5]) or the first buckling mode (Figs.[4.6, 4.9, 4.12]) have a horizontal asymptote that corresponds to the first buckling load indicated in Tables [4.4-4.5]. The load asymptotic value is the first buckling load also when a linear combination of the first and the second buckling load is considered as initial imperfection, as shown in Figs.[4.8, 4.11, 4.14]. On the other hand, when the imperfection exactly reproduces the second buckling load, the curve tends asymptotically to the corresponding second buckling load value (Figs.[4.7, 4.10, 4.13]).

Figs.[4.12-4.14] show that in all cases, the IG-96-2 load-deflection equilibrium paths are very well predicted by both the RZT and TBT, like the evaluation of the corresponding buckling loads.

The curves for the IG-32-5 and the WF-32-5 in Figs.[4.6-4.11] show that the accuracy of TBT is highly dependent on the initial imperfections, with higher deviations when the second buckling mode shape is assumed as initial deflection (Figs.[4.7]-[4.10]). Moreover, the mismatch between TBT and Abaqus is significantly bigger for the IG-32-5, because of both the low slenderness ratio and the higher heterogeneity between the materials of the core and facesheets of this beam. There is also a dependence on the boundary conditions with better predictions of both TBT and RZT when cantilever configurations are considered.

By contrast, the RZT solution is noticeably accurate for all the beams in all configurations, and this precision is reached in less than 10 seconds while the Abaqus total CPU time to perform the same analyses is two orders of magnitude higher. The time required by the RZT and the Abaqus models for the buckling and the postbuckling analyses is reported in Table [4.6].

---

load) and the minimum and maximum number of increments allowed has been set to 10 and 1000 respectively [18].
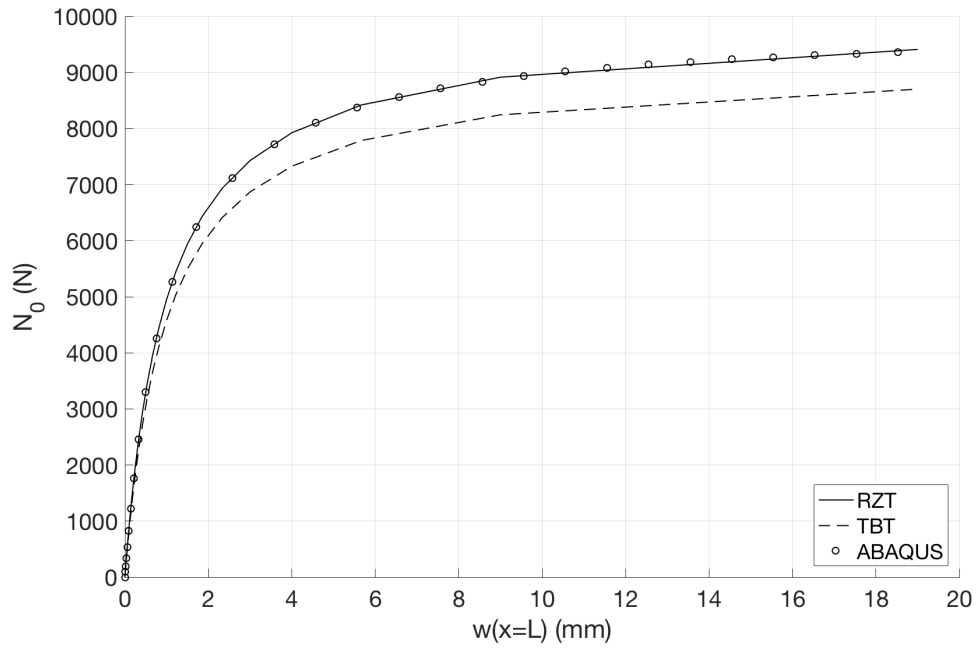
(a) *CF*
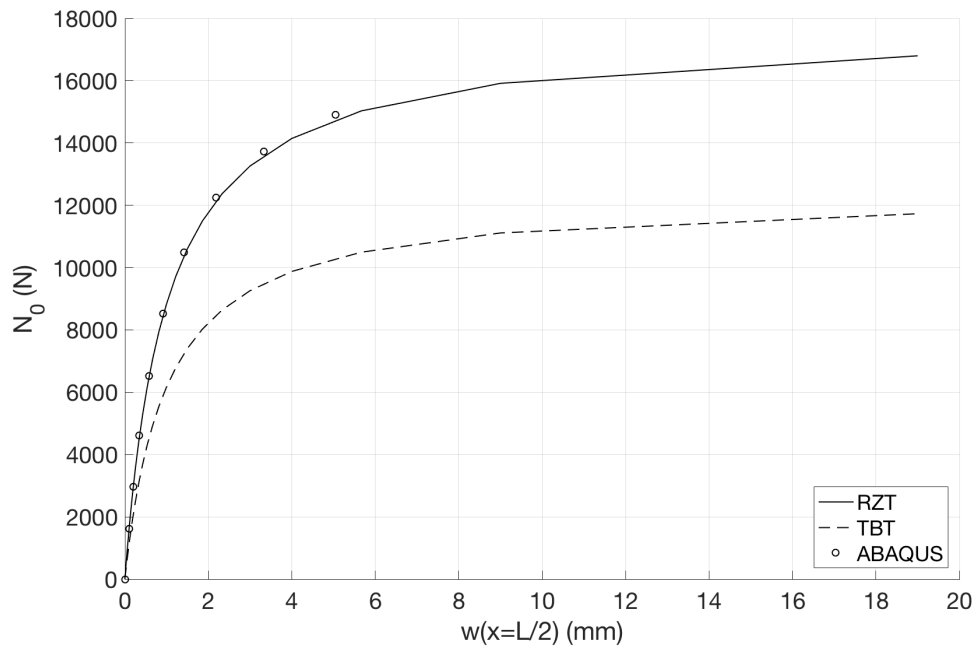
(b) *SS*

Figure 4.6: Load-displacement equilibrium path for the IG-32-5 sandwich beam with the initial imperfection corresponding to the first buckling mode.
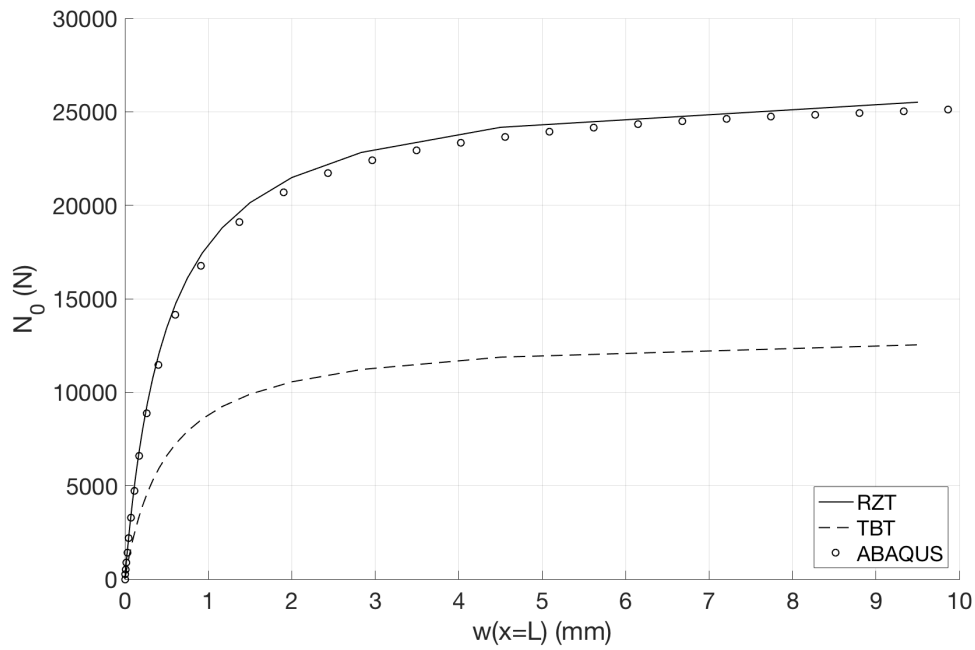
(a) *CF*
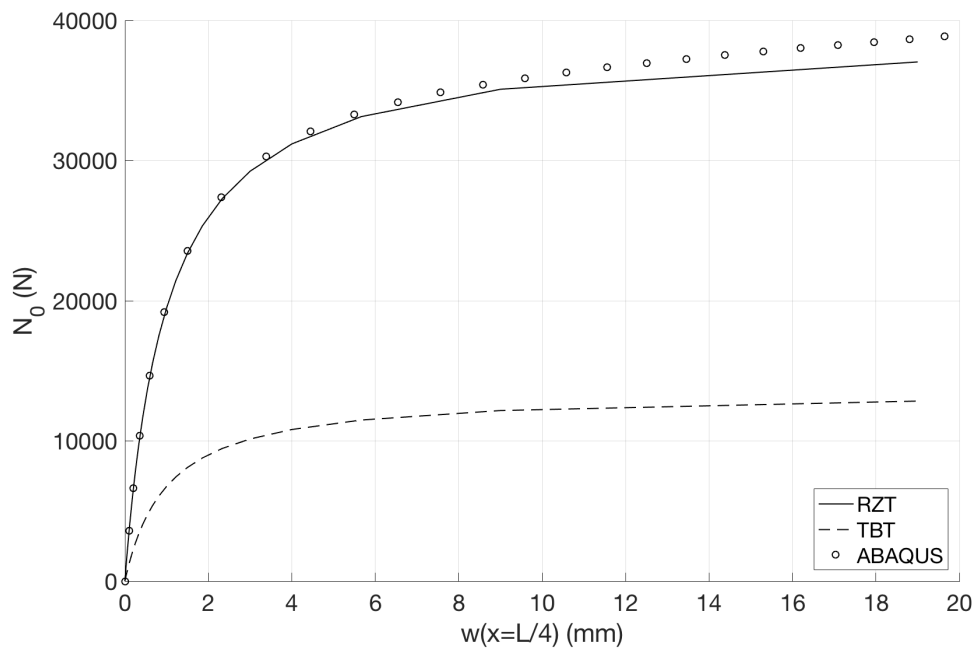
(b) *SS*

Figure 4.7: Load-displacement equilibrium path for the IG-32-5 sandwich beam with the initial imperfection corresponding to the second buckling mode.
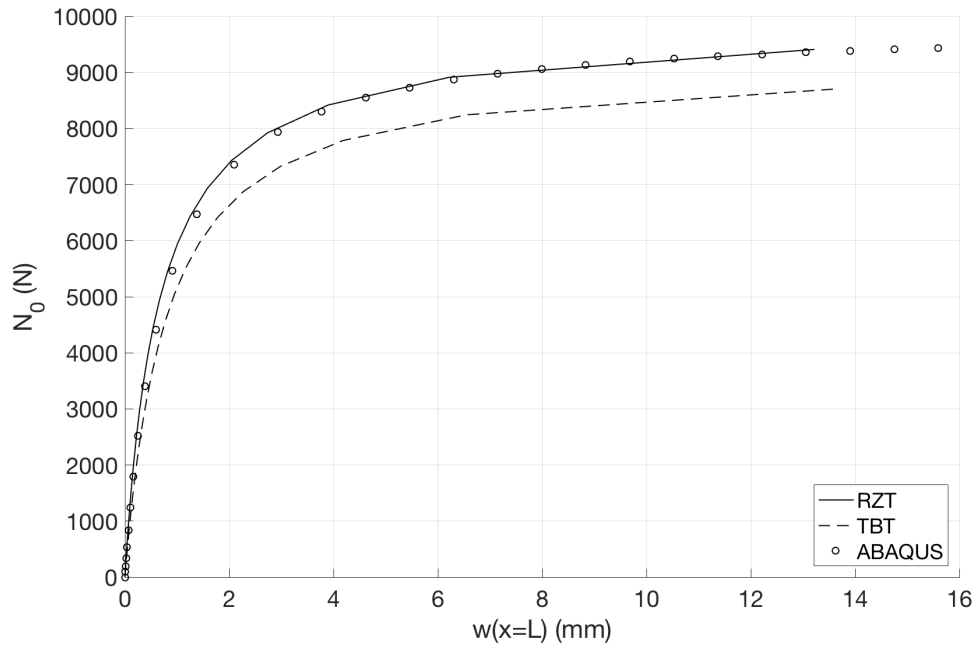
(a) *CF*
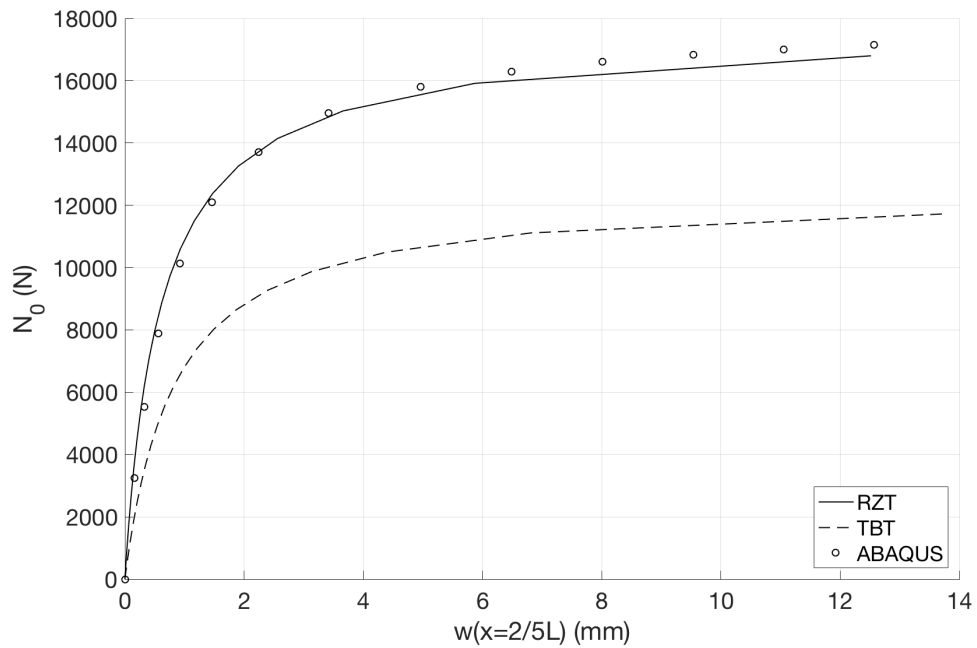
(b) *SS*

Figure 4.8: Load-displacement equilibrium path for the IG-32-5 sandwich beam with the initial imperfection corresponding to a linear combination of the first and the second buckling modes.
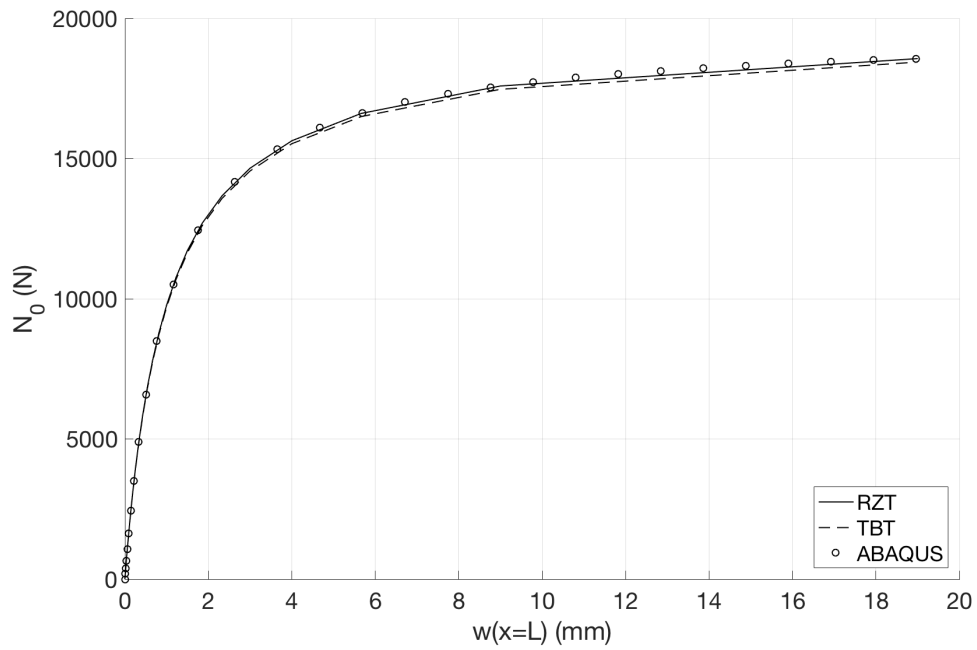
(a) *CF*
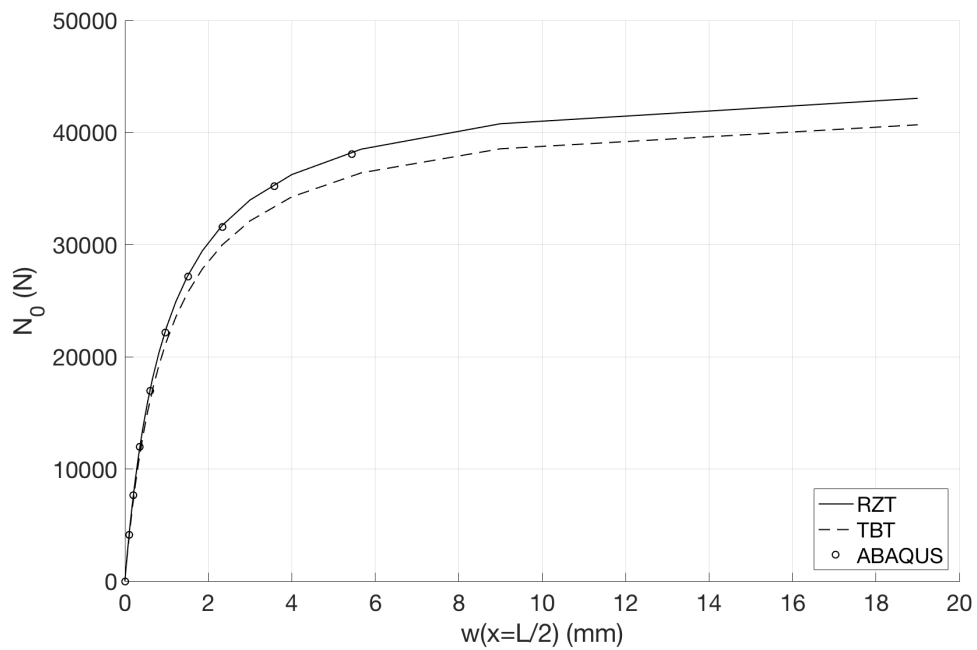
(b) *SS*

Figure 4.9: Load-displacement equilibrium path for the WF-32-5 sandwich beam with the initial imperfection corresponding to the first buckling mode.
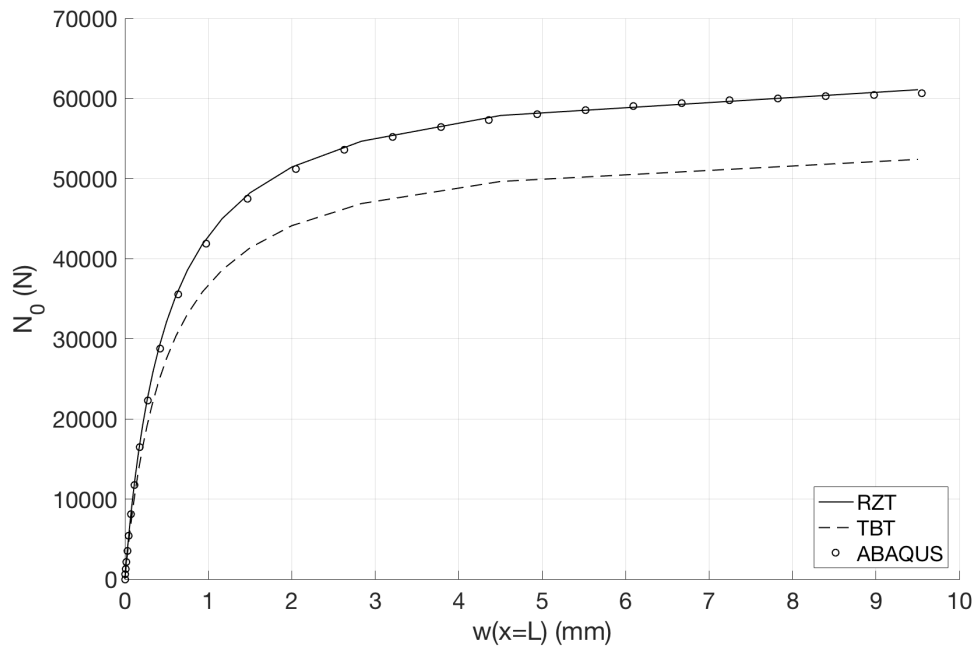
(a) *CF*
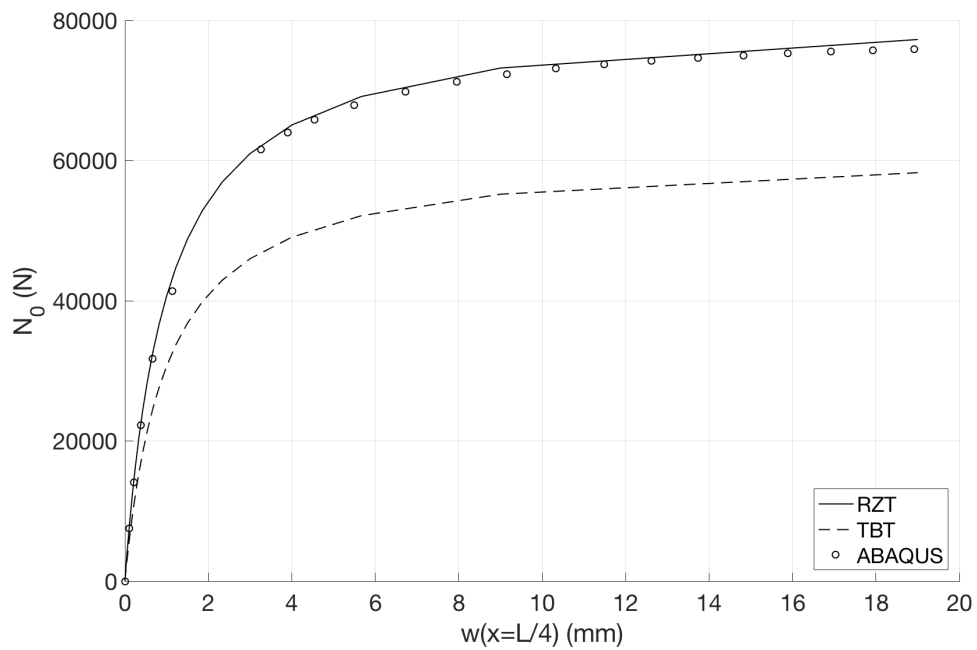
(b) *SS*

Figure 4.10: Load-displacement equilibrium path for the WF-32-5 sandwich beam with the initial imperfection corresponding to the second buckling mode.
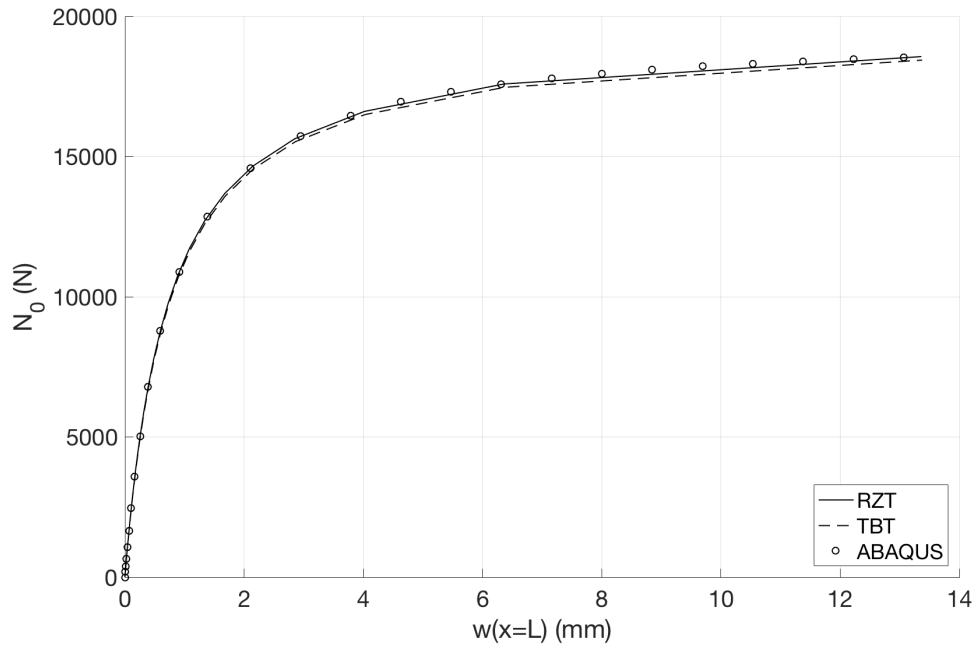
(a) *CF*
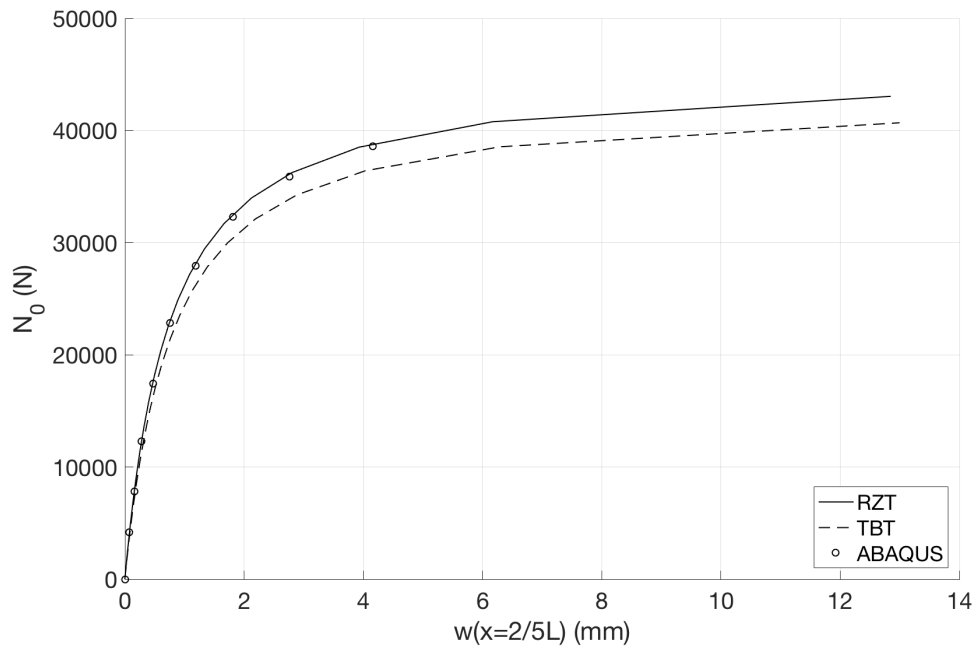
(b) *SS*

Figure 4.11: Load-displacement equilibrium path for the WF-32-5 sandwich beam with the initial imperfection corresponding to ta linear combination of the first and the second buckling modes.

85
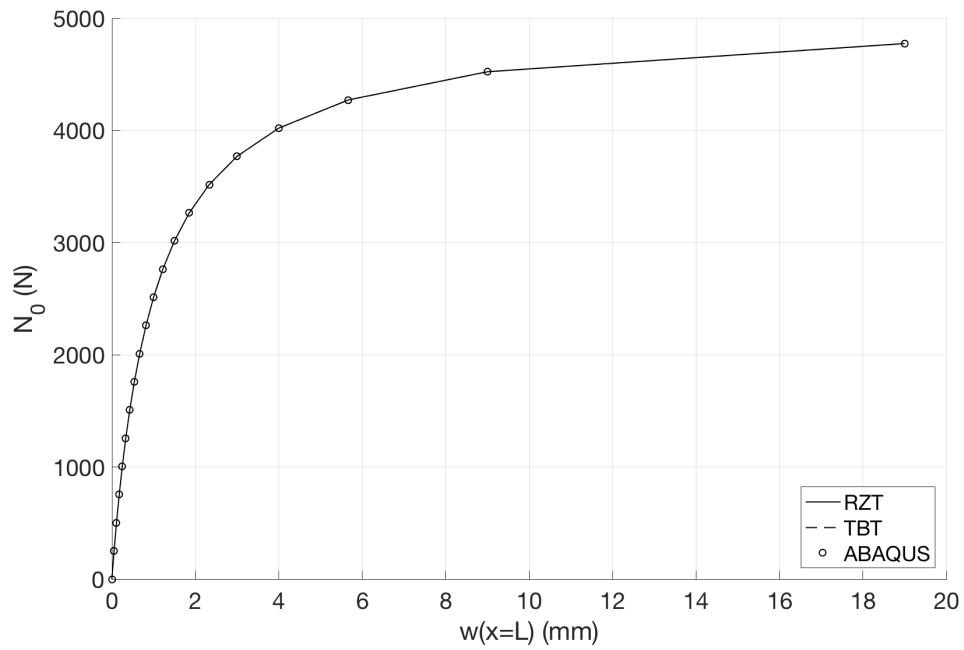
(a) *CF*
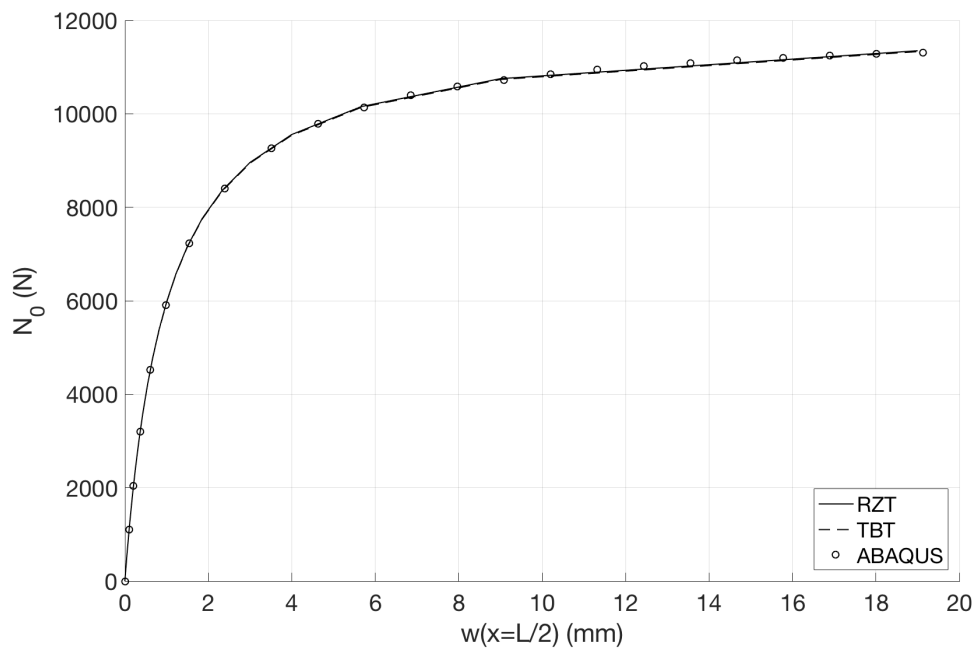
(b) *SS*

Figure 4.12: Load-displacement equilibrium path for the IG-96-2 sandwich beam with the initial imperfection corresponding to the first buckling mode.
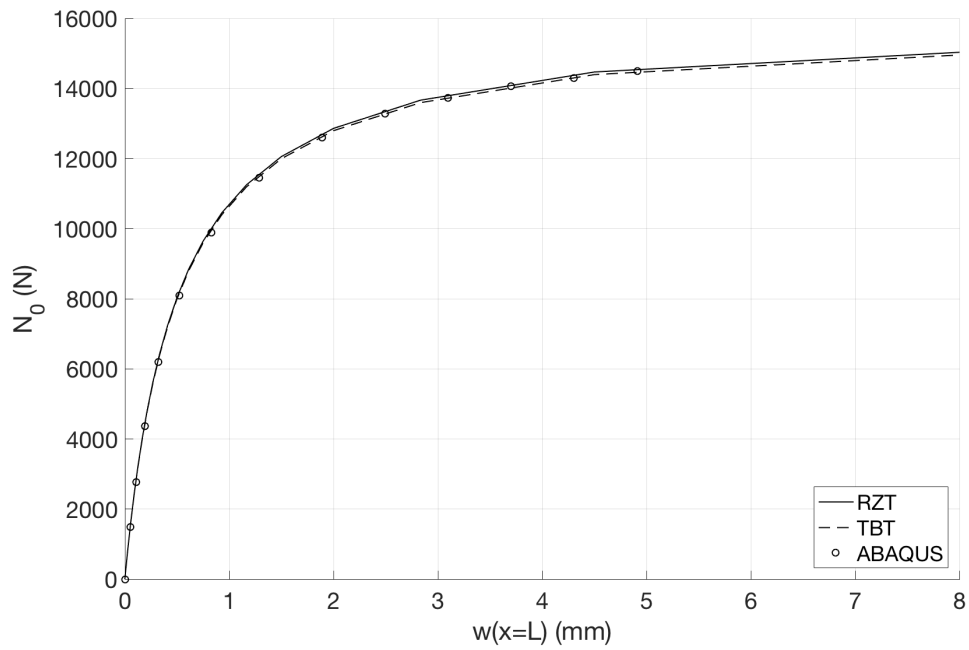
(a) *CF*
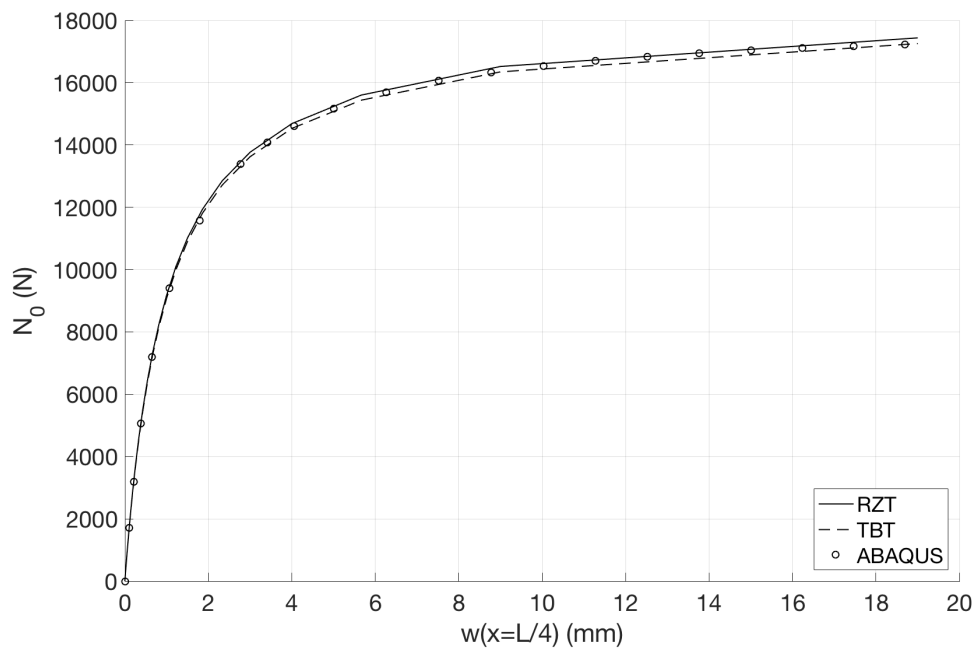
(b) *SS*

Figure 4.13: Load-displacement equilibrium path for the IG-96-2 sandwich beam with the initial imperfection corresponding to the second buckling mode.
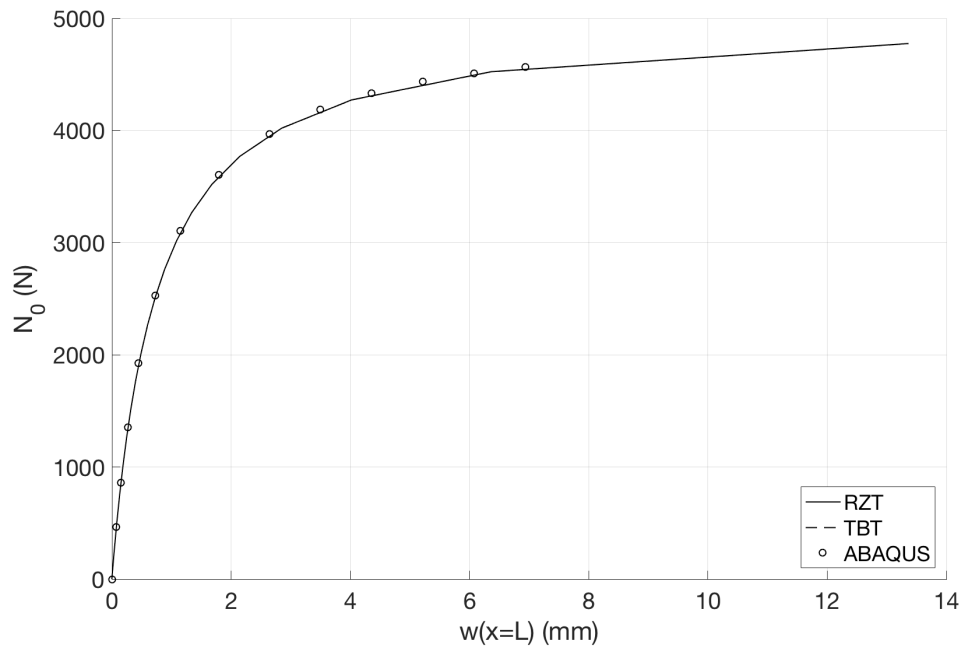
(a) *CF*
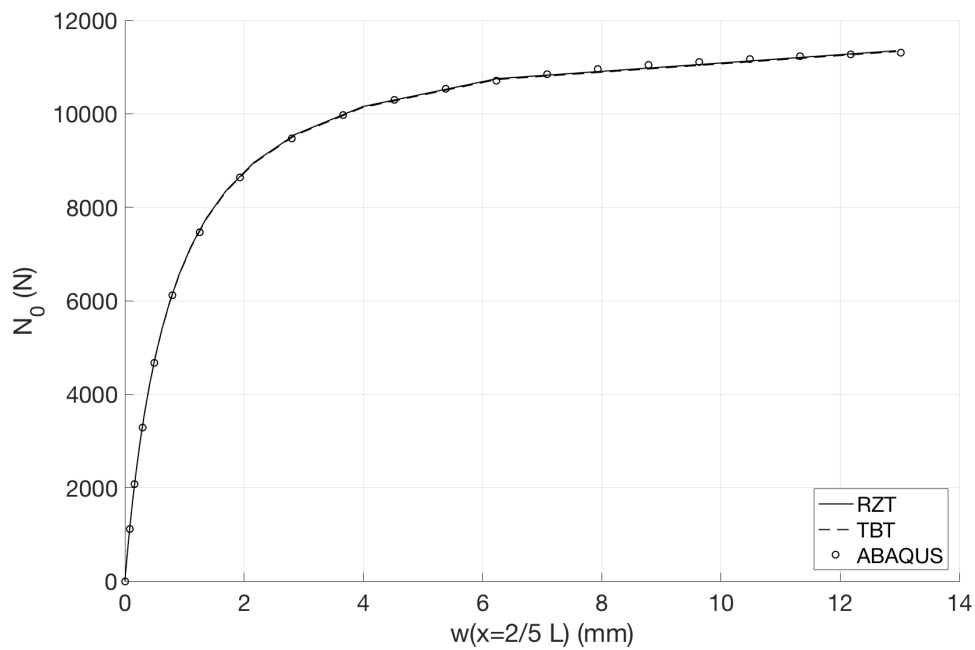
(b) *SS*

Figure 4.14: Load-displacement equilibrium path for the IG-96-2 sandwich beam with the initial imperfection corresponding to a linear combination of the first and the second buckling modes.

	Buckling Analysis				Nonlinear Analysis			
	RZT		ABAQUS		RZT		ABAQUS	
	SS	CF	SS	CF	SS	CF	SS	CF
IG-32-5	0.64	0.64	9.4	11	9.10	9.00	267	130
WF-32-5	0.64	0.64	9.5	11	9.10	9.00	267	130
IG-96-2	0.42	0.42	80	80	9.70	9.20	315	302

Table 4.6: Time (s) required by RZT and Abaqus for performing the buckling and the nonlinear analyses of the sandwich beams in simply-supported and cantilever configurations.

The load-deflection equilibrium paths in Figs.[4.6-4.14] report the transversal deflection of a single point on the beam axis as function of the applied load. To further verify the RZT accuracy, the deformed shape of the IG-32-5 has been compared to the transversal deflection of all points on the beam axis of the Abaqus two-dimensional model.

In order to prove the RZT capabilities in general conditions, the IG-32-5 with the initial imperfection corresponding to the linear combination of the first and second buckling modes has been chosen. The IG-32-5 is the beam with the lowest slenderness ratio and the biggest differences in the material properties, thus it is the most challenging problem. The deformed shapes for different values of applied load are reported in Figs.[4.15a-4.19a] for cantilever boundary conditions and in Figs.[4.15b-4.19b] for simply-supported boundary conditions. In Figs.[4.15a-4.15b] the applied load is $N_0 = 0$, thus the deformed shape corresponds to the initial imperfection. In Figs.[4.16-4.19] the applied load is, respectively, 25%, 45%, 66%, and 89% of the critical buckling load N_{cr}.

The perfect match between the Abaqus and the RZT deformed shapes demonstrate that RZT is highly accurate for the calculation of the nonlinear response, even for highly heterogeneous beams subjected to compressive loads very close to the critical buckling value, where the influence of the nonlinearities is predominant.
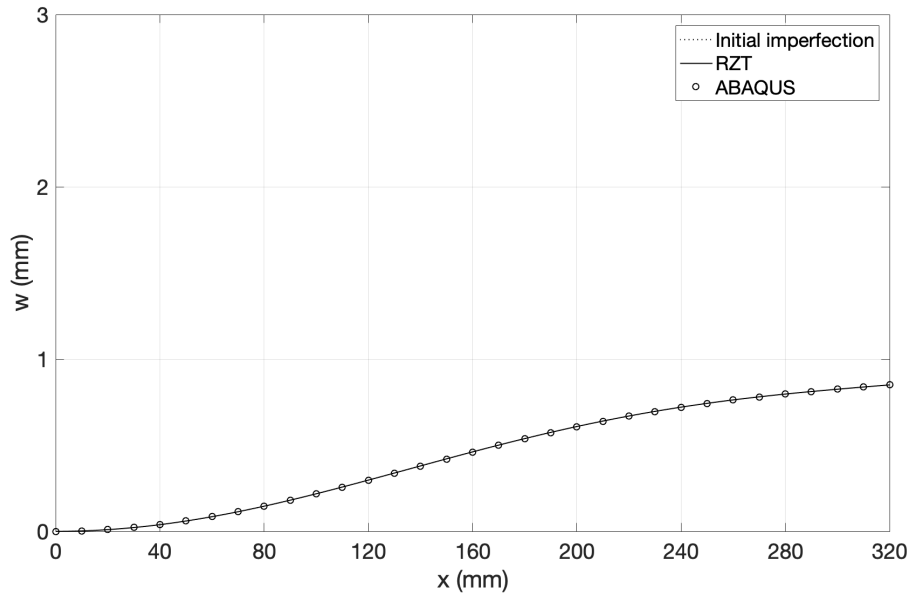
(a) *CF*
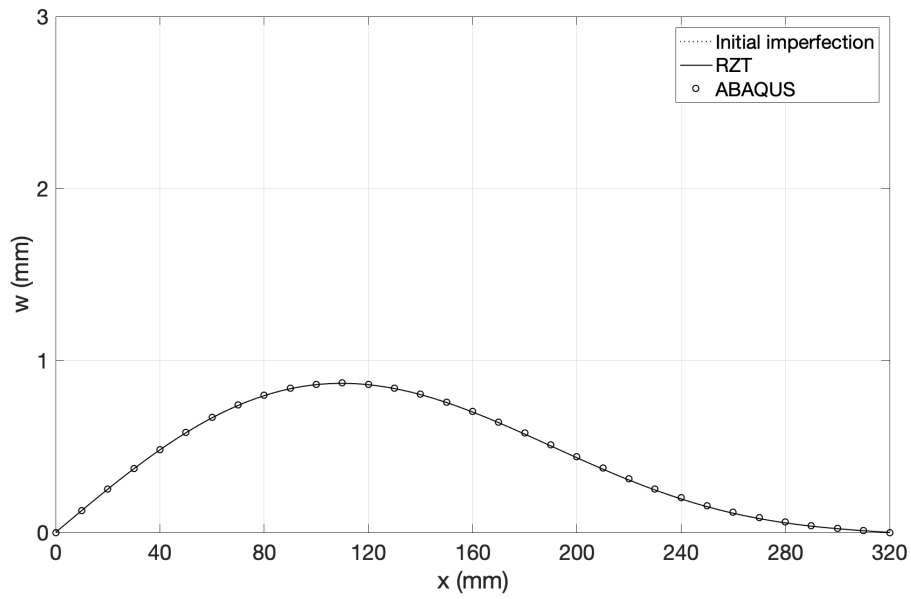
(b) *SS*

Figure 4.15: Deformed shape of the IG-32-5 with an initial imperfection corresponding to a linear combination of the first and the second buckling modes and for $N_0 = 0$.
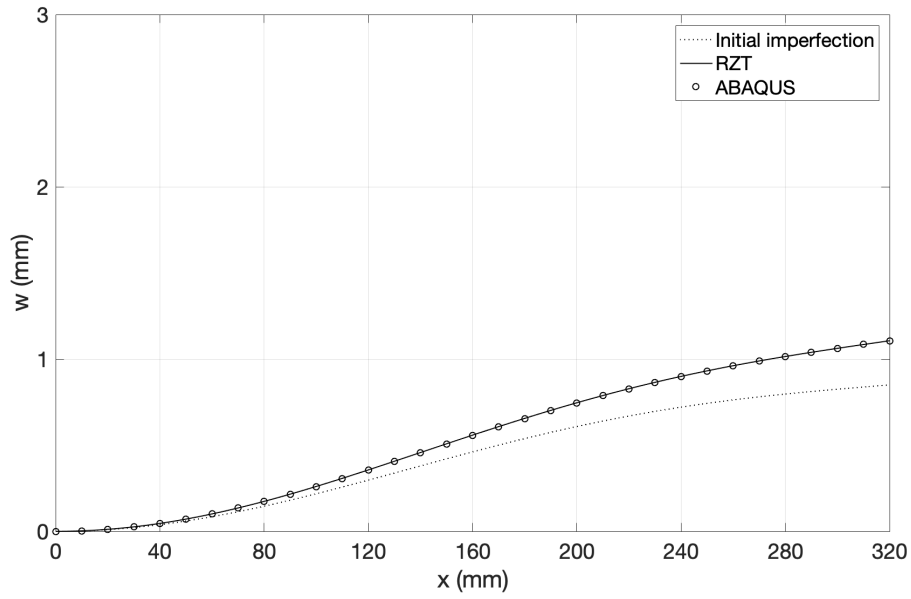
(a) *CF*
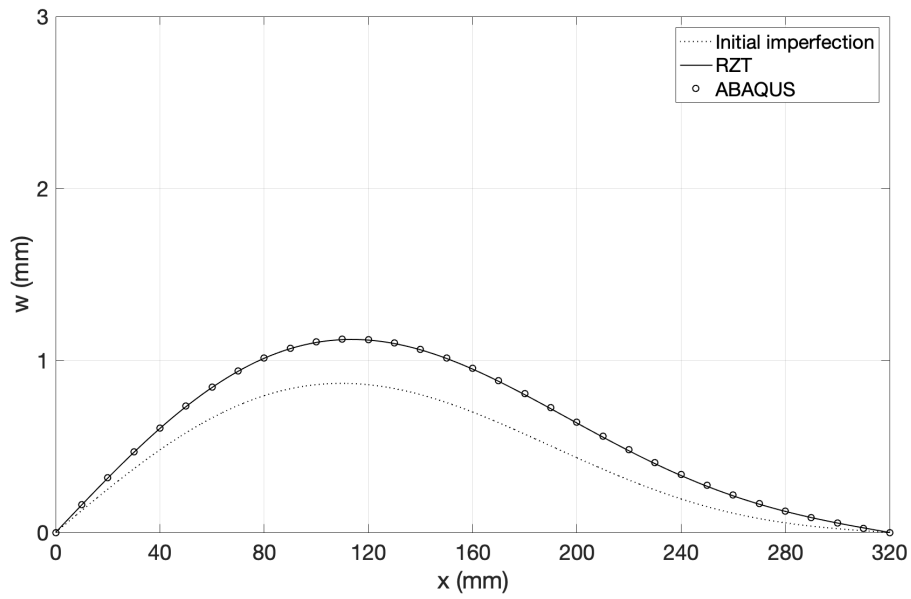
(b) *SS*

Figure 4.16: Deformed shape of the IG-32-5 with an initial imperfection corresponding to a linear combination of the first and the second buckling modes and for $N_0 = 0.25 N_{cr}$.
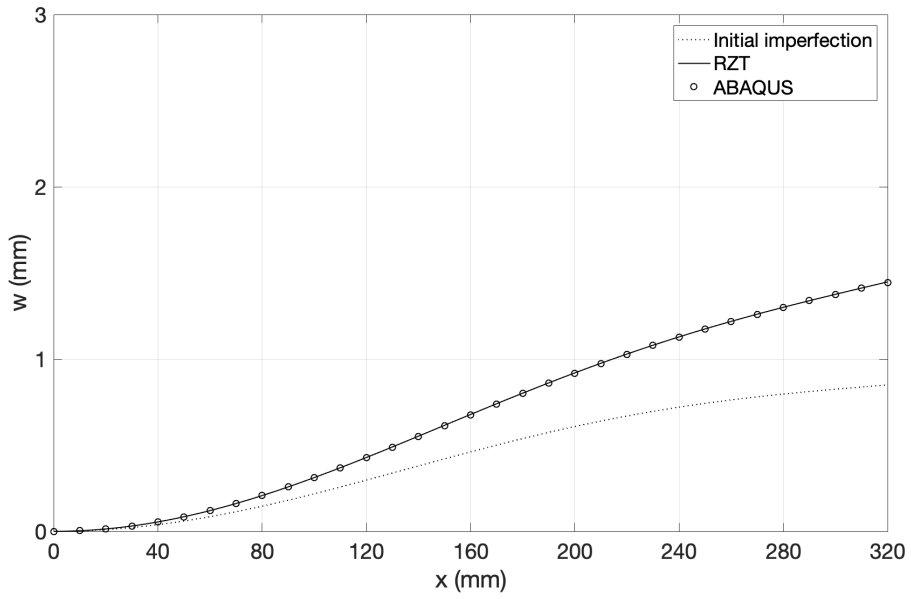
(a) *CF*
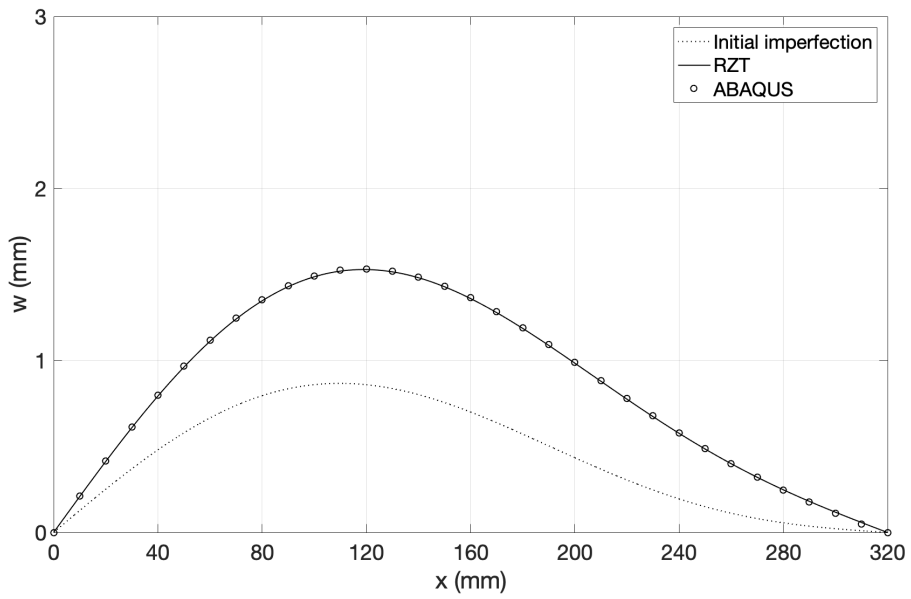
(b) *SS*

Figure 4.17: Deformed shape of the IG-32-5 with an initial imperfection corresponding to a linear combination of the first and the second buckling modes and for $N_0 = 0.45 N_{cr}$.
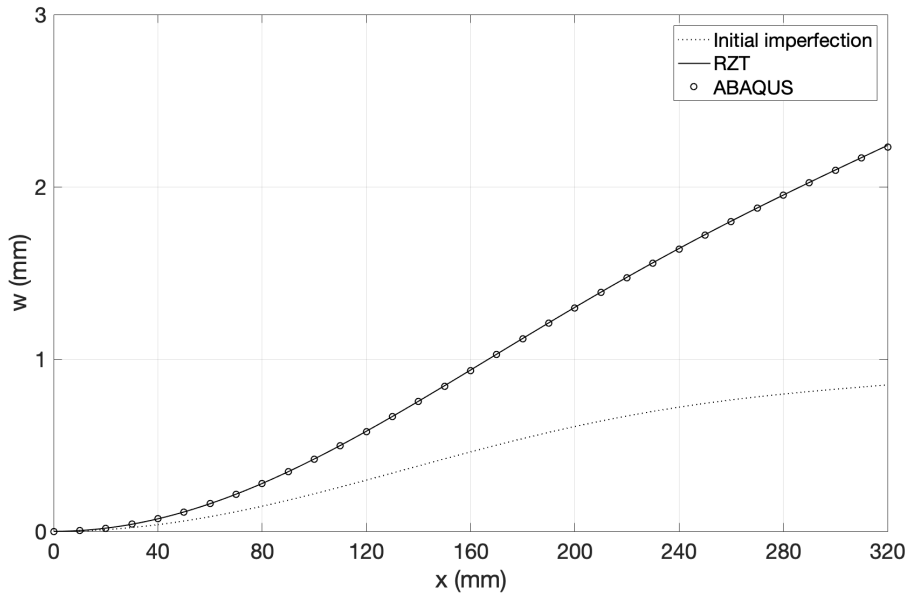
(a) *CF*
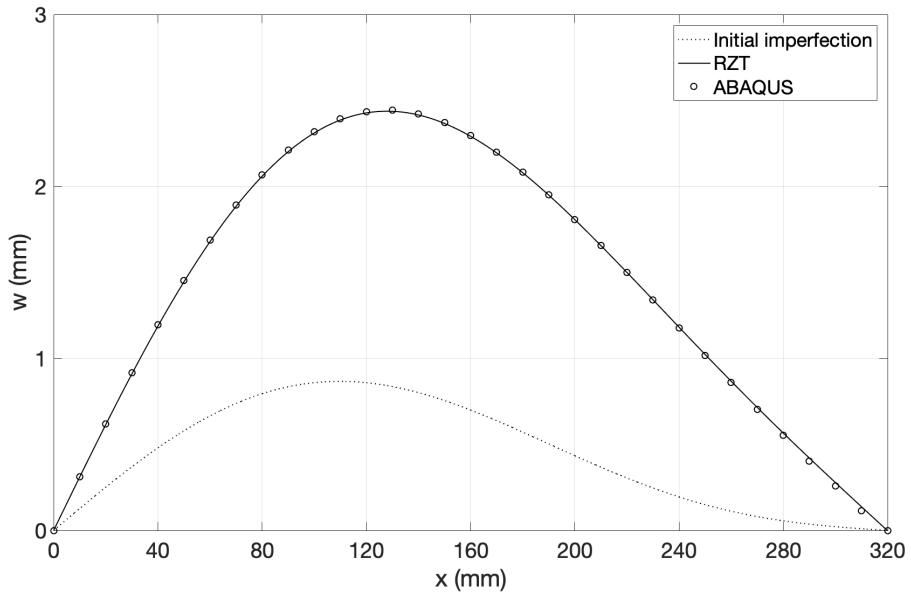
(b) *SS*

Figure 4.18: Deformed shape of the IG-32-5 with an initial imperfection corresponding to a linear combination of the first and the second buckling modes and for $N_0 = 0.66N_{cr}$.
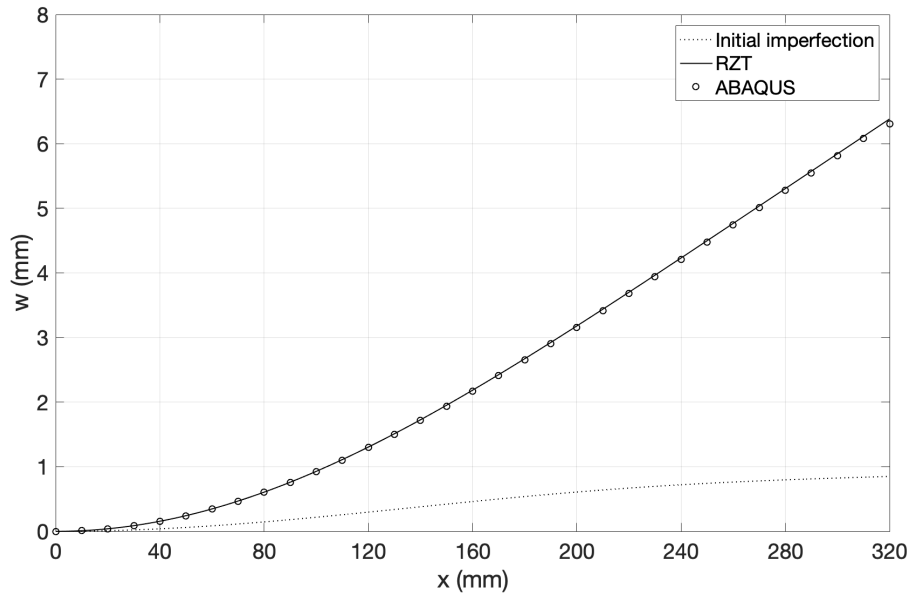
(a) *CF*
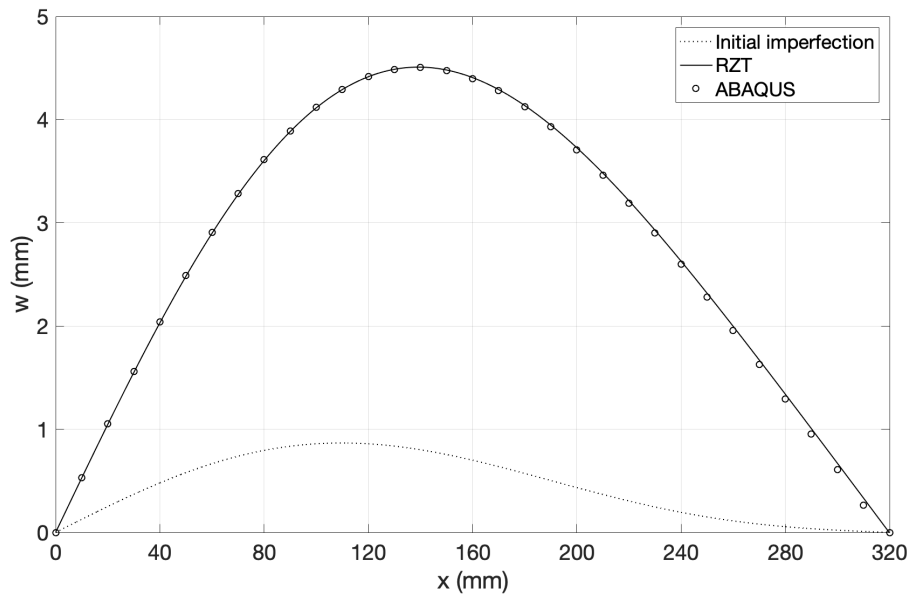
(b) *SS*

Figure 4.19: Deformed shape of the IG-32-5 with an initial imperfection corre-sponding to a linear combination of the first and the second buckling modes and for $N_0 = 0.89 N_{cr}$.

4.3 Nonlinear static and buckling analyses of composite beams with piezoelectric actuators

In this section, the finite element model based on the nonlinear RZT is employed for the buckling and nonlinear static analyses of composite multilayer beams with piezoelectric actuator patches bonded to the beam external surfaces.

In practical applications, the piezoelectric actuators can be used to reduce the beam initial deflection, making the beam axis closer to a straight configuration, in order to increase the critical buckling load. The presence of discrete elements on the beam surface, like the actuator patches, introduces a local change in the material and thickness properties. These geometrical discontinuities can be correctly modelled by the RZT using the strategy based on the Lagrange multipliers method described in 3.6.

The new RZT-FE model is assessed comparing the results and the corresponding computational cost to those obtained by equivalent Abaqus models. In Abaqus, the usual way to model piezoelectric actuator patches is by using solid elements because the piezoelectric properties can be attributed to them, thus three-dimensional models are necessary when the piezoelectric behaviour is considered.

The buckling loads and the nonlinear response to a compressive force are calculated for five composite beams with piezoelectric patches by both the RZT and the Abaqus finite element models. Various geometries and patch locations are considered to demonstrate the validity of the RZT predictions in general situations and to show its advantages in terms of computational cost. These two kinds of analyses do not involve the piezoelectric effect because the patches are not activated, but only the mechanical behaviour is considered. Then the same models but with piezoelectric finite elements are used to evaluate the beam transversal deflection due to the voltage applied to the actuators to verify the RZT predictions. The results reported in this chapter have been also validated experimentally, as shown in the following chapter.

4.3.1 Finite element models of the composite beams with piezoelectric actuators

The five beams are made of four Carbon Fibre Reinforced Polymer (CFRP) material layers, in either cross-ply symmetric, [0°/90°/90°/0°], or anti-symmetric, [90°/0°/90°/0°], orientation. The names and geometrical properties of the beams are indicated in Table [4.7]. As shown in Fig.[4.20], simply-supported boundary conditions are considered and one or two piezoelectric patches are bonded to the external surfaces of each beam. The location of the actuators is expressed by the distance between the hinged edge of the beam and the first section of the patch, indicated as l_a or l_b in Table [4.7].

Beam	L (mm)	b (mm)	h (mm)	Ply orientations	l_a (mm)	l_b (mm)
BPZT1	298.0	20.83	0.65	[0°/90°/90°/0°]	99.0	-
BPZT2	299.0	23.03	0.73	[90°/0°/90°/0°]	99.5	-
BPZT3	447.5	21.46	0.72	[0°/90°/90°/0°]	143.0	-
BPZT4	448.0	22.59	0.75	[90°/0°/90°/0°]	143.5	-
BPZT5	448.5	22.24	0.78	[90°/0°/90°/0°]	63.0	286.0

Table 4.7: Beams geometrical properties, material orientation and actuators location.
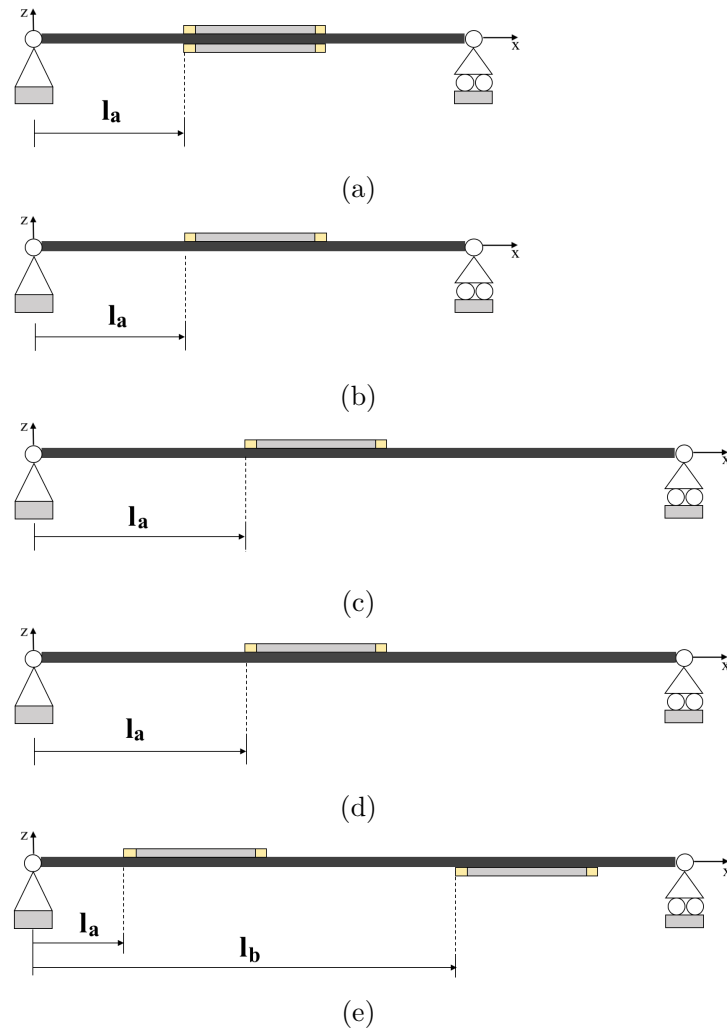
Figure 4.20: Composite beams with piezoelectric actuators patches: (a) beam BPZT1, (b) beam BPZT2 (c) beam BPZT3 (d) beam BPZT4 (e) beam BPZT5.

The beam BPZT1 has two actuators located symmetrically with respect to the mid-plane, one on the top and one on the bottom surface of the beam, at a distance l_a from the hinged edge. The BPZT2, BPZT3 and BPZT4 have only one actuator on the top surface whereas the beam BPZT5 has two actuators, one on each side of the beam, distant, respectively, l_a and l_b from the hinged edge. The actuator on the top surface of the BPZT3 makes the lamination anti-symmetric, thus the BPZT1 is the only symmetric beam.
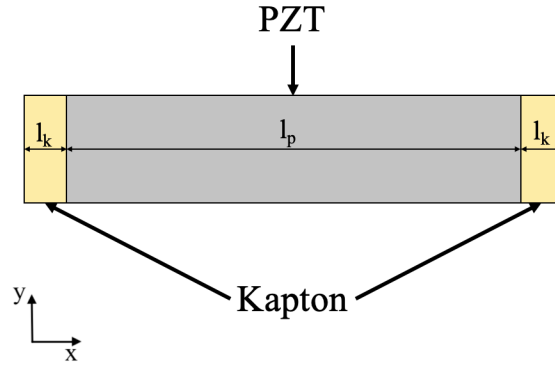
Figure 4.21: Model of the piezoelectric actuator patch.

The Macro Fiber Composite (MFC) M8514-P1 piezoelectric transducer has been taken as reference for the actuator modelling because they are the actuators used for the experimental assessments. The patch is modelled as Fig.[4.21], with two external parts made of Kapton and long $l_k = 8$ mm, and the internal area made of piezoelectric material whose length is $l_p = 85$ mm. The thickness is $h_p = 0.3$ mm, while the width is assumed to be the same of the beam on which the patch is bonded, since the RZT cannot model any variations of width along the thickness. The mechanical and electrical properties of the materials are reported in Table [4.8][4]. The properties of the CFRP correspond to those of carbon/epoxy unidirectional prepregs VTM264-T700 (35% of resin content, Advanced Composites Group); the characteristics of the Kapton and the piezoelectric materials are those indicated in the MFC transducer datasheets [125].

Fig.[4.22] outlines the type of geometrical interfaces introduced by the actuators. The BPZT1 has four discontinuities indicated by i_k ($k = 1,2,3,4$) for the change of lamination due to the actuators. Two interfaces, the i_1 and the i_4, correspond to

---

[4]The piezoelectric coefficient indicated in Table [4.8] is the d_{33} because the operational mode of the MFC P1-type actuators is the d_{33}-*effect*. The d_{33}-*effect* refers to a different behaviour from the one considered in the RZT model, the e_{31}-*effect*. The way this difference has been taken into account will be explained in Section 4.3.4.

CFRP-VTM264		Piezoelectric		Kapton	
E_1 (MPa)	120,000	E_1 (MPa)	30,340	E (MPa)	2,500
E_2 (MPa)	7,500	E_2 (MPa)	15,860	ν	0.34
E_3 (MPa)	7,500	E_3 (MPa)	15,860		
G_{12} (MPa)	3,900	G_{12} (MPa)	5,510		
G_{13} (MPa)	3,900	G_{13} (MPa)	5,510		
G_{23} (MPa)	2,300	G_{23} (MPa)	5,510		
ν_{12}	0.32	ν_{12}	0.31		
ν_{13}	0.16	ν_{13}	0.16		
		d_{33} (m/V)	4.6×10^{-10}		
		χ_{33} (F/m)	1.64×10^{-8}		

Table 4.8: Mechanical properties of the materials of the beams and actuators.

the sections between the *beam-only* part (part of the beam without the patch) and the regions of the beam with Kapton layers bonded to the external surfaces. The interfaces i_2 and i_3 correspond to the sections between the part of the beam with Kapton layers and the part of the beam with piezoelectric layers on the external surfaces.
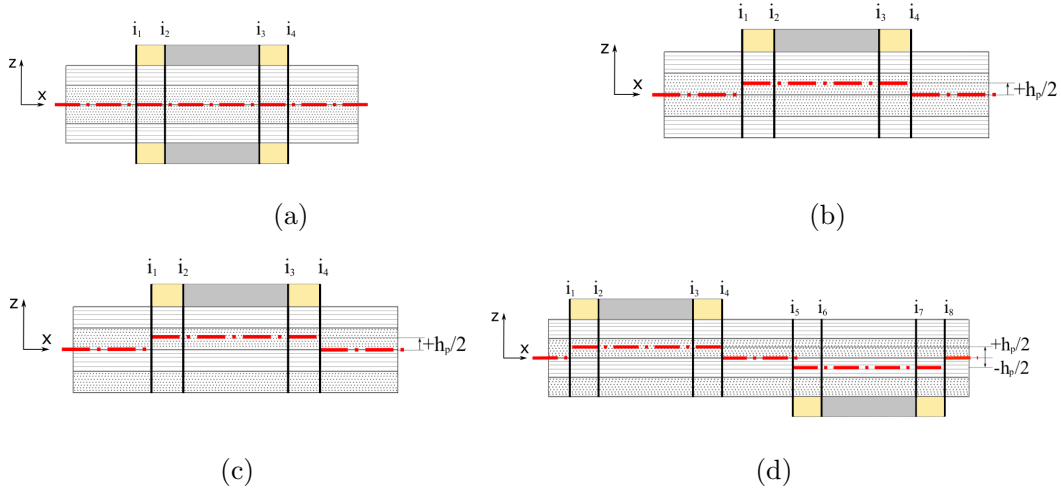
Figure 4.22: Geometrical discontinuities and corresponding offsets due to the actuator patches: four interfaces for (a) the BPZT1, (b) the BPZT3 and (c) the BPZT2 and BPZT4; (d) eight interfaces for the BPZT5.

The BPZT(2-4) have four interfaces too, whereas the BPZT5 has eight interfaces (i_k, $k = 1, 2, \ldots, 8$). In the BPZT(2-5), the use of only one actuator or two actuators not symmetrically located on the top and bottom surfaces of the beam, changes

the half-thickness axis location, thus, at the interfaces, there are both a change of material lamination and an offset of the half-thickness axis. The offset value is given by the distance between the half-thickness axis and the $x-$axis and it is positive for $z > 0$. The offset of the part of the beam with an actuator bonded to the top surface corresponds to $+h_p/2$ (for the BPZT(2-4) and the first actuator of BPZT5), whereas the offset of the actuator bonded to the bottom surface of the BPZT5 is $-h_p/2$.

Each beam can be considered as divided in different parts between two consecutive geometrical interfaces (including the sections at beam edges) characterised by the same material and geometrical properties. The BPZT(1-4) are then constituted of five parts while the BPZT5 is made of nine parts.

The number of RZT finite elements has been set taking into account the discontinuities along the beam length by considering a node at each interface. In addition, the shortest parts on the beams are those with the Kapton layers and they are $l_k = 8$ mm, thus 8 mm is the maximum length the elements can have to guarantee a uniform mesh. The buckling and postbuckling analyses have been performed several times increasing the number of finite elements by progressively reducing the element average length. It has been verified that there are not appreciable differences between the solutions obtained for a mesh with elements 2 mm long and the solutions with smaller elements, thus the average length of the finite elements considered in the RZT models is 2 mm.
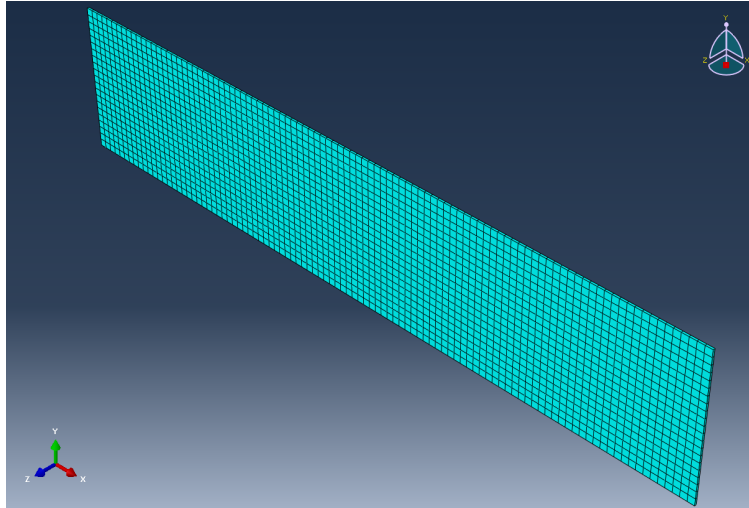
Figure 4.23: Abaqus finite element model of the piezoelectric actuator using 3D elements.

The mesh of the three-dimensional Abaqus models has been realised using continuum shell elements (SC8R type) for the *beam-only* parts, whereas 3D stress

elements (C3D8/C3D8E type) have been used for the actuator patches. Two finite elements has been set along the z-coordinate in order to have a minimum number of three nodes along the beam thickness. The average dimensions of the continuum shell elements are then $1 \times 1 \times h$ mm^3, where h is half thickness of the beam considered. Fig.[4.23] shows the mesh of the actuator part of the Abaqus models; only one element has been considered along the actuator thickness direction, thus the average dimensions of the finite elements are $1 \times 1 \times h_p$ mm^3.

The resulting number of nodes and finite elements for both the RZT and the Abaqus models are indicated in Tables [4.9-4.10], specifying the values of both the individual and the assembled parts for the Abaqus models. The numbers of nodes and elements of the actuator part of the BPZT1 and the BPZT5 refer to one actuator only.

	No. of nodes			
	ABAQUS			**RZT**
	Beam	Actuator	total	
BPZT1	19,800	4,488	28,776	145
BPZT2	21,672	4,896	26,568	145
BPZT3	29,634	4,488	34,122	223
BPZT4	32,400	4,896	37,296	225
BPZT5	31,050	4,692	40,434	219

Table 4.9: Number of nodes of the Abaqus and the RZT models.

	No. of elements			
	ABAQUS			**RZT**
	Beam	Actuator	total	
BPZT1	12,558	2,121	16,800	144
BPZT2	13,800	2,323	16,123	144
BPZT3	18,816	2,121	20,937	222
BPZT4	20,654	2,323	22,977	224
BPZT5	19,756	2,222	24,200	218

Table 4.10: Number of finite elements of the Abaqus and the RZT models.

A tie constraint is used to connect the patch to the beam surfaces in the Abaqus

models. The simply-supported boundary conditions have been defined at the half-thickness nodes of the beam edges while compressive concentrated forces have been applied to all the nodes at the supported edge. A representation of the Abaqus models for all the beams can be found in Figs.[4.24].
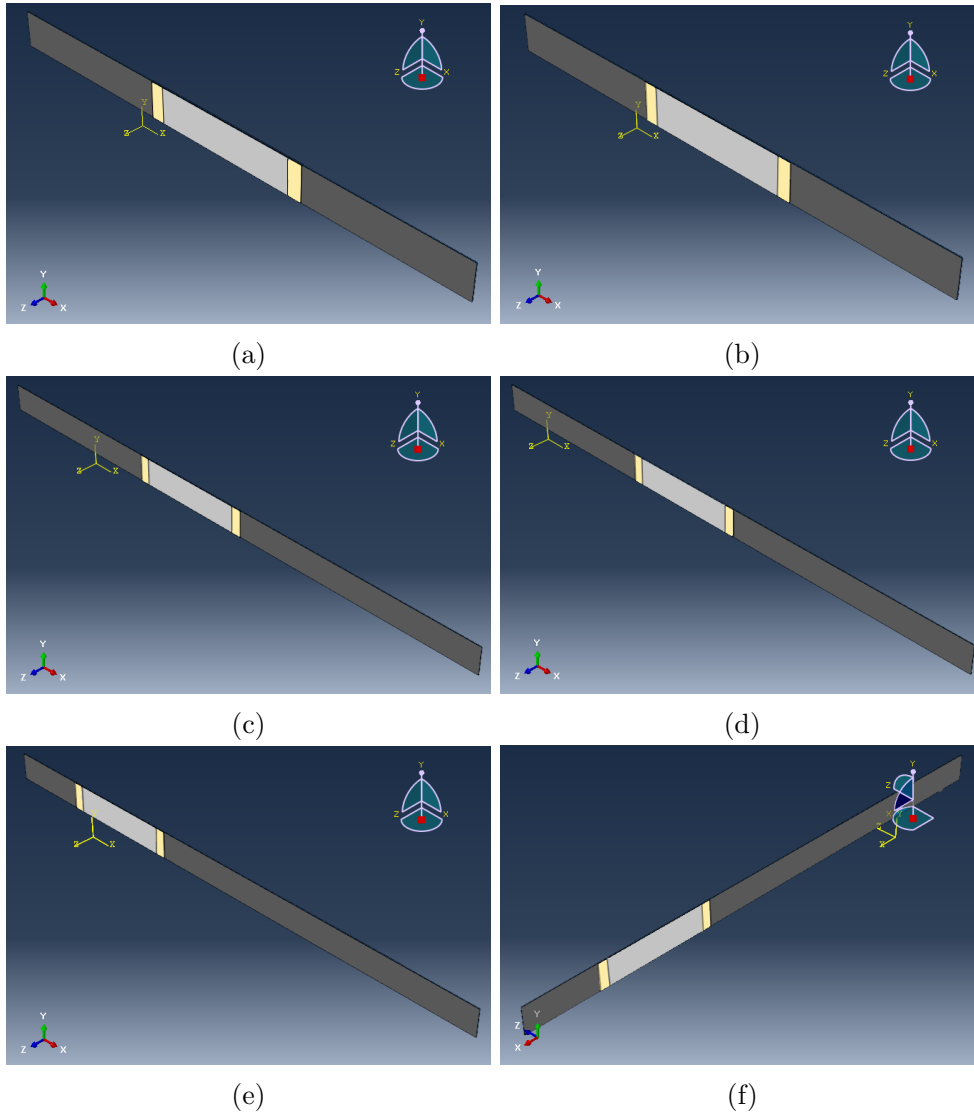
Figure 4.24: Abaqus models: (a) BPZT1, (b) BPZT2, (c) BPZT3, (d) BPZT4, (e) top surface of the BPZT5 and (f) bottom surface of the BPZT5.

4.3.2 Buckling analysis of the composite beams with piezoelectric actuators

The RZT buckling loads have been calculated solving the eigenvalue problem of Eq.[3.110] in 3.4.1. In Abaqus, C3D8 elements have been considered for the actuators because the piezoelectric behaviour is not involved in the buckling analysis. Axial-compressive forces of the same intensity have been applied to the nodes at the supported edge and their sum is equal to 1 N, thus the eigenvalues correspond to the actual buckling loads.

The first two buckling loads calculated with Abaqus and RZT are reported in Table [4.11]. The percentage deviation of the RZT with respect to Abaqus is always less than 3%, with values higher than 2% only for the BPZT5, which is the beam with the highest anti-symmetry because of both the beam lamination and the patch locations.

Beam	ABAQUS (N)	RZT (N)	Δ %
BPZT1	8.56	8.40	-1.88
	24.61	24.40	-0.86
BPZT2	6.00	5.90	-1.71
	19.08	18.90	-0.92
BPZT3	4.07	4.00	-1.65
	14.57	14.47	-0.67
BPZT4	2.56	2.52	-1.41
	8.97	8.90	-0.80
BPZT5	2.92	2.85	-2.62
	14.46	14.07	-2.67

Table 4.11: Buckling loads of composite beams with piezoelectric actuators.

The remarkable advantage of the RZT is in the computational effort because the time to run the buckling analysis in Matlab for the RZT model is of just 3 s while in Abaqus it is ten times bigger, being 30 s on average.

4.3.3 Nonlinear response of the composite beams with piezoelectric actuator patches subjected to a compressive force

The nonlinear response to a compressive load acting at the supported edge is calculated for both the RZT and the Abaqus models. The actuators are imagined

102

to be disconnected from any power supply, thus the piezoelectric behaviour has not been taken into account and C3D8 finite elements have been used for the actuators parts in Abaqus. An initial geometric imperfection is considered for each beam introducing it as a linear combination of the buckling modes of the beam without imperfections.

In the RZT, the function $w^*(x)$ describes the imperfection distribution and it is defined by the following linear combination of the first three buckling modes:

$$w^*(x) = a_1 \cdot sin\left(\frac{\pi x}{L}\right) + a_2 \cdot sin\left(\frac{2\pi x}{L}\right) + a_3 \cdot sin\left(\frac{3\pi x}{L}\right). \qquad (4.3)$$

The coefficients a_k of the linear combination are different for each beam, and they are indicated in Table [4.12][5]. The same values have been used in Abaqus to define the imperfection as a linear combination of the buckling modes calculated in previous analyses.

	BPZT1	BPZT2	BPZT3	BPZT4	BPZT5
a_1	1.66	3.97	1.60	8.62	9.24
a_2	0.10	0.19	0.76	-0.15	-0.36
a_3	0.27	0.30	0.22	0.72	0.46

Table 4.12: Coefficients of the linear combination approximating the imperfection function.

The nonlinear response of the beams increasing the compressive load, N_0, from $N_0 = 0$ to $N_0 = 0.99N_{cr}$ is shown in Figs.[4.25-4.29] for both the RZT and the Abaqus models. An almost perfect match between the two solutions can be observed for the BPZT(1-4) in Figs.[4.25]-[4.28] for values of N_0 up to $N_0 = 0.5N_{cr}$. Moreover, the RZT is remarkably precise for the BPZT1 and the BPZT3 (Figs.[4.25]-[4.27]), even for higher values of N_0 and very close to the critical buckling load. A slight difference can be observed, instead, for the BPZT2 and the BPZT4 when N_0 approaches N_{cr} but for all the beams BPZT(1-4) the RZT response indicates a softer behaviour than Abaqus when N_0 is close to N_{cr} (Figs.[4.25-4.28]).

By contrast, the RZT response for the BPZT5 in Fig.[4.29] indicates a stiffer behaviour of the beam than that predicted by Abaqus for any value of applied compressive load. This difference is probably due to the difference in the initial deflection of the RZT and the Abaqus models.

---

[5]The finite element models in this section reproduce the beams realised for the experiments presented in the following chapter. The values a_k are used to define the function $w^*(x)$ which approximates the initial deflection measured on the real beams.

Indeed, the initial deflection of the nodes on the beam axis in the two-dimensional Abaqus models does not perfectly correspond to the initial imperfection of the one-dimensional RZT models, because the imperfection has been introduced both in Abaqus and in RZT as a linear combination of the corresponding buckling modes. The same coefficients for linear combination have been considered in both cases, but Abaqus combines the buckling modes of a two-dimensional model whereas RZT combines the modes of a one-dimensional model. This results in an initial deviation of the BPZT(1-4) RZT models that is slightly higher than the Abaqus imperfection, leading to a moderately softer response. In the points where the response is calculated, the RZT initial deflection is only 0.2% higher than the Abaqus' for the BPZT1 and the BPZT3, whereas it is 0.9% and 0.8% higher than Abaqus for the BPZT2 and the BPZT4, respectively. The slightly higher mismatch between the initial deviations of the two models and also the non-symmetric beam lamination could explain the bigger difference in the RZT and Abaqus solutions for high values of N_0 in the response of the BPZT2 and the BPZT4.

On the other hand, the RZT model of the BPZT5 has an initial deflection that is 2.3% lower than the Abaqus imperfection in the same point, explaining the stiffer behaviour of the RZT. The high mismatch between the RZT and the Abaqus initial deflection for the BPZT5 is probably the cause of the discrepancy between the two solutions, bigger than the other cases.

Nevertheless, even if the two curves in Fig.[4.29] do not overlap perfectly for most of the load values considered, there is a very good agreement between in the initial-linear range with very similar changes in the curve slope. The RZT results are acceptable for both the buckling load values and the nonlinear response, even for this beam and it can be concluded that the RZT is able to correctly predict beam nonlinear behaviour of composite beams, even for anti-symmetric laminations and with with geometrical interfaces.
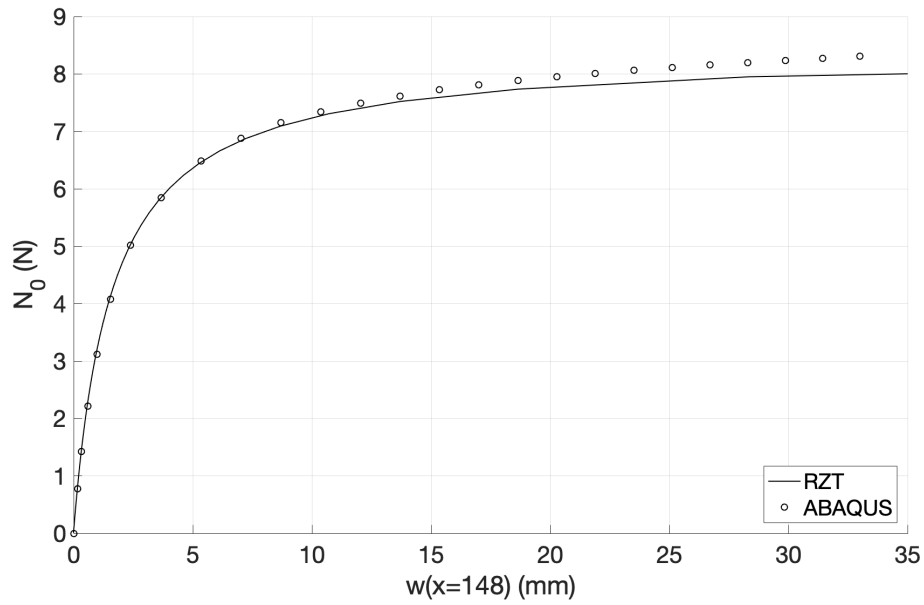
Figure 4.25: Load-displacement equilibrium path for the BPZT1.
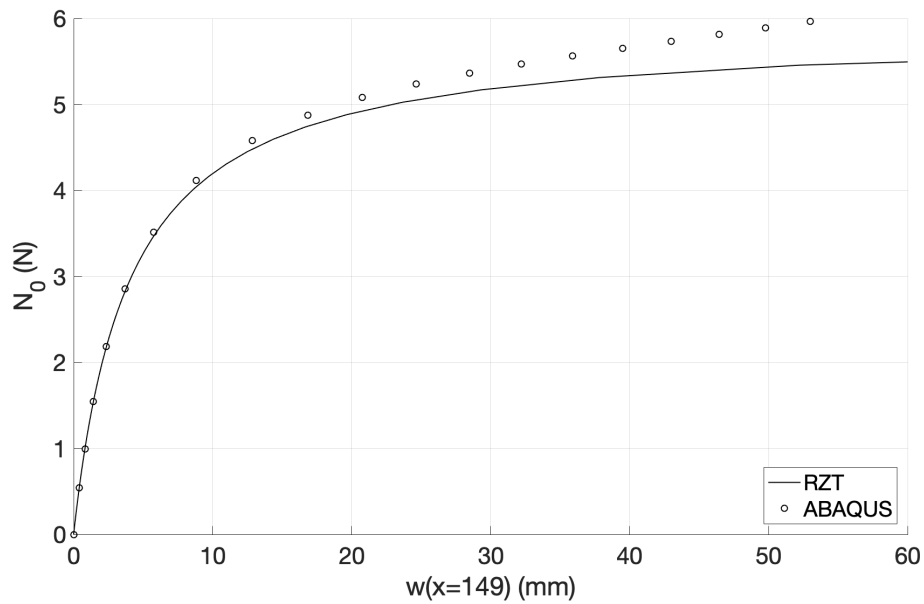
Figure 4.26: Load-displacement equilibrium path for the BPZT2.
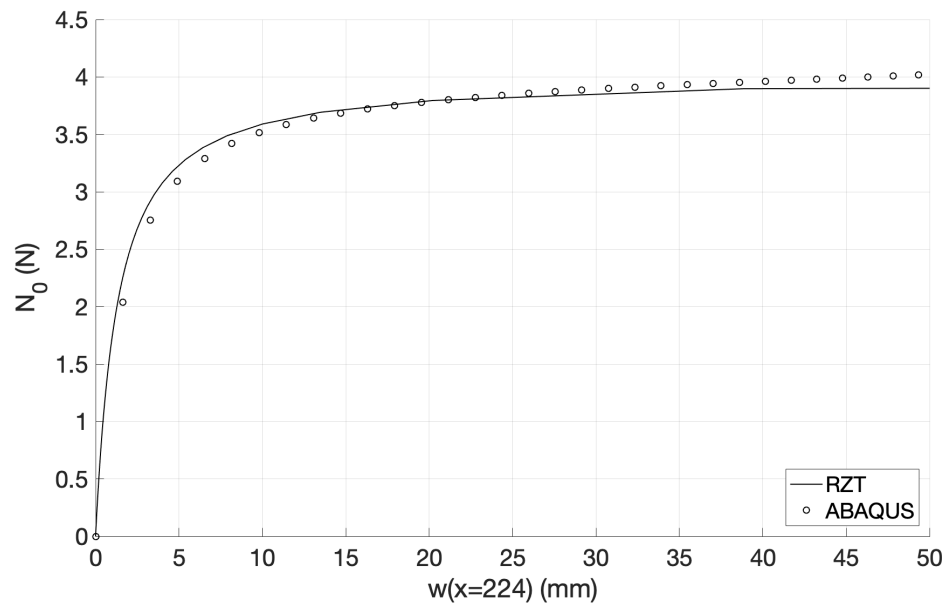
Figure 4.27: Load-displacement equilibrium path for the BPZT3.
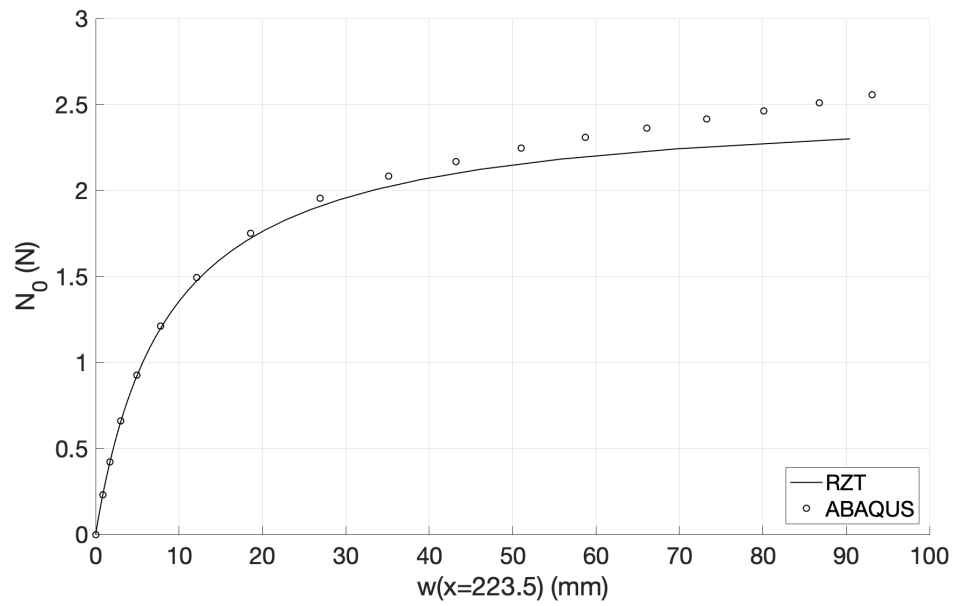
Figure 4.28: Load-displacement equilibrium path for the BPZT4.
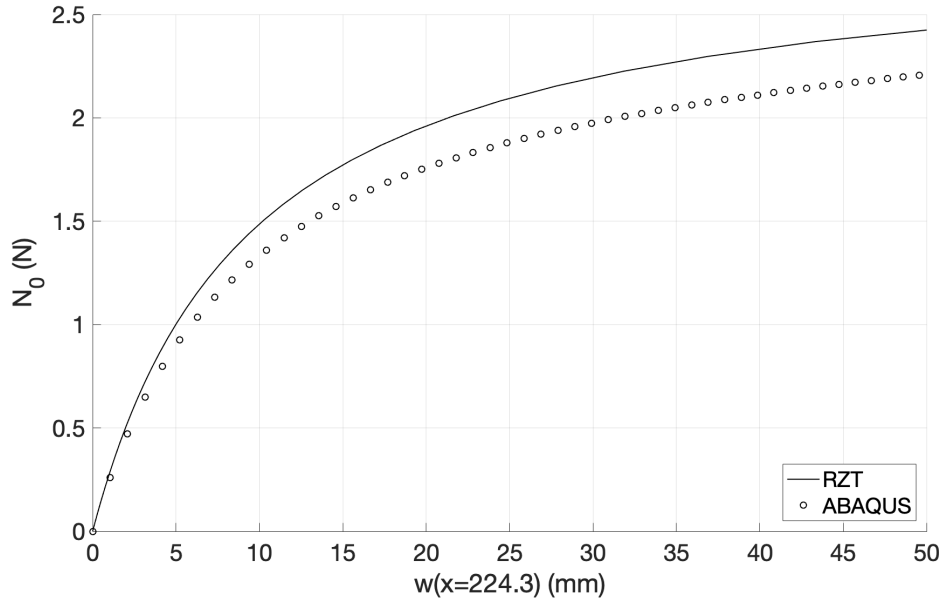
Figure 4.29: Load-displacement equilibrium path for the BPZT5.

This is the application where the RZT capabilities are best shown because, even for very slender beams and simple geometries, the computational cost significantly increases for the Abaqus solutions. The average time for the nonlinear analyses of the BPZT(1-4) is less than 1 minute for the RZT whereas it is 5 minutes for Abaqus. The BPZT5 analyses require more computational effort in both models, but the time is 80 s for RZT and 40 minutes for Abaqus. It is clear then even a small variation in the geometry complexity results in a higher computational cost, but while for RZT it slightly increases, in Abaqus it is ten times bigger than simpler geometries and it is obviously not acceptable when many analyses have to be performed. The actual time required for the buckling and postbuckling analyses of each beam using the RZT or the Abaqus model is reported in Table [4.13] at the end of the next section.

4.3.4   Model of the MFC-P1 actuators

The MFC multilayer structure allows a bigger elongation for the same applied voltage compared to the conventional configuration of piezoceramic actuators. Depending on the operational mode, two type of MFCs are available, the P1 and the P2 types [125]. The MFC-P1 type actuators have been chosen in this work because, for the same applied voltage, their elongation is double the MFC-P2 type contraction.
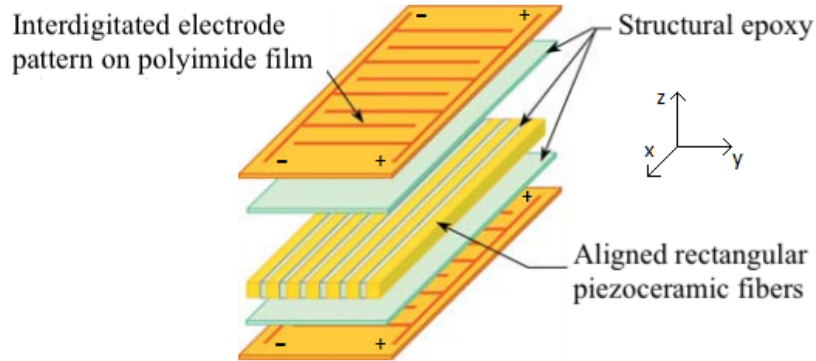
Figure 4.30: Structure of the MFC-P1 actuator [125].

Fig.[4.30] illustrates the structure of the MFC-P1 type piezoelectric transducers. They have an inner layer made of rectangular piezoceramic rods, aligned along their longitudinal direction and bonded to each other by a structural epoxy adhesive. The top and bottom layers are made of two interdigitated electrodes (IDE) bonded to the piezoceramic layer with the same epoxy adhesive used between the piezoceramic rods. The P1-MFC actuator operational mode is the d_{33} coupling, where the strain component and the electric field have the same direction indicated by the subscripts 3, that corresponds to fibre longitudinal direction ($x-$axis in Figs.[4.30-4.31]). The interdigitated electrodes are orthogonal to the piezoelectric rods which have an alternate polarisation along the longitudinal direction (see Fig.[4.31]). For this reason, when a positive voltage is applied to the IDEs, the electric field and the poling direction in each part of the piezoelectric fibres between two microelectrodes will have the same orientation and the fibres will expand.

The piezoelectric strain coefficient $d_{33} = 460 \times 10^{-12}$ m/V indicates the strain along x of a single portion of a piezoelectric rod between two consecutive microelectrodes for a unitary electric field component, E_3, along x and under a constant stress field.
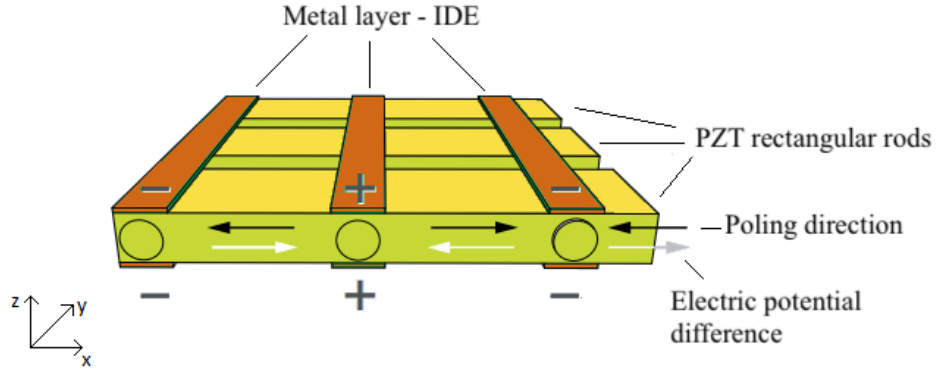
Figure 4.31: Operational mode of the MFC-P1 actuator [125].

In Chapter 3, the inverse piezoelectric behaviour is introduced in the RZT model considering the d_{31} coupling, where the electric field direction is orthogonal to the actuator axial strain. The two piezoelectric effects are compared in Fig.[4.32], with the d_{33} coupling on the left side and the d_{31} coupling on the right. It is clear that the design of the actuator defines the kind of coupling: the positive and negative electrodes have to be spaced along the piezoelectric longitudinal direction to realise a d_{33} coupling, whereas they have to be on the bottom and top surface of the piezoelectric patch to create an electric potential difference along the vertical direction to get a d_{31} coupling .
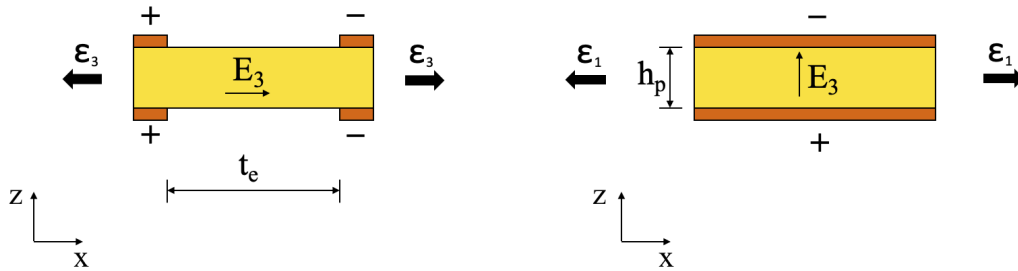
Figure 4.32: Comparison between the d_{33} piezoelectric coupling (on the left) and the d_{31} piezoelectric coupling (on the right).

Unlike the d_{33} effect, the subscript 3 in the d_{31} indicates the transversal direction while the longitudinal direction is indicated by the subscript 1. The axial strain is then $\epsilon_x = \epsilon_3 = d_{33}E_3$ for a d_{33} actuator whereas $\epsilon_x = \epsilon_1 = d_{31}E_3$ in a d_{31} actuator.

In order to use the same notation of the RZT equations, it is useful to model the MFC 8514-P1 as a d_{31} actuator. The piezoelectric coefficient value is calculated assuming that the axial strain for the d_{31} effect is the same as the actual d_{33} strain under the same applied voltage. The electric field E_3 corresponding to the electric potential difference $\Delta V^{(k)}$ is $E_3 = -\Delta V^{(k)}/t_e$ for a d_{33} actuator and $E_3 = -\Delta V^{(k)}/h_p$ for a d_{31} actuator. Equalling the strain in the two cases:

$$d_{31}\frac{\Delta V^{(k)}}{h_p} = d_{33}\frac{\Delta V^{(k)}}{t_e} \,. \tag{4.4}$$

The number of sections between two consecutive microelectrodes in a MFC 8514-P1 is 170 and the distance between the consecutive microelectrodes is $t_e = 0.5$ mm. The d_{31} coefficient to be used to model the d_{33} effect of this kind of actuator as a d_{31} effect is $d_{31} = 276 \times 10^{-12}$ m/V. The corresponding piezoelectric stress coefficient is $e_{31} = E_1 \times d_{31} = 0.0084$ N/mm/V, where E_1 is the Young modulus in the longitudinal direction of the piezoelectric material defined in Table [4.8].

4.3.5 Nonlinear static response of the piezo-composite beams to the voltage

In this section, the transversal deflection of the beams is calculated considering a voltage source connected to the actuators. The e_{31} operational mode has been considered for the actuators in both the RZT and the Abaqus model, with a piezoelectric stress coefficient corresponding to $e_{31} = 0.0084$ N/mm/V. The beams are hinged at both ends and subjected to only the voltage in the actuators, without any mechanical load.

Eq.[3.109] cannot be used for double-hinged boundary conditions, thus the RZT solution has been obtained solving Eq.[3.111] with the Newton-Raphson method for increments on the electric voltage and $\mathbf{F} = 0$. The voltage has been increased from 0 V to 700 V deflecting the beams in the opposite direction of the imperfection, thus a negative voltage has been applied to all the actuators but the one on the bottom surface of the BPZT1, which has positive values instead. The geometric imperfection of the beams has been also included as in the previous analyses.

The piezoelectric behaviour has been introduced in Abaqus modelling the piezoelectric part of the actuators with C3D8E finite elements and defining the voltage as a boundary condition. In general, the positive value of the e_{31} coefficient indicates that the actuator expands along its longitudinal direction when the applied voltage is positive.

In Abaqus, the voltage has to be defined as a difference between two values applied on the top and the bottom surfaces of each piezoelectric part; if the electric field vector corresponding to the voltage difference has the same direction of the z-axis, the actuator expands because $e_{31} > 0$ (refer to Fig.[3.3] for the electric field

and voltage difference directions). The voltage on the top surface (with respect to the z-axis) of the piezoelectric part is set to 0 V, whereas the desired voltage, $\bar{V}$, is applied to the bottom surface of the piezoelectric part with its positive or negative sign (see Fig.[4.33]). In this way, when $\bar{V} > 0$ the electric field is positive and the actuator expands, whereas when $\bar{V} < 0$ the actuator contracts.
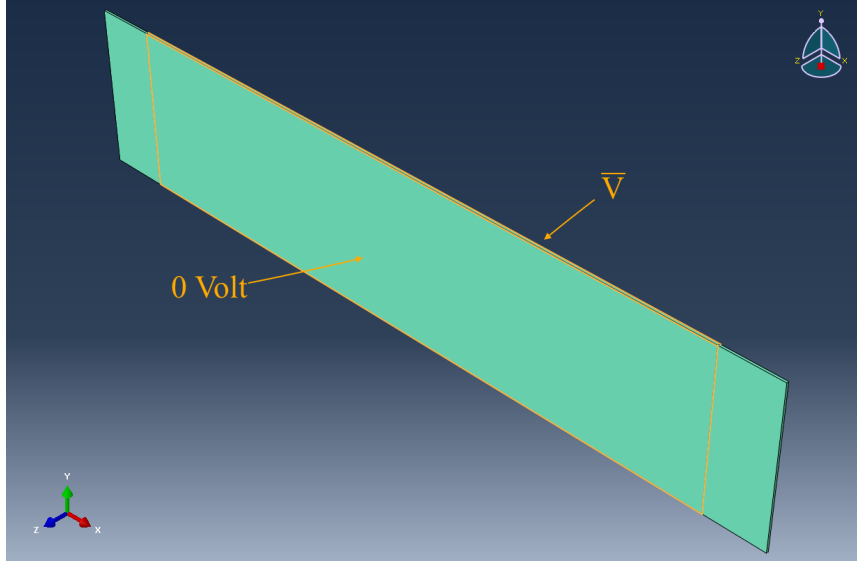
Figure 4.33: Application of the voltage to the actuators of the Abaqus models.

The Abaqus general nonlinear static analysis has been performed for the beams with the geometric imperfections defined as a linear combination of the buckling modes, as described in the previous section. The analysis has been run 17 times, every time for a different voltage[6].

The transversal deflection of the beams as a function of the increasing voltage is reported in Figs.[4.34-4.38] for both the RZT and the Abaqus models. The curves refer to the same points along the x-direction considered in the analyses of Section 4.3.3. The comparison between the two solutions indicates that RZT is extremely accurate, even for very high voltage values. Moreover, RZT correctly predicts the curvature change in the response of the BPZT1 and the BPZT3 (Figs.[4.34]-[4.36]), which takes place when the transversal displacement w reaches exactly the opposite value of the beam initial deviation in that point. Further increasing the voltage, the beam starts to bend in the opposite direction, and the curvature changes. The other beams do not exhibit this behaviour in the range of voltage considered because their initial imperfection is too big and higher voltages would be needed to invert

---

[6]The voltage values considered are $\bar{V}$ =25, 50, 75, 100, 125, 150, 175, 200, 225, 250, 275, 300, 350, 400, 500, 600, 700 V.

the deflection. The slight difference between the two solutions, especially for the anti-symmetric beams (BPZT(2-5), Figs.[4.35]-[4.38]) depends on the fact that the initial deflection is not exactly the same in the two models, since the imperfection is introduced as a linear combination of the buckling modes of a one-dimensional model for the RZT and a three-dimensional model for Abaqus.

The remarkable advantage of the RZT is that the nonlinear response can be evaluated performing just one analysis for each beam, specifying the highest voltage value desired, 700 V in this case. The routine calculates the solution for any applied voltage from 0 V up to 700 V, with increments that can vary between a certain range. The minimum and the maximum values chosen for the increments are 0.01 V and 25 V respectively, and the effective increment at each step is the maximum value in this range which satisfies the convergence criterion. This means that the nonlinear equation has been solved for at least 28 increments, and the average time for the analysis is 40 seconds. In Abaqus several analyses have to be run, one for each voltage value, and the time required by each analysis is 15 seconds on average. Consequently, the time to perform the same analysis in Abaqus is one order of magnitude higher than RZT. The comparison between the time of the RZT analyses and the resulting time for the Abaqus analyses can be found in Table [4.13].
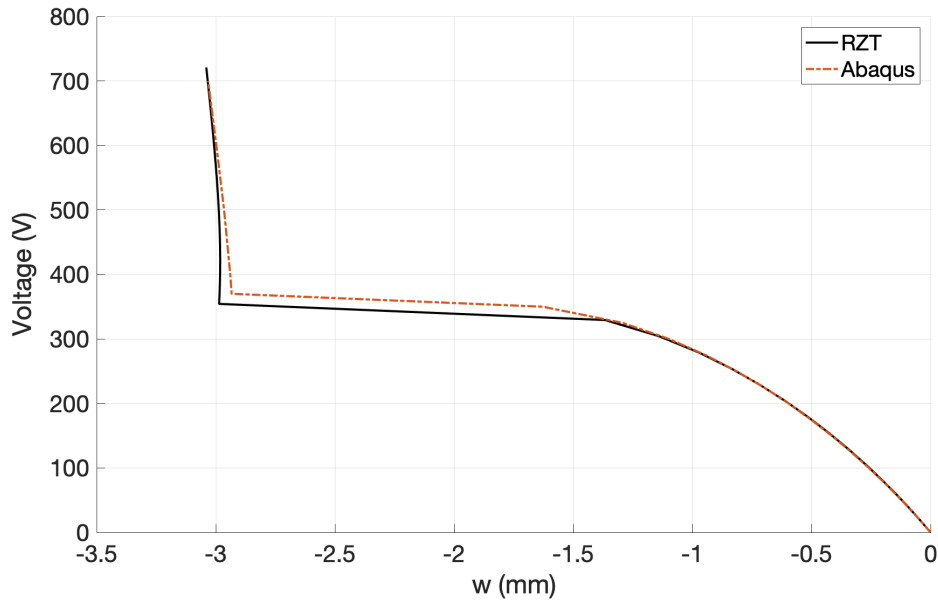
Figure 4.34: Transversal displacement ($x = 148$ mm) of the BPZT1 increasing the voltage in the actuators.
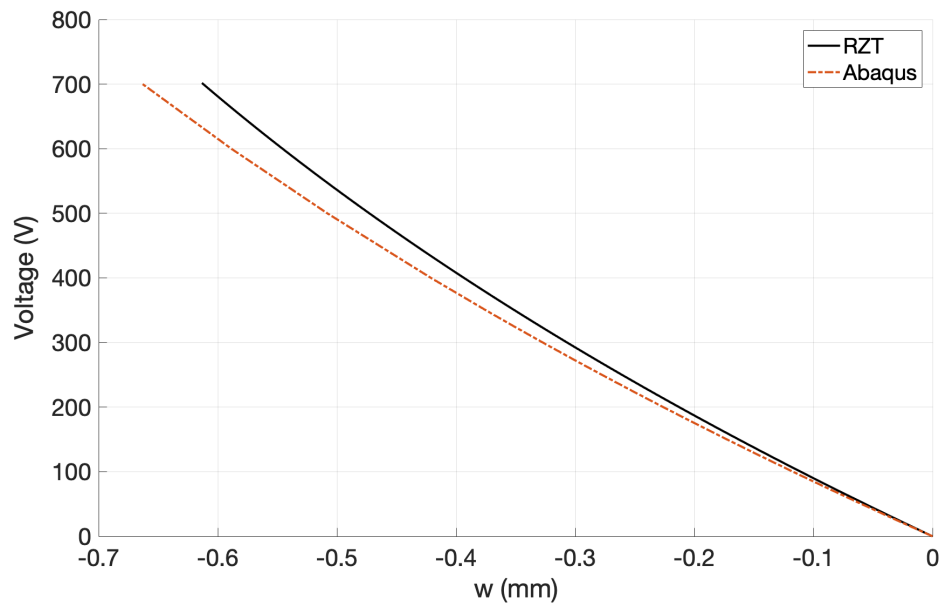
Figure 4.35: Transversal displacement ($x = 149$ mm) of the BPZT2 increasing the voltage in the actuators.
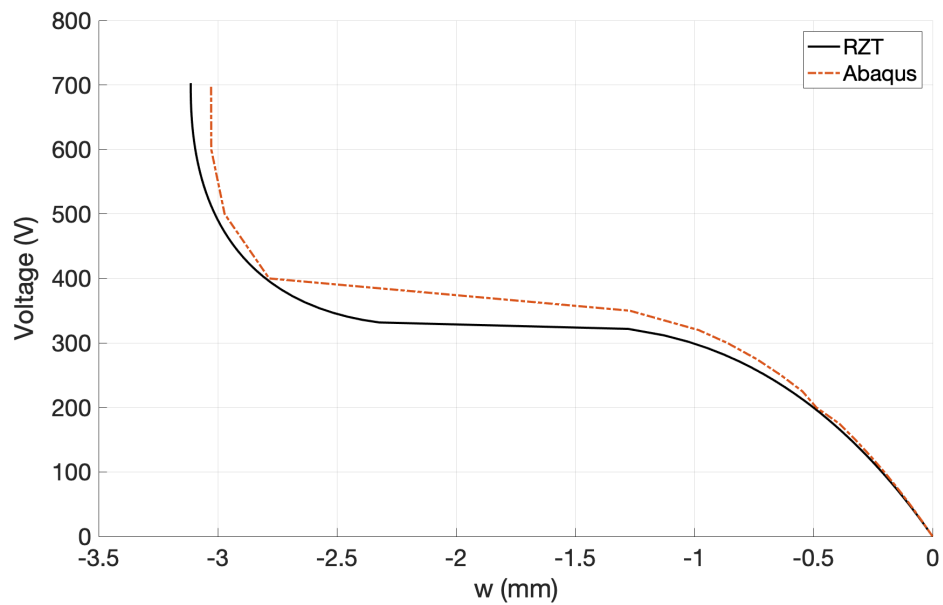
Figure 4.36: Transversal displacement ($x = 224$ mm) of the BPZT3 increasing the voltage in the actuators.
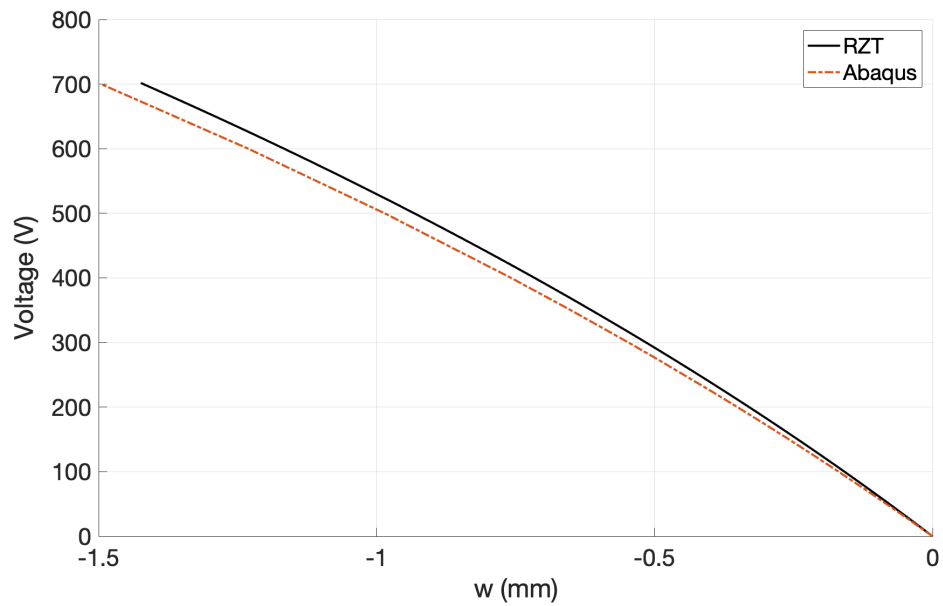
Figure 4.37: Transversal displacement ($x = 223.5$ mm) of the BPZT4 increasing the voltage in the actuators.
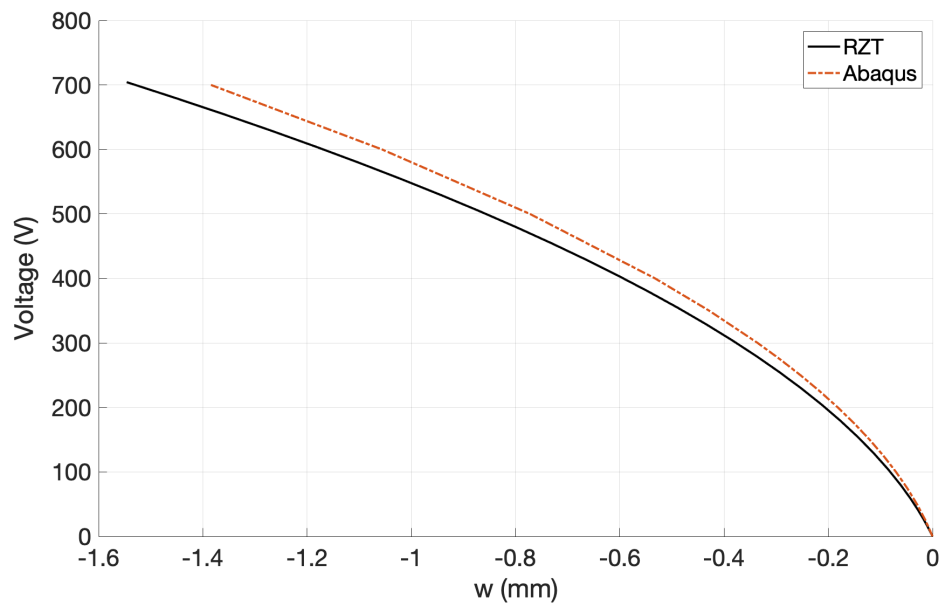
Figure 4.38: Transversal displacement ($x = 224.3$ mm) of the BPZT5 increasing the voltage in the actuators.

	Buckling Analysis		Nonlinear Analysis		Actuation Response	
	RZT	**ABAQUS**	**RZT**	**ABAQUS**	**RZT**	**ABAQUS**
BEAM1	2.5	23	42	272	35	289
BEAM2	2.3	26	38	280	30	170
BEAM3	2.8	32	53	305	41	255
BEAM4	2.8	32	56	366	42	238
BEAM5	3.1	31	80	2400	50	340

Table 4.13: Time (s) required by RZT and Abaqus for performing the buckling analysis, the nonlinear analysis and the nonlinear static analysis of the beams subjected to the piezoelectric voltage.

4.4   Conclusion

The new FE model based on the nonlinear Refined Zigzag Theory has been numerically validated for the buckling and nonlinear static analyses of highly heterogeneous sandwich beams and composite multilayer beams with piezoelectric actuator patches.

A Matlab routine has been realised to implement the new FE-RZT model for the buckling and the nonlinear static analyses of composite beams using RZT-beam finite elements. The model includes the inverse piezoelectric effect and the possibility to have geometric discontinuities along the beam length, thus it is able to model more complex geometries like beams with actuator patches bonded to the external surfaces.

A similar Matlab routine has been realised for the FE models based on the Timoshenko Beam Theory, including the calculation of a shear correction factor based on the transverse-shear strain energy to increase the solution accuracy.

The RZT model has been assessed in terms of both accuracy and computational cost for the buckling and postbuckling analyses through comparisons with highly-detailed FE commercial codes. The TBT solution represents the most efficient option for the beam-like structure modelling in the commercial codes, thus it has been used to evaluate the most desirable computational effort. Two-dimensional and three-dimensional models realised in Abaqus and Nastran have been considered as reference to verify the RZT accuracy.

The first analyses have been performed considering sandwich beams of various geometries and material properties. The comparison between RZT, TBT and two-dimensional Abaqus and Nastran solutions has proven that the RZT is very accurate for the buckling and nonlinear analyses of sandwich beams, even in case of

115

low slenderness ratios and highly heterogeneous materials that cannot be correctly predicted using TBT finite elements. In addition, the RZT computational cost is one order of magnitude lower than that of the analyses based on two-dimensional finite elements, but reaches the same level of precision.

The RZT capabilities to model beams with geometric discontinuities has been demonstrated comparing the RZT to three-dimensional Abaqus models for the buckling and postbuckling analyses of multilayer beams with patches bonded to the external surfaces. Several geometries, laminations and patch locations have been considered to generalise the conditions. The results show that the RZT can reach the same accuracy of three-dimensional Abaqus models with a remarkable saving of computational time. Subsequently, the inverse piezoelectric behaviour has been introduced to consider the patches as piezoelectric actuators. The static response of the beams has been calculated for different voltages applied to the actuators, taking into account both the geometric imperfections and the geometric nonlinearities. The RZT has proven to be highly accurate, even for high voltages and in case the beam inverts its deflection. Moreover, the use of the RZT Matlab routine saves a lot of time because only one analysis has to be performed to evaluate the response to an increasing voltage; it takes less than 40 seconds for a range 0-700 V. On the other hand, in Abaqus one analysis has to be run for each voltage value and each of them runs for 15 seconds on average.

In conclusion, the RZT has proved to be an excellent compromise between accuracy and computational cost for the buckling and the nonlinear static analyses of composite beams. It has been demonstrated that it is a very convenient alternative to the commercial codes when highly heterogeneous materials or piezoelectric elements are considered, especially if nonlinearities are taken into account.

Chapter 5

Experimental validation

5.1 Introduction

In this chapter, the new nonlinear RZT model is validated experimentally for the buckling of sandwich and composite laminated beams and for the nonlinear static analysis of beams with piezoelectric actuators.

The specimens manufacturing has been part of the activity, thus in Section 5.2 it is accurately described how the beams have been made and how the piezoelectric actuator patches have been bonded to the external surfaces of the monolithic beams. Particular supports have been realised for the boundary conditions to allow the beam rotation around the width-axis and to consider simply-supported boundary conditions also for the sandwich beams. The geometric imperfection of the monolithic beams is also taken into account and the way it has been measured and modelled is presented in Section 5.3.

The buckling tests of both kinds of beams are performed using the Instron compression testing machine available at the RMIT material testing laboratory, and the Southwell method is employed for the buckling loads evaluation (Sections 5.4-5.5.1). The RZT capabilities to predict the response of the beams subjected to the piezoelectric actuation, considering also the geometric nonlinearities and imperfections, is assessed performing static and buckling tests with voltage applied to the actuators. The experimental static response of the beams subjected to increasing values of voltage is compared to the RZT results to prove that RZT is able to evaluate the deflection of the beam due to the actuation (Section 5.5.2). Subsequently, different values of voltage are applied to reduce the geometric imperfection of the beams before performing the buckling tests in order to verify that RZT can evaluate the increasing value of the buckling load as the geometric imperfection decreases (Section 5.5.3).

5.2 Beams manufacturing

Composite laminated plates have been cut in stripes of various lengths and widths to make both the facesheets of the sandwich beams and the composite laminated beams on which the piezoelectric actuators have been subsequently bonded. The plates have been made using T700 carbon/epoxy unidirectional prepregs (VTM264, Advanced Composite Group).

For the sandwich beam facesheets, symmetric laminates with $[0°/90°/90°/0°]$ fibre orientation have been realised laying up a number of prepreg layers dependent on the final thickness of the facesheets (see Fig.[5.1]). Moreover, different plates have been made laying up, respectively, one, four or eight prepreg layers for each orientation angle resulting in thin plates made of 4 prepreg layers, medium-thickness plates made of 16 prepreg layers and thick plates made of 32 prepreg layers.
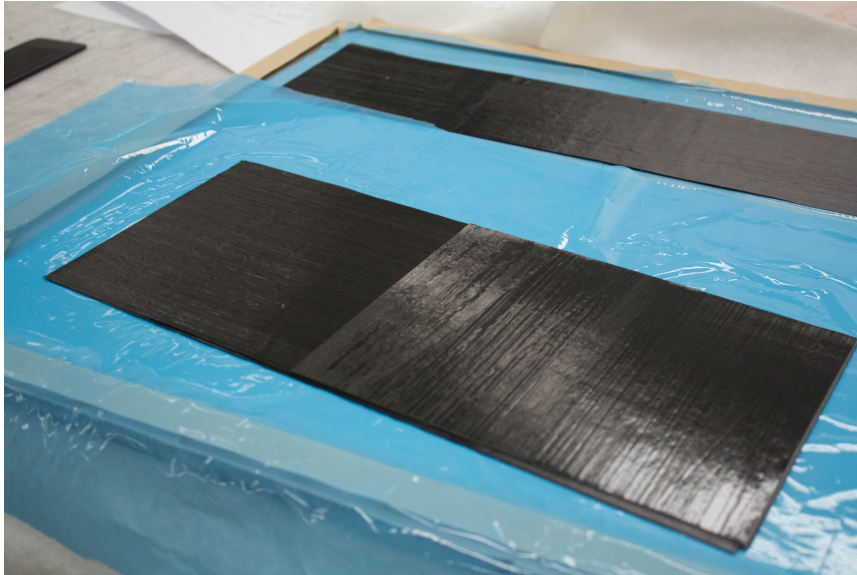
Figure 5.1: Layup of $0° - 90°$ CFRP prepreg layers.

The plates to realise the piezo-composite beams have been made of two different laminations, symmetric $[0°/90°/90°/0°]$ and anti-symmetric $[90°/0°/90°/0°]$, with one prepreg layer for each orientation angle.

The same manufacturing process has been followed for all the plates. During the lay-up, the assembled material has been vacuum debulked every subsequent fourth ply for 2 minutes (3 minutes for the thicker lay-ups made of 16 and 32 prepreg layers), covering it with a perforated release film (A2500) and a heavy weight polyester material layer (Airbleed 10, Fig.[5.2]) to ensure a good consolidation and remove any residual air from the laminate.

Figure 5.2: Debulking of a CFRP lay-up.

Subsequently, the laminates have been prepared for the autoclave hot-curing process following the scheme reported in Fig.[5.3] for the vacuum-bag.
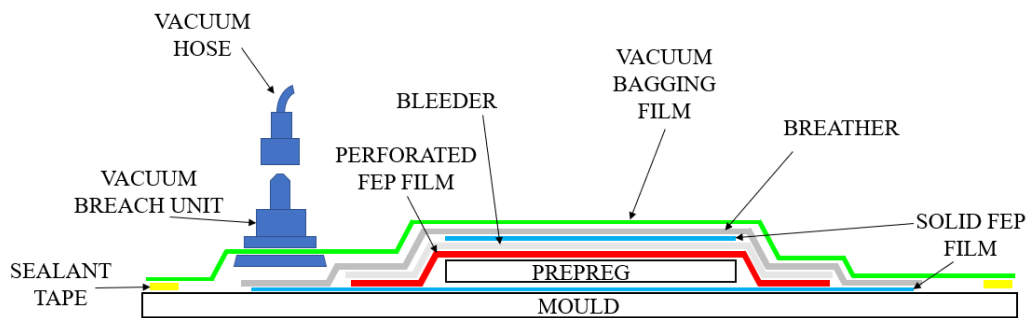
Figure 5.3: Vacuum bag scheme.

An aluminium plate has been used as mould and a VAC-PAK® A6200 EFEP solid release film has been placed on the plate top surface to protect the prepreg laminate from sticking to the mould. Once arranged on the EFEP film, the lay-up has been covered with an FEP perforated release film (A2500) to control the amount of resin flow during cure and protect the laminate from bonding to the rest of the vacuum bag materials. A porous nylon peel ply bleeder (B100) has been

used to absorb the excessive resin bleeding from the perforated film. An additional layer of solid EFEP film has been placed on the bleeder over the lay-up area to stop the resin bleed, extending it to 12 mm short of the edge of the bleeder to allow the gas flow under vacuum or autoclave pressure. The Airbleed 10 polyester material layer has been used as breather to allow the free passage of air and gases from the laminate while evenly distributing the vacuum or pressure within the bag. The vacuum valve has been laid on the breather, not in the area over the prepreg to not damage the laminate. The entire mould has been covered by a Quickdraw® HS8171 high performance nylon film, air-tightly sealing it using the Tacky Tape® SM5143 sealant tape. The sealed bag has been connected to a vacuum pump to apply a pressure of 1 atm to the prepreg. All the prepreg lay-ups have been cured in autoclave with a cure cycle of 1 hour, 120°C and 90psi (620 kPa).

Sandwich beams manufacturing

The sheets of structural foams Rohacell® IG31 and Rohacell® WF110 have been cut of the appropriate dimensions to make the cores of the sandwiches. The same dimensions have been considered for cutting the corresponding facesheets from the previously manufactured plates. One side of each facesheet has been prepared for bonding by sanding is with a 3M™ Sandpaper and using alcohol to clean the surface from dust and grease.

The 3M™ AF163-2K structural adhesive film has been used to bond together the facesheets and the core. Once assembled in sandwiches, the beams have been arranged in vacuum bags for the autoclave curing of the adhesive.

Aluminium frames have been realised to prevent the foam from squashing under the vacuum or autoclave pressure taking into account the various thicknesses and lengths of the beams. A polyester tape (Flashtape1) has been used to protect the beams from bonding to the surrounding frames, as shown in Fig.[5.4]. The same scheme of Fig.[5.3] has been followed for the bagging process and the cure cycle of 1 hour, 120°C and 90psi has been considered also in this case.
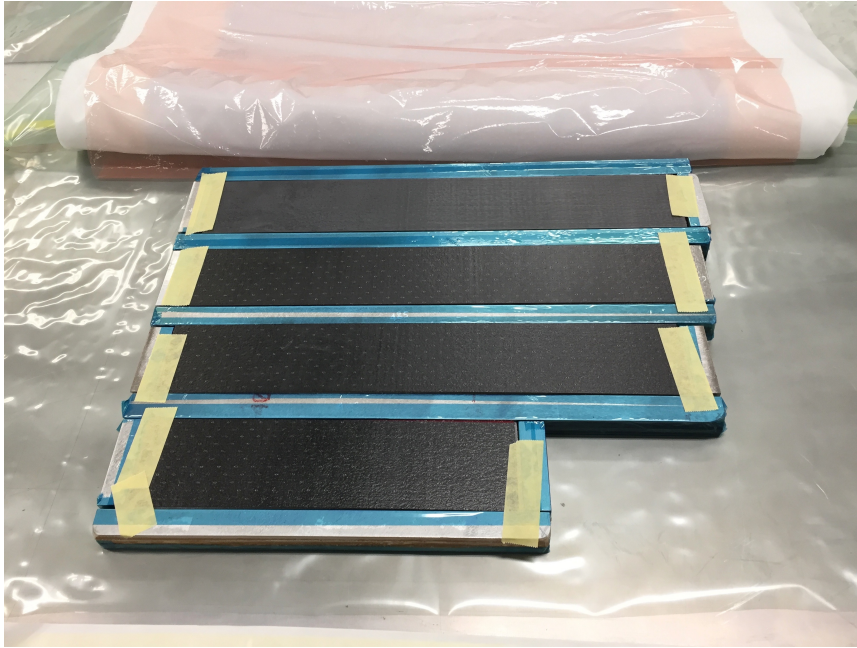
Figure 5.4: Vacuum bag with aluminium frames for the sandwich beams curing process.

After the curing, the beam edges have been adjusted and refined using the surface grinder shown in Fig.[5.5]. Two beams, the WF-1- L1 and the WF-1-L2, have been made using a WF110 foam core, whereas other three beams, named IG-2-L1, IG-4-L1 and IG-4-L2, have been made with an IG31 foam core. The total thickness and the width of the beams have been measured in three different locations along the length: at the beam ends and the centre and the values are reported in Tables [5.1-5.2]. In the Tables it is also indicated the average values of the thickness and the width, $\bar{h}$ and $\bar{b}$ respectively, the standard deviation, σ, and the coefficient of variation, CV.
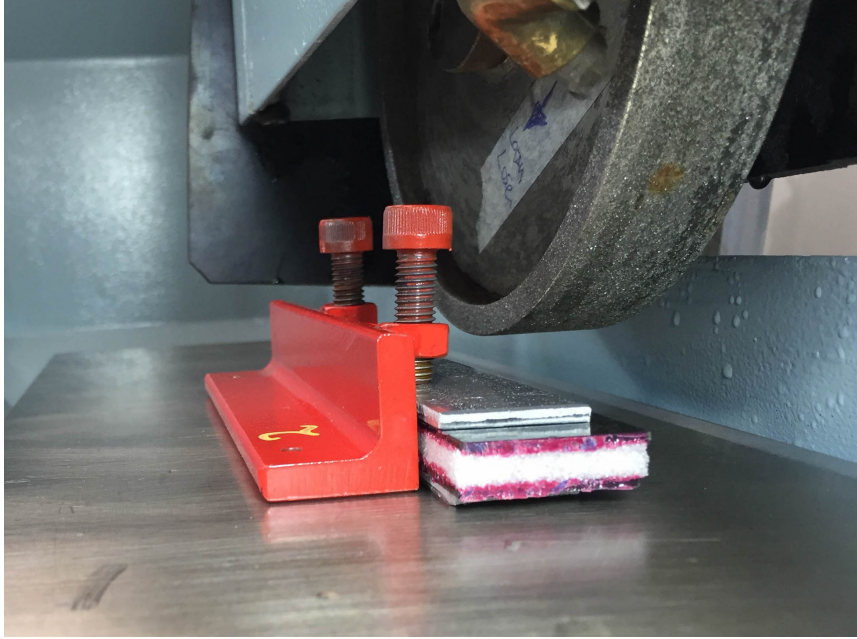
Figure 5.5: Surface grinder used to refine the sandwich beam edges.

	$\mathbf{h_1}$ (mm)	$\mathbf{h_2}$ (mm)	$\mathbf{h_3}$ (mm)	$\mathbf{\bar{h}}$ (mm)	$\boldsymbol{\sigma}$ (mm)	**CV** %
WF-1-L1	21.87	21.8	21.855	21.84	0.04	0.17
WF-1-L2	21.86	21.85	21.805	21.84	0.03	0.13
IG-2-L1	8.62	8.57	8.65	8.61	0.04	0.47
IG-4-L1	12.15	12.02	12.075	12.08	0.07	0.54
IG-4-L2	12.25	12.25	12.35	12.28	0.06	0.47

Table 5.1: Thickness measurements along the length of the sandwich beams: average, standard deviation and coefficient of variation.

The nominal values assumed for the geometrical properties of the five sandwich beams used in the tests are reported in Table [5.3]. The nominal width indicated in Table [5.3] correspond to the average $\bar{b}$ of Table [5.2] and it is approximately three times the total thickness. The thicknesses of the facesheets and the cores have been measured before the curing for bonding them together, whereas the adhesive thickness, h_a, has been measured as the difference between the total thickness of the sandwich after cured and the sum of core and facesheets thicknesses. The WF-1-L(1-2) have the biggest length, L, and the smallest facesheet thickness, h_f. The IG-2-L1 is the shortest, whereas the IG-4-L1 and the IG-4-L2 have the highest face-to-core thickness ratio (h_f/h_c).

122

	b$_1$ (mm)	b$_2$ (mm)	b$_3$ (mm)	$\bar{b}$ (mm)	σ (mm)	CV %
WF-1-L1	63.05	63.31	62.65	63.00	0.33	0.53
WF-1-L2	64.2	64.32	64.35	64.29	0.08	0.12
IG-2-L1	25.73	25.61	25.72	25.69	0.07	0.26
IG-4-L1	36.29	36.22	36.25	36.25	0.04	0.10
IG-4-L2	37.66	37.68	37.66	37.67	0.01	0.03

Table 5.2: Width measurements along the length of the sandwich beams: average, standard deviation and coefficient of variation.

	L	b	h$_c$	h$_f$	h$_a$
WF-1-L1	443	63	20	0.68	0.241
WF-1-L2	427	64.29	20	0.68	0.24
IG-2-L1	160	25.69	5.4	1.45	0.157
IG-4-L1	230	36.25	5	3.4	0.14
IG-4-L2	230	37.67	5	3.4	0.24

Table 5.3: Geometrical properties of the sandwich beams for the experimental validation (mm).

Piezo-composite beams manufacturing

The beams considered for the numerical validation in Chapter [4.3] have been made cutting four-layer plates. The thickness and the width have been measured in three different locations along the length of each beam and the values are indicated in Tables [5.4-5.5], where the average values, $\bar{h}$ and $\bar{b}$, the standard deviation, σ, and the coefficient of variation, CV, are also reported. $\bar{h}$ and $\bar{b}$ have been considered as nominal thickness and width; all the geometric characteristics correspond to those shown in Table [4.7].

The actuators chosen for the experiments are the Macro Fiber Composite (MFC) M8514-P1 (see Fig.[5.6]). The geometrical properties of the M8514-P1 are indicated in Table [5.6], where the actual length and width of the piezoelectric material part (L_{active} and b_{active} respectively) are distinguished from the total length and width of the patch.

Figure 5.6: MFC M-8514-P1 piezoelectric transducer.

	$\mathbf{h_1}$ (mm)	$\mathbf{h_2}$ (mm)	$\mathbf{h_3}$ (mm)	$\mathbf{\bar{h}}$ (mm)	$\mathbf{\sigma}$ (mm)	**CV** %
BPZT1	0.65	0.64	0.66	0.65	0.01	1.54
BPZT2	0.74	0.73	0.73	0.73	0.01	0.79
BPZT3	0.71	0.71	0.74	0.72	0.02	2.41
BPZT4	0.77	0.74	0.74	0.75	0.02	2.31
BPZT5	0.77	0.78	0.78	0.78	0.01	0.74

Table 5.4: Thickness measurements along the length of the piezo-composite beams: average, standard deviation and coefficient of variation.

	$\mathbf{b_1}$ (mm)	$\mathbf{b_2}$ (mm)	$\mathbf{b_3}$ (mm)	$\mathbf{\bar{b}}$ (mm)	$\mathbf{\sigma}$ (mm)	**CV** %
BPZT1	20.78	20.88	20.82	20.83	0.05	0.24
BPZT2	23.02	23.09	22.98	23.03	0.06	0.24
BPZT3	21.33	21.56	21.49	21.46	0.12	0.55
BPZT4	22.36	22.71	22.69	22.59	0.20	0.87
BPZT5	22.09	22.24	22.38	22.24	0.15	0.65

Table 5.5: Width measurements along the length of the piezo-composite beams: average, standard deviation and coefficient of variation.

The MFC actuators have been bonded to the external surfaces of the monolithic beams in the locations shown in Fig.[4.20]. The beams have been prepared for the bonding by uniformly sanding the external surfaces to have a constant thickness along the length. Subsequently, the surfaces have been degreased and cleaned to ensure a successful bonding

The upper side of the MFC has been covered with the polyester tape to protect the piezoelectric fibres from being damaged during the bonding process while the bottom side has been degreased using alcohol. A thin layer of 3M™Scotch-Weld™ DP460NS epoxy adhesive has been applied to the MFC's bottom surface, with a small additional quantity in the middle as adhesive reservoir. Once placed in the desired location on the beam surface, the MFC has been pressed against the beam to remove any air bubble from the adhesive layer. After removing the excessive resin, the flashtape has been used to keep the patch in that location.

A perforated FEP film has been placed around the beams, wrapping everything with a layer of breather cloth, as shown in Fig.[5.7].

L	b	h	L_{active}	b_{active}
101	20	0.3	85	14

Table 5.6: Geometrical properties of the MFC M8514-P1 piezoelectric transducer (mm).
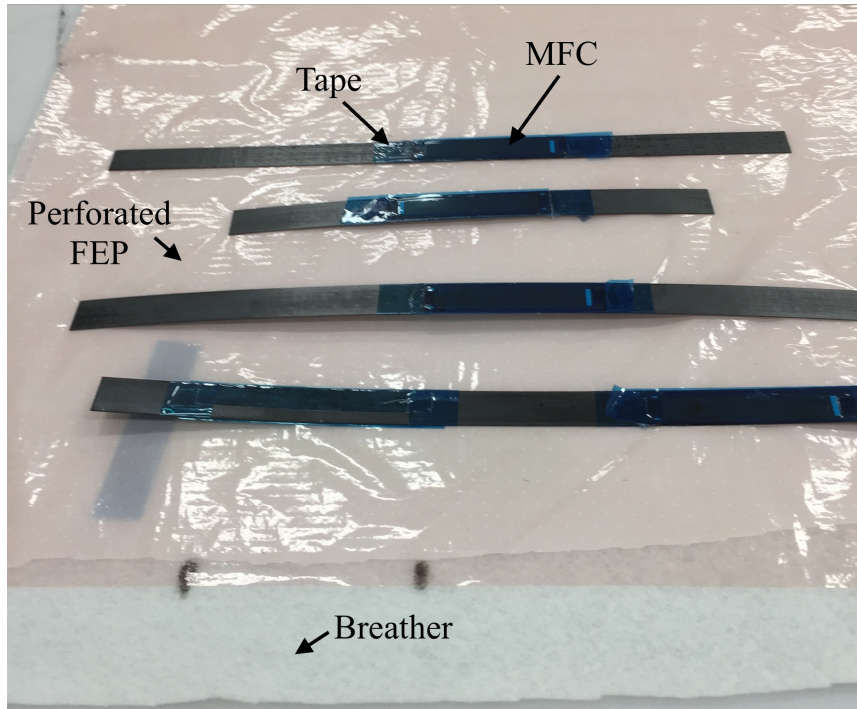
Figure 5.7: Vacuum bag for the MFC piezoelectric patches bonding.

A vacuum bag has been prepared with the HS8171 nylon film and, after the vacuum, the adhesive has been cured for 2hr at 49°C in the oven.
An antistatic wrist strap has been worn during the entire bonding process to protect the MFCs.

Edges for simply-supported boundary conditions

Many preliminary tests have been performed to determine the best way to reproduce either clamped or simply-supported boundary conditions for composite beams. For a buckling test, the beam cannot be directly clamped into the grips of a compression testing machine because the grips would apply a local compression along the thickness and a shear load on the top and bottom surfaces of the beam.

As a first attempt to realise full restraint conditions, the beam edges were immersed for 1/3 of their final length into resin poured into cylindrical moulds, aligning the beam x-axis with the cylinder axis (see Figs.[5.8]). The resulting specimens were beams with two blocks of resin, one on the top and one on the bottom.

(a) Broken specimen after the buckling test.
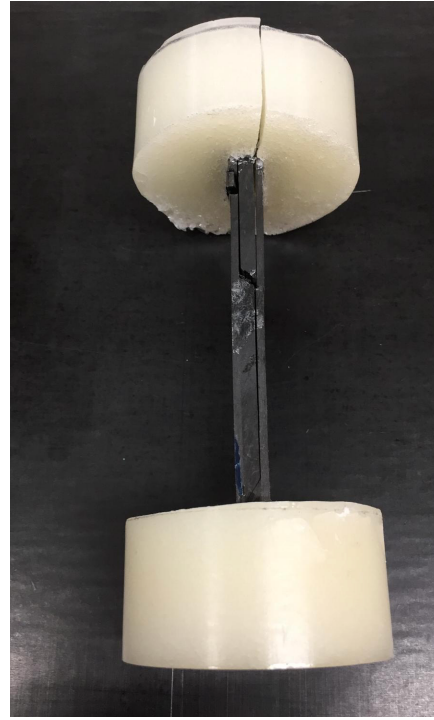
(b) Breakage of the resin support.

Figure 5.8: Composite beam (CFRP, $[0°/90°/90°/0°]$ ply orientation) with resin supports for clamped boundary conditions.

However, even if the specimens had all the same geometrical and material properties, the compression tests gave different results for the buckling load calculations. Indeed, Singer *et al.* [72] strongly recommend the simply-supported conditions for the buckling of columns for two main reasons, the first one is that with pinned-end conditions the critical cross-section is at half length of the beam, thus it is far less influenced by the ends, and the second reason is that, with clamped conditions, the effective length of the beam is hard to determine because it is highly dependent on the restraining method. The tests made on the specimens with resin blocks at the edges proved that even small imperfections of the restraint conditions (either material or geometrical) can strongly influence the effective length, thus the clamping method used was not reliable for buckling tests of composite beams.

For this reason, only simply-supported conditions have been considered for the tests. Particular kinds of supports have been designed for the beam edges in order to allow the free rotation of the beams around the width-axis direction (y-axis). Semi-cylindrical pin-ended supports (see Fig.[5.9]) have been realised for the sandwich beams because they are relatively thick. The radius of the semi-cylinder, R_e, has been set equal to the nominal thickness of the beam and the angle of the circular sector of the cylinder cross-sectional area has been set to 140°, a value much higher than the expected rotations around the y-axis. A hard material has to be used for the supports to not damage them during the tests with high compressive loads, thus they have been made of steel. The DP460NS epoxy adhesive has been used to bond them to the beams, locating the centroid of the beam end cross-section exactly coincident with the centre of the support surface, as shown in Fig.[5.10a].
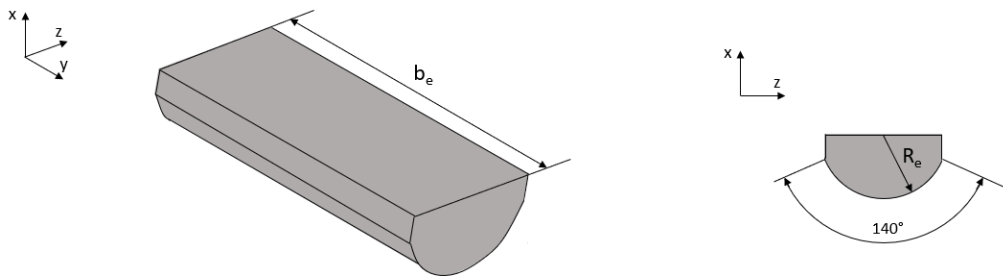
Figure 5.9: Steel edges for sandwich beams simply-supported boundary conditions: geometrical properties.
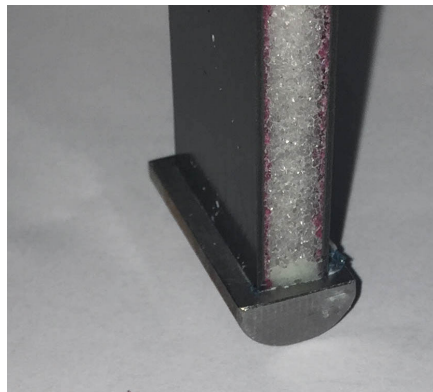
(a) Steel support bonded to a sandwich beam.
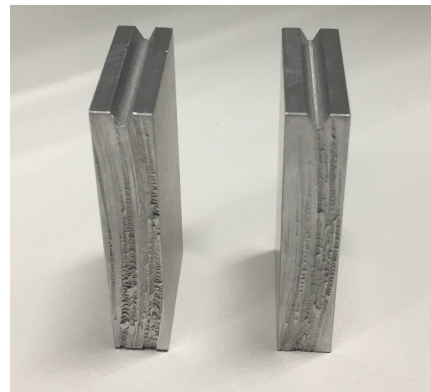
(b) Aluminium supports for the monolithic beams

Figure 5.10: Pin-ended supports for the buckling tests of the piezo-composite beams.

127

The aluminium supports shown in Fig.[5.10b] have been realised for the monolithic beams because the thickness of these beams is very small. The *V-shape* allows the beam to rotate around the $y-$axis; the support dimensions are indicated in Fig.[5.11].
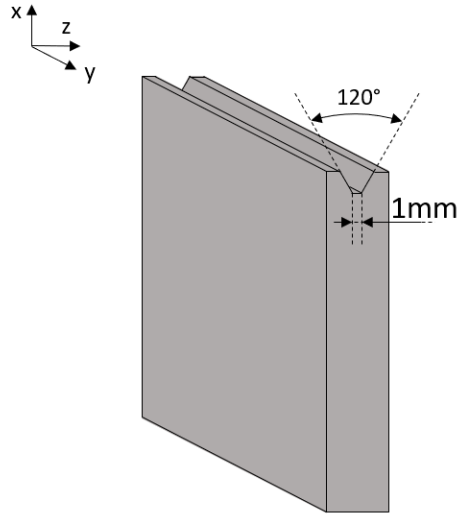
Figure 5.11: Geometric dimensions of the supports for simply-supported boundary conditions of the monolithic beams.

The advantage of this kind of fixture is that the same two supports have been used to test all the piezo-composite beams, whereas a couple of semi-cylindrical elements had to be realised for each sandwich beam.

5.3 Imperfection measurements and interpolation for the monolithic beams

The monolithic beams are highly bent in their initial stress-free state, especially those with an anti-symmetric lamination. The initial deviation from a straight axis configuration has been measured in a discrete number of points along the length and at half width using a Keyence LC-2320 laser displacement meter sensor, as shown in Fig.[5.12]. Neglecting thickness variations and assuming a constant transverse displacement along the beam thickness, the values represent the transverse deflection of the beam axis.

Figure 5.12: Geometric imperfection measurement of a monolithic beam.

One edge of the beam has been chosen as the origin of the $x-$axis and the locations of the measurement points have been referred to it. The imperfection has been measured before and after the actuators bonding, but the final measurements have been considered in the analyses. The $x-$coordinate of each point and the corresponding vertical deflection, $\bar{w}^*$, are reported in Table [5.7].

In order to introduce the geometric imperfection in the numerical models, whose solution has to be compared to the experiments, the geometric imperfection of each beam has been expressed by a function $w^*(x)$, obtained by the following linear combination:

$$w^*(x) = a_1 \cdot sin\left(\frac{\pi x}{L}\right) + a_2 \cdot sin\left(\frac{2\pi x}{L}\right) + a_3 \cdot sin\left(\frac{3\pi x}{L}\right) . \qquad (5.1)$$

The trigonometric functions in Eq.[5.1] correspond to the first three buckling mode shapes of a simply-supported beam in its perfect configuration, thus the imperfection function has been approximated by a linear combination of the first three buckling modes. The coefficient of the linear combination of each beam, a_1, a_2

129

BPZT1		BPZT2		BPZT3		BPZT4		BPZT5	
x	$\bar{w}^*$	x	$\bar{w}^*$	x	$\bar{w}^*$	x	$\bar{w}^*$	x	$\bar{w}^*$
0	0	0	0	0	0	0	0	0	0
30	0.95	37	1.94	56	1.16	56	3.9	56	3.8
60	1.23	75	3.19	112	2.12	112	6.37	112	6.5
149	1.43	149.5	3.68	168	1.96	168	7.60	168	8.0
238	1.02	224	2.82	224	1.52	224	7.97	224	8.8
268	0.85	262	1.65	280	0.64	280	7.75	280	8.64
298	0	299	0	336	0.4	336	6.67	336	7.34
				392	0.6	392	4.2	392	4.07
				447.5	0	448	0	448.5	0

Table 5.7: Values of the geometrical deviation measured along the monolithic beams (mm).

and a_3, have been found applying the least squares method using the experimental data of Table [5.7]. The obtained a_k values are those indicated in Table [4.12] used also for the numerical validation in Chapter 4. The R^2 values of the fits are reported in Table [5.8]; they are all above 0.90, indicating a good correlation between the imperfection prediction and the actual deflection of the beams in the points where it has been measured.

	BPZT1	BPZT2	BPZT3	BPZT4	BPZT5
R^2	0.96	0.99	0.95	0.99	0.99

Table 5.8: R^2 values of the fit used for the approximation of the geometric imperfection of the beams.

5.4   Buckling tests of sandwich beams

The Southwell method [91] has been employed to calculate the critical buckling load of the sandwich beams performing non-destructive buckling compression tests.

Before the tests, the beams have been numerically modelled to evaluate the buckling loads, using both the RZT and the TBT finite elements methods. The RZT results have been taken as reference values for the experiments to avoid the beam breakage.

The sandwich beams have been tested in compression using the Instron hydraulic testing machine with a 50 kN load cell. Compression platens have been

used as fixtures of the Instron to guarantee a uniformly distributed compressive load along the beam width. As shown in Fig.[5.13], the ends of the beams were simply placed on the platens without restricting any possible lateral displacement under compression. Nevertheless, the exceptional precision in aligning the centroids of the beam sections at the edges to the centre of the semi-cylindrical supports and to the centre of the plates prevented the beams from sliding laterally. The alignment between the beam and the supports was checked also at the end of each test.

A laser displacement sensor, the SICK OD1-B100H50U14, has been used for measuring the transversal displacement of the point located at half length and at half width of each beam. The experimental setup is shown in Figs.[5.13] for the beam IG-4-L1.

(a)   (b)
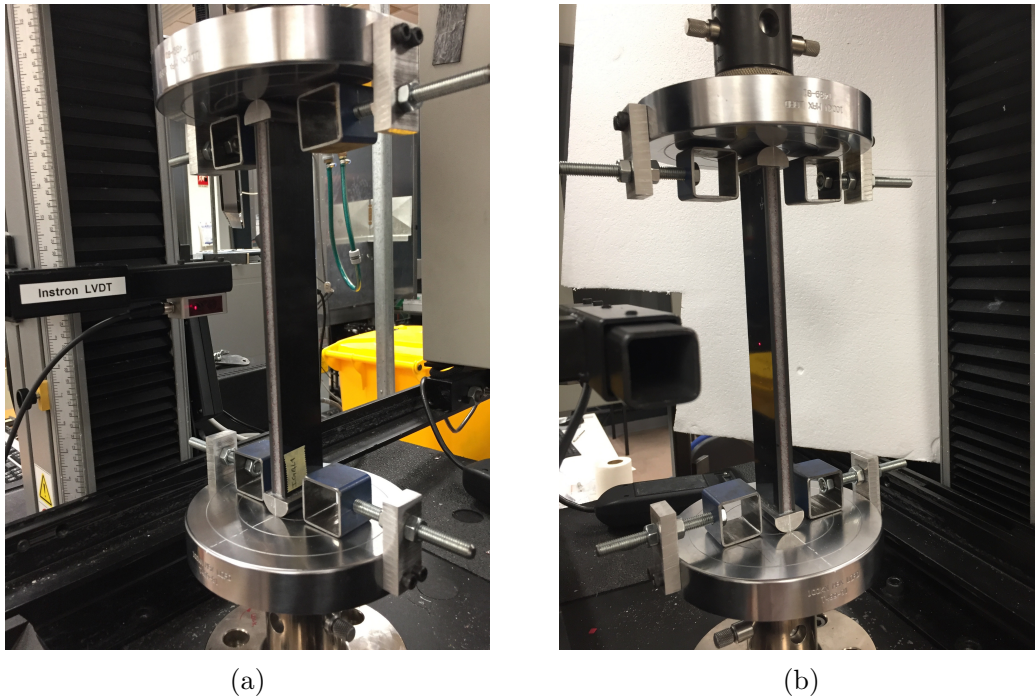
Figure 5.13: Experimental setup for the buckling tests of sandwich beams.

During the tests, the load, N_0, has been progressively increased measuring the corresponding transversal displacement, w, at each step. The test has been repeated three times for each beam and the displacement control has been used to prevent any beam damage.

The values of the applied load and the transversal deflection have been recorded and plotted in Figs.[5.14a-5.18a] as load-displacement equilibrium paths of each beam. The curves of the beams WF-1-L1 and WF-1-L2 (Figs.[5.14a-5.15a]) show a linear relation between the load and the transversal displacement for low values

of N_0. A rapid reduction of the slope can be seen for loads higher than 12,000 N for the WF-1-L1 and higher than 17,000 N for the WF-1-L2, and all the curves tend asymptotically to about $N_0 = 25,000$ N. The curve related to the Test 3 of the WF-1-L2 (Fig.[5.15a]) ends before 20,000 N because, during the test, one of the semi-cylindrical steel supports at the beam edges debonded, thus the test was stopped. A misalignment between the load direction and the beam axis and the consequent bending moment on the steel element is a reasonable cause of the failure.

The same trend of Figs.[5.14a-5.15a], with an initial linear behaviour and a subsequent decreasing of the slope, can be observed also in Fig[5.16a] for the IG-2-L1. On the other hand, the load-displacement curves of the IG-4-L1 and the IG-4-L2 in Figs.[5.17a-5.18a] exhibit some disturbances due to their high stiffness. These two beams have a very high face-to-core thickness ratio and a relatively low slenderness ratio. In addition, the geometric imperfections of the IG-4-L(1-2) measure hundredths of millimetre, which means they are very straight beams. The consequence of having small geometric imperfections is that the load-displacement curve tends to be the axis $w = 0$ (the typical load-displacement equilibrium path of a perfectly straight beam) until the applied load reaches the critical buckling value, and then even a small perturbation of the load direction can lead to a sudden rise of the transversal displacement and to the beam breakage. For this reason, the tests have been stopped even if the deflection measured was less than 1 mm, as it can be seen in Figs.[5.17a]-[5.18a], because the applied load was very close to the critical value calculated by RZT but the small geometric imperfection makes the curves very close to the $w = 0$ line.

Employing the Southwell method, these curves are approximated as rectangular hyperbolas with the asymptotes corresponding to the axes $w = 0$ and $N_0 = N_{cr}$. These hyperbolas can be transformed and become straight lines in the plane $\left(\dfrac{w}{N_0}, w\right)$ with a slope corresponding to N_{cr}. The method can be then used to evaluate the critical buckling load by plotting the recorded values of N_0 and w in the $\left(\dfrac{w}{N_0}, w\right)$ plane. The curves obtained applying the Southwell method to the load-displacement curves are reported in Figs.[5.14b-5.18b]. Only the values of load higher than 80% the maximum load and the corresponding transversal displacements have been considered, as prescribed in [72]. The least squares method has been applied to the remaining points and the slope of the line has been assumed as experimental critical buckling load of the test.
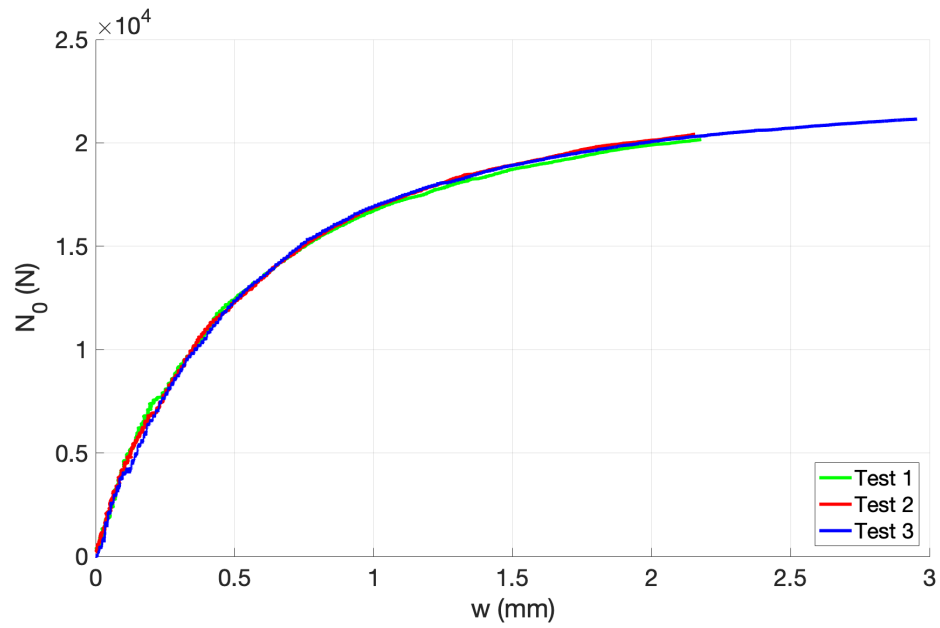
(a)
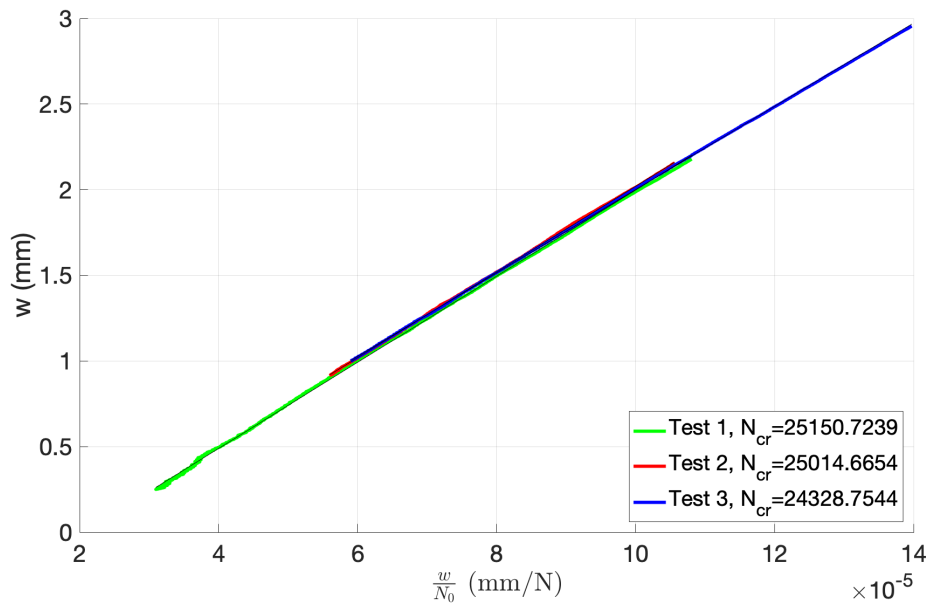
(b)

Figure 5.14: Buckling test of the WF1L1 sandwich beam.
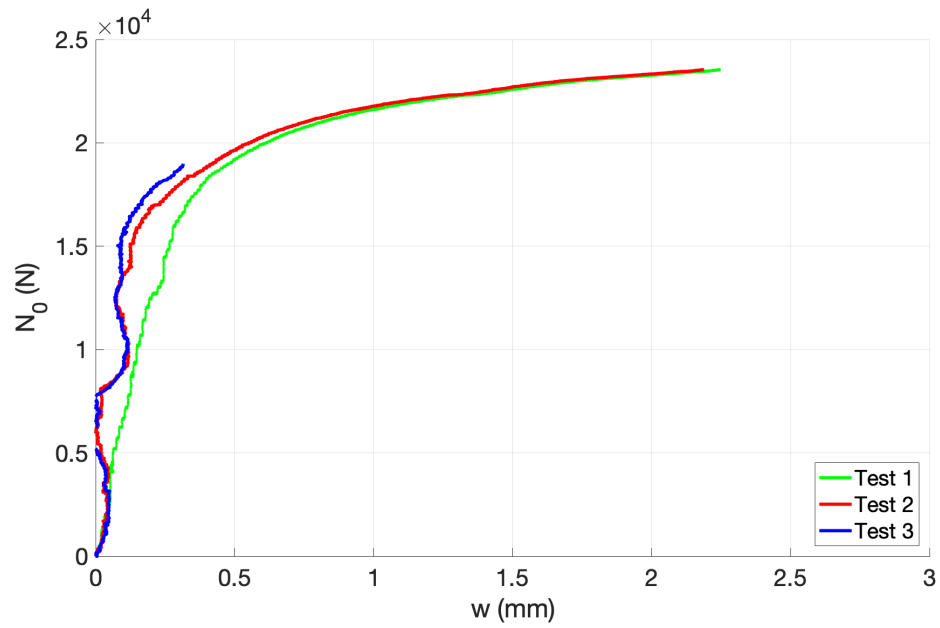
(a)
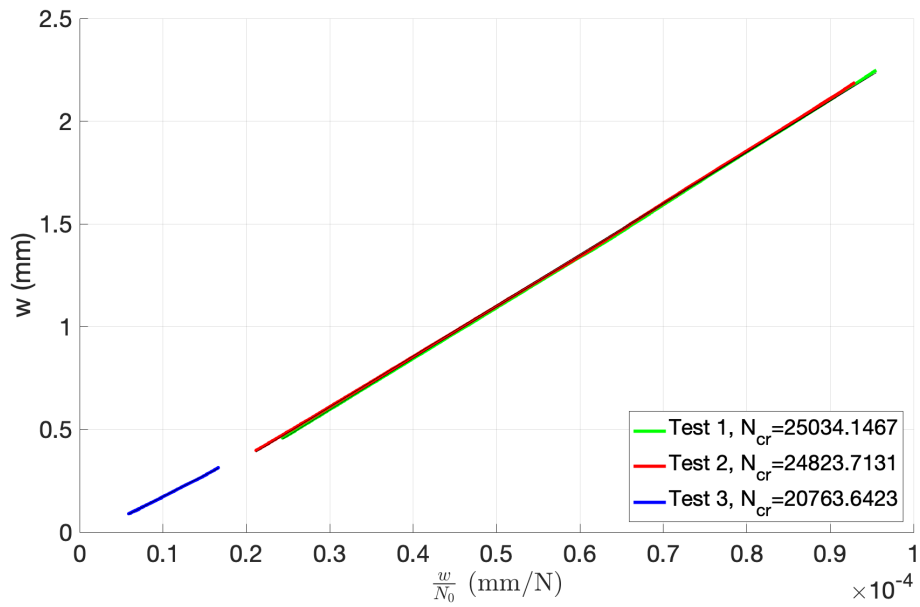
(b)

Figure 5.15: Buckling test of the WF1L2 sandwich beam.
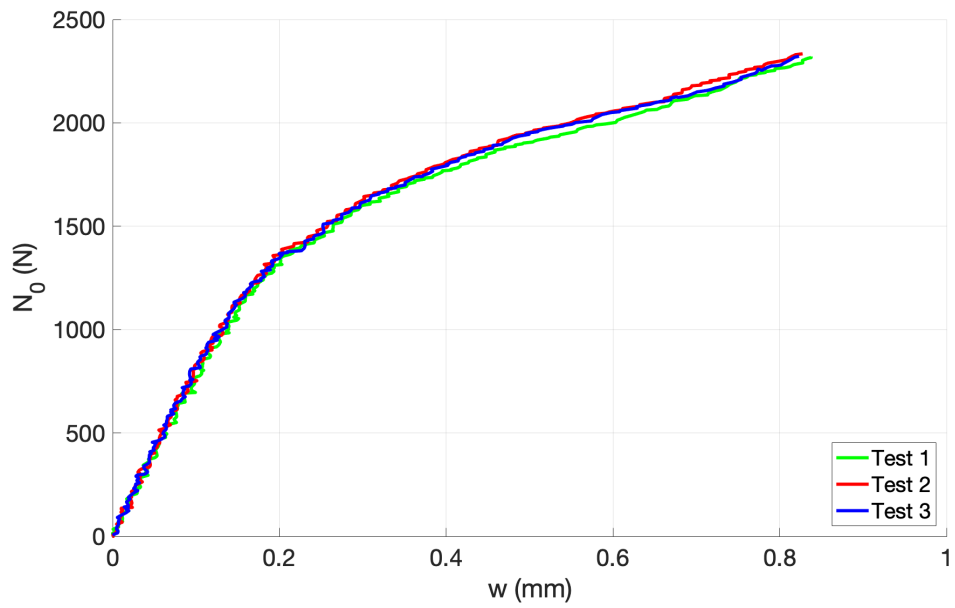
(a)
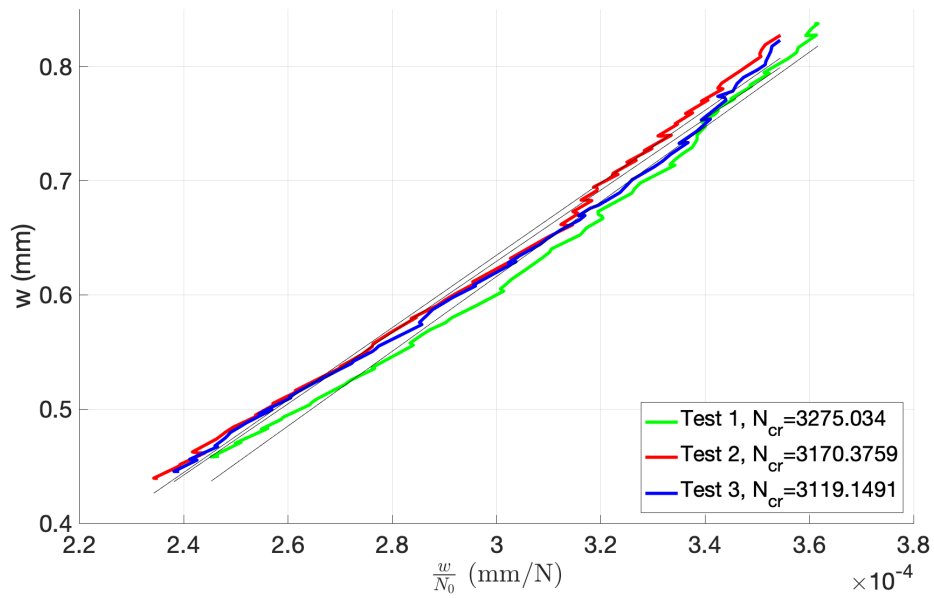
(b)

Figure 5.16: Buckling test of the IG-2-L1 sandwich beam.
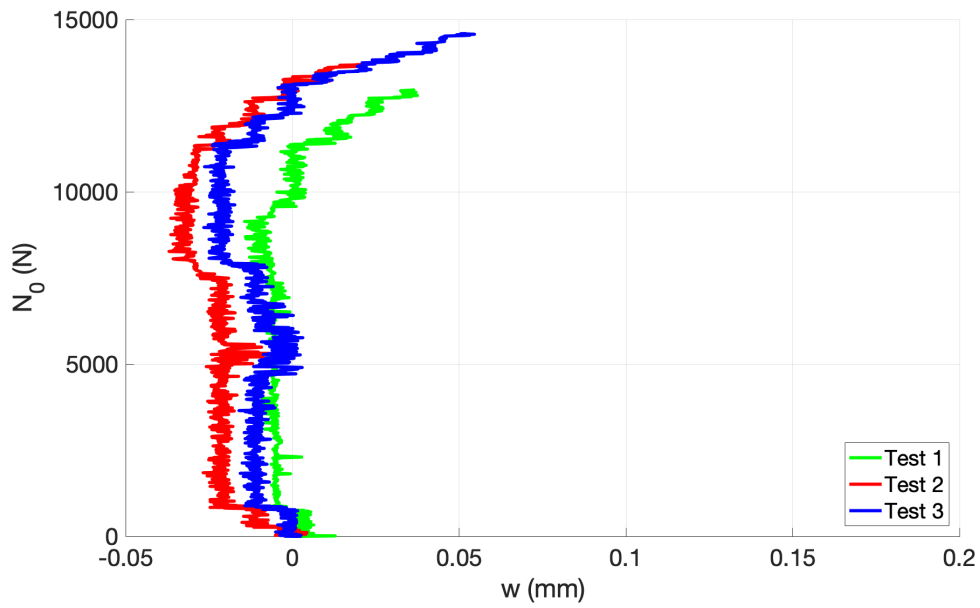
(a)
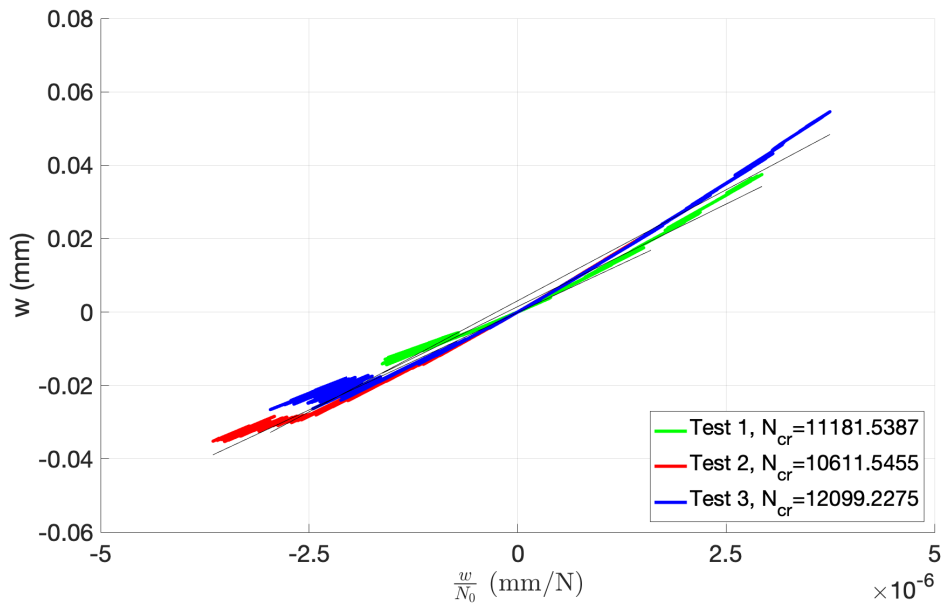
(b)

Figure 5.17: Buckling test of the IG4L1 sandwich beam.
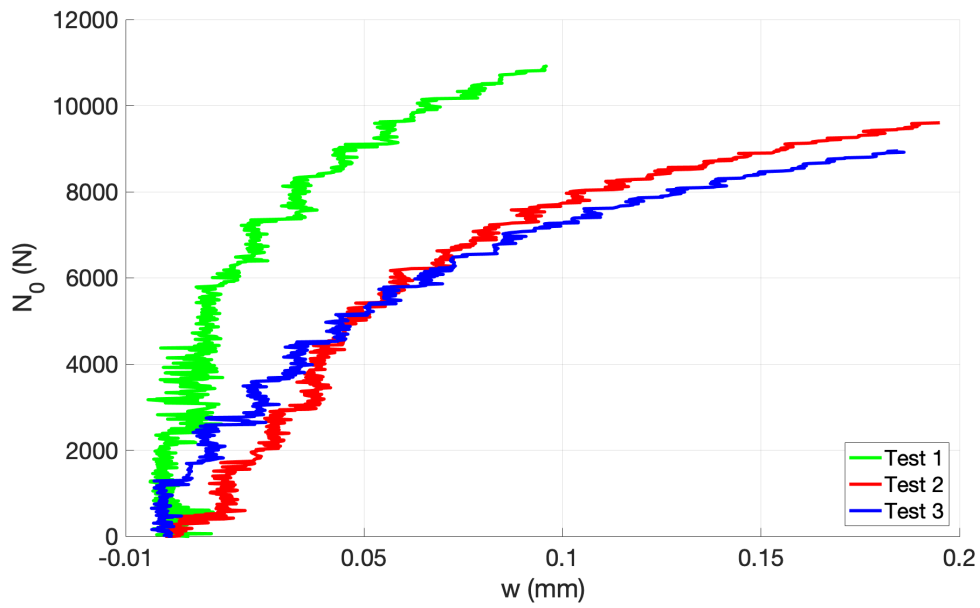
(a)
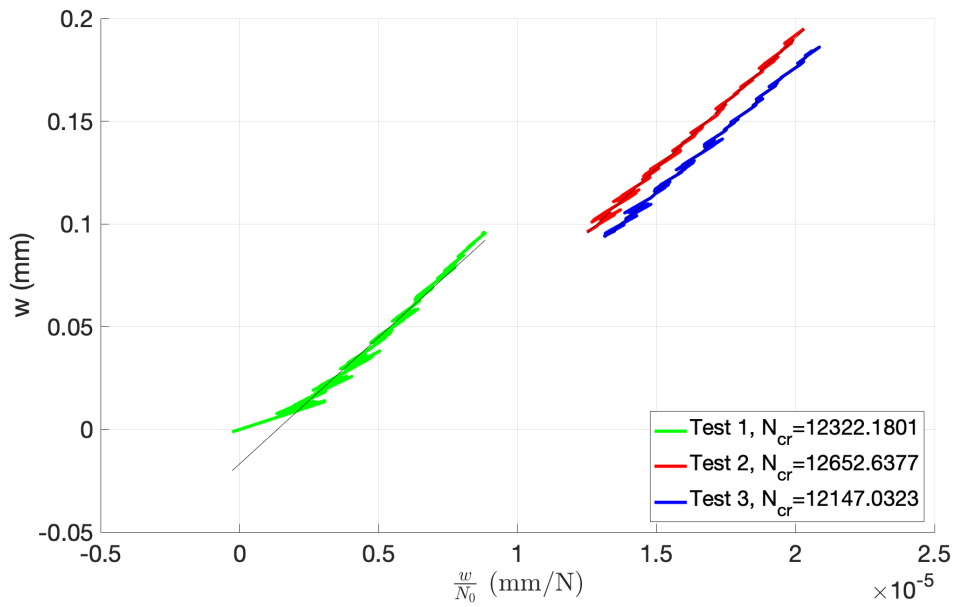
(b)

Figure 5.18: Buckling test of the IG-4-L2 sandwich beam.

The critical buckling loads have been experimentally evaluated for each beam

137

and compared to the numerical predictions of the RZT and TBT models. The material properties of the Rohacell foams, used for the cores, and the CFRP-VTM264, used for the facesheets, are reported in Tables [4.1]-[4.8] of 4.2, whereas the Young and transverse-shear moduli of the AF163-2K adhesive are 1,100 MPa and 400 MPa respectively. Comparing the material properties of the AF163-2K to those of the Rohacell structural foams (Table [4.1]), it is clear that the adhesive is much stiffer than the foams. For this reason, the adhesive layers have been also considered in the analyses since they influence the buckling loads, significantly increasing their value[1] even having a very small thickness, as indicated in Table [5.3].

The number of finite elements considered for the numerical analyses is 80 and the time to calculate the critical buckling loads is less than 10 seconds for both the RZT and the TBT.

	EXP (N)	σ (N)	CV %	RZT (N)	ERR %	TBT (N)	ERR %
WF-1-L1	24,831	440.57	1.77	23266	-6.30	23,264	-6.31
WF-1-L2	24,929	2407.13	10.23	25,053	0.50	25,052	0.49
IG-2-L1	3,188	79.46	2.49	3,224	1.13	2,809	-11.89
IG-4-L1	11,297	750.58	6.64	10,695	-5.33	7,061	-37.50
IG-4-L2	12,374	256.74	2.07	11,399	-7.88	7,617	-38.44

Table 5.9: Buckling loads of the sandwich beams: comparison between the experimental results (EXP), RZT and TBT.

The average of the buckling loads calculated experimentally for each beam is reported in Table [5.9], with the corresponding standard deviation, σ, and the coefficient of variation, CV used to indicate the dispersion of the results around the mean. Assuming a range for experimental variance of two standard deviations of the mean, the RZT predictions for the critical buckling loads exceed the range only in case of the WF-1-L1 and the IG-4-L2, for which the numerical critical buckling loads are 2.8% and 3.9% lower than the lower bound. This slight difference is probably due to the fact that the number of experiments is lower than five.

The WF-1-L2 was damaged during the Test 3 before a sufficient number of measurements were collected, thus the mean value in Table [5.9] is between the buckling loads of Test 1 and Test 2 only.

The comparisons between the numerical and the experimental results highlights a strong dependence of the TBT accuracy on the facesheets thickness. The predictions of RZT and TBT are both accurate for the WF110-core beams. The numerical

---

[1]The RZT critical loads calculated without the adhesive are all out of a range of experimental variance of three standard deviations of the mean.

results for the WF-1-L2 are excellent, with errors lower than 1%, whereas for the WF-1-L1 the error reaches only 6% error. However, considering beams with thicker facesheets and a lighter foam core, the TBT error increases a lot. The IG-2-L1 has a facesheets thickness that is two times the thickness of the WF-1-L(1-2) beams facesheets, and the TBT error on the buckling load is almost 12%. Moreover, the IG-4-L(1-2) have the facesheets thickness that is two times the thickness of the IG-2-L1 and the error goes up to 40%. On the other hand, the RZT buckling loads are very accurate in all cases. The RZT percentage error is only 1.13% for the IG-2-L1, and in the most challenging situations, the IG-4-L(1-2), it is lower than 8%, that is an excellent result for experimental validations.

5.5 Experiments on piezo-composite beams

The experimental buckling tests have been conducted also for the piezo-composite beams in order to validate the RZT predictions of the critical buckling loads of composite beams with piezoelectric actuator patches in both symmetrical and anti-symmetrical lamination conditions.

In the following section (5.5.1), the piezoelectric actuators are considered just as geometric entities because they are not connected to any power supply. The aim of the tests is to assess the RZT models of [4.3.2] in Chapter [4] for the buckling load calculation of beams with geometric discontinuities.

Subsequently (in 5.5.2-5.5.3), the possibility to increase the buckling load using the actuators is investigated and the RZT capabilities at modelling and predicting these situations are verified.

5.5.1 Buckling tests of piezo-composite beams

The buckling tests of the piezo-composite beams have been performed using the Instron machine with a load cell of 10 kN. The aluminium supports have been placed in the machine grips aligning the beam centroidal axis with the load direction. The laser LVDT has been used to record the beam transversal displacement of the beam half-length and half-width point, as shown in Fig.[5.19].

Figure 5.19: Experimental setup for the buckling test of beams with piezoelectric actuators.

The load has been progressively increased from $N_0 = 0$ N, measuring the transversal displacement at each step considering displacement control.

The tests have been repeated three times for each beam and the load-displacement curves are reported in Figs.[5.20a-5.24a].

Despite the geometrical characteristics, the load asymptotic value of the BPZT1 in Fig.[5.20a] is almost double the load asymptotic value of the BPZT2 in Fig.[5.21a]. The BPZT1 is stiffer because of the additional piezoelectric patch and the symmetric lamination.

Both the beams BPZT3 and BPZT4 have just one piezoelectric patch on the top surfaces, almost in the same location and the geometrical characteristics of the two beams are approximately the same, but the BPZT4 is slightly thicker and wider. Comparing the load-displacement curves of the two beams in Figs.[5.22a-5.23a] it can be seen that the transversal deflection of the BPZT4 is almost 12 times higher than the BPZT3 for the same applied load. The tests have been interrupted before the asymptotic load values were visible because, for the BPZT3 in Fig.[5.22a], the load was very close to the critical value predicted by RZT and for the BPZT4 in Fig.[5.23a] higher deflections could have damaged the actuator. For the same reason, even if the load was still considerably lower than the predicted buckling value of the BPZT5 and the curve slope had not reduced significantly, the transversal deflection was higher than 10 mm thus the tests have been stopped. The curves obtained applying the Southwell method are shown in Figs.[5.20b-5.24b].
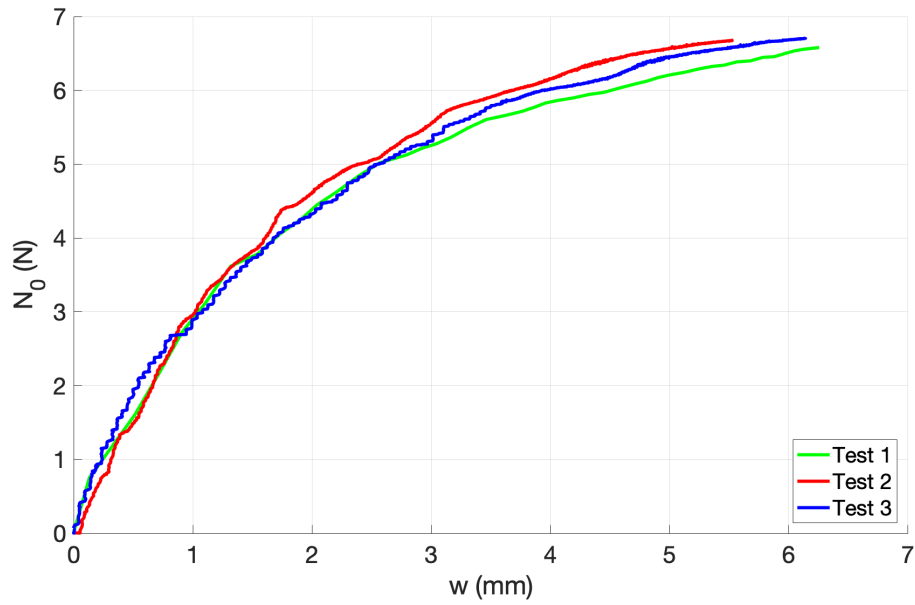
(a)
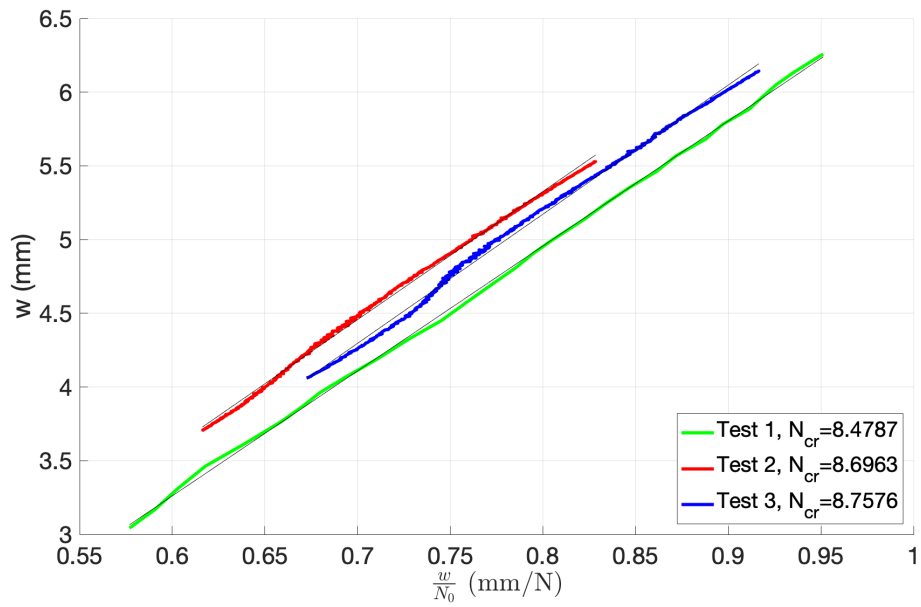
(b)

Figure 5.20: Buckling test of the BPZT1 beam.
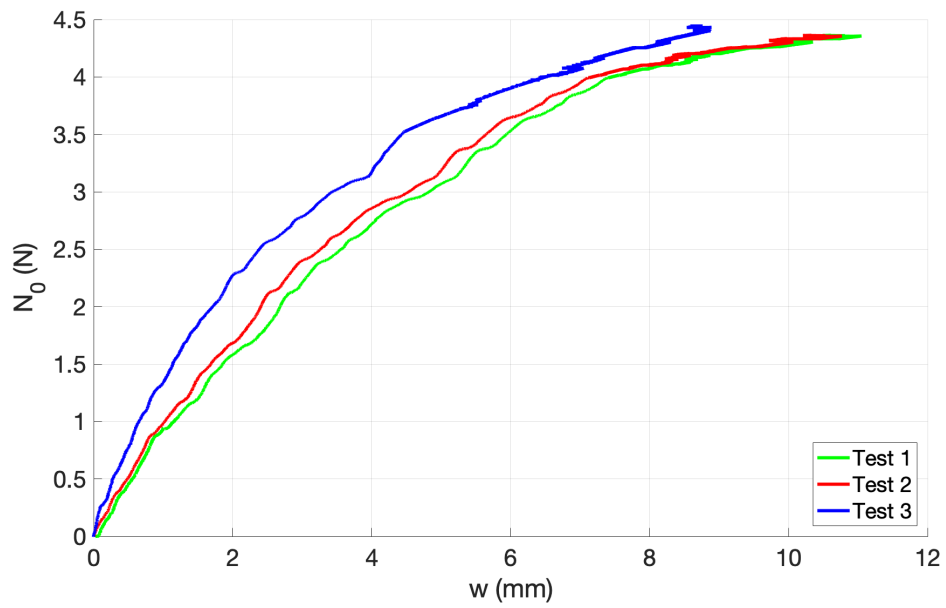
(a)
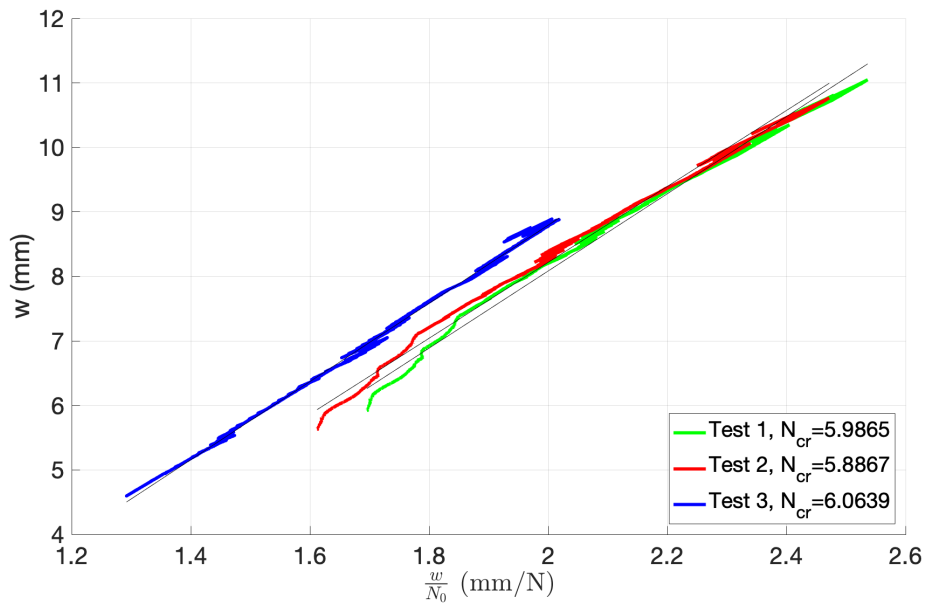
(b)

Figure 5.21: Buckling test of the BPZT2 beam.
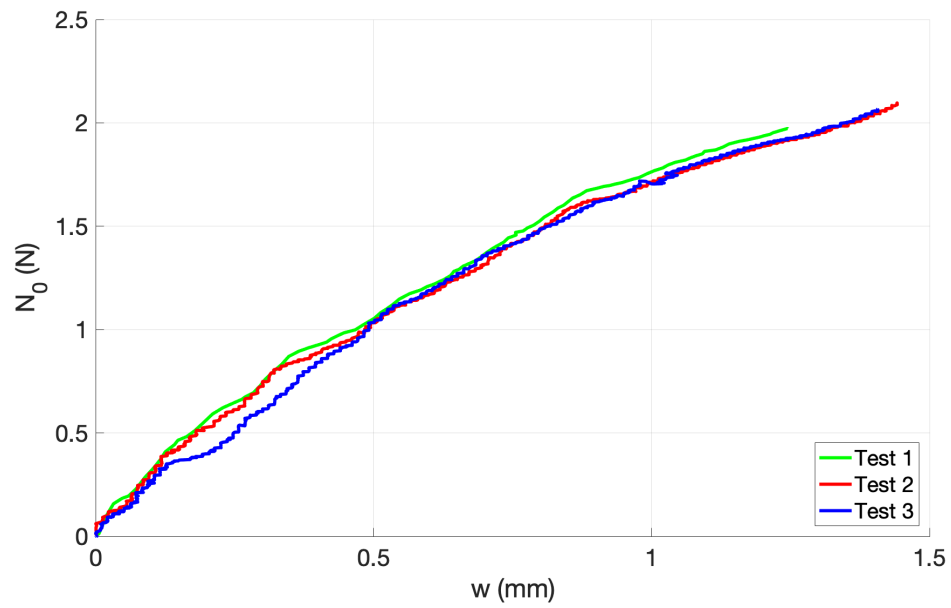
(a)
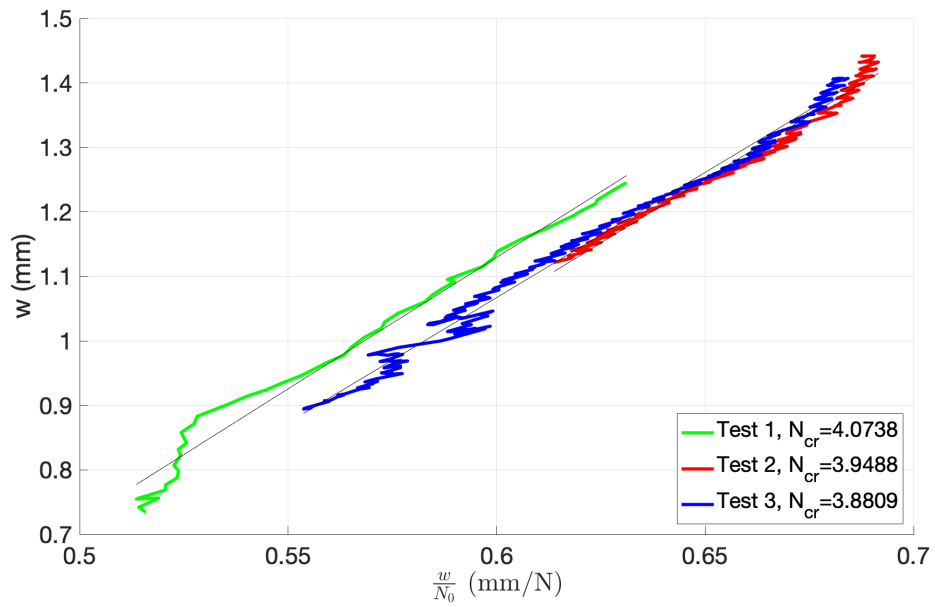
(b)

Figure 5.22: Buckling test of the BPZT3 beam.
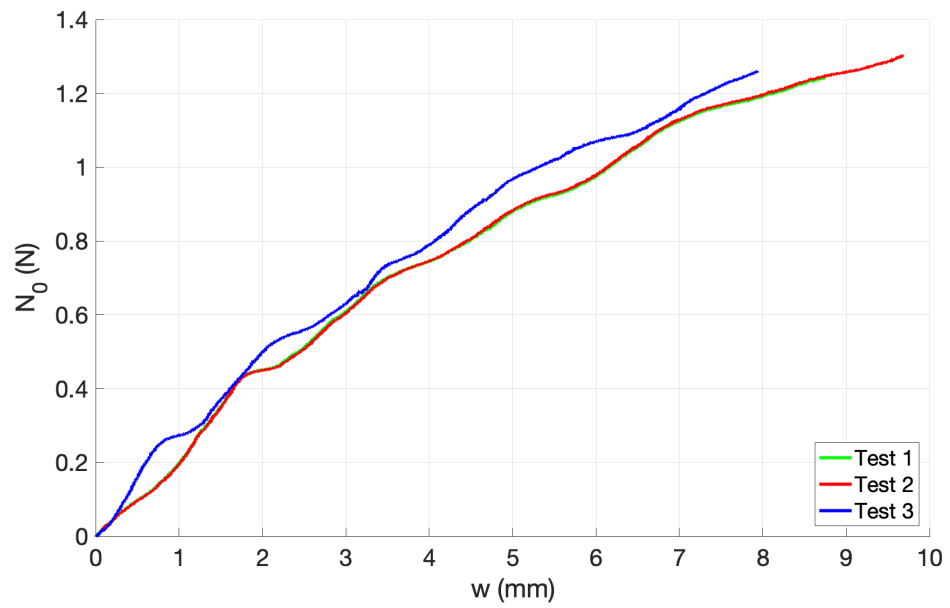
(a)
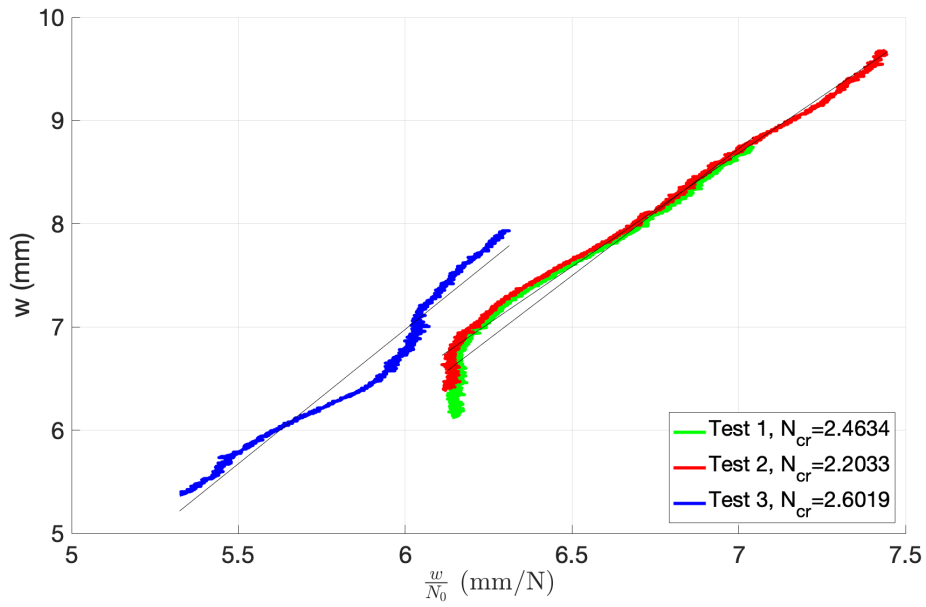
(b)

Figure 5.23: Buckling test of the BPZT4 beam.
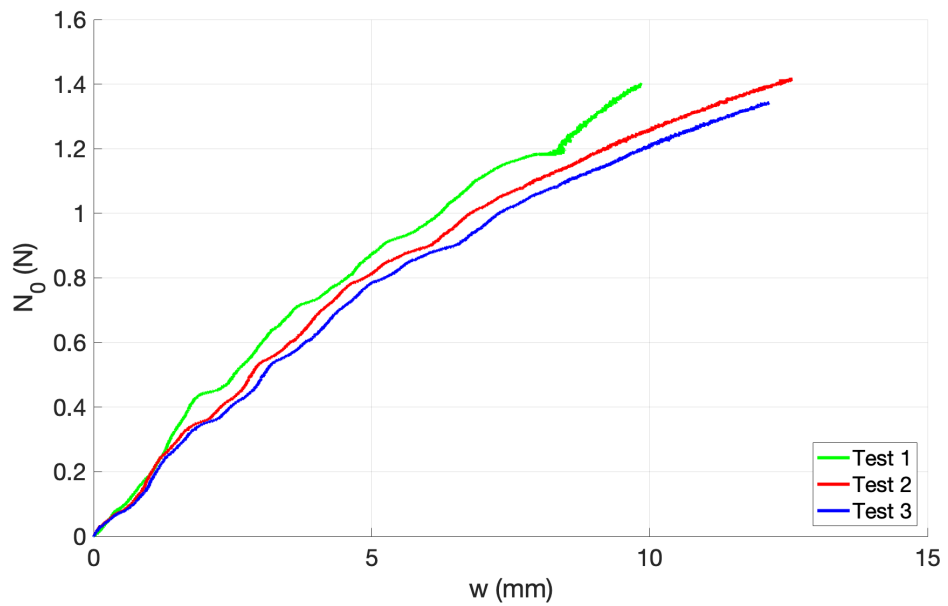
(a)
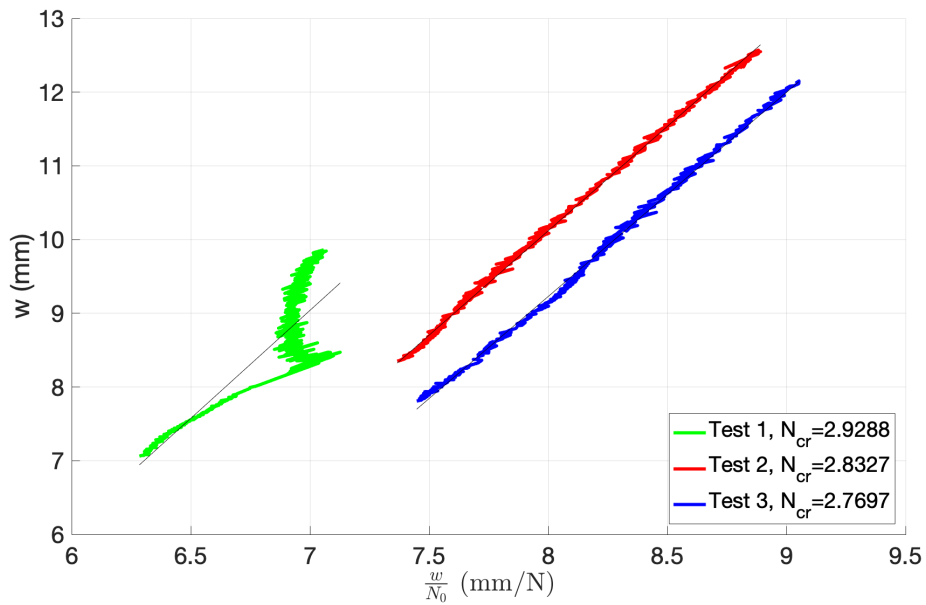
(b)

Figure 5.24: Buckling test of the BPZT5 beam.

Comparing the buckling loads of the BPZT3 and BPZT4 (Figs.[5.22b-5.23b]) it is evident that the anti-symmetric lamination influences the buckling load since the

value of the BPZT4 is almost half the BPZT3 value. The same happens between the BPZT1 and BPZT4 in Figs.[5.20b-5.21b], but in that case the higher buckling load of the BPZT1 is justified also by the additional patch which increases the beam stiffness. Moreover, comparing the results for the BPZT4 and the BPZT5, the buckling load of the BPZT5 is rightfully higher since the beam has an additional patch.

The mean values of the buckling loads evaluated experimentally for each beam are indicated in Table [5.10] with the corresponding standard deviation, σ, and coefficients of variation, CV. The RZT models are those shown in Chapter 4 and the buckling loads numerically calculated are those indicated in Table [4.11]. The RZT critical buckling load of the BPZT1 is within the range of two standard deviations of the mean of the critical loads found experimentally, whereas the numerical predictions for all the other beams are all within the range of one standard deviation of the mean of the experiments.

	EXP (N)	σ (N)	CV %	RZT (N)	ERR %
BPZT1	8.64	0.14	1.64	8.40	-2.78
BPZT2	5.97	0.09	1.51	5.90	-1.23
BPZT3	3.97	0.10	2.45	4.00	0.84
BPZT4	2.42	0.20	8.39	2.52	4.13
BPZT5	2.84	0.08	2.66	2.85	0.23

Table 5.10: Buckling loads of the monolithic beams: comparison between the experimental results (EXP) and RZT.

The results in Table [5.10] prove the high accuracy of the RZT also for the buckling load calculation of beams with geometric discontinuities and anti-symmetric laminations. The predictions are excellent for the BPZT(2,3,5), with errors lower than 1% for the BPZT(3,5) and with only -1.23% error for the BPZT2. The negative value can be explained by the fact that the adhesive used for the actuator bonding has not been considered in the numerical model because it has been applied only on a small portion of the beam. However, it probably has a small influence on the shortest beams, the BPZT2 and also the BPZT1, which has two actuators and the RZT error is -2.8%. The error is slightly higher for the BPZT4 reaching 4%, but it is still excellent for experimental results.

For these beams, the RZT load-displacement equilibrium paths shown in 4.3.3 have been compared to the corresponding experimental curves in Figs.[5.25-5.29]. It can be seen that RZT is extremely accurate not only for the buckling load calculation but also for prediction of the nonlinear response of beams with geometric discontinuities subjected to an axial-compressive load. A small difference can be

observed only for the BPZT5 in Fig.[5.29], but this beam has a very strong anti-symmetry due to its anti-symmetric lamination and location of the patches.

It can be noticed that some curves in the Southwell plots of Figs.[5.22b-5.24b] slightly deviate from the linear trend predicted by the Southwell method, indicating that the portion of the corresponding curves in the load-displacement path do not perfectly have the shape of rectangular hyperbolas (which become straight lines in the $\left(\frac{w}{N_0}, w\right)$ plane). In general, the Southwell method is very sensitive to which point is chosen to select the portion of curve in the load-displacement path that is approximated as a rectangular hyperbola (the starting point). In these experiments, the chosen points correspond to 80% of the maximum applied load of each case (value suggested by Southwell). Considering that Southwell formulated his method for homogeneous beams, it is reasonable to believe that the composite nature of the material of the piezo-composite beams, the anti-symmetric lamination and the geometric interfaces can affect the load-displacement path which deviates from a rectangular hyperbola trend. Moreover, for each beam, only one of the three curves in the Southwell plot significantly deviates from a straight line, but the slope of the fitting line is close to those obtained by the other tests. Only the curve of the Test 3 in Fig.[5.23b] exhibits a significant deviation, which is also indicated by the higher value of *CV* in Table [5.10]. However, also in this case the *CV* is less than 10%, thus it is reasonably acceptable for experiments.
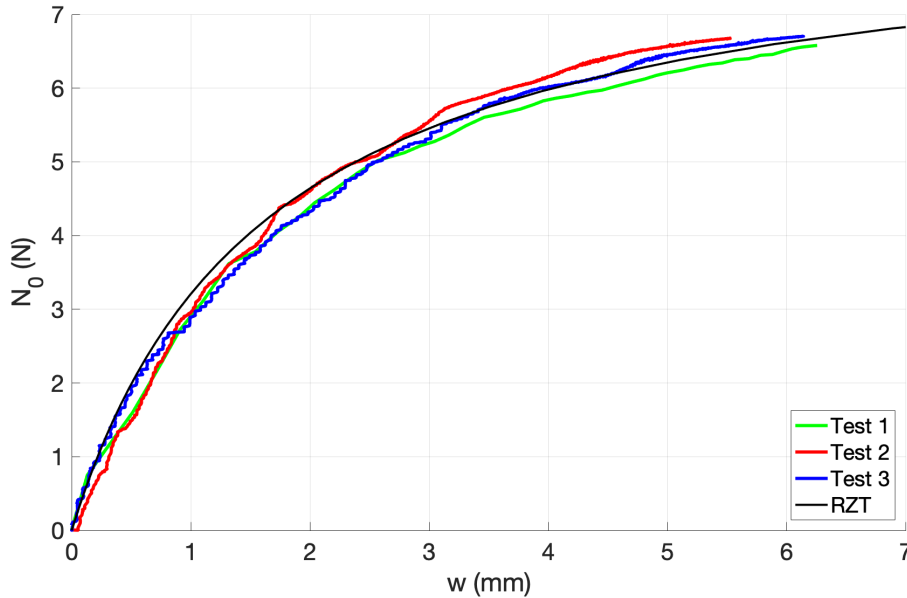
Figure 5.25: Comparison between the experimental and the RZT nonlinear response for the BPZT1.
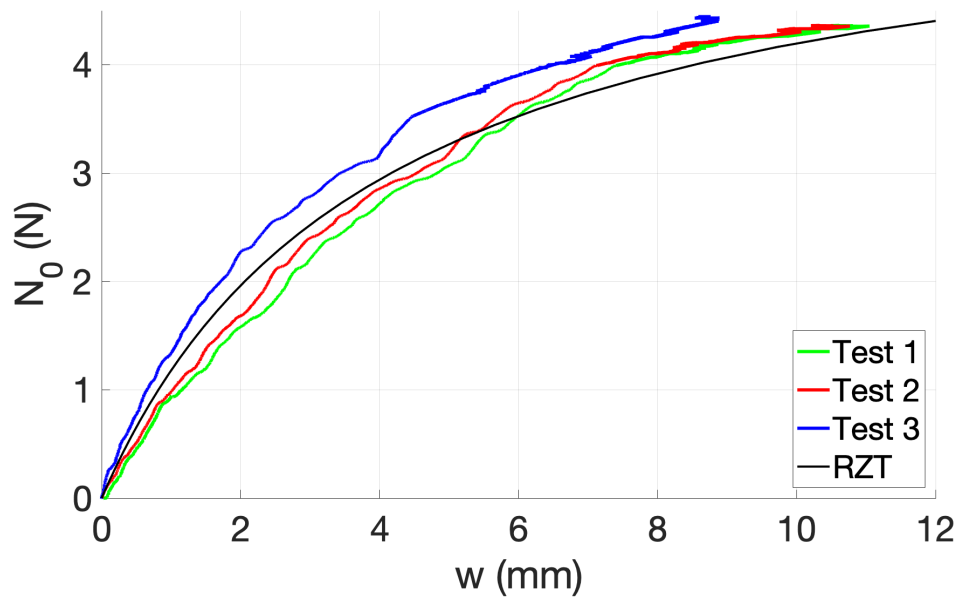
Figure 5.26: Comparison between the experimental and the RZT nonlinear response for the BPZT2.
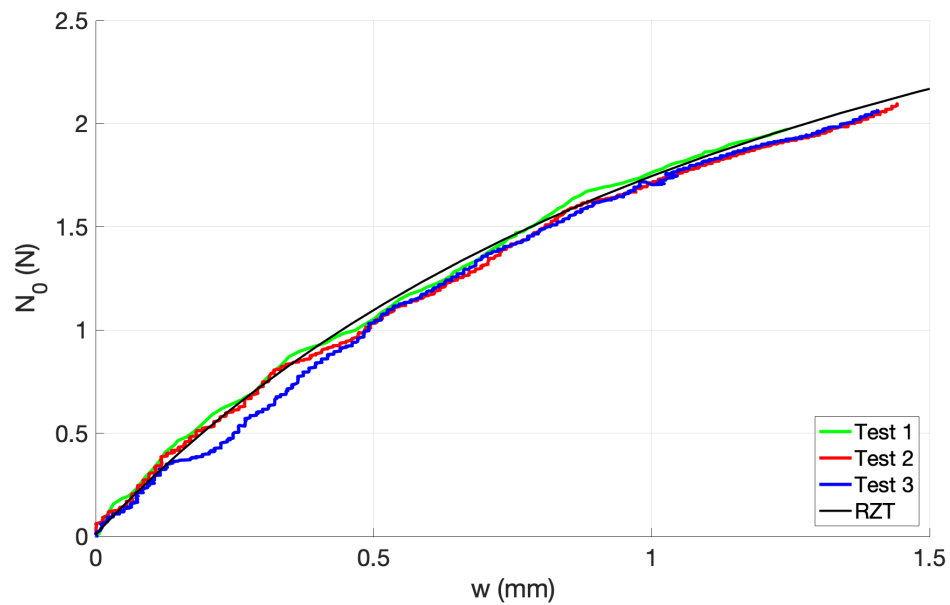
Figure 5.27: Comparison between the experimental and the RZT nonlinear response for the BPZT3.
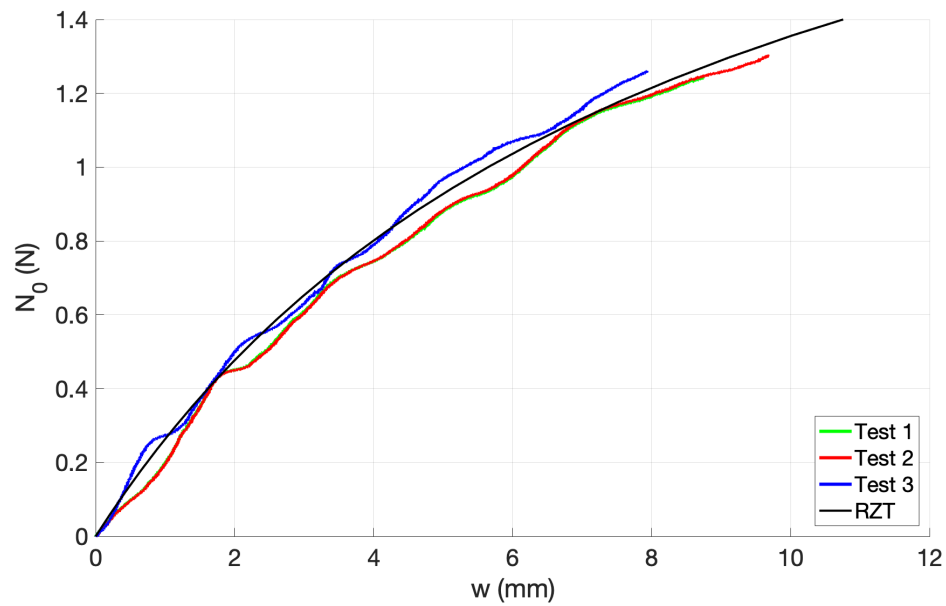
Figure 5.28: Comparison between the experimental and the RZT nonlinear response for the BPZT4.
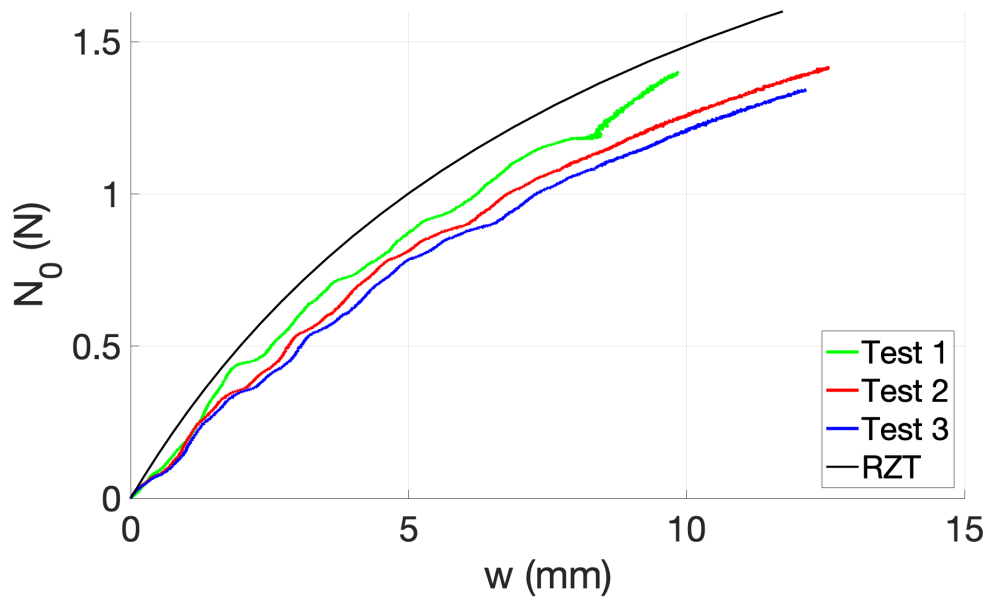
Figure 5.29: Comparison between the experimental and the RZT nonlinear response for the BPZT5.

5.5.2 Static response to the actuation

The BPZT(1-3) have been considered in the following analyses for investigating the possibility to use the piezoelectric actuators to decrease the initial geometric imperfection of the beams and increase the buckling load. The numerical analyses have been performed in Section 4.3.5 of Chapter 4, but considering a maximum voltage of -700 V. However, in practical application this is not possible because the maximum operational negative voltage for the MFC-P1 is -500 V, thus the maximum voltage considered for the tests is -350 V to not be too close to the limit. The BPZT(2,4-5) have an initial deviation that is too big to be significantly reduced in this voltage range, using one actuator or two actuators in the configuration of the BPZT5. The BPZT2 has been considered just as comparison to the BPZT1 because they have a similar geometry but symmetric (BPZT1) and anti-symmetric (BPZT2) laminations.

The voltage has been applied to the actuators of the BPZT(1-3) in order to deflect the beams in the opposite direction to their initial deviation. A negative voltage is then applied to the actuator on the top surfaces of the BPZT(1-3) and a positive voltage has been applied to the actuator on the bottom surface of the BPZT1. Two power supplies, the Trek 677A, have been used, one to apply the positive voltage and one for the negative.

The beams have been tested in the Instron machine in the same configuration of the buckling tests (Fig.[5.19]) but not applying any mechanical load. The voltage has been slowly increased from 0 to ± 350 V in steps of 50 V, waiting 30 s per each increment and measuring the corresponding transversal deflection. The test has been repeated three times for each beam.

Figs.[5.30-5.32] report the results of the tests and the RZT numerical predictions. For this kind of tests, the beams are hinged at both ends since the actuation tends to straighten them and the Instron grips do not move. The nonlinear response of the beams to the actuation is calculated solving Eq.[3.100] with the Newton-Raphson method, as explained in 4.3.5. It can be seen that the RZT model is able to accurately predict the beam response to a piezoelectric voltage for both the symmetric, BPZT(1,3), and the anti-symmetric, BPZT2, beams. The slight difference between the experiments and RZT in Figs.[5.30]-[5.32] for high values of voltage is due to the fact that the transversal deflection at the measuring point along the length of the BPZT1 and the BPZT3 is reaching the location corresponding to those of the beams in their straight axis configuration ($w * (x = 148) = 1.39$ for the BPZT1 and $w * (x = 224) = 1.37$ for the BPZT3). As explained in 4.3.5, the RZT curve changes its curvature because, for further increments of voltage, the beam starts to deflect in the opposite direction with respect to its axis. The deflection measured during the experiments, instead, simply increases with the voltage without changing its curvature because when the beam starts to bend in the opposite direction the actuation increases the imperfection and the supports used at the

150

beam ends become simply-supported boundary condition. It can be seen that the difference between the numerical prediction and the experiments for the BPZT1 in Fig.[5.30] is higher than that for the BPZT3 in Fig.[5.32]. This is probably due the fact that the BPZT1 is shorter, thus the difference between the RZT boundary conditions and the actual boundary conditions when the beam starts to deflect in the opposite direction affects the results more than in the BPZT3, which is also less stiff (it is longer and has only one piezoelectric patch). The modelling of the response of the beam when it bends in the opposite direction is not a purpose of this work because the actuators are supposed to reduce the imperfection. This is also the reason why the comparison for the BPZT3 has been done for a range of voltage 0-300 V, because further increments cause the imperfection inversion.
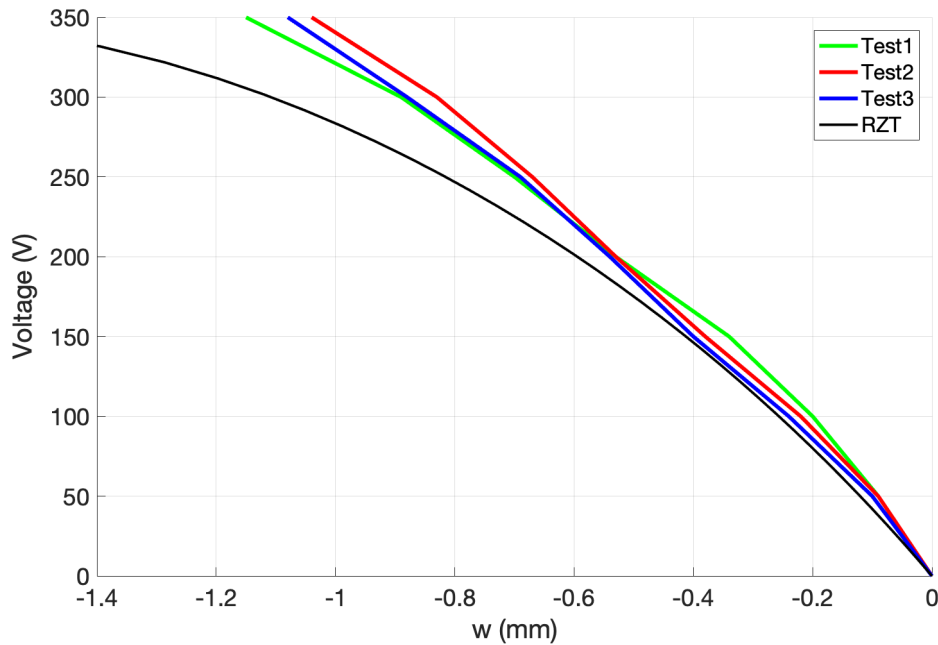
Figure 5.30: Transversal deflection of the beam BPZT1 in double-hinged boundary conditions increasing the voltage from 0 V to 350 V.
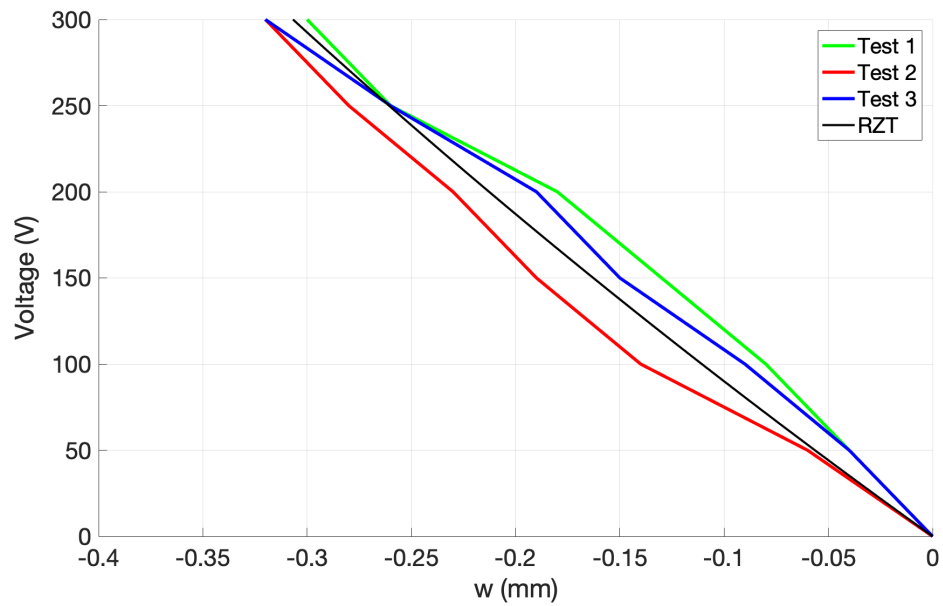
Figure 5.31: Transversal deflection of the beam BPZT2 in double-hinged boundary conditions increasing the voltage from 0 V to 350 V.
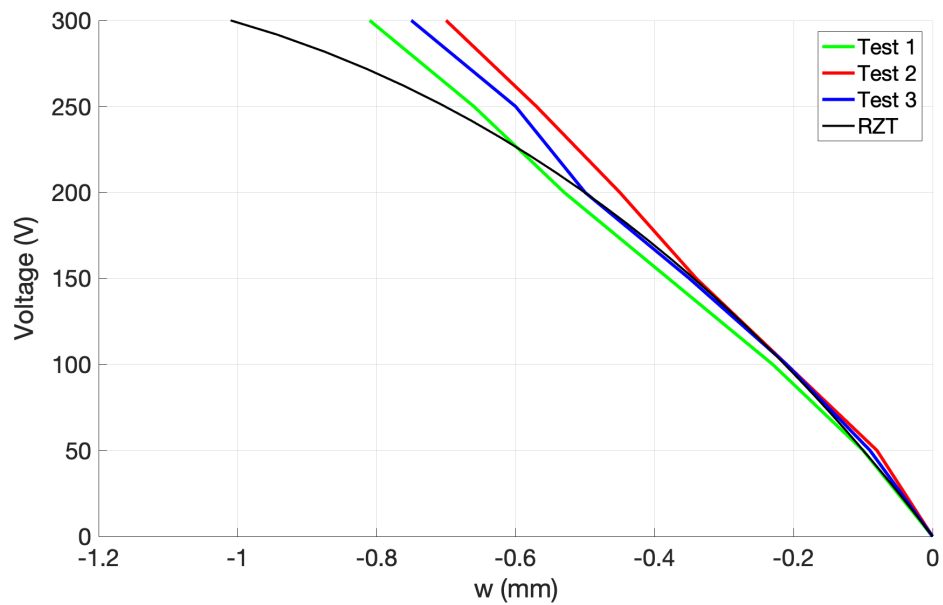
Figure 5.32: Transversal deflection of the beam BPZT3 in double-hinged boundary conditions increasing the voltage from 0 V to 300 V.

5.5.3 Use of the piezoelectric actuators for increasing the buckling load

The buckling tests have been repeated for the BPZT(1-3) applying a different voltage in the actuators every time. The voltage has been applied before the mechanical-compressive load in order to reduce the beam initial deflection and then it has been kept constant while the beam has been subjected to an increasing compressive load. Values of 50 V, 100 V, 200 V have been considered for the BPZT1 and BPZT3 tests, with negative values for the actuators on the top surfaces and positive values for the actuator on the bottom surface of the BPZT1. Higher voltages would have caused the imperfection inversion. The values of voltage considered for the BPZT2 are -50 V, -100 V, -200 V and also -350 V, since the beam has a higher imperfection than the BPZT1 and only one actuator, thus a lower deflecting capability.

In Figs.[5.33-5.35] the experimental load-displacement curves are compared to the RZT. To obtain the numerical results, a first nonlinear analysis has been performed for a two-hinged beam with only the electrical voltage applied and, subsequently, the beam nonlinear response to an increasing mechanical-compressive load has been calculated considering the initial imperfection corresponding to the final deformed shape of the previous analysis and simply-supported boundary conditions.

In general, it can be seen that the initial slope of the curve is higher decreasing the initial imperfection by applying an increasing value of voltage and this is much more evident for the BPZT1 (Fig.[5.33]) comparing the curves corresponding to 0 V to those corresponding to 200 V. Moreover, increasing the voltage, the experimental curves of all the beams do not translate simply backward, but the slope at higher value of voltage increases too. As a consequence, applying the Southwell method the experimental buckling load increases, as indicated in Table [5.11].

	N_{cr}				
	0 V	50 V	100 V	200 V	350 V
BPZT1	8.60	9.74	9.96	10.28	-
BPZT2	5.90	5.94	6.83	6.99	7.23
BPZT3	4.00	4.16	4.66	5.31	-

Table 5.11: Experimental critical buckling loads for different applied voltage.

The numerical methods based on the calculation of the buckling loads as the eigenvalues of Eq.[3.110] are not able to predict this increment, since the asymptotic value of the load does not change when the imperfection, and thus the initial slope of the load-displacement curve, reduces. Nevertheless, it can be seen that RZT is able to predict the curve trends for the considered voltages. For the BPZT1 and

the BPZT3 in Figs.[5.33-5.35] it can be seen that the RZT curves for 0 V, 50 V and 100 V are very close for low values of N_0, while the curve at 200 V has a clearly higher slope since the beginning. On the other hand, in Fig.[5.34] all the curves have the approximately the same initial slope in both experimental and numerical results.

In practical application, a non-destructive critical buckling load is defined as the load corresponding to the point of the curve before the slope decreases of a certain percentage (e.g. 20% in [120]), thus the initial slope is the most significant quantity to predict. Moreover, both the experimental results and RZT show that, increasing the voltage in the actuators, the load-displacement equilibrium paths of the beams become closer to the curve that ideally approximates the behaviour of a perfect column which implies an increasing value of the real critical buckling load determined by the yield-stress limit [72].
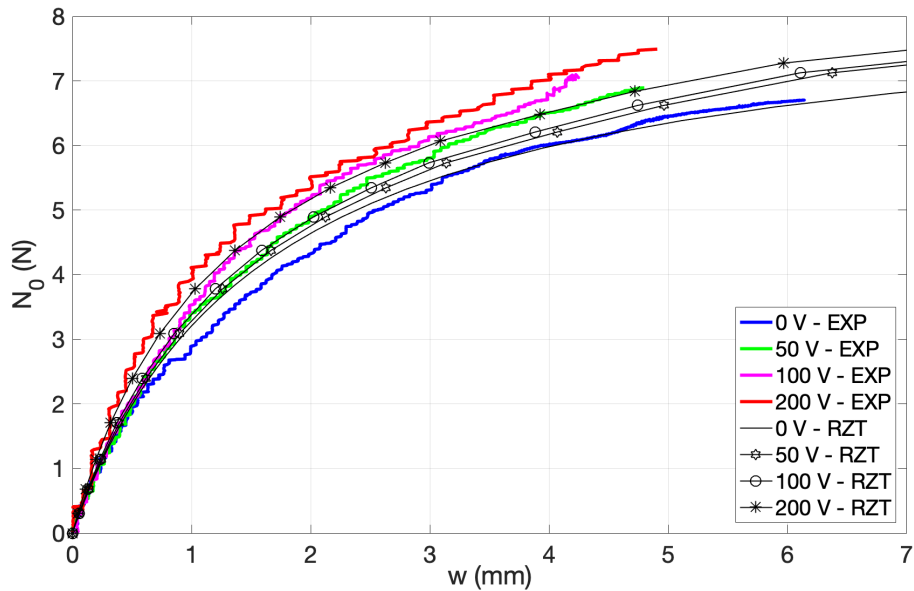
Figure 5.33: Load-deflection equilibrium curves for different values of voltage applied in the actuator of the BPZT1: experimental and RZT solution.
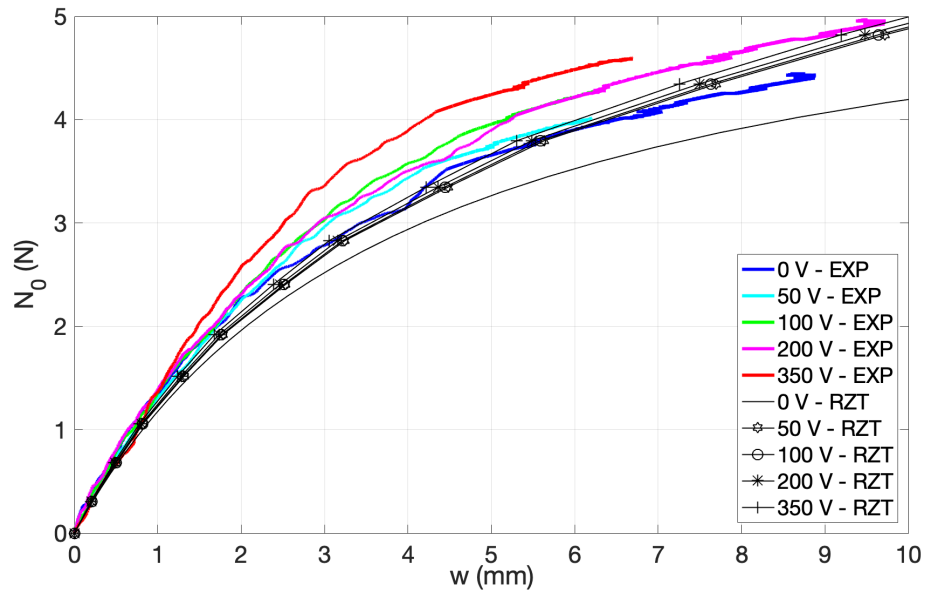
Figure 5.34: Load-deflection equilibrium curves for different values of voltage applied in the actuator of the BPZT2: experimental and RZT solution.
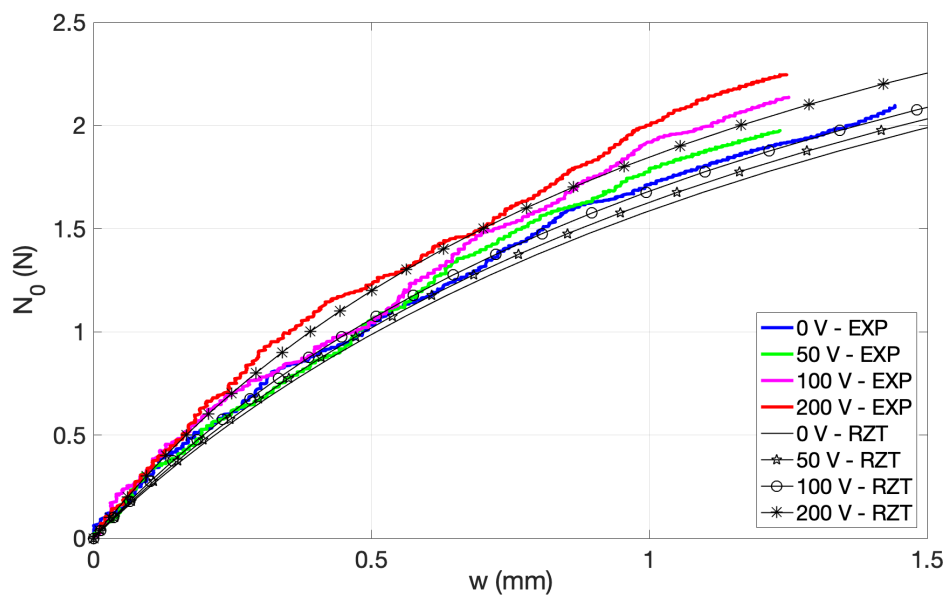
Figure 5.35: Load-deflection equilibrium curves for different values of voltage applied in the actuator of the BPZT3: experimental and RZT solution.

5.6   Discussion on the time required for manufacturing and testing

In order to compare the time required for calculating the critical buckling load with the numerical methods and the experiments, an estimate of the time spent for making one sample of each kind of beams considered in this thesis is here given. This estimate is clearly based on the author experience and knowledge.In general, the manufacturing time is strongly dependent on the equipment available in the laboratory, the number of people working and their abilities. The specimens used in this project were all manufactured and tested by the author only.

The overall time needed for manufacturing the beams and performing the tests was five months, not including the collection of the materials and the tools used in the experiments. The activity which required the biggest amount of time was the specimens manufacturing and the preliminary tests for characterising the boundary conditions.

The manufacturing of the CFRP plates for making the piezo-composite beams and the sandwich beam facesheets was done in one day. This estimate includes the prepreg thawing (a minimum time of six hours at $20\,degC$ was considered), the cutting, the laying-up and the debulking every fourth ply, the vacuum bag preparation and the autoclave curing process, which takes up to 4 hours if the heating up and the cooling down are considered.

Many other samples were fabricated for the boundary conditions testing and those specimens were made of various thickness, which meant that a higher number of plates had to be manufactured (one for each thickness and layer orientation). The specimens for the boundary conditions were relatively thick, thus the lay-up process was considerably longer than that for the specimens used in the tests for the RZT validation.

The piezo-composite beams were obtained from the CFRP plates, cutting them and bonding the piezoelectric patches to the CFRP stripes. The cutting, the surface preparation and the bonding of the piezoelectric patches (cured in oven for 3 hours) took up to one day. Nevertheless, the manufacturing of the sandwich specimens was much more time consuming. Indeed, once the facesheets were cured they had to be sanded and prepared for bonding. An additional cure cycle was required for bonding the facesheets to the core, and the specimens in the vacuum bag had to be protected with frames to avoid the squashing of the foam under the pressure (the frames had to be manufactured too). After the curing, the beam edges had to be refined to obtain very straight samples (parallel edges). The manufacturing of the sandwich beams, their refinement and the bonding to the supports used as simply-supported boundary conditions took one month, but this strongly depended on the available equipment.

Assuming that all the materials and the tools are available, such as the frames

for the sandwich beam bagging, the average time required for the fabrication and the testing of one piezo-composite beam is 2 days, whereas 4 days are necessary for one sandwich beam.

In conclusion, the need of experiments for validating the numerical methods is undisputed, but they can be extremely onerous in terms of both time and cost, especially for testing composites. Comparing these estimates to the time required by the RZT and Abaqus shown in the previous sections, it is clear that reliable numerical methods represent an essential instrument for the structural analysis, especially for parametric and design studies.

5.7   Conclusion

The new nonlinear RZT finite element model has been experimentally validated for the buckling analysis of composite beams in different situations, like highly heterogeneous sandwich beams and composite laminated beams with geometric discontinuities due to the presence of piezoelectric actuator patches.

Sandwich beams with CFRP facesheets and foam core have been realised and tested in compression for the buckling load evaluation using the Southwell method. For these beams, specific supports have been created to make simply-supported boundary conditions for thick beams, since they guarantee a higher reliability of the experimental buckling tests compared to other boundary conditions. The results of the tests have been used to verify the RZT predictions of buckling loads, demonstrating the superior capabilities of RZT also for highly heterogeneous and relatively thick beams.

The buckling load has been evaluated also for monolithic beams with piezoelectric patches actuators to assess the RZT predictions in case the beam has geometric discontinuities. Compared to the experimental data, the RZT buckling loads and the nonlinear responses are excellent. Moreover, it has been shown that the fibre orientation in the beam layers has a significant influence on the nonlinear response and the critical buckling load value, also for very thin beams, thus the importance of using finite elements based on theory suitable for composites has been demonstrated. Then, the static response to the voltage applied to the actuators has been measured and compared to the RZT. The voltage has been used to reduce the initial geometric imperfection of the beams in order to increase the buckling load. For this reason, the buckling tests have been performed again but with voltage applied to the actuators. The comparison between the experiments and the RZT has proven the excellent capabilities of the theory for predicting both situations, correctly evaluating the nonlinear static response of the beam to the voltage and the increment of the initial slope of the load-displacement curves for various values of voltage.

Chapter 6

Buckling and postbuckling analyses of a pre-debonded piezo-composite sandwich beam

6.1   Introduction

In this chapter the new RZT-FE model is extended to the analysis of pre-debonded beams subjected to axial-compressive loads.

The model is assessed for the challenging application of a sandwich beam with a debonding between the core and one of the facesheets. The first two buckling loads and buckling modes are calculated for several values of debonding length and compared to the results obtained by a highly-detailed FE model realised in Nastran.

Subsequently, the beam is modelled with two piezoelectric layers on the external surfaces, one on top and one on the bottom. The piezoelectric layers are activated considering different voltage values, either constant or variable along the beam length, to identify to best voltage distribution for controlling the local buckling.

6.2   Finite element models of a pre-debonded sandwich beam

The sandwich beam considered for this application, called WF-32-2-d, has CFRP facesheets and a Rohacell®WF110 foam core (see Tables [4.1 and 4.8] for the material properties). The facesheets are made of four layers with a ply orientation of [0°/90°/0°/90°] for the bottom facesheet and [90°/0°/90°/0°] for the top facesheet. Each facesheet has a thickness $h_f = 2$ mm whereas the thickness of the core is $h_c = 4$ mm. The assumed width, b, is three times the total thickness and the total length of the beam is $L =320$ mm.

A debonding is assumed between the core and the top facesheet. The total length of the debonding is indicated as L_d and it is symmetrically distributed on the left and the right of the beam centre, as shown in Fig.[6.1]. The extension of RZT model to this application does not include any control on the contact between the two sublaminates, thus the method cannot predict the initiation or the propagation of the debonding. The aim of this study is a numerical verification of the RZT for the calculation of the buckling loads and modes of a sandwich beams with one facesheet locally separated from the core in the way it is done by other authors in the literature using commercial finite element codes. For this reason, the adhesive layer between the core and the facesheets has not been considered neither in the RZT nor in the finite element model realised using the commercial code.
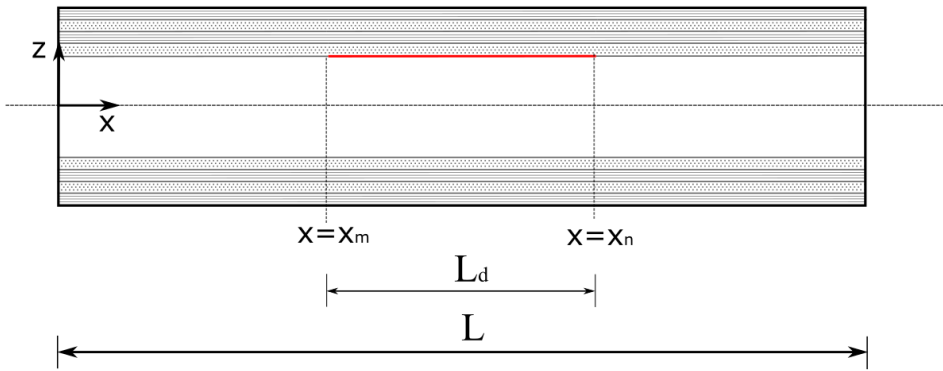
Figure 6.1: Sandwich beam with a debonding between the core and the top facesheet.

The strategy adopted for modelling beams with delaminations/debondings using the new RZT model is explained in 3.6.1 of Chapter 3.

The debonding between the core and the top facesheet divides the beam into two sub-laminates in the region where they separate; one sublaminate corresponds to the bottom facesheet and the core and the other sublaminate corresponds to the top facesheet. As a consequence, both the sublaminates have an anti-symmetric lamination whereas the intact parts of the beam are symmetric. Two RZT-beam finite elements are considered across the thickness along L_d, whereas only one finite element is considered across the thickness of the intact parts of the beam (see Fig.[6.2]). Indicating with x_m and x_n the axial coordinates where the debonding respectively starts and ends, two geometrical interfaces are considered at $x = x_m$ and at $x = x_n$. At $x = x_m$, the first interface is between the intact beam and the bottom sublaminate, whereas the second interface is between the intact beam and the top sublaminate (the top facesheet). Vice versa, for $x = x_n$ the first interface is between the bottom sublaminate and the intact beam, whereas the second interface

is between the top sublaminate and the intact beam. In all cases, the geometrical interface is due to a variation of both the thickness and the materials between two consecutive finite elements, and the strategy based on the Lagrange multipliers method is employed to correctly link the finite elements at the interfaces.
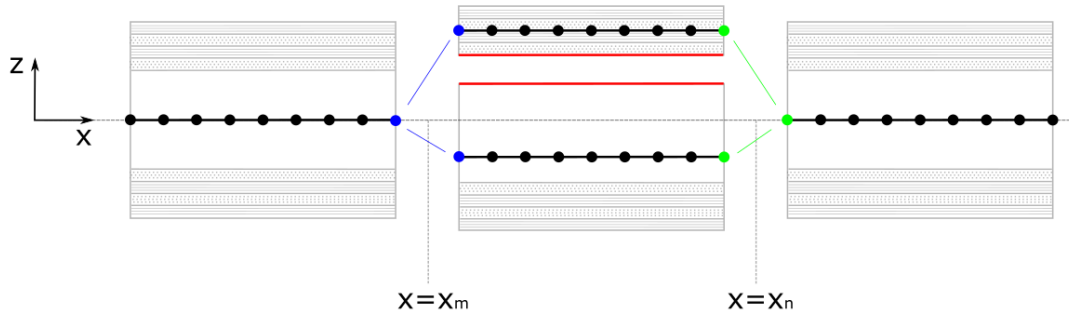
Figure 6.2: Finite element model of the sandwich beam with a debonding between the core and the top facesheet.

Six different values are assumed for L_d, corresponding to 0%, 10%, 20%, 50%, 80% and 90% of the total length of the beam.

The number of finite elements of the RZT model depends on the value of L_d. The same number of finite elements is considered in the two intact parts and the same number of finite elements is considered in the two sublaminates. Assuming a length of 4 mm for each finite element, the resulting numbers of elements for each value of L_d are those shown in Table [6.1].

$\mathbf{L_d}$	**No. of elements**		
(mm)	intact part	along L_d	total
0	80	-	80
32	36	8	88
64	32	16	96
160	20	40	120
256	8	64	144
288	4	72	152

Table 6.1: Number of finite elements of the one-dimensional RZT model.

The reference, plane-stress, model is realised in Nastran using 2D shell elements in the (x, z) plane. The debonding is taken into account uncoupling the nodes at the interface between the core and the top facesheet for a length corresponding to L_d. Since the beam material and geometrical properties do not change from one

case to the other because the only difference is the number of uncoupled nodes depending on L_d, the creation of a Nastran session file is very convenient.

6.3   Buckling analysis of the pre-debonded beam

The RZT model is assessed for the buckling analysis of the sandwich beam presented in the previous section considering simply-supported boundary conditions. The first two buckling loads and mode shapes are compared to those obtained from a buckling analysis of a Nastran highly-detailed two-dimensional finite element model.

The buckling loads of the RZT models are calculated solving the eigenvalue problem of Eq.[3.110] in 3.4.1.

In Table [6.2], the first two buckling loads are reported and compared to the corresponding Nastran values.

L_d	Nastran (N)	RZT (N)	ERR %
0%	4569.77	4579.37	0.21
	10215.96	10265.48	0.48
10%	4567.66	4227.60	-7.45
	7011.456	7019.18	0.11
20%	3409.43	3206.70	-5.95
	4528.39	4053.13	-10.50
50%	1093.79	1028.92	-5.93
	2030.26	2141.94	5.50
80%	767.18	741.46	-3.35
	879.27	924.80	5.18
90%	700.71	735.00	4.89
	750.19	735.72	-1.93

Table 6.2: First two buckling loads of the sandwich beam for various debonding lengths L_d expressed as percentage of the total beam length L.

As already demonstrated in the previous chapters, RZT is extremely accurate for predicting the buckling loads of the intact beam. In the other cases, the percentage error is higher than 1% (in modulus), but the results show that the error and the debonding length value are uncorrelated. Indeed, the maximum error on the first buckling load is obtained for the shortest value of L_d, where RZT underestimates the critical load of 7.45%. Increasing the value of L_d, the percentage error on

the first buckling load slightly diminishes, reaching a minimum of 3.35% when $L_d = 0.8L$. At the maximum debonding length considered ($L_d = 0.9L$) instead, the RZT critical buckling load is 4.89% higher than the prediction obtained by Nastran. A similar trend can be observed for the percentage error on the second buckling load, however, in this case the error is lower than 1% for both $L_d = 0$ and $L_d = 0.1L$. The maximum error on the second buckling load is obtained for $L_d = 0.2L$, where RZT underestimates the buckling load of 10.50%, whereas for $L_d = 0.5L$ and $L_d = 0.8L$ the RZT overestimates the buckling load of 5%. At $L_d = 0.9L$, the RZT second buckling load is lower than Nastran, and the percentage error is only -1.93%.

This results show that even small debondings cause a reduction of the buckling loads. The percentage difference ($\Delta\%$) between the buckling loads obtained for each value of L_d and the corresponding buckling load of the intact beam are reported in Table [6.3]. In the RZT analysis, the buckling loads are reduced by 7.7% and 30% when a debonding of 10% is considered, whereas in Nastran there is a significant decrement only for the second buckling load (30% as RZT). In any other case, the reduction of the buckling load value with respect to the intact beam calculated by RZT and Nastran are almost the same, reaching -84% on the critical buckling load and -92% on the second buckling load for $L_d = 0.9L$.

$\mathbf{L_d}$	$\boldsymbol{\Delta}\%$			
	1st buckling load		2nd buckling load	
	Nastran	RZT	Nastran	RZT
10%	-0.04	-7.67	-31.37	-31.62
20%	-25.40	-29.96	-55.68	-60.52
50%	-76.06	-77.53	-80.13	-79.13
80%	-83.22	-83.82	-91.40	-90.99
90%	-84.66	-83.95	-92.66	-92.83

Table 6.3: Percentage difference between the buckling load obtained for $L_d \neq 0$ and the corresponding buckling load of the intact beam, for each value of L_d.

The first two buckling mode shapes obtained by RZT and Nastran are plotted in Figs.[6.3-6.8] for every value of L_d considered. The conventional buckling mode shapes of a simply-supported beam can be seen in Figs.[6.3] for the case of the intact beam, where the Nastran solution is plotted as a two-dimensional model.

(a) 1st mode Nastran.

(b) 2nd mode Nastran.

(c) 1st mode RZT.

(d) 2nd mode RZT.
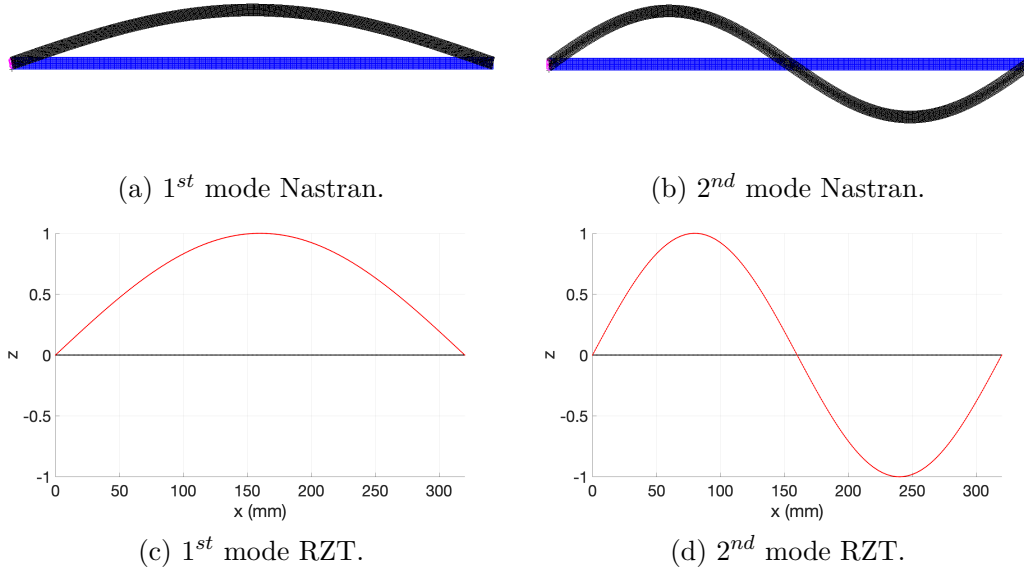
Figure 6.3: Buckling mode shapes of the WF-32-2-d sandwich beam for $L_d = 0$.

In Figs.[6.4a-6.8a], the mode shapes obtained in Nastran are represented reporting the transversal displacements of only the nodes at half thickness of each part of the beam (as the black nodes indicated in Fig.[6.2]), with those corresponding to the upper sublaminate in red to distinguish them from the lower sublaminate.

In Figs.[6.4] it can be seen that the presence of even a small debonding between the core and the top facesheet influences both the mode shapes. The effect on the first buckling mode is more evident for RZT (Fig.[6.4c]), where it can be seen that the two sublaminates tend to separate. However, it is still a global buckling because the order of magnitude of the displacements in both sublaminates is the same. The second buckling mode shape is anti-symmetric, as for an intact beam, but the shape is slightly different because the locations of the points which have the maximum or minimum transversal displacements are not $x = L/4$ and $x = 3/4L$, but they are closer to the beam centre. For higher values of L_d the two mode shapes exchange (Figs.[6.5-6.7]) and the buckling mode corresponding to the critical buckling load is anti-symmetric (Figs.[6.5a-6.7d]). The maximum and minimum peaks of the transversal displacement move from the centre of the beam to the beam ends the higher is the value of debonding length, for $0.2L \leq L_d \leq 0.8L$. The second buckling mode shape, instead, is similar to the first and symmetric buckling mode of the intact beam. The two sublaminates deflect on the same side of the beam but the upper sublaminate (the top facesheet in the debonded part of the beam) has a higher deflection than the lower sublaminate.

When L_d reaches 90% of the total length, the two mode shapes exchange again

163

(Fig.[6.8]). At the critical buckling load, the beam exhibits a local buckling because the deflection of the top sublaminate is significantly higher than the bottom sublaminate which remains almost flat.

The inversion of the two buckling mode shapes was proven experimentally in [120], where it is shown that increasing the debonding length in a composite multilayer beam, the beam buckles in an anti-symmetric mode when the debonding has a length between the values corresponding to the global and the local buckling.

(a) 1st mode Nastran.

(b) 2nd mode Nastran.

(c) 1st mode RZT.

(d) 2nd mode RZT.
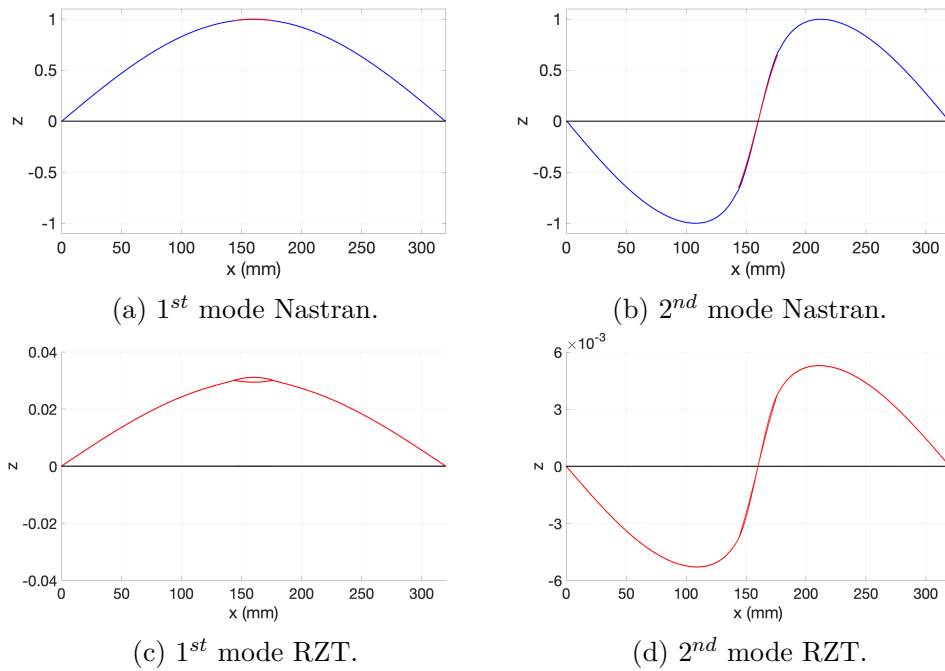
Figure 6.4: Buckling mode shapes of the WF-32-2-d sandwich beam for $L_d = 0.1L$.

(a) 1st mode Nastran.

(b) 2nd mode Nastran.

(c) 1st mode RZT.

(d) 2nd mode RZT.
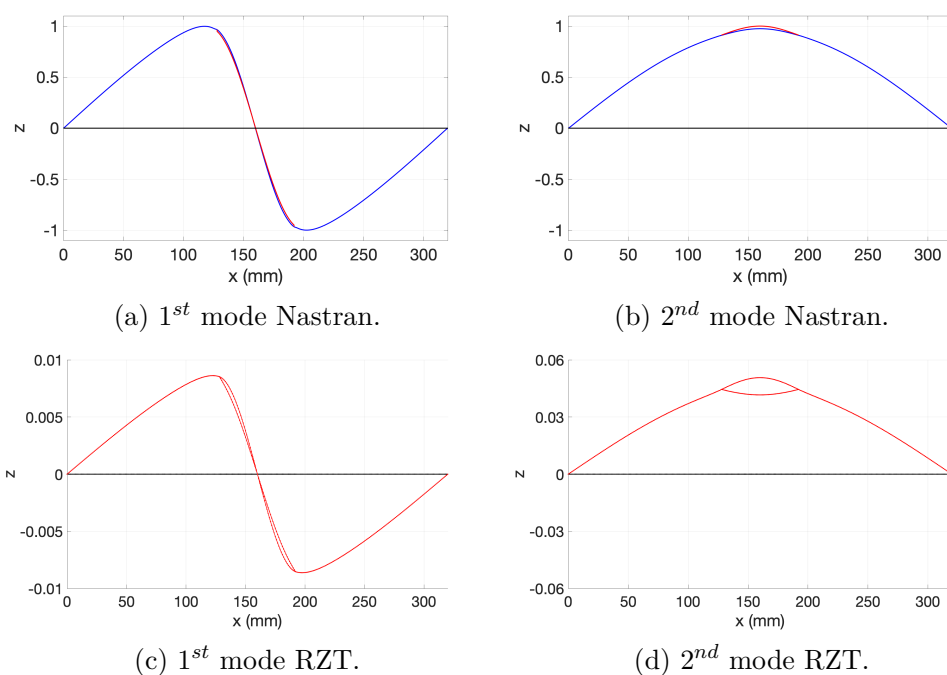
Figure 6.5: Buckling mode shapes of the WF-32-2-d sandwich beam for $L_d = 0.2L$.

(a) 1st mode Nastran.

(b) 2nd mode Nastran.

(c) 1st mode RZT.

(d) 2nd mode RZT.
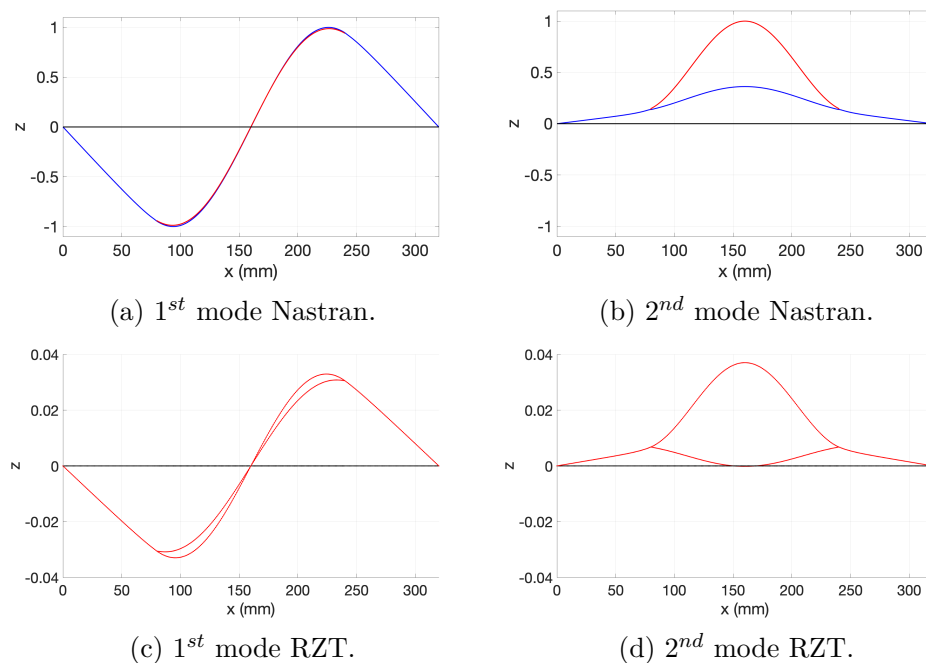
Figure 6.6: Buckling mode shapes of the WF-32-2-d sandwich beam for $L_d = 0.5L$.

(a) 1st mode Nastran.

(b) 2nd mode Nastran.

(c) 1st mode RZT.

(d) 2nd mode RZT.
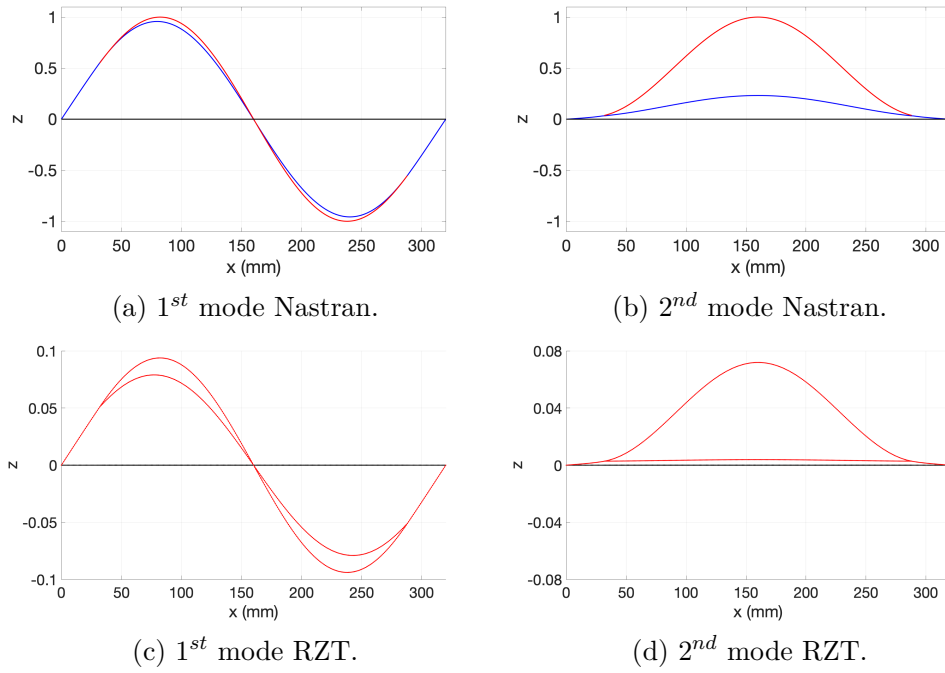
Figure 6.7: Buckling mode shapes of the WF-32-2-d sandwich beam for $L_d = 0.8L$.

(a) 1st mode Nastran.

(b) 2nd mode Nastran.

(c) 1st mode RZT.

(d) 2nd mode RZT.
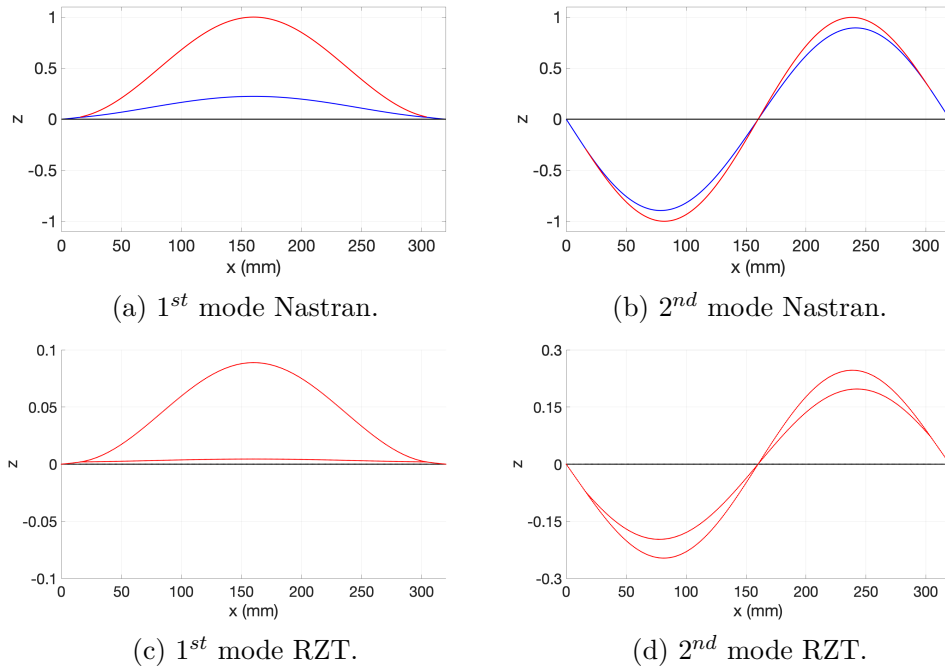
Figure 6.8: Buckling mode shapes of the WF-32-2-d sandwich beam for $L_d = 0.9L$.

In Fig.[6.9], the ratio between the critical buckling load, N_{cr}, and the critical buckling load of the intact beam N_{cr0} is reported as function of L_d/L. Initially, the ratio slightly decreases to 0.9 for $L_d/L = 0.1$. In this region the analysis of the buckling mode shapes indicates that the buckling is still global. For higher values of L_d/L the curve rapidly drops down to almost $N_{cr}/N_{cr0} = 0.2$ for $L_d/L = 0.5$ and then the slope starts to diminish in modulus and the curve almost becomes flat. The behaviour of the beam for $0.2L \leq L_d \leq 0.8L$ is usually indicated as *mixed-mode* buckling because the beam exhibits both a global and a local instability. The beam behaviour for $L_d/L = 0.9$ is a local buckling because the bottom sublaminate do not deflect significantly compared to the top sublaminate.
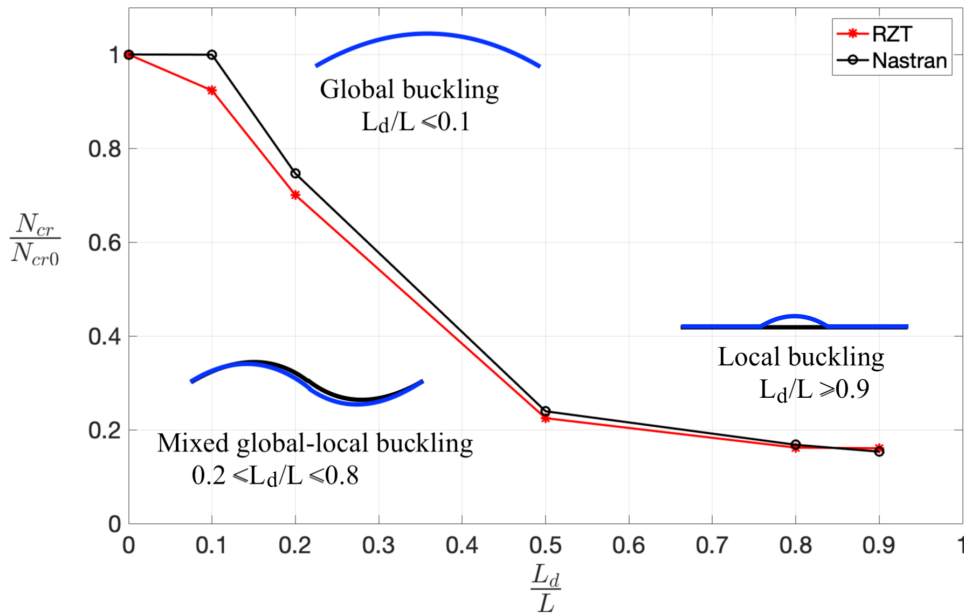
Figure 6.9: Critical buckling load reduction increasing the value of the debonding length L_d.

6.4 Nonlinear analysis of the pre-debonded sandwich beam with piezoelectric actuators

Two layers of piezoelectric material are considered on the top and the bottom surfaces of the sandwich beam. The material properties of the pieoelectric layers are those indicated in Table [4.8] and the e_{31}−effect is assumed as operational mode of the piezoelectric actuators. The critical buckling load changes because of the additional piezoelectric layers, increasing from 4579.37 N to 5015.5 N for the intact beam and from 735 N to 867.81 N for the debonded beam with $L_d/L = 0.9$

($L_d = 288$ mm).

The first buckling mode shapes of the sandwich beam with piezoelectric actuator layers are reported in Fig.[6.10] for the intact and the debonded configurations.

(a) Intact beam.

(b) Debonded beam, $L_d/L = 0.9$.
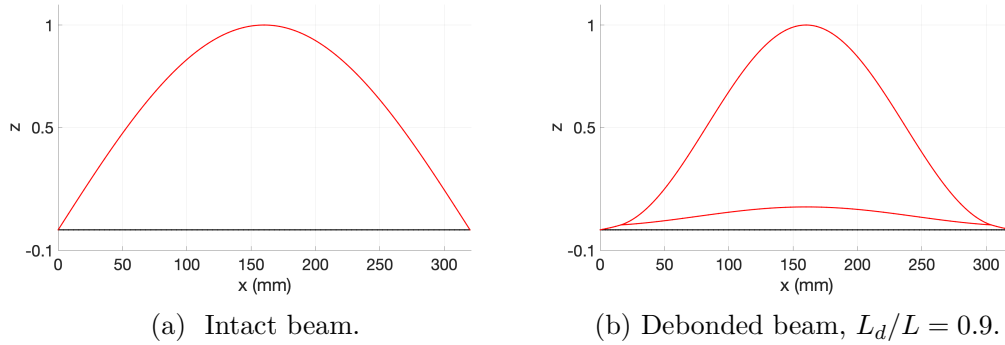
Figure 6.10: First buckling mode of the sandwich beams with piezoelectric actuator layers.
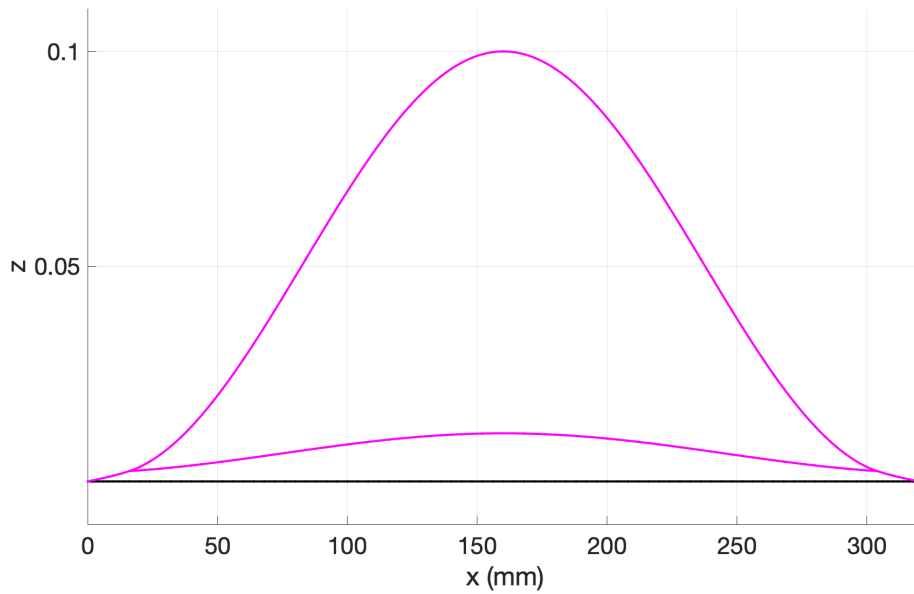
Figure 6.11: Initial geometric imperfection for the debonded beam corresponding to 1% of the first buckling mode shape.

The nonlinear response of the debonded beam to an increasing axial-compressive load is calculated assuming that the beam has an initial geometric imperfection corresponding to 1% of the first buckling mode shape normalised setting to 1 mm the

maximum transversal displacement. As a consequence, the beam initial imperfection has a maximum deflection of 0.1 mm at x=160 mm, as shown in Fig.[6.11].

The beam nonlinear response is calculated solving Eq.[3.109] with $N_{xc}^e = -N_0$. The value of the applied compressive load, N_0, is increased from $N_0 = 0$ to $N_0 = 0.9N_{cr}$ in steps of $\Delta N_0 = 60.8$ N. For each N_0, the beam deformed shape and the transversal displacements of the two nodes at x=160 mm are calculated. Indeed, the two sublaminates have different finite elements, thus there are two nodes at x=160 mm, one belonging to the lower sublaminate and one belonging to the upper sublaminate. The corresponding transversal displacements are indicated as w_b and w_t, respectively. Fig.[6.12a] reports the deformed shapes for all the values of N_0 considered, whereas Fig.[6.12b] shows the load-displacement equilibrium paths of w_b and w_t. Each colour in Figs.[6.12a-6.12b] corresponds to a specific value of N_0, thus the load corresponding to a certain deformed shape in Fig.[6.12a] can be derived from the ordinate of the markers in Fig.[6.12b] with the same colour as the deformed shape.
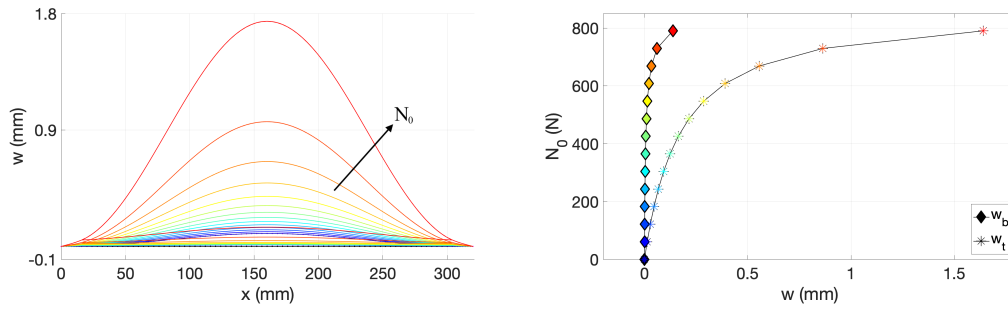
(a) Deformed shapes for the values of N_0 reported in Fig.[6.12b].

(b) Equilibrium paths for x=160 mm.

Figure 6.12: Beam response increasing N_0.

6.5 Local buckling control using piezoelectric actuators

In this section, the possibility of controlling the local buckling using the piezoelectric actuator layers is investigated performing the postbuckling analysis of the beam considering various values of voltage in the actuator. Ideally, the equilibrium paths of the nodes of the sublaminates should be the same to avoid the local buckling, which is characterised by a significantly bigger deflection of the top sublaminate than the lower sublaminate for the same value of load applied to the sandwich beam.

Seven different combinations of voltage value and distribution are considered

to identify the most efficient combination for the local buckling control. They are indicated as *case B, C, D, E, F, G, H* whereas *case A* indicates the solution obtained in the previous section for zero applied voltage.

Case B

A first analysis is conducted activating the entire upper piezoelectric layer with a voltage $\bar{V}^B = -50$ V, constant along the beam length. As a consequence of the negative voltage, the piezoelectric layer contracts and the beam deflects opposite to the $z-$coordinate, towards its perfect configuration. In Fig.[6.13a] it is indicated the beam in its initial configuration, with a geometric imperfection corresponding to 1% of the first buckling mode, and the deformed shape after the application of $\bar{V}^B = -50$ V. It can be seen that the maximum deflection of the top sublaminate decreases from 0.1 mm to 0.09 mm whereas the bottom sublaminate almost reaches the perfect configuration. In Fig.[6.13b], the nonlinear response of the beam increasing N_0 is reported in terms of the transversal displacement of the node of each sublaminate for x=160 mm. The results obtained in this case correspond to the blue curves, indicated as *B*, to distinguish them from those of obtained for zero actuation, indicated as *case A*.

The comparison between the *case A* and the *case B* in Fig.[6.13b] indicates that the application of $\bar{V}^B = -50$ V to the top layer does not affect the nonlinear response significantly, thus in the following case a higher voltage is considered.
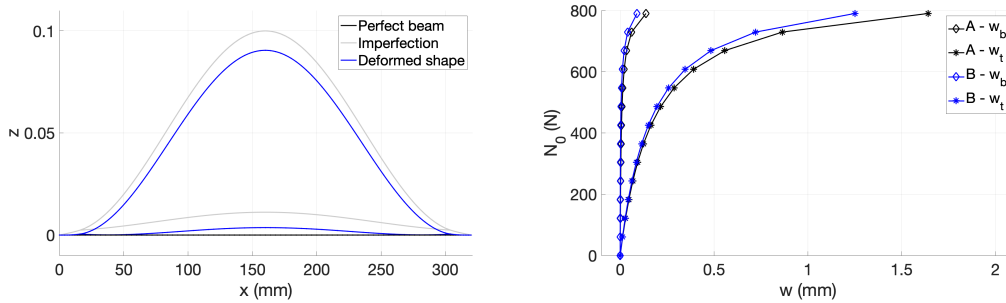
(a) Deformed shape due to the actuation. (b) Equilibrium paths for x=160 mm.

Figure 6.13: Nonlinear analysis of the beam: (a) deformed shape due to the actuation (*case B*) and for $N_0 = 0$, (b) nonlinear response increasing N_0.

Case C

The results obtained applying a voltage $\bar{V}^C = -100$ V to all the top layer are reported in Fig.[6.14]. After the actuation, the maximum deviation of the top sublaminate from the straight axis configuration is 0.08 mm, lower than the corresponding value in *case B*. The bottom sublaminate translates downward, indicating

that the high voltage in the top piezoelectric layer is able to considerably influence also the bottom sublaminate (see Fig.[6.14a]). The effect of the actuation $\bar{V}^C$ on the nonlinear response of the beam is shown in Fig.[6.14b]. The curve corresponding to w_t is slightly closer to w_b than the previous case (as an example, it can be seen that for $N_0 = 700$ N, the value of $w_t = 0.5$ mm in *case C* whereas it is $w_t = 0.6$ mm in *case B*) indicating a better performance than before.

(a) Deformed shape due to the actuation.   (b) Equilibrium paths for x=160 mm.

Figure 6.14: Nonlinear analysis of the beam: (a) deformed shape due to the actuation (*case C*) and for $N_0 = 0$, (b) nonlinear response increasing N_0.

Case D

In *case D* the effect of different voltage values along the beam length is investigated to assess the influence of the actuation location on the beam response. For this reason, the piezoelectric layers are assumed to be made of 20 piezoelectric patches, each of them 16 mm long. Consequently, on the external surface of each sublaminate there are 18 patches. In *case D*, only the patches on the top sublaminate are activated with constant values of $\bar{V}^D_1 = -50$ V in the first six patches, $\bar{V}^D_2 = -100$ V in the following six patches and $\bar{V}^D_3 = -50$ V in the remaining six patches. The results for this configuration are shown in Fig.[6.15]. Comparing the two deformed shapes of *case C* and *case D* after the actuation, it can be seen a much better result for *case D*, where both sublaminates are closer to the straight axis configuration than *case C*. This is obtained using $\bar{V}^D_2 = -100$ V, which means that -100 V are applied to less than 1/3 of the beam length and in the remaining part the voltage is lower (either $\bar{V}^D_1 = \bar{V}^D_3 = -50$ V or null). In *case C* instead, it is $\bar{V}^C = -100$ V along the entire top layer. This clearly indicates a strong dependence of the beam deflection on the actuators location. However, the better initial configuration due to the *case D* actuation does not significantly improve the beam postbuckling behaviour (Fig.[6.15]), which is almost the same as *case B* (Fig.[6.14b]), but it is worth noting that the same result has been obtained with an average lower voltage.

171

(a) Deformed shape due to the actuation.   (b) Equilibrium paths for x=160 mm.

Figure 6.15: Nonlinear analysis of the beam: (a) deformed shape due to the actuation (*case D*) and for $N_0 = 0$, (b) nonlinear response increasing N_0.

In the following cases (*case E, F, G*) it is assumed a continuous distribution of the applied voltage dependent on the initial imperfection. In each finite element, the average of the initial imperfection values measured at the two nodes is taken as factor to create a distribution of voltage along the piezoelectric layers.

Cases E and F

In *case E* and *case F*, the voltage is applied only to the top sublaminate assuming a distribution of the voltage values proportional to the initial geometric imperfection of the beam in that region. In *case E*, the maximum applied voltage is $\bar{V}^E_{max} = -100$ V whereas in *case F* the maximum value is $\bar{V}^F_{max} = -200$ V.

The results obtained for *case E* are reported in Fig.[6.16]; despite the better effect of the actuation on the deformed shape for $N_0 = 0$, there is not any significant improvement on the nonlinear response with respect to *case D* (compare Fig.[6.16b] to Fig.[6.15b]).

A considerably better response is obtained in *case F*. The two sublaminates are much closer after the actuation (Fig.[6.17a]) and also the curve indicating the postbuckling response of the upper sublaminate almost doubles its slope moving towards the equilibrium-path of the lower sublaminate (as an example in Fig.[6.17b] for $N_0 = 700$ N, $w_t = 0.25$ mm).

(a) Deformed shape due to the actuation.

(b) Equilibrium paths for x=160 mm.
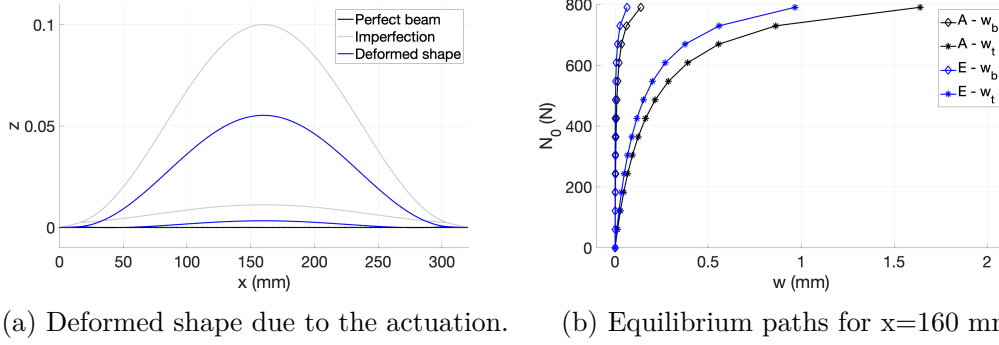
Figure 6.16: Nonlinear analysis of the beam: (a) deformed shape due to the actuation (*case E*) and for $N_0 = 0$, (b) nonlinear response increasing N_0.

(a) Deformed shape due to the actuation.

(b) Equilibrium paths for x=160 mm.
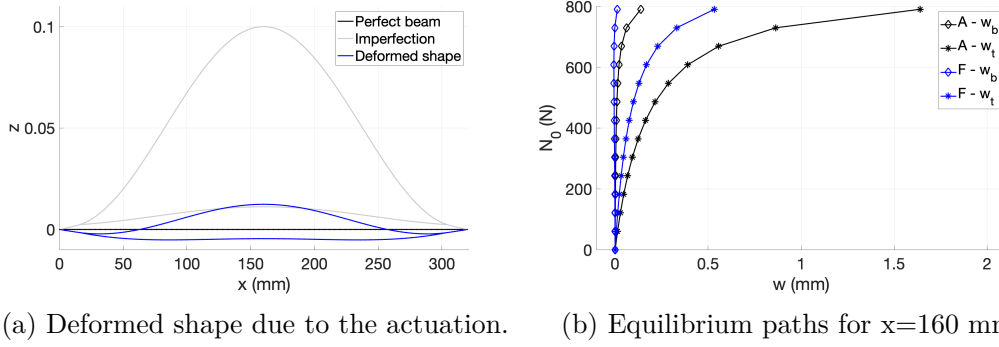
Figure 6.17: Nonlinear analysis of the beam: (a) deformed shape due to the actuation (*case F*) and for $N_0 = 0$, (b) nonlinear response increasing N_0.

Case G

To further improve the response, a negative voltage is applied to the bottom piezoelectric layer. The contraction of the actuator layer deflects the lower sublaminate upward, toward the upper sublaminate. In *case G*, the voltage is applied as a continuous distribution in both the piezoelectric layers. The distribution is proportional to the initial geometric imperfection of the beam but its maximum value is defined independently in each piezolectric layer. Moreover, the maximum (negative) value applied to the top layer is $\bar{V}^G_{max} = -200$ V, whereas it is $\bar{V}^G_{max} = -400$ V in the bottom layer. The results for *case G* are reported in Fig.[6.18]. It is clear that the actuation of also the bottom layer does not significantly improve the postbuckling behaviour of the beam since the equilibrium paths in Fig.[6.18b] are very similar to those of Fig.[6.17b] for the *case F*.

173

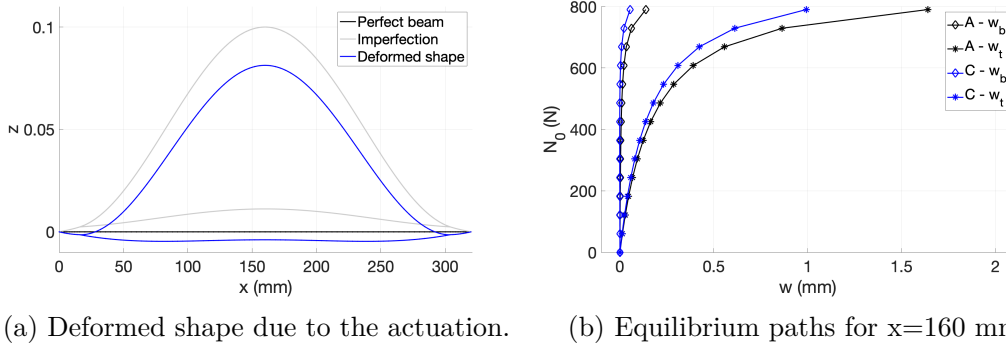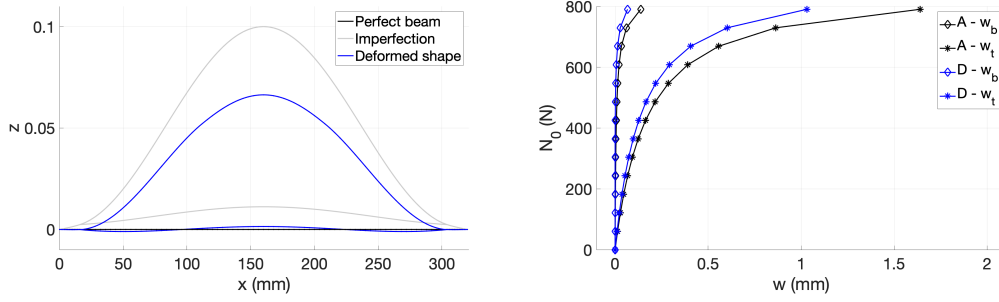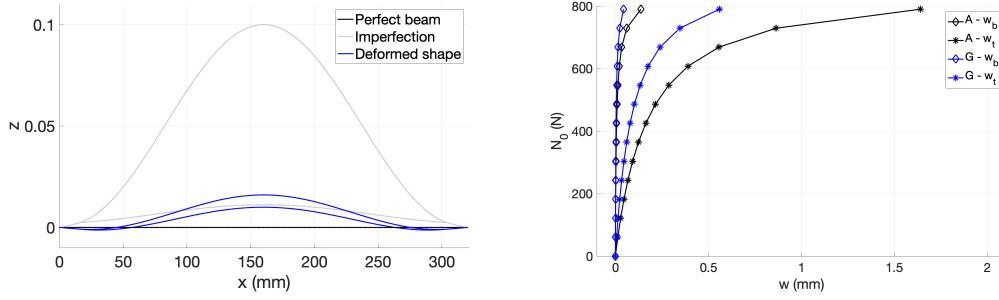(a) Deformed shape due to the actuation. (b) Equilibrium paths for x=160 mm.

Figure 6.18: Nonlinear analysis of the beam: (a) deformed shape due to the actuation (*case G*) and for $N_0 = 0$, (b) nonlinear response increasing N_0.

Case H

The best performances are obtained in *case H* (Fig.[6.19]), where the voltage is distributed along the beam as in *case G* but the values are linearly increased from $\bar{V}^G_{max} = -200$ V and $\bar{V}^G_{max} = -400$ V to $\bar{V}^G_{max} = -350$ V and $\bar{V}^G_{max} = -450$ V, respectively (these are the maximum values of the distributions), while increasing the value of N_0 for the postbuckling analysis.

In Fig.[6.19a], the deformed shape of the beam for $N_0 = 0.95N_{cr}$ is shown for both *case G* and *case H*, indicating *case G* with V_{const} and *case H* with V_{var}. It can be seen that the beam deflection is considerably lower in *case H* and, more important, that the two sublaminates are much closer than *case G* even if the applied load N_0 has almost the critical buckling value. Moreover, the equilibrium paths of the two sublaminates in Fig.[6.19b] are almost the same which indicates a behaviour corresponding to a global buckling.
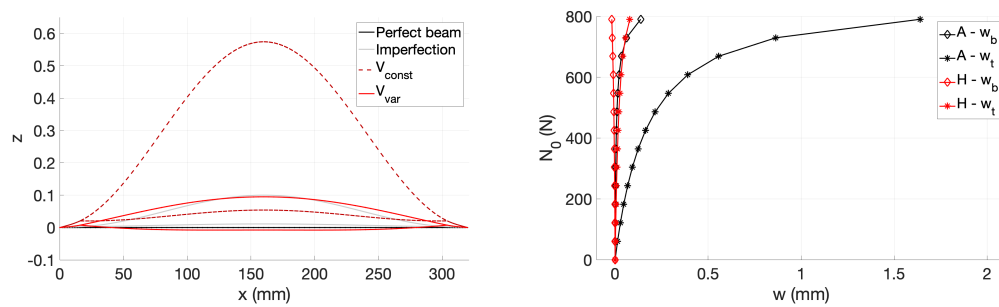
(a) Deformed shape due to the actuation. (b) Equilibrium paths for x=160 mm.

Figure 6.19: Nonlinear analysis of the beam: (a) comparison between the deformed shapes of *case G* and *case H* for $N_0 = 0.95N_{cr}$, (b) nonlinear response increasing N_0.

174

6.6   Conclusion

The new RZT-FE model has been extended to the analysis of a pre-debonded sandwich beam subjected to axial-compressive loads.

A separation between the core and the top facesheet has been considered and the buckling loads and mode shapes have been calculated. The comparison with a highly-detailed two-dimensional finite element model realised in Nastran has proven the accuracy and efficiency of the RZT method. Indeed, both the buckling loads and mode shapes have been accurately predicted by RZT, despite the simplicity of the finite element model which employs one-dimensional beam finite elements. In addition, the analysed structure is a foam core sandwich beam with CFRP facesheets, which means a highly heterogeneous material lamination.

As conclusive application, the model has been employed for studying the possibility of controlling the local buckling using piezoelectric actuators. To this purpose, two continuous layers of piezoelectric material have been considered on the top and bottom surfaces of the beam. An initial geometric imperfection has also been considered to perform nonlinear postbuckling analyses.

Firstly, the entire top layer has been activated with a uniform negative voltage along the beam length. Then, different voltages along the beam length have been considered applying higher voltages where the initial imperfection is higher. The deformed shapes of the beam obtained applying the voltage to the actuator have been shown for each case, but the effect on the local buckling control has been investigated by analysing the load-displacement equilibrium paths of the two nodes at the centre of the beam of each sublaminates. The best results have been obtained for a continuous distribution of the voltage proportional to the geometric imperfection of the beam. In this case, the two equilibrium paths are closer than the other cases considered.

Subsequently, the bottom layer has been activated too, and excellent results have been obtained by linearly increasing the voltage during the postbuckling analysis. Activating both the top and bottom piezoelectric layers with a continuous voltage distribution proportional to the geometric imperfection and increasing the values in the way that the maximum voltage varies linearly from -200 V and -400 V to -350 V and -450 V, respectively, on the top and bottom layer, the two equilibrium paths almost coincide even for values of compressive load N_0 close to the critical buckling.

As a result, the new RZT model has been successfully employed for the buckling and postbuckling analyses of debonded sandwich beams. It has been numerically assessed for the buckling load calculation, proving its accuracy compared to highly-detailed two-dimensional finite element models. In addition, it has been shown how to use this tool for efficiently studying the local buckling control using piezoelectric actuators and the results show that it is possible to control the local buckling applying voltages that do not exceed the range of the maximum allowed negative voltages

of conventional piezoelectric actuators [125]. This study has also highlighted the possibility of successfully using piezoelectric actuators on relatively thick beams for static applications.

Chapter 7

Summary and conclusions

7.1 Summary of major findings

The aim of this work was to create a new method, as accurate as highly-detailed finite element commercial code models but more efficient, for performing buckling and postbuckling analyses of composite laminated and sandwich beams with piezoelectric actuators, with the possibility to use the piezoelectric actuators for controlling the global and local postbuckling response of the beams.

A detailed literature review identified the Refined Zigzag Theory (RZT) as suitable theory to use for the development of a finite element formulation highly accurate and efficient for the buckling and the nonlinear postbuckling analyses of both composite laminated and sandwich beams with piezoelectric actuators. A general formulation based on C^0 RZT-beam finite elements was created for studying both the global and the local buckling and postbuckling of composite beams with geometric imperfections and piezoelectric actuator layers or patches. The numerical and experimental assessments shown in the previous chapters demonstrated the successful achievement of the main objective of this work.

The outcomes have already been discussed in detail at the end of each chapter, but they are also summarised below.

The literature review about the most used technique for the analyses of composite beams pointed out the inaccuracy of both the classical Bernoulli-Euler and the Timoshenko beam theories and identified more suitable analytical methods for composites: the High-order Shear Deformation Theories, the Layer-Wise theories and the Zigzag theories. The Refined Zigzag Theory resulted very attractive because of its superior capabilities for the analyses of both composite laminated and highly heterogeneous sandwich structures, in terms of both high accuracy and computational effort. On the other hand, the finite element commercial codes had beam finite elements based on TBT, thus accurate FE model of composite beams

could be obtained only with two- or three-dimensional models, with a consequently higher computational cost.

The RZT was then chosen as analytical method for the creation of a new finite element model for the buckling and postbuckling analyses of composite beams with geometric imperfections and piezoelectric actuators.

A general analytical formulation for the buckling and postbuckling analyses of composite beams with geometric imperfections and piezoelectric actuators was created introducing the geometric imperfections and nonlinearities, and the inverse piezoelectric effect in the RZT beam formulation. The nonlinear equilibrium equations based on the RZT for imperfect composite beams with piezoelctric actuators were obtained and their solution could provide the nonlinear equilibrium configuration of the beam.

A finite element formulation was generated to solve the equilibrium problem for general beams (any lamination, boundary and loading condition) and the matrix nonlinear FE equation was solved employing the Newton-Raphson method. In addition, a strategy based on the Lagrange multipliers approach was used to extend the method to the analysis of beams with geometric discontinuities, like the presence of piezoelectric patches bonded to the beam external surfaces or pre-debondings/delaminations in the beams.

The new RZT-FE method was implemented in a Matlab routine and numerically assessed through a comparison with highly-detailed two-dimensional finite element models realised in Nastran and Abaqus.

The buckling and postbuckling analyses of imperfect sandwich beams proved the superiority of RZT with respect to TBT finite element models for highly heterogeneous and relatively thick sandwich beams. In addition, the comparison with the results of FE commercial codes demonstrated both the excellent accuracy of the RZT and also the greater efficiency, since the same analyses were performed in less time.

The excellent performances of the RZT method were demonstrated also for the analysis of composite multilayer beams with piezoelectric actuator patches. The reference solution was obtained in Abaqus, and the FE model was realised with three-dimensional finite element to include the piezoelectricity. The RZT predictions for the buckling and postbuckling response were extremely accurate and the time required to perform the analyses was considerably less than Abaqus. Moreover, RZT was assessed also for the evaluation of the nonlinear static response to a piezoelectric actuation and it was demonstrated that the method was as accurate as the Abaqus three-dimensional model also for very high voltages.

The experimental validation of the new RZT method included the manufacturing of composite beams, both sandwich and monolithic with piezoelectric patches

178

bonded to the external surfaces. *Ad-hoc* supports were created for each beam to realise the simply-supported boundary conditions.

All the beams were tested in compression for calculating the critical buckling load employing the Southwell method. The obtained values demonstrated that RZT accurately predicted the critical buckling loads of both highly heterogeneous sandwich beams and also monolithic beams with geometric interfaces due to piezoelectric actuator patches.

The experiments with the monolithic beams proved that the RZT method correctly evaluated the nonlinear static response to the piezoelectric actuation and also excellently predicted the nonlinear postbuckling response.

The conclusive application of the method was the buckling and postbuckling analyses of a sandwich beam with a pre-debonding between the core and the top facesheet. The new RZT method was firstly successfully assessed for the calculation of the buckling loads and mode shapes depending on the debonding length. The assessment was made comparing the RZT results to a highly-detailed Nastran model.

Subsequently, the RZT method was used for investigating the possibility of controlling the local buckling by using piezoelectric actuators. The study identified the best voltage values and distribution which could control the local buckling of the top facesheet. The method proved to be an excellent tool, both accurate and efficient if compared to FE commercial codes, that also allowed the active use of piezoelectric actuators in the nonlinear postbuckling analyses.

7.2 Further work

Despite the major advances provided in this work for the modelling of composite beams, further extensions of the new RZT method and experiments could provide significant improvements to the analysis of composite and sandwich structures. Below some suggestion for possible future investigations.

Firstly, for completely validating the results presented in this thesis, experiments could be performed evaluating the buckling response of sandwich beams with debondings of various length between the core and the facesheets.

Experiments could be also performed for validating the predictions of RZT in terms of local buckling control depending on the voltage value and distribution.

The new RZT model could be extended including the dynamic behaviour of the beam. Indeed, the piezoelectric elements are widely used for dynamic applications (vibration control, Structural Health Monitoring, noise reduction, etc...).

The model could be extended including the thermal loads in the formulation.

179

Finally, a major extension of the method would be the modelling of two-dimensional structures employing the Refined Zigzag Theory for plates [49]. Indeed, in the FE commercial codes the shell elements are based on FSDTs, that were proven to be not suitable for composites, thus accurate models for composite and sandwich plates can be obtained, in the FE commercial codes, only by three-dimensional models. The computational cost is then significantly higher than RZT even for linear static analyses. Then, a remarkable application of the RZT would be the nonlinear postbuckling analysis of composite plates.

Although researcher have been working for decades on methods able to predict the behaviour of composite beams in general conditions, with high accuracy and low computational costs, the most used approaches remains the use of FE commercial codes. However, they are not optimised to be the most efficient technique in general. In addition, the increasing usage of highly heterogeneous composites for primary structural components of the aircraft structure, leads to the need of proper modelling techniques that are both accurate for heterogeneous structures and also able to efficiently perform nonlinear analyses, like the study of the postbuckling behaviour.

This project attempted to fill this gap, in particular in the framework of composite and sandwich beams, and it is hoped that it will significantly contribute to future works on the modelling of composite structures.

Bibliography

[1] S. P. Timoshenko. «On the correction for shear of differential equations for transverse vibrations of prismatic bars». In: *The London, Edinburgh, and Dublin Philosophical Magazine and Journal of Science* 41.245 (1921), pp. 744–746. DOI: https://doi.org/10.1080/14786442108636264.

[2] S. P. Timoshenko. «X. On the transverse vibrations of bars of uniform cross-section». In: *The London, Edinburgh, and Dublin Philosophical Magazine and Journal of Science* 43.253 (1922), pp. 125–131. DOI: https://doi.org/10.1080/14786442208633855.

[3] O. C. Zienkiewicz et al. *The finite element method*. Vol. 3. McGraw-hill London, 1977.

[4] T. J. R. Hughes and R. L. Taylor and W. Kanoknukulchai. «A simple and efficient element for plate bending». In: *International Journal for Numerical Methods in Engineering* 11 (1977), pp. 1529–1543. DOI: https://doi.org/10.1002/nme.1620111005.

[5] A. Tessler and S. B. Dong. «On a hierarchy of conforming Timoshenko beam elements». In: *Computers & Structures* 14 (1981), pp. 335–344. DOI: https://doi.org/10.1016/0045-7949(81)90017-1.

[6] A. Tessler. «An efficient, conforming axisymmetric shell element including transverse shear and rotary inertia». In: *Computers & Structures* 15.5 (1982), pp. 567–574. DOI: https://doi.org/10.1016/0045-7949(82)90008-6.

[7] A. Tessler and T. J.R. Hughes. «A three-node Mindlin plate element with improved transverse shear». In: *Computer Methods in Applied Mechanics and Engineering* 50.1 (1985), pp. 71–101. DOI: https://doi.org/10.1016/0045-7825(85)90114-8.

[8] A. Tessler. «A priori identification of shear locking and stiffening in triangular Mindlin elements». In: *Computer Methods in Applied Mechanics and Engineering* 53.2 (1985), pp. 183–200. DOI: 10.1016/0045-7825(85)90005-2.

[9]   I. Fried, A. Johnson, and A. Tessler. «Minimal-degree thin triangular plate and shell bending finite elements of order two and four». In: *Computer Methods in Applied Mechanics and Engineering* 56.3 (1986), pp. 283–307. DOI: https://doi.org/10.1016/0045-7825(86)90043-5.

[10] A. Tessler and L. Spiridigliozzi. «Resolving membrane and shear locking phenomena in curved shear-deformable axisymmetric shell elements». In: *International Journal for numerical methods in engineering* 26.5 (1988), pp. 1071–1086. DOI: https://doi.org/10.1002/nme.1620260506.

[11] A. Tessler. «A C0-anisoparametric three-node shallow shell element». In: *Computer methods in applied mechanics and engineering* 78.1 (1990), pp. 89–103. DOI: https://doi.org/10.1016/0045-7825(90)90154-E.

[12] A. Barut, E. Madenci, and A. Tessler. «Nonlinear elastic deformations of moderately thick laminated shells subjected to large and rapid rigid-body motion». In: *Finite elements in analysis and design* 22.1 (1996), pp. 41–57. DOI: https://doi.org/10.1016/0168-874X(95)00063-Y.

[13] A. Barut, E. Madenci, and A. Tessler. «Nonlinear analysis of laminates through a Mindlin-type shear deformable shallow shell element». In: *Computer Methods in Applied Mechanics and Engineering* 143.1-2 (1997), pp. 155–173. DOI: https://doi.org/10.1016/S0045-7825(96)01140-1.

[14] A. Barut et al. «A new stiffened shell element for geometrically nonlinear analysis of composite laminates». In: *Computers & Structures* 77.1 (2000), pp. 11–40.

[15] J. Liu, H. R. Riggs, and A. Tessler. «A four-node, shear-deformable shell element developed via explicit Kirchhoff constraints». In: *International Journal for Numerical Methods in Engineering* 49.8 (2000), pp. 1065–1086. DOI: https://doi.org/10.1002/1097-0207(20001120)49:8<1065::AID-NME992>3.0.CO;2-5.

[16] A. Barut, E. Madenci, and A. Tessler. «Nonlinear thermoelastic analysis of composite panels under non-uniform temperature distribution». In: *International Journal of Solids and Structures* 37.27 (2000), pp. 3681–3713. DOI: 10.1016/S0020-7683(99)00119-5.

[17] A. Tessler. «Comparison of interdependent interpolations for membrane and bending kinematics in shear-deformable shell elements». In: *Proceedings of the 8th International Conference on Computational Engineering and Sciences* (Los Angeles, CA, USA). 2000, pp. 18–24.

[18] *Abaqus analysis user's manual.* Dassault Systemes Simulia Corporation. 2014.

[19] *MD/MSC Nastran reference guide.* CA: MSC Software Corporation. 2010.

[20] Dassault Systèmes Simulia Corp. *ABAQUS Theory Manual - Beam element overview*. 2009. URL: https://classes.engineering.wustl.edu/2009/spring/mase5513/abaqus/docs/v6.5/books/stm/default.htm?startat=ch03s05ath73.html.

[21] N. J. Pagano. «Exact solutions for composite laminates in cylindrical bending». In: *Journal of Composite Materials* 3.3 (1969), pp. 398–411. DOI: 10.1177/002199836900300304.

[22] P. Madabhusi Raman and J. F. Davalos. «Static shear correction factor for laminated rectangular beams». In: *Composites Part B: Engineering* 27.3 (1996), pp. 285–293. DOI: https://doi.org/10.1016/1359-8368(95)00014-3.

[23] J. M. Whitney and C. T. Sun. «A refined theory for laminated anisotropic, cylindrical shells». In: *Journal of Applied Mechanics* 41.2 (1974), pp. 471–476. DOI: 10.1115/1.3423312.

[24] R. B. Nelson and D. R. Lorch. «A refined theory for laminated orthotropic plates». In: *Journal of Applied Mechanics* 41.1 (1974), pp. 177–183. DOI: 10.1115/1.3423219.

[25] K. H. Lo, R.M. Christensen, and E.M. Wu. «A high-order theory of plate deformation - Part 1: Homogeneous plates». In: *Journal of Applied Mechanics* 44.4 (1977), pp. 663–668. DOI: 10.1115/1.3424154.

[26] K. H. Lo, R.M. Christensen, and E.M. Wu. «A high-order theory of plate deformation - Part 2: Laminated plates». In: *Journal of Applied Mechanics* 44.4 (1977), pp. 669–676. DOI: 10.1115/1.3424155.

[27] A. K. Noor and W. S. Burton. «Assessment of shear deformation theories for multilayered composite plates». In: *Applied Mechanics Reviews* 42.1 (1989), pp. 1–13. DOI: https://doi.org/10.1016/0263-8223(90)90050-O.

[28] D. Liu and X. Li. «An overall view of laminate theories based on displacement hypothesis». In: *Journal of Composite Materials* 30.14 (1996), pp. 1539–1561. DOI: 10.1177/002199839603001402.

[29] J. N. Reddy. «A generalization of two-dimensional theories of laminated composite plates». In: *Communications in Applied Numerical Methods* 3.3 (1987), pp. 173–180. DOI: https://doi.org/10.1002/cnm.1630030303.

[30] E. J. Barbero, J. N. Reddy, and J. Teply. «An accurate determination of stresses in thick laminates using a generalized plate theory». In: *International Journal for Numerical Methods in Engineering* 29.1 (1990), pp. 1–14. DOI: https://doi.org/10.1002/nme.1620290103.

[31] E. Carrera et al. «Advanced models for free vibration analysis of laminated beams with compact and thin-walled open/closed sections». In: *Journal of Composite Materials* 49.17 (2015), pp. 2085–2101. DOI: 10.1177/0021998314541570.

[32] E. Carrera et al. «Accurate static response of single-and multi-cell laminated box beams». In: *Composite Structures* 136 (2016), pp. 372–383. DOI: 10.1016/j.compstruct.2015.10.020.

[33] M. Filippi and E. Carrera. «Bending and vibrations analyses of laminated beams by using a zig-zag-layer-wise theory». In: *Composites Part B: Engineering* 98 (2016), pp. 269–280. DOI: http://dx.doi.org/10.1016/j.compositesb.2016.04.050.

[34] A. Pagani et al. «Analysis of laminated beams via Unified Formulation and Legendre polynomial expansions». In: *Composite Structures* 156 (2016), pp. 78–92. DOI: 10.1016/j.compstruct.2016.01.095.

[35] E. Carrera. «Theories and finite elements for multi-layered plates and shells: a unified compact formulation with numerical assessment and benchmarking». In: *Archives of Computational Methods in Engineering* 10 (3 2003), pp. 5216–5296.

[36] C.Y. Lee and D. Liu. «An interlaminar stress continuity theory for laminated composite analysis». In: *Computers & Structures* 42.1 (1992), pp. 69–78. DOI: https://doi.org/10.1016/0045-7949(92)90537-A.

[37] D.H.J. Robbins and J.N. Reddy. «Modeling of thick composites using a layer-wise theory». In: *International Journal for Numerical Methods in Engineering* 36.4 (1993), pp. 337–343. DOI: https://doi.org/10.1002/nme.1620360407.

[38] M. Di Sciuva. «A refined transverse shear deformation theory for multilayered anisotropic plates». In: *Atti Accademia delle Scienze di Torino* 118 (1984), pp. 279–295.

[39] A. Tessler, M. Di Sciuva, and M. Gherlone. *Refinement of Timoshenko Beam Theory for composite and sandwich beams using zigzag kinematics*. Technical report. NASA/TP-2007-215086, 2007.

[40] R. C. Averill. «Static and dynamic response of moderately thick laminated beams with damage». In: *Composites Engineering* 4.4 (1994), pp. 381–395. DOI: 10.1016/S0961-9526(09)80013-0.

[41] H. Murakami. «Laminated composite plate theory with improved in-plane responses». In: *Journal of Applied Mechanics (Trans. ASME)* 53.3 (1986), pp. 661–666. DOI: 10.1115/1.3171828.

[42] E. Reissner. «On a certain mixed variational theorem and a proposed application». In: *International Journal for Numerical Methods in Engineering* 20.7 (1984), pp. 1366–1368. DOI: https://doi.org/10.1002/nme.1620200714.

[43] E. Carrera. «On the use of the Murakami's zig-zag function in the modeling of layered plates and shells». In: *Computers & Structures* 82.7-8 (2004), pp. 541–554. DOI: 10.1016/j.compstruc.2004.02.006.

[44] L. Demasi. «Refined multilayered plate elements based on Murakami zig-zag functions». In: *Composite Structures* 70.3 (2005), pp. 308–316. DOI: 10.1016/j.compstruct.2004.08.036.

[45] S. Brischetto, E. Carrera, and L. Demasi. «Improved response of unsymmetrically laminated sandwich plates by using zig-zag functions». In: *Journal of Sandwich Structures & Materials* 11.2-3 (2009), pp. 257–267. DOI: https://doi.org/10.1177/1099636208099379.

[46] U. Icardi and F. Sola. «Assessment of recent zig-zag theories for laminated and sandwich structures». In: *Composites Part B: Engineering* 97 (2016), pp. 26–52. DOI: http://dx.doi.org/10.1016/j.compositesb.2016.04.058.

[47] U. Icardi and A. Urraci. «Free and Forced Vibration of Laminated and Sandwich Plates by Zig-Zag Theories Differently Accounting for Transverse Shear and Normal Deformability». In: *Aerospace* 5 (4 2018), pp. 108–150. DOI: doi:10.3390/aerospace5040108.

[48] A. Tessler and M. Di Sciuva and M. Gherlone. «A refined zigzag beam theory for composite and sandwich beams». In: *Journal of Composite Materials* 43 (2009), pp. 1051–1081. DOI: https://doi.org/10.1177/0021998308097730.

[49] A. Tessler and M. Di Sciuva and M. Gherlone. «A consistent refinement of first-order shear deformation theory for laminated composite and sandwich plates using improved zigzag kinematics». In: *Journal of Mechanics of Materials and Structures* 5 (2010), pp. 341–367. DOI: 10.2140/jomms.2010.5.341.

[50] A. Tessler and M. Di Sciuva and M. Gherlone. «A homogeneous limit methodology and refinements of computationally efficient zigzag theory for homogeneous, laminated composite, and sandwich plates». In: *Numerical Methods for Partial Differential Equations* 27 (2011), pp. 208–229. DOI: https://doi.org/10.1002/num.20646.

[51] M. Gherlone, A. Tessler, and M. Di Sciuva. «C^0 beam elements based on the Refined Zigzag Theory for multilayered composite and sandwich laminates». In: *Composite Structures* 93 (2011), pp. 2882–2894. DOI: 10.1016/j.compstruct.2011.05.015.

[52] L. Iurlaro et al. «Assessment of the Refined Zigzag Theory for bending, vibration, and buckling of sandwich plates: a comparative study of different theories». In: *Composite Structures* 106 (2013), pp. 777–792. DOI: 10.1016/j.compstruct.2013.07.019.

[53] L. Iurlaro, M. Gherlone, and M. Di Sciuva. «Bending and free vibration analysis of functionally graded sandwich plates using the Refined Zigzag Theory». In: *Journal of Sandwich Structures and Materials* 16 (2014), pp. 669–699. DOI: https://doi.org/10.1177/1099636214548618.

[54] M. Gherlone. «On the use of zigzag functions in equivalent single layer theories for laminated composite and sandwich beams: a comparative study and some observations on external weak layers». In: *Journal of Applied Mechanics* 80 (6 2013). DOI: doi:10.1115/1.4023690.

[55] R. M. J. Groh and P. M. Weaver. «On displacement-based and mixed-variational equivalent single layer theories for modelling highly heterogeneous laminated beams». In: *International Journal of Solids and Structures* 59 (2015), pp. 147–170. DOI: https://doi.org/10.1016/j.ijsolstr.2015.01.020.

[56] A. Tessler. «Refined zigzag theory for homogeneous, laminated composite, and sandwich beams derived from Reissner's mixed variational principle». In: *Meccanica* 50.10 (2015), pp. 2621–2648. DOI: 10.1007/s11012-015-0222-0.

[57] R. M. J. Groh and A. Tessler. «Computationally efficient beam elements for accurate stresses in sandwich laminates and laminated composites with delaminations». In: *Computer Methods in Applied Mechanics and Engineering* 320 (2017), pp. 369–395. DOI: https://doi.org/10.1016/j.cma.2017.03.035.

[58] K. A. Hasim. «Isogeometric static analysis of laminated composite plane beams by using refined zigzag theory». In: *Composite Structures* 186 (2018), pp. 365–374. DOI: https://doi.org/10.1016/j.compstruct.2017.12.033.

[59] A. Kefal, K. A. Hasim, and M. Yildiz. «A novel isogeometric beam element based on mixed form of refined zigzag theory for thick sandwich and multi-layered composite beams». In: *Composites Part B: Engineering* 167 (2019), pp. 100–121. DOI: https://doi.org/10.1016/j.compositesb.2018.11.102.

186

[60] M. Patni et al. «Efficient 3D Stress Capture of Variable Stiffness and Sandwich Beam Structures». In: *AIAA Scitech 2019 Forum*. 2019, p. 1763.

[61] M. Gherlone. «Exact formulas for bending of sandwich beams using the Refined Zigzag Theory». In: (Barcelona, Spain). XI World Congress on Computational Mechanics. 2014.

[62] L. Iurlaro et al. «Experimental assessment of the Refined Zigzag Theory for the static bending analysis of sandwich beams». In: *Journal of Sandwich Structures and Materials* 20 (2018), pp. 86–105. DOI: 10.1177/1099636216650614.

[63] L. Iurlaro et al. «Free vibration analysis of sandwich beams using the Refined Zigzag Theory: an experimental assessment». In: *Meccanica* 50 (2015), pp. 2525–2535. DOI: 10.1007/s11012-015-0166-4.

[64] M. Di Sciuva et al. «A class of higher-order C0 composite and sandwich beam elements based on the refined zigzag theory». In: *Composite Structures* 132 (2015), pp. 784–803. DOI: https://doi.org/10.1016/j.compstruct.2015.06.071.

[65] E. Oñate, A. Eijo, and S. Oller. *Two-noded beam element for composite and sandwich beams using Timoshenko theory and refined zigzag kinematics.* Publication CIMNE No-346, 2010.

[66] E. Oñate, A. Eijo, and S. Oller. «Simple and accurate two-noded beam element for composite laminated beams using a refined zigzag theory». In: *Computer Methods in Applied Mechanics and Engineering* 213 (2012), pp. 362–382. DOI: 10.1016/j.cma.2011.11.023.

[67] L. Iurlaro, M. Gherlone, and M. Di Sciuva. «The (3, 2)-Mixed Refined Zigzag Theory for generally laminated beams: theoretical development and C0 finite element formulation». In: *International Journal of Solids and Structures* 73 (2015), pp. 1–19. DOI: https://doi.org/10.1016/j.ijsolstr.2015.07.028.

[68] A. Treviso, D. Mundo, and M. Tournour. «A C0-continuous RZT beam element for the damped response of laminated structures». In: *Composite Structures* 131 (2015), pp. 987–994. DOI: https://doi.org/10.1016/j.compstruct.2015.06.049.

[69] A. Eijo, E. Oñate, and S. Oller. «A numerical model of delamination in composite laminated beams using the LRZ beam element based on the refined zigzag theory». In: *Composite Structures* 104 (2013), pp. 270–280. DOI: https://doi.org/10.1016/j.compstruct.2013.04.035.

[70] A. Eijo, E. Oñate, and S. Oller. «Delamination in laminated plates using the 4-noded quadrilateral QLRZ plate element based on the refined zigzag theory». In: *Composite Structures* 108 (2014), pp. 456–471. DOI: https://doi.org/10.1016/j.compstruct.2013.09.052.

[71] D. O. Brush and B.O. Almroth. *Buckling of bars, plates and shells*. New York, NY: McGraw-Hill, 1975.

[72] J. Singer, J. Arbocz, and T. Weller. *Buckling Experiments: Experimental Methods in Buckling of Thin-Walled Structures: Basic Concepts, Columns, Beams and Plates*. John Wiley & Sons, 2007.

[73] J. L. Jr Sanders. «Nonlinear theories for thin shells». In: *Quarterly of Applied Mathematics* 21.1 (1963), pp. 21–36.

[74] L. Euler. «Sur la force des colonnes». In: *Memoires de l'Academie des Sciences de Berlin* (1759), pp. 252–282.

[75] S. Timoshenko and J. M. Gere. *Theory of elastic stability*. New York: McGraw-Hill New York, 1961.

[76] R. M. Rivello. *Theory and analysis of flight structures*. McGraw-Hill College, 1969.

[77] I. Sheinman I and M. Adan. «The effect of shear deformation on post-buckling behavior of laminated beams». In: *Journal of Applied Mechanics* 54.3 (1987), pp. 558–562. DOI: 10.1115/1.3173069.

[78] G. A. Thurston. «Newton's method applied to problems in nonlinear mechanics». In: *Journal of Applied Mechanics* 32.2 (1965), pp. 383–388. DOI: 10.1115/1.3625811.

[79] E. J. Barbero and I. G. Raftoyiannis. «Euler buckling of pultruted composite columns». In: *Composite Structures* 24.2 (1993), pp. 139–147. DOI: 10.1016/0263-8223(93)90035-O.

[80] A. A. Khdeir and J. N. Reddy. «Buckling of cross-ply laminated beams with arbitrary boundary conditions». In: *Composite Structures* 37.1 (1997), pp. 1–3. DOI: https://doi.org/10.1016/S0263-8223(97)00048-2.

[81] S. A. Emam and A. H. Nayfeh. «Postbuckling and free vibrations of composite beams». In: *Composite Structures* 88.4 (2009), pp. 636–642. DOI: 10.1016/j.compstruct.2008.06.006.

[82] Z. M. Li and P. Qiao. «Buckling and postbuckling behavior of shear deformable anisotropic laminated beams with initial geometric imperfections subjected to axial compression». In: *Engineering Structures* 85 (2015), pp. 277–292. DOI: 10.1016/j.engstruct.2014.12.028.

[83] G. He, D. Wang, and X. Yang. «Analytical solutions for free vibration and buckling of composite beams using a higher order beam theory». In: *Acta Mechanica Solida Sinica* 29.3 (2016), pp. 300–315. DOI: https://doi.org/10.1016/S0894-9166(16)30163-X.

[84] F. G. Canales and J.L. Mantari. «Buckling and free vibration of laminated beams with arbitrary boundary conditions using a refined HSDT». In: *Composites Part B: Engineering* 100 (2016), pp. 136–145. DOI: `https://doi.org/10.1016/j.compositesb.2016.06.024`.

[85] V. N. Van Do and C.H. Lee. «Numerical investigation on post-buckling behavior of FGM sandwich plates subjected to in-plane mechanical compression». In: *Ocean Engineering* 170 (2018), pp. 20–42. DOI: `https://doi.org/10.1016/j.oceaneng.2018.10.007`.

[86] A. Karrech et al. «Buckling and post-buckling analysis of geometrically non-linear composite plates exhibiting large initial imperfections». In: *Composite Structures* 174 (2017), pp. 134–141. DOI: `https://doi.org/10.1016/j.compstruct.2017.04.029`.

[87] E. H. Salmon. *Columns: A Treatise on the Strength and Design of Compression Members.* H. Frowde and Hodder & Stoughton, 1921.

[88] T. von Kármán. «Untersuchungen über knickfestigkeit». In: *Mitteilungen über Forschungsarbeiten auf dem Gebiete des Ingenieurwesens insbesondere aus den Laboratorien der technischen Hochschulen.* Springer, 1910, pp. 1–44.

[89] B. Kirsch. *Ergebnisse von Versuchen über die Knickfestigkeit von Säulen mit fest eingespannten.* Franz Deuticke, 1905.

[90] L. von Tetmajer. *Die Gesetze der Knickungs-und der zusammengesetzten Druckfestigkeit der technisch wichtigsten Baustoffe.* Franz Deuticke, 1903.

[91] R. V. Southwell. «On the analysis of experimental observations in problems of elastic stability». In: (London). Ed. by The Royal Society. Vol. 135.Mathematical, Physical and Engineering Sciences. Series A. 1932, pp. 601–616. DOI: `https://doi.org/10.1098/rspa.1932.0055`.

[92] E. E. Lundquist. *Generalized analysis of experimental observations in problems of elastic stability.* TN 658. NACA, 1938.

[93] LH L. H. Donnell. «On the application of Southwell's method for the analysis of buckling tests». In: *S. Timoshenko 60th Anniversary Volume* (1938), pp. 27–38.

[94] W. T. Tsai. «Note on Southwell's Method for Buckling Tests of Struts». In: *Journal of applied mechanics* 53.4 (1986), pp. 953–954.

[95] K. Chandrashekhara and K. Bhatia. «Active buckling control of smart composite plates-finite-element analysis». In: *Smart Materials and Structures* 2.1 (1993).

[96] A. A. Berlin. «Towards intelligent structures: active control of buckling». PhD thesis. Massachusetts Institute of Technology, 1994.

[97] S. P. Thompson and J. Loughlan. «The active buckling control of some composite column strips using piezoceramic actuators». In: *Composite Structures* 32.1-4 (1995), pp. 59–67. DOI: https://doi.org/10.1016/0263-8223(95)00048-8.

[98] A. R. de Faria and S. F. M. de Almeida. «Enhancement of pre-buckling behavior of composite beams with geometric imperfections using piezoelectric actuators». In: *Composites Part B: Engineering* 30.1 (1999), pp. 43–50. DOI: 10.1016/S1359-8368(98)00047-X.

[99] J. G. Chase and M. Yim. «Optimal stabilization of column buckling». In: *Journal of engineering mechanics* 125.9 (1999), pp. 987–993.

[100] J. G. Chase and S. Bhashyam. «Optimal stabilization of plate buckling». In: *Smart materials and structures* 8.2 (1999), p. 204.

[101] A. Mukherjee and A. S. Chaudhuri. «Active control of dynamic instability of piezolaminated imperfect columns». In: *Smart materials and structures* 11.6 (2002), p. 874. DOI: 10.1088/0964-1726/11/6/307.

[102] Y. Fridman and H. Abramovich. «Enhanced structural behavior of flexible laminated composite beams». In: *Composite Structures* 82.1 (2008), pp. 140–154. DOI: 10.1016/j.compstruct.2007.05.007.

[103] H. Waisman and H. Abramovich. «Active stiffening of laminated composite beams using piezoelectric actuators». In: *Composite structures* 58.1 (2002), pp. 109–120. DOI: 10.1016/S0263-8223(02)00035-1.

[104] L. Edery-Azulay and H. Abramovich. «Piezoelectric actuation and sensing mechanisms—-closed form solutions». In: *Composite Structures* 64.3-4 (2004), pp. 443–453. DOI: 10.1016/j.compstruct.2003.09.045.

[105] A. R. Damanpack et al. «Active control of geometrically non-linear transient response of sandwich beams with a flexible core using piezoelectric patches». In: *Composite Structures* 100 (2013), pp. 517–531. DOI: http://dx.doi.org/10.1016/j.compstruct.2012.12.029.

[106] A. Muc, P. Kędziora, and A. Stawiarski. «Buckling enhancement of laminated composite structures partially covered by piezoelectric actuators». In: *European Journal of Mechanics-A/Solids* 73 (2019), pp. 112–125. DOI: https://doi.org/10.1016/j.euromechsol.2018.07.002.

[107] T. H. Brockmann. *Theory of Adaptive Fiber Composites*. Springer, 2009.

[108] H. Chai, C. D. Babcock, and W. G. Knauss. *Fracture energy of graphite-epoxy composite laminates*. Solid Mechanics publication, California Institute of Technology. Galcit SM Rep. 79-13, 1979.

[109] H. Chai, C. D. Babcock, and W. G. Knauss. *On the interaction of buckling and delamination.* Solid Mechanics publication, California Institute of Technology. Galcit SM Rep. 79-14, 1979.

[110] H. Chai, C. D. Babcock, and W. G. Knauss. *The incorporation of bending into the buckling delamination analysis.* Solid Mechanics publication, California Institute of Technology. Galcit SM Rep. 79-15, 1979.

[111] H. Chai, C. D. Babcock, and W. G. Knauss. *Interaction of buckling and delamination in a delaminated beam under pure bending.* Solid Mechanics publication, California Institute of Technology. Galcit SM Rep. 79-16, 1979.

[112] H. Chai, C. D. Babcock, and W. G. Knauss. «One dimensional modelling of failure in laminated plates by delamination buckling». In: *International Journal of Solids and Structures* 17.11 (1981), pp. 1069–1083. DOI: https://doi.org/10.1016/0020-7683(81)90014-7.

[113] G. A. Kardomateas and D. W. Schmueser. «Buckling and postbuckling of delaminated composites under compressive loads including transverse shear effects». In: *AIAA journal* 26.3 (1988), pp. 337–343. DOI: https://doi.org/10.2514/3.9894.

[114] D. Shu. «Buckling of multiple delaminated beams». In: *International Journal of Solids and Structures* 35.13 (1998), pp. 1451–1465. DOI: https://doi.org/10.1016/S0020-7683(97)00124-8.

[115] U. Hansen. «Compression behaviour of FGM sandwich specimens with interface debonding». In: *Journal of Composite Materials* 32 (4 1998), pp. 335–360.

[116] H. Mahfuz and S. Islam and L. Carlsson and G. Kardomateas and S. Jeelani, «Buckling response of sandwich composites: Effect of core density and implanted interface cracks». In: *Extended Abstracts of the 13th International Conference on Composite Materials.* 2001.

[117] F. Chen and P. Qiao. «Buckling of delaminated bi-layer beam-columns». In: *International Journal of Solids and Structures* 48 (2011), pp. 2485–2495. DOI: 10.1016/j.ijsolstr.2011.04.020.

[118] S. D. Akbarov and N. Yahnioglu. «Buckling delamination of a sandwich plate-strip with piezoelectric face and elastic core layers». In: *Applied Mathematical Modelling* 37.16-17 (2013), pp. 8029–8038. DOI: http://dx.doi.org/10.1016/j.apm.2013.02.051.

[119] S. Wang et al. «Post-local buckling-driven delamination in bilayer composite beams». In: *Composite Structures* 133 (2015), pp. 1058–1066. DOI: http://dx.doi.org/10.1016/j.compstruct.2015.08.012.

[120] Z. Juhász and A. Szekrényes. «The effect of delamination on the critical buckling force of composite plates: Experiment and simulation». In: *Composite Structures* 168 (2017), pp. 456–464. DOI: http://dx.doi.org/10.1016/j.compstruct.2017.02.052.

[121] W. Li and H. J. Shen. «A refined layerwise finite element modeling of delaminated composite laminates with piezoelectric layers». In: *Thin-Walled Structures* 131 (2018), pp. 792–804. DOI: https://doi.org/10.1016/j.tws.2018.07.030.

[122] R. G. Ballas. *Piezoelectric Multilayer Beam Bending Actuators*. Springer, 2007.

[123] M. A. Crisfield. *Non-linear Finite Element Analysis of Solids and Structures*. John Wiley & Sons, 1991.

[124] F. C. Fasano. «Sviluppo e implementazione di tecniche di interfaccia per elementi finiti trave». MSc Thesis. Politecnico di Torino, 2008.

[125] Smart Material. *Macro Fiber Composite Data Sheet*. URL: https://www.smart-material.com/media/Datasheets/MFC_V2.3-Web-full-brochure.pdf.

This Ph.D. thesis has been typeset by means of the TEX-system facilities. The typesetting engine was pdfLATEX. The document class was `toptesi`, by Claudio Beccari, with option `tipotesi=scudo`. This class is available in every up-to-date and complete TEX-system installation.